2D materials, colloidal nanocrystals and mixed dimensional heterostructures for nanoelectronics and optoelectronics in high doping regime

Ulrich Noumbe Nguetchuissi

UNIVERSITÉ DE STRASBOURG

ÉCOLE DOCTORALE DE PHYSIQUE ET CHIMIE-PHYSIQUE

Institut de Physique et Chimie des Matériaux de Strasbourg

THÈSE présentée par :

Ulrich NOUMBE NGUETCHUISSI

soutenue le : **02 novembre 2020**

pour obtenir le grade de : **Docteur de l'Université de Strasbourg**

Discipline / Spécialité : Physique / Nanophysique

2D materials, colloidal nanocrystals and mixed dimensional van der Waals heterostructures for nanoelectronics and optoelectronics in high doping regime

THÈSE dirigée par :

M. Jean-François DAYEN	Maitre de conférence, Université de Strasbourg

RAPPORTEURS :

M. Paolo BONDAVALLI	Senior Expert HDR, CRN, Thalès
M. Vincent DERYCKE	Chercheur, CEA Saclay

EXAMINATEURS :

M. Paolo SAMORI	Professeur, Université de Strasbourg
Mme Maria-Luisa DELLA ROCCA	Docteur, Université Paris-Diderot

Contents

Remerciements

J'aimerai remercier premièrement les membres de mon jury qui non seulement ont accepté d'évaluer mon travail de thèse, mais aussi dans cette situation de crise sanitaire de la Covid-19 n'ont ménagé aucun effort pour suivre la présentation de mon travail. Notamment Paolo Samori de l'Institut Supramoléculaire de Strasbourg (ISIS) qui, au delá de m'avoir fait l'honneur de présider mon jury, était en présentiel lors de ma présentation, à Paolo Bondavalli du Centre des Recherches sur les Nanomatériaux à Thalès et Vincent Dérycke du CEA de Paris Saclay pour avoir été rapporteurs de mon travail et des échanges très intérressants et pertinants pendant la présentation bienqu'étant en visio, enfin à Maria-Luisa Della Rocca de l'Université de Paris-Diderot, pour avoir été examinatrice et pour nos échanges très enrichissants en viso durant ma présentation. J'ai beaucoup apprécié ce moment de discussions, et surtout votre intérêt et votre enthousiame envers mes résultats de thèse.

Bien évidemment, je souhaite exprimer ma reconnaissance à mon directeur de thèse Jean-François Dayen, pour m'avoir accuellir dans son groupe depuis mon stage de Master et pour m'avoir fait confiance en me proposant ce projet de thèse. Tu as très vite compris la manière dont je travaille, cela nous a permis d'être plus efficace dans nos discussions scientifiques tout le long de ma thèse. Je te remercie pour ton écoute attentive, tes conseils au quotidien et les collobarations que tu as initié pour le bon déroulement de ma thèse.

Je tiens également à remercier nos collaborateurs du groupe d'Emmanuel Lhuillier à l'Institut des Nanosciences de Paris (INSP). En partiulier, merci Emmanuel pour m'avoir permis de venir plusieurs fois dans ton laboratoire pour faire mes mesures optoélectroniques, pour nos échanges scientifiques, pour tes conseils, sans oublier les réunions de groupre du vendredi soir autour d'une bière. Merci également à Charlie Gréboval thésard du groupe pour la synthèse des nanocristaux et avec qui j'ai travaillé pendant mes déplacements à Paris, sans oublier Clément Livache et Prachi Rastochi thésard et postdoc à l'époque dans le groupe.

Je remercie Abdelkarim Ouerghi et Julien Chaste du Centre de Nanosciences et Nan-

otechnologies (C2N) Paris-Saclay et Thibault Brule à HORIBA Scientific de Palaiseau pour notre bonne collaboration et les mesures Raman.

Merci à Donald Mouafo ancien thésard du groupe à l'IPCMS qui m'a accueilli et a facilité mon insertion dans le groupe. Tu as été pour moi une grande source d'inspiration. Un merci particulier à Guillaume Chaumy qui a été plus qu'un collègue pour moi dans le groupe, merci pour ta bonne humeur et ton savoir vivre. Je remercie également Etienne Lorchat pour m'avoir former à l'exfoliation et aux transferts des feuillets de matériaux bi-dimenesionnels.

Je souhaite également à dire merci à mes collègues de bureau notamment Peter Dune pour sa grande culture scientifique, Xin Zhang, Loic Mockzo, Léo Colombier, Nikita Konstantinov pour notre bonne ambiance de bureau et des repas de midi. Merci également aux doctorants et stagiaires du labo: Luis Parra Lopez, Matias Grassi, José Solano, Olivier Ngassam, Gladice Manifouet, Anatolii Makhort, Khaleb Rassoul, Mauricio Gomez, Brice Zanguim, Louis David Mohgouk et tous les autres.

Je remercie également tous les membres de l'IPCMS en général qui d'une manière ou d'une autre ont facilité ces trois années au laboratoire. Je remercie particulièrement Mebarek Alouani au DMONS, responsable du Master Matière Condensée et Nanophysique, qui m'a accueilli dès mon arrivé en 2016 pour ce Master. Votre passion et votre amour pour la science en général et la physique en particulier m'ont beaucoup motivé à faire cette thèse. Mes remerciements vont aussi vers les autres membres de l'équipe Nano-dispositifs notamment Bernard Doudin, Stéphane Berciaux, Bodhan Kundys pour les nombreuses discussions techniques, scientifiques et, à Fabien Chevrier pour son aide technique au quotidien. Une mention très spéciale au personnel de STnano notamment Sabine Siegwald, Romain Bernard et Hicham Majjad pour leur formation et soutient technique en salle blanche. Romain et Sabine, vous avez été patient envers moi depuis mon arrivé et avez su me guider lors de mon apprentissage, puis me motiver et m'encourager lors cet étape très importante de ma thèse qui était la fabrication de mes échantillons. Grace à vous, j'ai pris du plaisir à processer mes échantillons et j'ai developpé un intérêt particulier pour la nanofabrication et le travail en salle blanche, encore merci.

Pour finir, un grand merci à toute ma famille et à mes amis. Un "MERCI" particulier à mes parents **M. et Mme. Nguétchuissi** qui m'ont toujours soutenu et fait confiance dans tout ce que j'entreprends. Je vous dédie cette thèse en signe de ma profonde reconnaissance. Trouver en ce travail tout l'amour que je vous porte.

Résumé de thèse

Les semi-conducteurs conventionnels tels que l'arséniure de silicium et d'indium gallium (InGaAs) ont rencontré un goulot d'étranglement dans l'électronique et la photonique modernes en termes de couverture spectrale, de basse résolution et de non-transparence [Huo18]. En effet, malgré le niveau de technologie mature des dispositifs à base de silicium, ces derniers rencontrent des limitations fondamentales. Par exemple, les capteurs d'image à base de la technologie métal oxyde sémiconducteur (MOS) sont limités par les bruits et l'efficacité quantique dans le visible (bande interdite indirecte de 1,1 eV) tandis que les photodiodes infrarouges (IR) InGaAs (0,5 eV à 0,73 eV) en plus du bruit et des problèmes d'efficacité sont limités par les procédés de fabrication dus aux complexes techniques de croissance par épitaxie dans des conditions de vide poussé. De plus, ces détecteurs de silicium sont opaques car une région optiquement active avec une assez grande épaisseur de l'ordre du micron est nécessaire pour absorber efficacement la lumière. Celà rend donc ces détecteurs non compatible pour les applications dans l'électronique et optoélectronique flexible, portable et transparente. Les nouveaux matériaux émergents de faible dimension appelé nanomatériaux peuvent contourner tous ces problèmes en profitant de leur flexibilité mécanique, leurs propriétés électroniques et optiques intéressantes, ainsi que leur production à grande échelle et leur facile intégration dans les dispositifs.

Ces dernières années, les nanomatériaux (c'est-à-dire les matériaux dont l'une des dimensions est inférieure à la centaine de nanomètres) ont suscité un intérêt croissant pour la recherche dans le domaine électronique et optoélectronique. Il s'agit notamment des matériaux bi-dimensionels ou 2D (graphène, dichalcogénure de métaux de transition (DMTs), ...), des matériaux 1D (nanofils, nanotubes, ...) et des matériaux 0D (nanoparticules, nanocristaux, molécules, ...) avec une, deux et trois dimensions inférieures à 100 nm respectivement. Leurs petites dimensions permettent de faire émerger de nouvelles propriétés inaccessibles dans les matériaux massifs, ceci principalement à cause du confinement quantique aux petits échelles. La prédominance des effets quantiques à l'échelle nanométrique a ainsi ouvert de nombreux domaines de recherche fondamentale dont la nanoélectronique et la spintronique ainsi que l'optoélectronique [Radisavljevic13, Seneor07, Lhuillier17, Huo18]. Lorsque la taille du semi-conducteur est inférieure à la taille d'une paire électron-trou, ou exciton, des propriétés de confinement quantique apparaissent. Les propriétés optiques, optoélectroniques ainsi que les propriétés de transport deviennent alors dépendantes de la taille. Tandis que les matériaux 2D semi-conducteurs (DMTs qui sont des matériaux en feuilles et flexibles) présentent une transition de bande interdite indirecte à directe de la multi-couche à la monocouche, les propriétés optiques et électriques des nanocristaux colloïdaux quant à eux peuvent être ajustées en changeant leurs tailles et formes au cours de leur synthèse en solution par rapport aux complexes techniques épitaxiales et coûteuses de la technologie existante. Ainsi, les matériaux 2D et les nanocristaux sont considérés comme des candidats prometteurs pour la nouvelle génération d'appareils à faible coût et de faible puissance en raison de leurs propriétés électroniques et optiques flexibles, petites et

remarquables.

Lorsqu'on implémente les nanomateriaux semi-conducteurs dans les dispositifs, la modulation de leur densité de porteurs est essentielle pour adapter leurs propriétés électriques et leurs fonctions, ceci avec de nouveaux phénomènes physiques devant se produire à un niveau de dopage plus élevé. En effet, lors de leur mise en œuvre dans des transistors à effet de champ (FET), des phototransistors ou des photodiodes, l'énergie de barrière pour les porteurs aux interfaces métal/semi-conducteur (contacts Schottky) est un phénomène universel qui limite les performances du dispositif. Réduire ces barrières énergétiques en régime dopage élevé, ou l'utilisation d'électrodes en graphène pour otenirr des contacts modulables devient évident pour améliorer la performance de ces dispositifs. De manière générale, deux stratégies principales ont été utilisées jusqu'à présent pour doper des nanomatériaux: les diélectriques conventionnels (typiquement la couche de silice sur une tranche de silicium) et les électrolytes (liquide ionique, gel ionique, ...). Dans la première approche, le diélectrique a l'avantage d'être simple à mettre en œuvre mais nécessite une tension de fonctionnement élevée et est limité par une éventuelle fuite électrique, puis la densité de porteurs accumulée maximale est limitée à de 10^{12} cm^{-2}. La deuxième méthode est d'un intérêt extrême lorsque les densités de surface plus grande ($> 10^{13}$ cm^{-2}) sont ciblées [Lhuillier14, Zanettini15a]. En effet, avec l'électrolyte, la capacité de grille est pilotée par le rapport de la constante diélectrique divisé par l'épaisseur de la double couche ionique. Cette dernière d'épaisseur de l'ordre de 1 nm, permet d'atteindre une grande capacité à faible tension de polarisation pour le dispositif, mais encore plus important est la possibilité de réaliser une injection de charge massive dans les nanomatériaux. D'un autre côté, l'électrolyte nécessite une température relativement élevée pour fonctionner. Une telle contrainte n'est pas compatible avec un matériau infrarouge qui nécessite généralement un fonctionnement à basse température. Un autre inconvénient de la technologie de grille d'électrolyte est que ce dernier recouvre le matériau, c'est donc un obstacle pour une excitation optique directe supérieure car il peut absorber ou diffuser la lumière et empêcher son utilisation pour les appareils optoélectroniques et les études optiques. Des alternatives au diélectrique et à l'électrolyte ont été proposées et reposent sur le polymère ferroélectrique et plus récemment sur l'utilisation de verres ioniques. Le groupe de Shukla sur les matériaux 2D en utilisant des verres classiques tels que le borosilicate et le verre sodocalcique. Le verre est d'abord chauffé à haute température pour donner aux ions une certaine mobilité, et un grand champ électrique est appliqué sur le substrat pour les faire bouger. Les verres conventionnels nécessitent cependant une température de fonctionnement autour de 500 K, ce qui est incompatible avec la plupart des nanomatériaux tels que les NCs, les molécules ou polymères, pour lesquels les températures de fusion sont bien inférieures. C'est notamment le cas pour les chalcogénures de plomb et de mercure couramment utilisés dans l'infrarouge, dont les températures de synthèse sont de l'ordre de 80 à 150 °C. Récemment, le groupe de Cui a exploré l'utilisation du verre ionique LaF_3 pour induire un effet de grille dans un feuillet de MoS_2 [Wu18]. Le LaF_3 est à l'origine utilisé pour les optiques infrarouges et présente une forte transparence dans l'infrarouge

moyen, ce qui est promettant pour la conception des phototransistors avec une excitation en face arrière. De plus, les mobilités ioniques restent suffisamment élevées pour induire un effet de grille pour des températures jusqu'à 180 K, contournant le besoin d'un grand champ électrique et d'une température élevée imposée par les verres en borosilicate et sodocalcique. Cependant, il n'y a pas de rapport à ce jour sur l'utilisation du verre ionique LaF_3 pour doper les nanocristaux et pour la photodétection sur les nanocristaux, les matériaux 2D et leur hétérostructures.

C'est dans ce cadre que s'inscrivent mes travaux de thèse. Mon projet de thèse vise à développer et étudier des approches alternatives pour induire un dopage élevé pour la photodétection à basse température dans les matériaux 2D, les nanocristaux colloïdaux (NCs) et leurs hétérostructures. J'ai utilisé un substrat de trifluorure de lanthane LaF_3 en verre ionique comme grille solide pour obtenir un régime de dopage élevé dans les nanomatériaux avec des densités de charge supérieures 10^{13} cm^{-2} (non accessible avec un diélectrique conventionnel telque le SiO_2 et à des températures de fonctionnement entre 160 K et 260 K impossible pour des grilles électrolytiques. Cela a permis de moduler et de réduire les barrières énergétiques aux contacts Schottky pour des injections ou des extractions efficaces d'électrons et/ou de trous générés par la lumière aux électrodes, ainsi d'améliorer les performances des phototransistors à base de tellure de mercure (HgTe) et de diséléniure de molibdène ($MoSe_2$). La possibilité de fabriquer des électrodes de graphène à grande échelle, ceci avec une transparence au champ électrique vertical combinées avec une grille en verre ionique à haute capacité nous ont permis de concevoir et d'étudier une nouvelle configuration de photo-détecteurs infrarouges 2D/0D avec de propriétés intéressantes.

Ces travaux ont été réalisé en étroite collaboration avec le groupe d'Emmanuel Lhuillier à l'Institut des Nano-Sciences de Paris (INSP) qui a une grande expertise sur la synthèse des NCs et où j'ai fait plusieurs sessions de mesures et toutes les mesures optoélectroniques pendant ma thèse.

Ce résumé est organisé en 3 parties.
Dans la première partie, j'introduis le substrat de verre ionique LaF_3 en tant que grille solide à haute capacité pour étudier les propriétés de transport et de photo-transport des nanocristaux. Pour la première fois, nous sondons la dynamique de la photoréponse de nanocristaux de HgTe à bande interdite étroite en dopage élevé régime utilisant la technologie du verre ionique.
La partie 2 est dédiée à l'étude des propriétés de transport et de photo-transport des matériaux 2D en régime de dopage élevé. Nous étendons la technique de gating au $MoSe_2$, MoS_2, WSe_2 et au WS_2. Puis, nous utilisons l'adressabilité optique directe du substrat verre ionique pour étudier le mécanisme de photo-transport et de recombinaison des porteurs dans des FET à base de feuillet de $MoSe_2$.

Enfin, je présente la réalisation et l'étude de phototransistors très originaux basés sur l'utilisation d'un canal en nano-cristaux de HgTe combiné à des électrodes en graphène. L'utilisation d'électrodes de graphène sélectives en porteurs combinée à la haute capacité du verre ionique permet de mettre en oeuvre une nouvelle architecture d'hétérojonction 2D-0D qui sont reconfigurables et peuvent être réglés de la configuration p-p' ou n-n' à une diode p-n.

1: FET et Photo-FET de nanocristaux colloidaux en régime de fort dopage en utilisant le verre ionique LaF_3

Au-delà de leur luminescence dans le visible, les nanocristaux colloïdaux (NCs) ont suscité l'intérêt pour le design des dispositifs optoélectroniques et en particulier pour les capteurs infrarouges (IR) en raison de leur traitement facile des solutions et de leurs excellentes performances [Hafiz19, Lhuillier17]. Tandis que les chalcogénures de plomb ont attiré beaucoup d'attention pour la conception de cellules solaires collectant dans le proche infrarouge (NIR) (800 nm à 1μm), les chalcogénures de mercure en particulier les nanocristaux de HgTe à bande interdite étroite [Livache19, Killilea19, Kershaw13, Keuleyan11] suscitent actuellement un vif intérêt pour la conception de capteurs infrarouges de hautes performances dans le SWIR (1 à 1,7 μm) et MWIR (3 à 5 μm) [Lu19, Livache18b, Lhuillier17]. Les développements récents incluent des photodiodes à haute détection pour l'imagerie thermique [Ackerman18]. L'intégration du matériau actif HgTe dans les FET a permis de construire des phototransistors efficaces dans MWIR [Lhuillier13]. De très hautes responsivité au-dessus de 100 mA/W et une détectivité élevée au-dessus de 10^{10} Jones dans le SWIR ont été signalés sur les phototransistors d'HgTe à température ambiante [Chen17]. Dans les phototransistors en général, la grille ne sert pas à sonder les porteurs majoritaires du film mais plutôt à réduire le courant d'obscurité et amener la couche mince dans un point de fonctionnement qui maximise le rapport signal sur bruit.
Dans cette partie de mon travail, j'étudie le verre ionique LaF_3 comme substrat pour induire un effet de grille en configuration arriére dans les nanocristaux.

Substrat en verre ionique de LaF_3 pour de dopage élevé

Le trifluorure de lanthane LaF_3 cristallise dans une structure hexagonale avec le groupe d'espace $P6_3/mcm$. C'est un conducteur ionique à l'état solide, il est transparent avec une conduction d'ions fluorure [Schoonman80, Solomon]. à cause les vacances des ions fluorures déjà existantes dans le cristal, ces derniers, de petite masse (F^-) peuvent se déplacer en par saut à travers le réseau cristallin tandis que les ions lanthanes restent immobiles en raison de leur grande taille et masse (voir Fig.2.2.(a)) [Hoff97]. Le LaF_3 est un isolant électrique (bande interdite électrique de 4,9 eV) et a une bonne stabilité mécanique, il peut ainsi être utilisé à la fois comme substrat et comme diélectrique de grille solide compatible avec les procédés de fabrication de dispositifs à base de silicium. Pour comprendre le mécanisme de charge dans

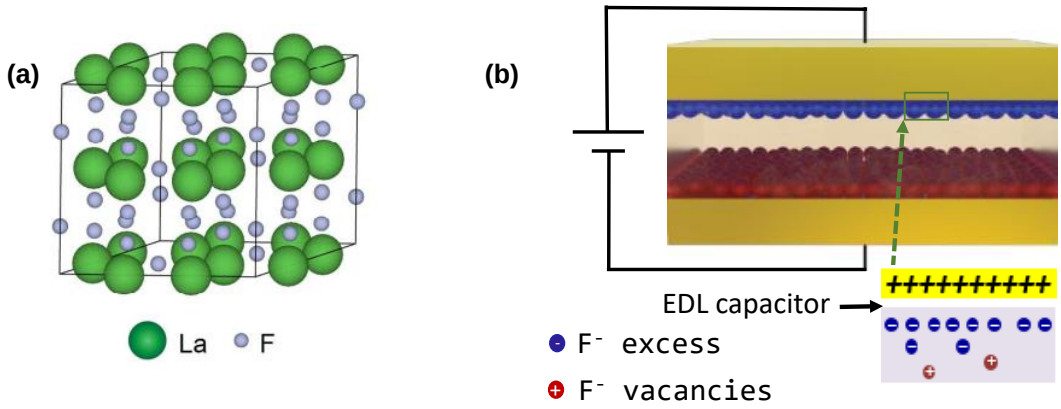

Figure 1 *– (a) Structure cristalline de LaF_3, adapté de [Wu18]. (b) Schéma d'un substrat de LaF_3 pris en sandwich par des électrodes métalliques.*

le substrat, nous avons pris en sandwich 1 mm d'épaisseur de substrat de 25 mm^2 avec des contacts Ti/Au (50nm) (Métal/LaF_3/Métal) et nous avons réalisé des mesures spectroscopies d'impédance électrochimique (EIS). Lorsqu'une polarisation externe est appliquée, les ions fluorures négatifs se déplacent vers l'électrode positive tandis que les lacunes de fluorure positives s'accumulent au niveau de l'électrode négative et forment une double couche électrique (EDL) aux interfaces à l'équilibre comme le montre la figure 2.2. (b).
L'EIS est une technique précieuse qui a été utilisée par de nombreuses institutions pendant plus d'un siècle à des fins telles que l'analyse de la corrosion, adsorption propriétés des molécules (phénomène interfacial) et aussi utilisé pour suivre le fonctionnement des batteries et des piles à combustible [Warburg99, Nernst94, Gomadam05, He09, Mohsen12]. La méthode implique l'application d'une petite perturbation (une faible tension sinusoïdale ou une superposition de tension sinusoïdale) au niveau des électrodes et analyser le courant résultant dans le domaine fréquentiel. Ainsi, lors de l'application d'une petite tension alternative V (jω) par un potentiostat interfacé avec le logiciel d'analyse de contrôle NOVA comme nous l'avons fait dans ce travail, à partir de sa réponse de mesure I (jω), l'impédance opérationnelle est définie comme le rapport entre la tension complexe et le courant [Randviir13]:

$$Z = \frac{V(j\omega)}{I(j\omega)} = \frac{|V| * \exp(j\omega t)}{|I| * \exp(j\omega t + \theta)} = |Z| * \exp(j\theta) = Z' + jZ'' \quad (1)$$

où Z est l'impédance, j le nombre complexe, θ la phase entre le courant et la tension et ω la fréquence. Les données extraites du logiciel peuvent être presentées soient dans le diagramme de Nyquist où la partie imaginaire Z" est representée en fonction de la partie réelle Z', ou dans le diagramme de Bode avec une lecture directe de l'impédance et phase en fonction de la fréquence. On observe une tendance générale sur les courbes de Bode (voir 2. (a) et (b)). Trois régions peuvent clairement être identifiées sur les 2. (a): Une pente à haute fréquence, un plateau et une autre plateau à plus basses Nous avons modélisé le système par deux circuits RC en série, l'un pour le substrat massif et l'autre pour la double couche électrique dans lequel la résistance double couche est en série avec l'impédance de

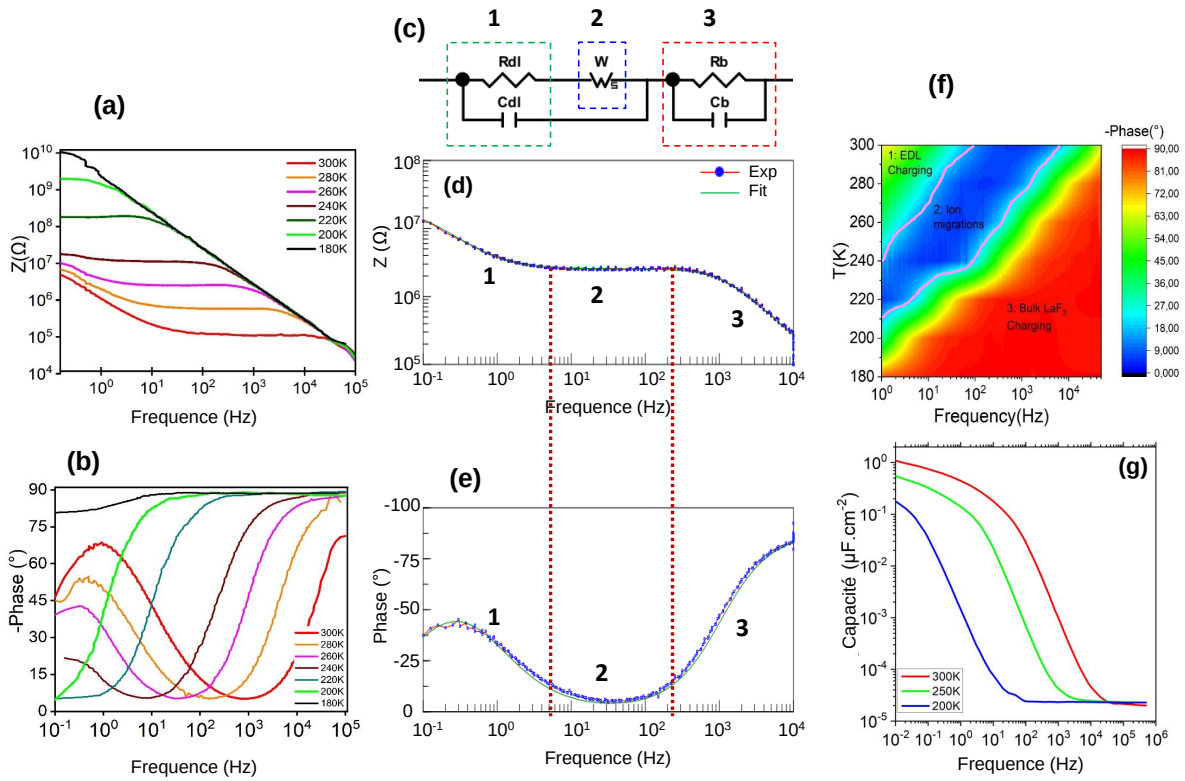

Figure 2 *– Courbes de Bodes à 10 mV AC. (a) \|Z\| en fonction de la fréquence. (b) Phase en fonction de la fréquence. (c) Circuit équivalent du système. (d) A 260 K: Fit de \|Z\| en fonction de la fréquence en verte, donnée expérimentale en rouge. (e) A 260 K: Fit de la phase en fonction de la fréquence en verte, donnée expérimentale en rouge. (f) Carte expérimentale de température-fréquence en fonction de la phase. 3: comportement du sustrat massif, 2: migration des ions, 1: double couche électrique. (g) Capacité en fonction de la fréquence à differentes températures.*

Warburg, ce dernier permet d'avoir les effets diffusifs du système donc prend en compte la migration des ions dans le substrat (2. (a). On a observé un très bon accord entre les données expérimentales et les simulations avec nos trois régions (2. (d) et (e)). On a également caractérisé la dépendance de la phase en fonction de la temperature et la frequence en fonction de la phase. Pour chaque température en fonction du début et la fin du plateau, on a pu délimiter les 3 régions. **Il en ressort de cette carte pour avoir une capacité double couche électrique, on doit être à faible fréquence pour permettre aux ions atteindre la surface et à des temperatures pas très élévé pour limiter la fuite mais suffisante pour permettre la mobilité des ions**. Enfin nous effectuer les mesures lock-in de la capacité en fontion de la fréquence à Paris, comme observé sur la 2. (g) , on a le même cormportement que les mesures de spectroscopie d'impédance avec les trois régimes et on arrive bien à quantifié la capacité dans le régime qui nous intéresse i.e à basses fréquences. On arrive à obtenir des capacités atteignant le micro Farad, nécessaire pour induire des dopages électrostatiques élevés dans les nanomatériaux.

Phototransistor de nanocristaux d'HgTe en régime de fort dopage

Après avoir montré que le substrat de LaF_3 peut être utilisé pour induire des dopages élevés, dans cette partie nous comparons les performances obtenues avec une grille diélectrique conventionnelle à travers le SiO_2 et avec un électrolyte. Nous démontrons que non seulement la transconductance dans l'obscurité peut être contrôlée avec la grille des verres ioniques mais aussi la photoréponse.

Des nanocristaux de HgTe avec une absorption dans l'infrarouge (énergie de bande

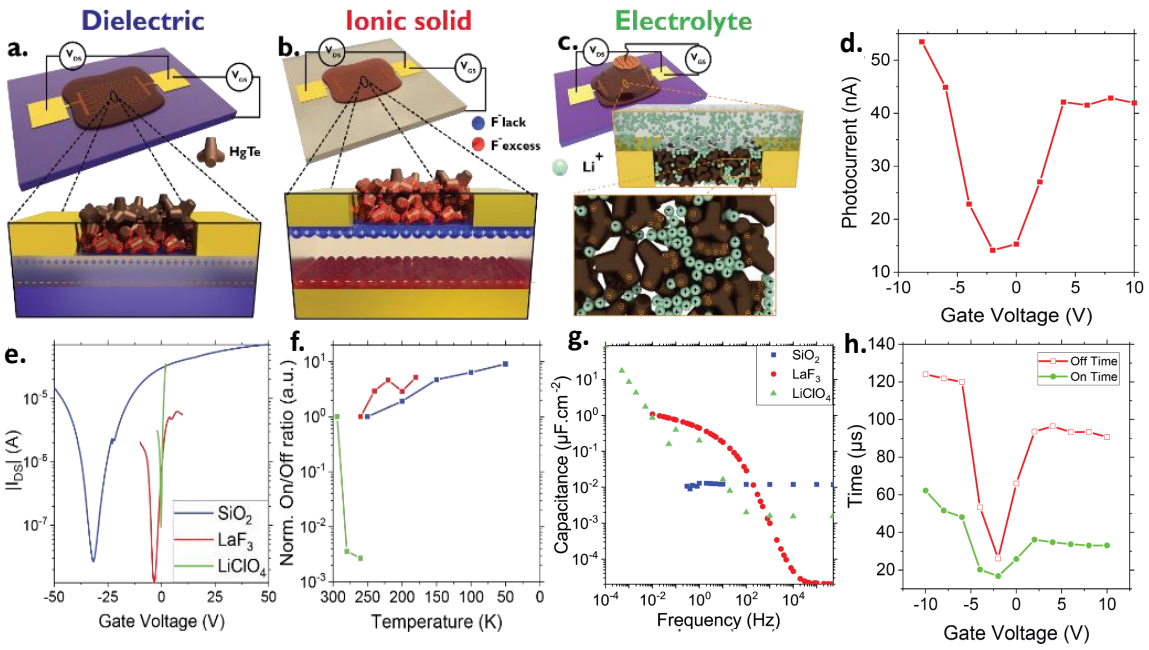

Figure 3 *– Schéma du transistor à base nanocristaux d'HgTe à grille arrière lorsque $V_{gs} > 0$ sur: (a) SiO_2. (b) LaF_3. (c) Schéma du transistor à base HgTe à grille supérieure avec l' electrolyte $LiClO_4$. (d) Photocourant mesuré sous une excitation de 4 mW avec une longueur d'onde de 1,55 µm en fonction de la tension de grille de LaF_3 à 200 K. (e) Courbes de transconductance obtenues pour les nanocristaux de HgTe avec différentes techniques de dopage: SiO_2 et LaF_3 sont mesurées à 200 K, celle de l'électrolyte est mesurée à 300 K. (f) Rapports On/Off normalisés par le rapport à la température la plus élevée des courbes de transfert mesurées à différentes températures pour différentes techniques de dopage. (g) Capacité de la grille mesurée à 300 K sous un signal AC de 300 mV pour différentes configurations de grilles. (h) Temps de réponses à 1 kHz mesurés à 200 K pour différentes tensions de grille de LaF_3 sous une excitation de 4 mW à 1,55 Âţm.*

d'environ 500 meV $\approx$ 4000 cm^{-1} ou 2,5 μm) ont été synthétisés par nos collaborateurs à l'INSP en utilisant une suspension colloïdale en solution. Nous avons par la suite processé des échantillons pour chacune des trois techniques de grille (diélectrique SiO_2, verre ionique LaF_3, électrolyte) en utilisant les lithographies optique et électronique, et fait une étude comparative des performances de chaque technique, voir Fig. 3 (a), (b) et (c).

Il ressort de cette étude que la grille en verre ionique LaF_3 permet d'obtenir un dopage élevé dans les NC HgTe de l'ordre de 10^{13} charges.cm^{-2} impossible avec une grille de SiO_2, et peut être utiliser dans une fenêtre de température inaccessible avec des électrolytes (260 K à 180 K) à cause des gels électrolytiques en dessous de 260 K. Le verre ionique fonctionne dans une petite plage de tension de grille 10 fois plus faible que pour SiO_2 et 2-3 fois plus grand que pour l'électrolyte (Fig. 3 (e)), ceci sans possibilité de claquage de grille comme parfois observé avec une grille SiO_2. Les mesures de spectroscopies d'impédance nous ont permis d'identifier à basse fréquence un dopage électrostatique dans avec les grille SiO_2 et LaF_3, tandis dans l'électrolyte un dopage électrochimique est possible pouvant induire des défauts dans les nanocristaux (Fig. 3 (g)). En plus, la capacité du verre ionique et de l'électrolyte augmente fortement et atteint 1 μF.cm^{-2} avec LaF_3 à 300 K. En appliquant 5 V de tension de grille avec le LaF_3, cela correspond à une densité de surfacique de 3x10^{13} charges.cm^{-2}. Notre verre ionique LaF_3 a été également implémenté avec success dans des transistors à base NCs de PbS et les NCs de pérovskites hybrides.
Pour finir, nous avons testé le potentiel de cette grille pour contrôler également le courant photogénéré. En excitant le transistor avec une diode laser pulsée fonctionnant à 1,55 μm, nous avons effectué des mesures de photocourant. La tension de grille influe fortement sur le photocourant et la dynamique de la photoréponse, voir Fig. 3 (d) et (h). Une modulation d'un facteur 4 peut être observée. Ainsi la grille peut donc être utiliser pour amener le système dans son minimum de conductance où le rapport signal sur bruit est de 100. La réponse temporelle (temps d'activation et de désactivation) de notre phototransistor est plus rapide lorsque la polarisation de grille correspond au minimum de conductance de la courbe de transconductance sans illumination. Une modulation d'un facteur 6 de la dynamique peut être induite avec la grille ionique LaF_3 (Fig. 3 (h)).

2: Phototransistor de matériaux lamellaires 2D à grille de verre ionique LaF_3

Dans cette deuxième partie, l'utilisation du verre ionique LaF_3 comme grille à haute capacité est explorée pour développer un phototransistor à base de $MoSe_2$ fonctionnant avec une concentration de porteurs élevée jusqu'à 5x10^{13} cm^{-2}. Quelques feuillets de $MoSe_2$ ont été mécaniquement exfoliés à partir d'un cristal massif et transférés sur un substrat LaF_3. La transparence optique du substrat LaF_3 permet une identification simple des feuillets par contraste optique. Nous avons fait les mesures Raman et la microscopie à force atomique pour trouver l'épaisseur du feuillet d'environ 3 nm correspondant à 3-4 monocouches, puis nous avons utilisé la lithographie par faisceau électronique pour fabriquer les électrodes sur le feuillet. Une image du dispositif est montrée à la Fig. 3 (a). Une fois l'échantillon inséré dans le cryostat, nous avons effectué les mesures de transport et phototransport.

La transconductance du transistor présente une caractéristique de type n qui est cohérente avec les transistors obtenus dans la littérature basée sur $MoSe_2$ utilisant le SiO_2 comme diélectrique [Mouafo17], voir la Fig. 3 (b). Dans notre système, l'effet de champ est conservé même pour un fonctionnement en dessous de la température ambiante, ceci avec une modulation maximale de courant pour une température autour de 200 K. A cette température, la modulation de courant I_{ON}/I_{OFF} dépasse 4 à 5 ordres de grandeur, avec une mobilité électronique de 15 $cm^2.V^{-1}.s^{-1}$. Cette valeur est très similaire à celle rapportée pour la multicouche de $MoSe_2$ avec de la silice [Mouafo17]. Nous avons étendu la grille de LaF_3 sur d'autres matériaux 2D et avons démontré un transport par les électrons dans le MoS_2 et le WS_2 tandis qu'un transport par les trous a été observé dans le WSe_2. Dans ce dernier nous avons fait une caractérisation détaillée des contacts Schottky à l'interface WSe_2/Ti-Au en fonction de la grille de LaF_3.

Nous avons par la suite sondé les propriétés optoélectroniques du FET à base de $MoSe_2$.

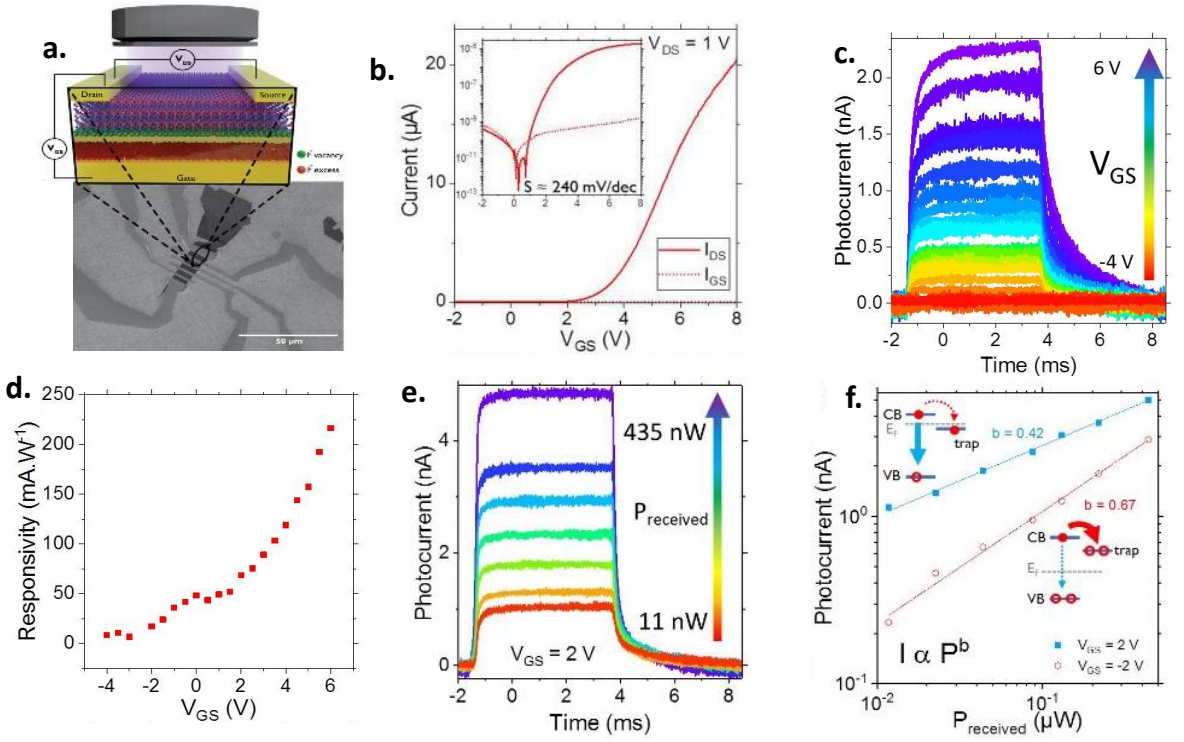

***Figure 4** – Schéma du transistor à base $MoSe_2$ sur LaF_3 avec une image SEM des électrodes (b) Courbes de transconductance à 200 K sous une tension source-drain de 1V. En insertion la courbe à l'échelle logarithmique. (c) Amplitude du photocourant mesuré sous une excitation de 12 nW avec une longueur d'onde de 405 nm d'un laser chopper à 100 Hz à differentes tension de grille à 180 K. (d) Responsivité du système en fonction de la tension de grille à 180 K. (e) Amplitude du photocourant mesuré à differentes puissances du laser à 180 K à 2V de grille. (f) Photocourant en fonction de la puissance du laser 180 K. pour -2V et 2 V de grille. Fit en loi de puissance. Les schémas en insertion illustrent le mécanisme de relaxation associé à chaque courbe (le processus bimoléculaire est représenté par la flèche bleue et le processus monomoléculaire par la flèche rouge).*

Sous illumination du transistor avec un laser bleu à 405 nm (dont l'énergie est supérieure à l'énergie de la bande interdite du $MoSe_2$), nous observons un photocourant dont l'amplitude peut être fortement modulée par la grille (Fig. 3 (c)). Typiquement, la responsivité du film atteint 50 mA/W à 0 V de grille et augmente d'un facteur 4 sous une forte tension de grille positive dépassant 0,2 A/W, Fig. 3 (d). Les temps de réponse de montée et de descente (respectivement t_{ON} et t_{OFF}) extraites des caractéristiques de photocourant sous polarisation de grille négative sont proches de 200 μs et 600 μs respectivement. Ceci est 2 ordres de grandeur plus rapide que les réponses temporelles précédemment observées sur les $MoSe_2$ exfoliés et CVD habituels [Abderrahmane14, Jung15, Dai19, Xia14], 50 fois plus rapides que les dispositifs avec le $MoSe_2$ encapsulé [Kufer16a], et plus 10 fois plus petit que le phototransistor $MoSe_2$ le plus rapide obtenu jusqu'à présent [Lee18].

Nous avons également étudié les mécanismes de recombinaison des porteurs en utilisant la dépendance à la puissance de la photoréponse. Lorsque la puissance incidente augmente, le photocourant augmente avec une loi de puissance qui est accordable par la grille, voir Fig. 3 (e) et (f). Ainsi nous avons montré que dans notre système, sous injection d'électrons (tension de grille positive), on remplit tous les états de pièges peu profond en dessous de la bande de conduction et on assiste à un processus bimoléculaire sous illumination dans lequel on observe une recombinaison directe des trous de la bande de valence avec les électrons de la bande de conduction (Fig. 3 (f), flèche bleue). En revanche, sous injection de trous (tension de grille négative), le niveau de Fermi est amené plus profondément dans la bande interdite et on assiste à un processus monomoléculaire sous illumination dans lequel les centres de recombinaison se remplissent et peuvent agir comme les états de piège (Fig. 3 (f), flèche rouge).

3: Jonction p-n reconfigurable à base d'hétérostructure 2D/0D graphène/HgTe pour la détection dans l'infrarouge

Dans cette troisième partie, nous exploitons d'une part les avantages clés du graphène: sa très faible absorption d'environ 2% dans l'infrarouge ($\lambda < 5$ μm), la possibilité de moduler son niveau de Fermi au-dessus et en dessous du point de Dirac permettant ainsi la conception d'électrodes à dopage sélectif (d'électrons ou de trous) et enfin sa transparence au champ électrique vertical induit par la grille inférieure. Puis d'autre part la forte absorption infrarouge de nanocristaux d'HgTe avec des mobilités de porteurs élevées (> 1 $cm^2V^{-1}s^{-1}$) pour fabriquer une hétérostructure graphène/HgTe. Il faut que les hétérostructures 2D/0D ont déjà été démontré par le passer avec des responsivités élevées au détriment des temps de réponses faibles, en raison du transport s'effectuant seulement dans le matériau 2D [Konstantatos12, Kufer15]. Ici, nous visons plutôt à concevoir un dispositif où le transport se produit dans un réseau de NC, tout en absorbant plus fortement la lumière incidente. En effet, l'introduction d'électrodes de graphène combinées au dopage élevé du verre ionique

permet de reconfigurer sélectivement les NC de HgTe et les électrodes de graphène entre les électrons (n) et les trous (p) dopés afin de concevoir une jonction p-n 2D/0D qui s'étend dans les nanocristaux, avec un champ électrique induit qui aide à la dissociation des charges.

Nous avons fabriqué les électrodes interdigitées de graphène en utilisant de la lithogra-

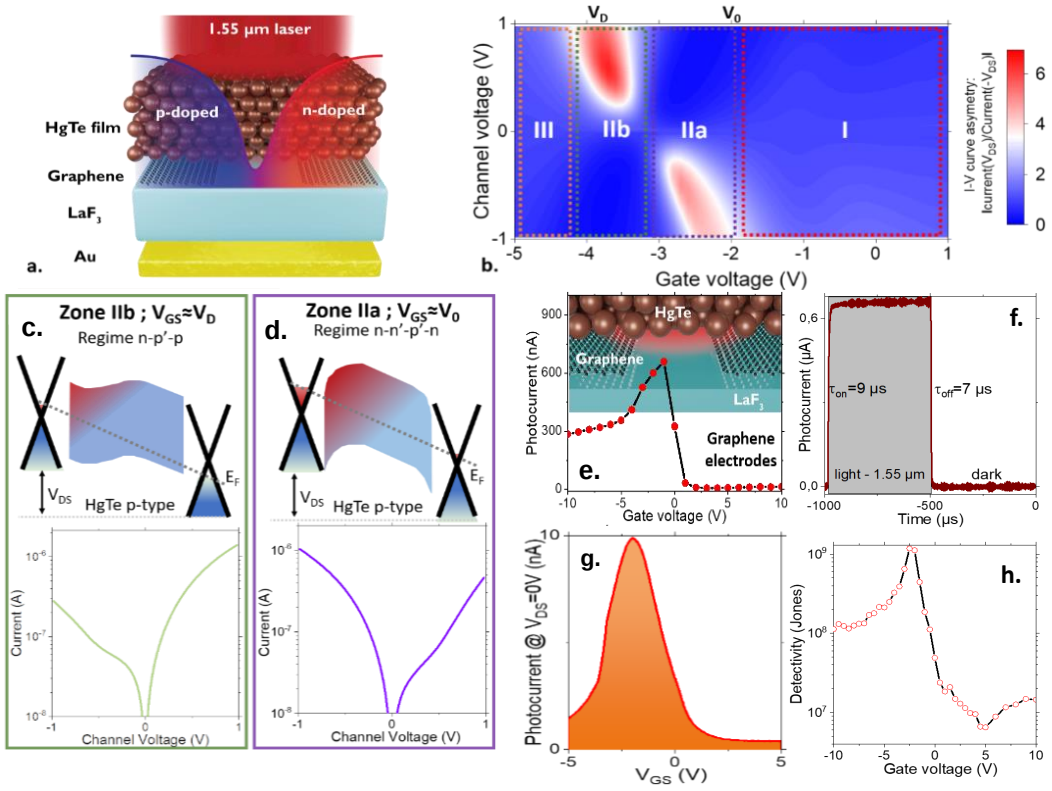

Figure 5 – *Schéma du transistor à grille de LaF_3, les électrodes de drain et de source sont constituées d'électrodes de graphène interdigitées et le canal est constitué d'un réseau de NC HgTe. (b) Carte 2D de l'asymétrie de la courbe IV, quantifiée par le rapport du courant sous une polarisation donnée et du courant sous la polarisation opposée, en fonction de la tension de canal entre les électrodes de source et de drain, et la tension de grille V_{GS}. Les régions en rouge correspondent aux domaines existants pour une jonction p-n au sein de l'hétérostructure graphène/HgTe/graphène. (c) Alignement de bande de l'hétérostructure dans la configuration n-p'-p et la courbe I-V de rectification associée, dans la zone IIb de la partie b. (d) Alignement de bande de la de l'hétérostructure dans la configuration n-n'-p'-n et la courbe I-V de rectification associée, dans la zone IIa de la partie b. (e) Photocourant en fonction de la tension de grille de l'hétérostructure. (f) Temps de réponse la jonction. (g) Photocourant sous 0 V, lorsque la lumière est chopée à 1 kHz, en fonction de la tension de la grille. (h) Détectivité (rapport signal/bruit) de l'hétérostructure à 1 kHz et à 220 K en fonction de la tension de grille.*

phie laser et une gravure physique du graphène CVD précédament transferé sur les substrats de LaF_3. Puis, nous avons déposé le même ancre de NC d'HgTe utlisé à la section 1 afin de fabriquer l'hétérostructure 2D/0D graphène/HgTe/graphène, un schéma du dispositif est présenté à la Fig. 5 (a). A 220 K, la carte d'asymétrie des courbes IV en fonction de la tension de grille nous a permis d'identifier les régions où les jonctions p-n sont formées avec un signal rectificatif élevé (zones en rouge Fig. 5 (b)). Il faut noter que dans notre système, c'est une

combinaison de la haute capacité grille du LaF_3, l'accordabilité de la polarité des porteurs de charge des électrodes de graphène (impossible dans le cas des électrodes métalliques) et des NC HgTe et enfin le faible écrantage du graphène au champ électrique qui rendent possible l'observation de la jonction p-n. Nous démontrons que dans cette configuration spécifique, le rapport signal sur bruit pour la détection infrarouge peut être amélioré de deux ordres de grandeur et que le fonctionnement photovoltaïque peut être atteint, voir Fig. 5 (g). La détectivité atteint 10^9 Jones alors que le dispositif n'absorbe que 8% de la lumière incidente (Fig. 5 (h)). De plus, notre dédecteur a un temps de réponse rapide (<10 μs, Fig. 5 (f)), ce qui le rend compatible avec des applications dans le domaine de l'optoélectronique. Cette reponse rapide contraste fortement la réponse lente couramment observée dans les hétérostructures de dimensions mixtes 2D/0D, où des gains de photoconduction plus importants se font au prix d'une réponse plus lente [Konstantatos12].

Introduction

Conventional semiconductors such as silicon- and indium gallium arsenide (InGaAs) have encountered a bottleneck in modern electronics and photonics in terms of spectral coverage, low resolution and non-transparency [Huo18]. Indeed, despite the mature technology level of silicon based devices, the latter suffers from fundamental limitations. For instance, complementary metal oxide semiconductor (CMOS) image sensors are limited by noises and quantum efficiency in the visible (indirect band gap of 1.1 eV) while InGaAs infrared (IR) photodiodes (0.5 eV to 0.73 eV) in addition to noise and efficiency issues suffer from large fabrication issues due to complex epitaxy growth techniques under high vacuum conditions. Moreover, an optically active region with rather large thickness in the order of microns required to absorb light efficiently, makes silicon detectors opaque, thus not compatible for applications in flexible, wearable and transparent electronics and optoelectronics. New emerging low dimensional materials (nanomaterials) however can circumvent all these issues benefitting from their mechanical flexibility, efficient electronic and optical properties, as well as their large scale production and wafer-integration.

Nanomaterials have attracted increasing research interests for electronic and optoelectronic devices in recent years. These include two-dimensional or 2D materials (graphene, transition metal dichalcogenides (TMDCs),...), 1D materials (nanowires, nanotubes,...) and 0D materials (nanoparticles, nanocrystals,...) where respectively one, two and three dimensions remain below 100 nm. Their low dimensions allow to rise new properties not accessible in bulk materials mostly because of quantum confinement at small scales. The prominence of quantum effects at nanometer scale thus opened numerous fundamental research fields including nanoelectronics and spintronics as well as optoelectronics [Radisavljevic13, Seneor07, Lhuillier17, Huo18].

When implementing semiconducting nanomaterials in devices, the modulation of their carrier densities is essential to adapt their electrical properties and functions, with new physical phenomena expected to occur at a higher doping level. Indeed, during their implementation in field effect transistors, phototransistors or photodiodes, the energy barrier for the carriers at the metal/semiconductor interfaces (Schottky contacts) is an universal

phenomenon limiting the device performances. Reduce these energy barriers in high doping regime, or the use of graphene electrodes to modulate these Schottky contacts becomes interesting to improve the device performances. It is in this context that my thesis work falls.

My thesis projet aims to develop and study alternative approaches to induce high doping for the photodetection at low temperature in 2D materials, colloidal nanocrystals and their heterostructures. I used ionic glass lanthanum trifluoride (LaF_3) substrate as solid gating to induce a high doping regime in those nanomaterials with charge densities higher than 10^{13} cm^{-2} at low gate voltage not accessible with a conventional dielectric, in an operating temperature from 160 K to 260 K not possible for electrolytic gating. This gating technique allows to modulate and reduce the energy barriers height at Schottky contacts for efficient injections or extractions of photogenerated carriers, then to improve the performance of phototransistors based on mercury telluride (HgTe) nanocrystals and molibdenum diselenide ($MoSe_2$). The possibility of manufacturing graphene electrodes on a large scale also makes possible to design and study a new configuration of 2D/0D infrared photo-detectors based on graphene-HgTe heterostucture with remarkable properties.

This work has been done and planed in close collaboration with the group of Emmanuel Lhuillier at Institut des Nanosciences de Paris (INSP, Sorbonne Université) which has great expertise on IR-nanocrystals systems. During the collaboration with several measurement campaigns at INSP, I brought all the process and technology on LaF_3 and the know how of 2D materials and Charlie Gréboval (PhD student in the team), his expertise on NCs and opto-electronic measurements. I am grateful to Emmanuel Lhuillier's team for the nice interaction and collaboration on the different projects I explored with them during my PhD. I thank especially Charlie Gréboval, with who I mostly worked during the measurement campaigns I did at INSP, and interacted also for other collaborative projects of our two teams. I thank them for NCs synthesis, their set-ups and their availability to welcome me several times in their laboratory for all the optical measurements.

This thesis manuscript is organized in five chapters.
The **first chapter** is dedicated to the state of the art of nanomaterials involved in this thesis, from the structural and electronic properties of graphene, TMDCs and colloidal nanocrystals to their implementation into devices. I also address the transport processes taking place in those nanomaterials.

In the **second chapter**, I introduce ionic glass substrate LaF_3 as high capacitance solid gating to study transport and photo-transport properties of nanocrystals. For the first time, we probe the photoresponse dynamics of narrow-bandgap HgTe nanocrystals in high doping regime using ionic glass technology.

The **third chapter** is dedicated to study of the transport and photo-transport properties of 2D materials in high doping regime. We extend the gating technique on MoS_2, $MoSe_2$,

WS_2 and WSe_2 flakes. We present the investigation of the Schottky junctions at Metal/WSe_2 interfaces with Ti/Au contacts using ionic glass gating using a back-to-back model from the thermionic emission theory. We observed that the Ti/WSe_2 interface energy barrier height is efficiently reduced by the gate. Finally, we use the direct optical adressability of ionic glass substrate to investigate the photo-transport and carrier recombination mechanism in $MoSe_2$ FET.

In the **fourth chapter**, I report on an infrared photodetector combining the properties of these two classes of nanomaterials to demonstrate the reconfigurable 2D-0D graphene-HgTe heterojunction. The use of carrier selective graphene electrodes combined with high capacitance gating of ionic glass allow to implement a new architecture of 2D-0D heterojunction that are reconfigurable and can be tuned from the p-p' or n-n' configuration to a p-n diode. The p-n junction expands throughout the device, with a built-in electric field that assists charge dissociation in order to improve device performances.

Finally, I resume the main results obtained in this work and I outline some important perspectives to explore in the continuity of my thesis.

Chapter 1

Context and state of the art

The performance of a device is not only related to its architecture and proccessing but also to the properties of materials involved which are strongly correlated to their structures. While material properties such as band gap governs the optical range sensitivity, the device design has strong impact on the carriers injection and detection mechanisms which govern the performances of the device. This chapter presents properties of materials explored in this thesis and some important device and technological parameters that will also be adressed. I start by presenting the basic properties of 2D materials (graphene, transition metal dichalcogenides (TMDCs)), colloidal nanocrystals (CNCs) and mixed-dimensional van der Waals heterostructures (MD-vdW-h). I particularly focus on their intrinsic nanoelectronic and optoelectronic properties related to this work which mostly depend on the size and the thickness of the nanomaterials [Jariwala16, Liu16b]. Then, I introduce the gating techniques used so far to tune their charge carrier densities, and finally I recall some figures of merit for photodetection.

1.1 2D materials (Graphene and TMDCs)

1.1.1 Graphene

Crystal structure and band structure

Graphene is one of the first and famous example of 2D materials so far experimentally isolated and characterized in 2004 by Novoselov and Geim [Novoselov04, Geim09]. Compare to quantum wells, there are atomically thin layer materials of a few nanometers. It is the thinnest material ever reported. Graphene is a sheet of graphite consisting of a single layer of carbon atoms in honeycomb lattice structure as shown in Fig.1.1(a), where each carbon atom is covalently bonded with three orther carbon atoms. Thanks to sp^2 hybridization between one s and two p orbitals in xy-plane which gives up to a trigonal structure with 120° between them. Then, graphene lattice can be seen as two trigonal sublattices with atoms A (purple filled circles at 60°, 180° and 300°) and atoms B (red filled circles at 0°, 120° and 240°) or one triangular lattice with a basis of two atoms A and B with a=0.142 nm the distance between two neighboring atoms A and B (Fig.1.1(a)). Therefore, the basic vectors of the primitive unit cell are given by:

$$\boldsymbol{a_1} = \frac{a}{2}(3, \sqrt{3}) \quad and \quad \boldsymbol{a_2} = \frac{a}{2}(3, -\sqrt{3}) \tag{1.1}$$

Also, the three vectors connecting an atom B to its nearest neighbors A are given by:

$$\boldsymbol{\delta_1} = \frac{a}{2}(1, \sqrt{3}) \quad ; \quad \boldsymbol{\delta_2} = \frac{a}{2}(1, -\sqrt{3}) \quad and \quad \boldsymbol{\delta_3} = -a(1, 0) \tag{1.2}$$

Given $\boldsymbol{a_i b_j} = 2\pi\delta_i j$, ($\delta_i j = 1$ if $i = j$; 0 if $i \neq j$, the reciprocal basis vectors in (Fig.1.1(b)) are:

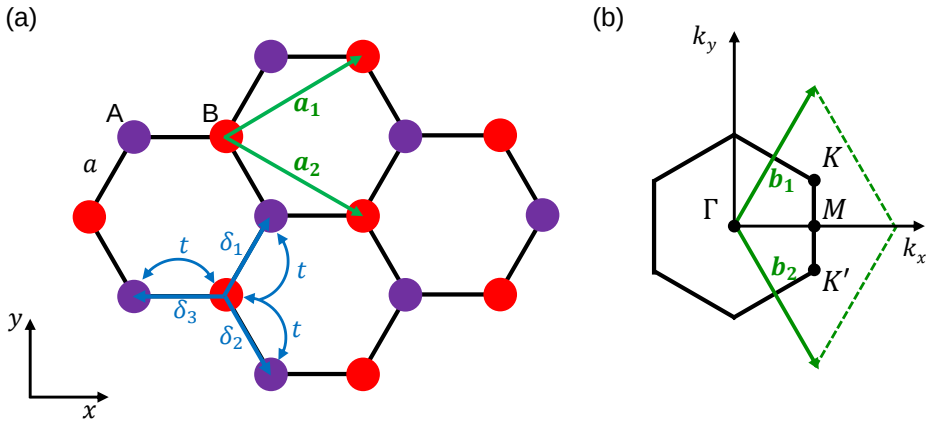

Figure 1.1 *– (a) Honeycomb lattice structure of Gr composed of a triangular lattice with a basis of two inequivalent carbon atoms, A and B. $\boldsymbol{a_1}$ and $\boldsymbol{a_2}$ are the primitive unit vectors. The vectors $\boldsymbol{\delta_1}$, $\boldsymbol{\delta_2}$ and $\boldsymbol{\delta_3}$ connect an atom B to its three nearest neighbors A. Electron can hope from a given carbon atom to one of its three nearest neighbor with a hopping parameter t. (b) The first Brillouin zone. $\boldsymbol{b_1}$ and $\boldsymbol{b_2}$ are the basis vectors of the reciprocal lattice. High symmetry points are indicated with black dots and labeled.*

$$\boldsymbol{b_1} = \frac{2\pi}{3a}(1, \sqrt{3}) \quad and \quad \boldsymbol{b_2} = \frac{2\pi}{3a}(1, -\sqrt{3}) \tag{1.3}$$

The first Brillouin zone (FBZ) of graphene is hexagonal and has four high symmetry points Γ, M, K and K' (Fig.1.1(b)). Particularly, the two points K and K' called Dirac points are not equivalent and their positions in momentun space are given by the vectors $\boldsymbol{K} = \frac{2\pi}{3a}(1, \frac{1}{\sqrt{3}})$ and $\boldsymbol{K'} = \frac{2\pi}{3a}(1, -\frac{1}{\sqrt{3}})$ [Mouafo19].
To describe the electronic properties of grahene, it is sufficient to consider only out of plane π and π^* electronic bands at low energy [Fuchs08]. The first precise description of the π and π^* bands in graphite has been proposed by Wallace in 1947 [Wallace47] using a tight-band model. This approach has so far been adapted to describe the π bonding and π^* antibonding bands in graphene [Charlier07, Cresti08]. Using the tight-binding Hamiltonien in the calcu-

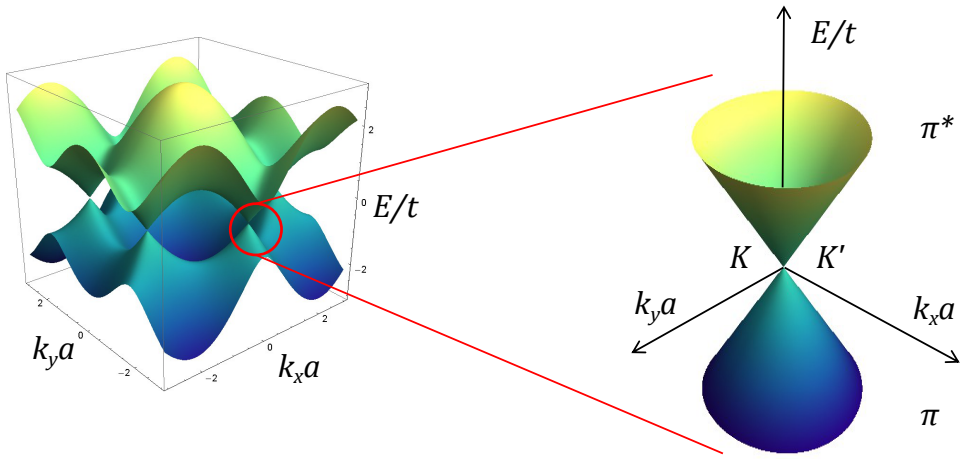

Figure 1.2 *– Graphene's electronic dispersion relation calculated using a first nearest neighbor tight-binding model. The valence and conduction bands touch each other at the six corners of the FBZ. A zoom close to the K and K' points shows the Dirac cone. Adapted from[Peres07].*

lation of energy bands in graphene, the electronic dispersion relation of $\pi(-)$ and $\pi^*(+)$ bands can be described as [Wallace47]:

$$E_{\pm}(\boldsymbol{k}) = \pm t\sqrt{3 + f(\boldsymbol{k})} - t^{'} f(\boldsymbol{k}) \tag{1.4}$$

$$f(\boldsymbol{k}) = 2\cos(\sqrt{3}k_y a) + 4\cos\left(\frac{\sqrt{3}}{2}k_y a\right)\cos\left(\frac{3}{2}k_x a\right), \tag{1.5}$$

where $\boldsymbol{k}(k_x, k_y)$ is the electron wave vector, $t \approx 2.8$ eV the nearest neighbor (A-B) hopping energy and $t^{'} = -0.1eV$ [Reich02, Deacon07] is the next nearest-neighbor hopping energy. Fig.1.2 (a) shows the dispersion relation using the first nearest neigbor approximation. At low energy limit ($\left|E(\vec{k})\right| \prec t$), one can write $\vec{k} = \vec{K} + \boldsymbol{\kappa}$, with $|\boldsymbol{\kappa}| \ll |\boldsymbol{K}| \sim 1/a$ (or $|\boldsymbol{\kappa}|a \ll 1$). Then, in the first order approximation, the dispersion relation is linear with $\boldsymbol{\kappa}$ (Eq.1.6).

$$E_{\pm}(\boldsymbol{\kappa}) = \pm\hbar v_{\mathrm{F}}|\boldsymbol{\kappa}|, \quad \text{with } v_{\mathrm{F}} = \frac{3ta}{2\hbar} \approx 10^6 \text{ m s}^{-1}. \tag{1.6}$$

Here, v_{F} denotes the Fermi velocity. This linear dispersion relation of graphene is reminiscent of the solution of Dirac's equation for relativistic particles $E = \pm\sqrt{p^2c^{*2} + m^{*2}c^{*4}}$ which in the limit of ultra relativistic particles ($m \to 0$) yields a simple linear expression $E = \pm pc^*$ in anal-

ogy with Eq.(1.6) for $c^* = \frac{3a}{2\hbar}t$ and $p = \hbar|\kappa|$ [Peres07, Avouris10, Das Sarma11, Castro Neto07]. For this reason, $\boldsymbol{K}$ and $\boldsymbol{K'}$ are called "Dirac points" in the vicinity of which electrons in graphene are considered to be massless. At these particular points, the upper unoccupied cone (conduction band (CB) $\pi^*(+)$) and the lower filled cone (valence band (VB) $\pi(-)$) touch each other and make **graphene a semimetal**. A zoom in Fig. 1.2 shows the famous 'Dirac cones'. Indeed, the density of state is proportional to the energy as $g(E) = \frac{2E}{\pi(\hbar v_F)^2}$ and for this reason *graphene has low available states at low energies*.

Properties of graphene

Graphene is the strongest known material with a Young modulus $\approx 1 \times 10^9$ Pa. Indeed, graphene is harder than diamond yet more elastic than rubber, tougher than steel yet lighter than aluminium. Graphene has a high thermal conductivity and a transparency of more than 97 %. So, **graphene can be used as a transparent conductor electrode** to replace indium tin oxide (ITO) and fluorine tin oxide (FTO) in photovoltaic and photoelectric devices which are limited not only by their transparency in infrared because of the plasmonic absorption [Garcia11, Qu19] but also by their contact resistances as it has been demonstrated in touch screen panel device [Bae10]. *Graphene absorbs only* 2.3 % *of light in the wide range of the electromagnetic spectrum from far infrared to ultraviolet range* with two main contributions: interband transitions in undoped graphene and intraband transitions for doped graphene [Froehlicher16]. Moreover the absence of the band gap in graphene makes it not efficient as light emitter because of very fast efficient non-radiative carrier relaxation [Mak12b, Nair08]. **So graphene is a good candidate to design electrodes in nano and opto electronic devices as we used in this work**.

Concerning the electronic propeties of grahene, it reveals to be a promising material for devices as it can be used as charge carrier selective electrode. Many studies have been done both theoretically and experimentally [Chen15]. Theoretically, the charge carrier mobility can reached 2×10^6 $cm^2V^{-1}s^{-1}$, however this value considerably decreases with the substrate and the presence of charge impurities. Experimentally, measurements demonstrated 10000 – 15000 $cm^2V^{-1}s^{-1}$ on Si/SiO_2 substrate and 6×10^4 $cm^2V^{-1}s^{-1}$ on hexagonal boron nitride substrate [Morozov08, Dean10]. Controlling the doping in graphene (i.e change the position of the Fermi energy E_F) has been done both chemically and physically. The latter made use of electrostatic doping in field effect transistor (FET) geometry. Fig.1.3(a) shows FET similar with a parallel plate capacitor where one electrode is the gate and the other one is replaced by graphene [Froehlicher16]. Applying a transverse field (gating) through an external potential V induces charge carriers (either electrons or holes depending on the sign of V) at the surface with the density $n = \frac{CV}{e}$, C being the specific capacitance. Fig.1.3(c) shows *the ambipolar transport in graphene and the Dirac point neutrality (where the electron density equals to the hole density) at* $V_{Dirac} = 0V$ *for ideal undoped graphene. This Dirac point can change depending of the substrate, defects, inducing additional charges in graphene. Applying a negative voltage with respect to the Dirac point shifts down the Fermi energy to the lower cone, and conduction occurs through holes. Contrary, when a positive bias with respect to the Dirac point is applied,* E_F *moves*

to the upper cone and we have electron's conduction.

The density of charge carrier in graphene is linked to the Fermi energy E_F by [Ashcroft76]

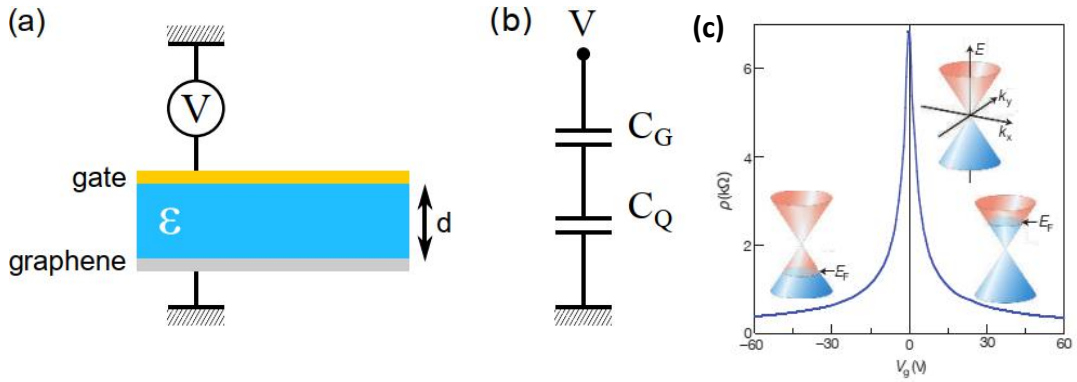

Figure 1.3 *– (a) Schematic cross-section of a parallel plate capacitor composed of a single layer graphene and a metallic electrode separated by a dielectric of thickness d. (b) Equivalent electrical circuit. (c) Graphene's electrical resistivity ρ as a function of gate voltage V_g in a FET. The insets show the conical low-energy dispersion with changing V_g. Adapted from Ref. [Li08, Geim07].*

$$n_e = \int_0^{+\infty} f(E)g(E)\mathrm{d}E \quad \textit{and} \quad n_h = \int_0^{+\infty} [1-f(E)]g(E)\mathrm{d}E, \tag{1.7}$$

where n_e and n_h are the electron and hole density, respectively, and $f(E) = [1+\exp((E-E_F)/k_BT)]^{-1}$ is the Fermi-Dirac distribution at a temperature T. Because of the electron-hole symmetry, it is more convenient to define only one density n counted positively for the electrons and negatively for holes. At $T = 0$,

$$E_F = \mathrm{sgn}(n)\hbar v_F\sqrt{\pi|n|}, \tag{1.8}$$

where sgn is the sign function. In practice, finite temperature effects only induce a very minor correction to this simple scaling [Li11b], therefore we will use this expression at any temperature.

In a graphene FET, due to the two-dimensional (2D) nature of the electron as studied in 2D electron gases (2DEGs) in quantum wells or inversion layers , the capacitance C is not simply equal to the geometrical capacitance C_G of the parallel plate capacitor but to this capacitance in series with the **quantum capacitance** C_Q [Luryi88] (Fig. 1.3(b)). This capacitance comes from the fact that, contrary to the metallic gate electrode which can be viewed as a reservoir of electrons, injection in the graphene layer leads to a change of E_F, it also comes from the limited number of available states around the Dirac point at low energy. Xia et al [Xia09a]

have been measured for the first time the quantum capacitance of graphene using ionic liquid gating. Successively other groups by means of electrolytes gating [Ye11] and high dielectric constant insulators [Xu11]. The quantum capacitance in graphene is given by

$$C_{\mathrm{Q}} = \mathrm{sgn}(n)\frac{e^2}{\hbar v_{\mathrm{F}}\sqrt{\pi}}\sqrt{|n|} = \frac{e^2}{2}g(E_{\mathrm{F}}), \tag{1.9}$$

where $g(E_{\mathrm{F}})$ is the density of states at the Fermi level. It is important to note that, this capacitance starts to play a role in the systems where high charge densities are involved. In addition, the contribution of C_{Q} dominates at low E_{F} while C_{G} dominates at high E_{F}.

Transport mechanism in graphene

In graphene based devices, depending of the effective channel length with respect to the carrier (usually electron) mean free path described as the average length that the electron can travel freely i.e before a collision, two transport regimes can be discriminated: the ballistic and the diffusive transports.

Ballistic transport regime : The perfect regularity of the crystallography structure of graphene consolidated by the strong sp^2 chemical bonds provides the ideal conditions for carriers to propagate with a large mean free path and negligible scattering deflecting their trajectories in pristine graphene. This favors a ballistic type of transport mechanism in graphene particularly at low carrier density. In ballistic regime, carriers propagate at constant velocity v_F between two consecutive collisions with a mean free path reaching a micrometer [Mayorov11]. Scattering are negligible when the effective channel length is comparable to the mean free path (quite often the case in GFETs) and the conductivity increases linearly with n close to the Dirac points. Already in their pioneering contribution, Novoselov et al. reported carriers mean free path of 0.4 μm for graphene on SiO_2 [Novoselov04]. Later, the encapsulation of graphene in hexagonal boronitride (hBN) allowed to reduce scattering and to achieve a mean free path superior to 3 μm at low temperature [Mayorov11]. One characteristic of graphene is its non zero minimum conductivity with a high resistance at Dirac point (Fig.1.3 (c)). This follows theoretical predictions that in the ballistic regime, although the carrier density vanishes at the vicinity of the Dirac point, the conductivity of Gr converges to ballistic conductance minimum limit of $G_{min} = 4\frac{e^2}{\pi h}$ (4 stands for valley and spin degeneracy) [Castro Neto09, Das Sarma11].

Diffusive transport regime : When the scattering of carriers becomes important, the transport in graphene changes from ballistic to diffusive mechanism. This happens when the effective channel length exceeds the mean free path or when the density of impurities becomes important [Das Sarma11]. Theoretical development based of the general Boltzmann transport theory in semiclassical regime demonstrated the conductivity of graphene in presence of scattering to be given by [Castro Neto09, Das Sarma11].

$$\sigma = \frac{e^2 v_F^2}{2}\rho(E_F)\tau(E_F) \tag{1.10}$$

Where τ is the transport scattering time of carriers.
In diffusive regime, the transport mechanism in graphene is essentially explained by long and short range scattering [Mouafo19]. The long range scattering consists of randomly distributed Coulomb impurities such as local gate potential fluctuation of the substrate and intentional or unintentional charged impurities doping. The short range scattering comprises of neutral point defects or C atom vacancies, phonon scattering due to lattice vibration and finally e-e interaction at very high doping regime. At low density of carriers and in presence of charged impurities scattering, the transport scattering time τ is proportional to the square root of carrier density ($\tau \propto \sqrt{n}$) and Eq.1.10 yields the usually observed linear dependency with $\sigma \propto n$. As n increases, charged impurities scattering sources are progressively screened by the 2DEGs. Thus, short range scattering become dominating (at high Vg) limiting the mobility of graphene. Consequently, its conductivity undergoes a sublinear behavior [Chen08, Das Sarma11]. The total conductivity (or resistivity) can be written as a sum of two contributing terms : $\sigma = \sigma_L + \sigma_S$ where the long range scattering term σ_L is proportional to n and the short range term σ_S independent of n [Morozov08, Chen08].

Optoelectronic applications

The remarquable properties of graphene already presented, especially the wide absorption spectra, the high charge mobility and carrier selectivity, make graphene interesting for opto and nano electronic applications. For optoelectronics, graphene photodetectors allow ultra-fast charge carrier dynamic enabling the conversion of incident photon into current with multi-gigahertz bandwidth [Xia09b, Mueller10]. In addition, graphene is suitable for applications in optical communications [Pospischil13, Gan13] and long-wavelength detection [Vicarelli12]. An example of a graphene-based photodetector is shown Fig. 1.4(a), it consists of a lateral p-n junction created by doping differently two regions of graphene electrostatically. The built-in electric field in the junction separates the photogenerated electron-hole pair giving rise to a photocurrent with an important contribution at the electrodes, see Fig. 1.4(b). However, the semimetal nature of graphene limits the performances of graphene

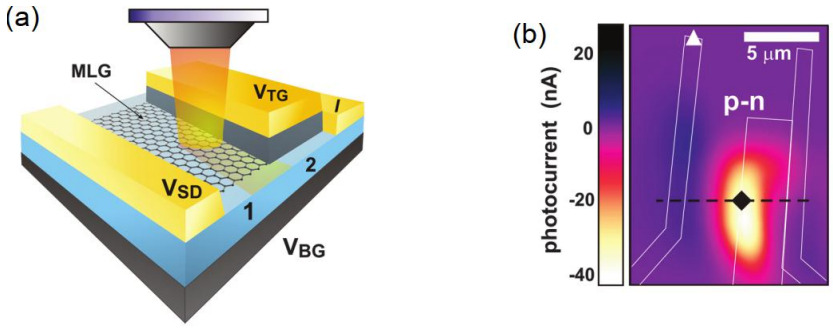

Figure 1.4 *– (a) Three-dimensional schematic view of double-gated (back and top) device used to demonstrate the photo-thermionic effect. By applying appropriate biases to the top (V_{TG}) and back (V_{BG}) gates, two differently doped regions (1 and 2) are created. (b) Photocurrent map of the corresponding device. White lines mark location of gold contact and gate electrodes. A hot spot at the p-n junction is observed. Figures extracted from Ref. [Gabor11].*

based photodetector because of high dark current allowing small On/Off ratio, then a lot of noise and high power consumption. The idea was to move to layered semiconductors where the presence of the band gap and their layered nature make them interesting for nanoelectronic and optoelectronic applications as we will see in the next section.

1.1.2 Semiconducting transition metal dichalcogenides

Transition metal dichalcogenide (TMDC) refers to a large family of materials of chemical formula MX_2 where M is a transition metal element from group IV to X of the periodic table of chemical element [Chhowalla13, Wang12, Ajayan16, Li17] and X is a chalcogen element of group XVI (S, Se, Te) [Chhowalla13]. As graphene, they are layered materials with a strong intra-layer covalent bonds between atoms, dangling-bond free lattice and a weak van der Waals inter-layer coupling. This makes possible the isolation of one or few layers from the bulk crystal by mechanical and liquid phase exfoliation, it can also facilitate their synthesis by chemical vapor deposition (CVD). Contrary to graphene which has only one atomic plane of carbon in monolayer, a monolayer TMDC consists of 3 atomic plans of X-M-X with a transition metal atomic plan M sandwiched between two chalcogen atomic plans X. The large possibility of combination of transition metal atoms with chalcogen atoms in MX_2 stoichiometry, gives rise to a large variety of TMDCs with diverse electronic structures and completely different electrical properties. One distinguishes **insulators, semiconductors** [Wang12, Chhowalla13], **metals, semimetals and superconductors** [Yang17, Ajayan16, Li17]. These electronic properties are essentially controlled by the occupation rate of the non-bonding d orbitals of M atoms by electrons [Schmidt15]. This electronic occupation rate of the non-bonding d orbitals of M atoms differs in TMDCs depending on the group of the transition metal and determines the spatial coordination geometry of the later and hence the crystal structure of TMDCs to which their electronic structures are closely related.

Crystal structure, band structure, and properties of semiconducting TMDCs

The transition metal's coordination can be either trigonal prismatic or octahedral resulting to a variety of polymorph and polytype phases. The three frequently encounter polymorphs are the hexagonal phase (2H), the trigonal phase (1T) and the rhombohedral phase (3R) [Chhowalla13] with respectively two, one and three X-M-X layers required to form the primitive cell. To distinguish from few layers or bulk, the nomenclature adopts the notation (1H) when referring to a monolayer TMDC in hexagonal polymorphic phase. Metallic TMDCs composed of group IV and V such as TaS_2 and TiS_2 are thermodynamically stable in 1T phase contrary to their semiconductor counterpart such as MoS_2, $MoSe_2$ and WS_2 stable in 2H phase [Chhowalla13, Kappera14b, Li17]. The 1T metastable metallic phase in MoS_2, $MoSe_2$ and WS_2 requires a relatively high activation energy of approximately 1 eV to relax back into the semiconducting 2H phase [Voiry13, Kappera14a]. Furthermore, engineering the occupation of the non-bounding d-orbital of the M atom by chemical or electrostatic doping enables to induce a transition from the stable 2H phase to the metastable 1T phase which has important applications in nanoelectronic for contact resistance engineering [Kappera14a].

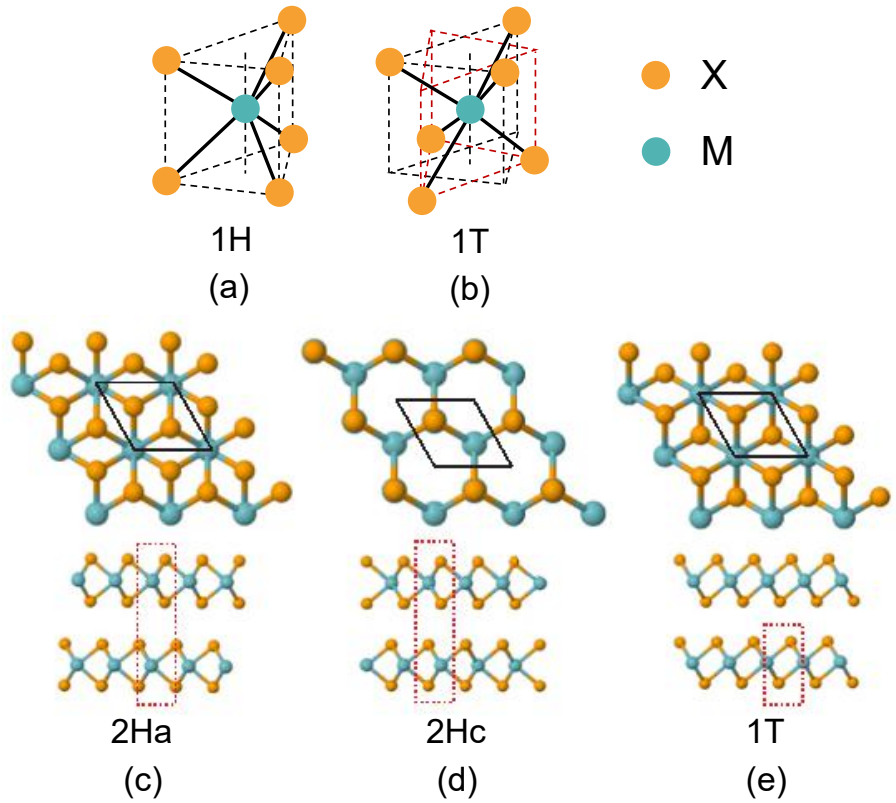

Figure 1.5 *– Transition metal atom coordination for (a) trigonal prismatic (H) and (b) octahedral (T) polymorph. The blue and orange spheres represent the transition metal and chalcogen atoms respectively. Top and side views of (c) 2Ha, (d) 2Hc and (e) 1T bulk polytypes. The primitive cells are highlighted by black rhombuses in the top views and red dashed squares in the side views. The primitive cells of 2H and 1T polytypes contain six and three atoms respectively. The stacking orders are indicated in brackets. Adapted from Ref. [Ribeiro-Soares14, Mouafo19].*

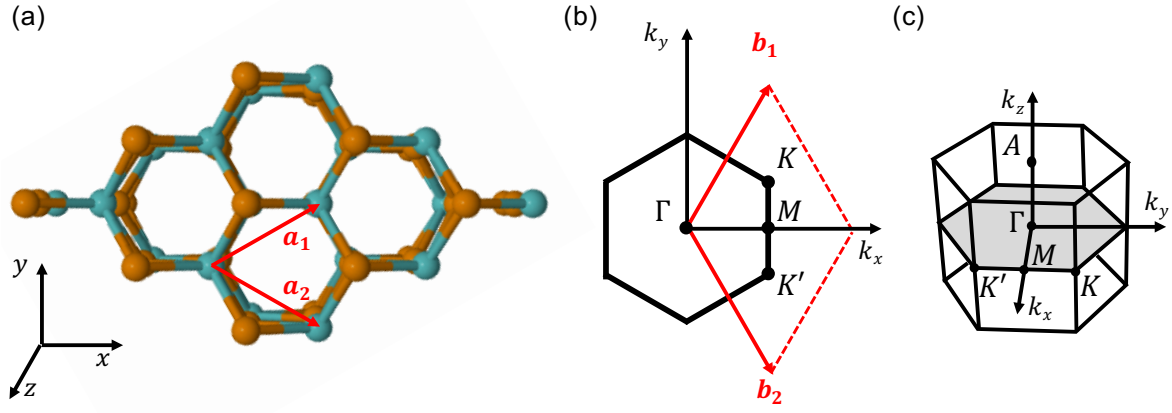

Figure 1.6 *– (a) Top view of 2Hc TMDCs. $\boldsymbol{a}_1$ and $\boldsymbol{a}_2$ are the in-plane primitive unit vectors. (b) Corresponding first Brillouin zone. $\boldsymbol{b}_1$ and $\boldsymbol{b}_2$ are the in-plane reciprocal primitive unit vectors. The main four points are labeled: Γ, K, K′ and M. (c) Three-dimensional first Brillouin zone of bulk 2Hc TMDCs. In addition to the four points depicted in (b), there is a fifth point labeled A. Adapted from [Froehlicher16].*

Regarding their geometrical organization, atoms in each of the three monoatomic layers constituting a monolayer MX_2 TMDCs have a triangular organization comparable to the Gr

sublattices. Only the vertical intra-layer arrangement differentiates the (1H) and more generally the (2H) polymorphic phase to the (1T) polymorphic phase (Fig.1.5 (a,b)). The hexagonal 1H polymorph results from a trigonal prismatic coordination of the transition metal atoms M with its six chalcogen nearest neighbors half distributed in the top and bottom chalcogen plan where chalcogen atoms of the top and bottom layer are vertically aligned along the z-axis (Fig.1.5 (a)). The 2H TMDCs (thickness superior to one MX_2 layer of trigonal prismatic polymorph) exist in two forms with different stacking symmetries [Ribeiro-Soares14] reported as 2Ha and 2Hc (Fig.1.5 (c,d)). The 2Ha polytype reported for group V based TMDCs such as $Nb(S,Se)_2$ and $Ta(S,Se)_2$, in which all the transition metal atoms align in the z-direction as shown in Fig.1.5 (c). The 2Hc polytype stable including molybdenum and tungsten based-TMDCs ($Mo(S,Se)_2$ and $W(S,Se)_2$) corresponds to the sequence where each transition metal atom is vertically aligned with the two chalcogen atoms of the subsequent layer (Fig.1.5 (d)), it is the one we use in this work. The 1T polymorph or octahedral phase results from octahedral coordination of the metal atoms with its six nearest chalcogens of the two chalcogen layers still organized as in the 1H polymorph but rotated with respect to each other relatively to a vertical axis containing the transition metal atoms. Hence, the chalcogen atoms of both layer are not anymore aligned along the z-axis (Fig.1.5 (b)). Consequence of the trigonal atomic organization, the Bravais lattice as well as the subsequent FBZ are hexagonal with the basis vectors $(\boldsymbol{a_1}, \boldsymbol{a_2})$ and $(\boldsymbol{b_1}, \boldsymbol{b_2})$ respectively (Fig.1.6(a, b)). It results two set of inequivalent points K and K' located at the vertexes of FBZ with a direct consequence of introducing a double valley degeneracy. The FBZ has four high symmetry points Γ, M, K and K' (Fig.1.6(b)). For bulk TMDCs, the FBZ becomes hexagonal prismatic with an additional high symmetry point (A) located on the same vertical with the Γ point at half high of bulk FBZ [Mouafo19].

The electronic structure of TMDCs mostly depends on the number of layer. The latter plays an important role on both quantum confinement[1] *and the screening of the Coulomb interaction in the materials*. This relates to a change of the hybridization of p_z-obitals on chalcogen atoms and d-orbitals on transition metal atoms, which mainly affects the conduction band at Γ. Molybdenum and tungsten-based TMDCs are semiconductors with optical bandgaps in the range 1 – 2 eV (Fig.1.7 (b)) making them very attractive for visible and near-infrared applications, but also for fundamental studies. Indeed, they provide a unique platform to investigate the evolution of the physical properties from three-dimensional bulk to quasi two-dimensional monolayer systems. *From their bulk indirect gap band, they undergo a transition to a direct bandgap in monolayer [Schmidt15] with an increase of the bandgap, thanks to quantum confinement*. Fig.1.7 (a) shows an example of the transition for MoS_2 (from 1.2 eV to 1.8 eV). This transition was first observed experimentally by Mak *et al.* [Mak10]. The indirect-to-direct band gap transition induces an important enhancement of the photoluminescence (PL) in monolayers of $Mo(S,Se)_2$ and $W(S,Se)_2$ whereas only a weak emission is observed in their multilayer counterpart [Chhowalla13] (Fig.1.7 (d) for monolayer MoS_2) since the interband transition required

[1] Quantum confinement is a phenomenon that occurs in semiconductors when at least one of its dimensions becomes smaller than the Bohr exciton radius, which is the average distance between the electron and the hole generated after absorption of a photon

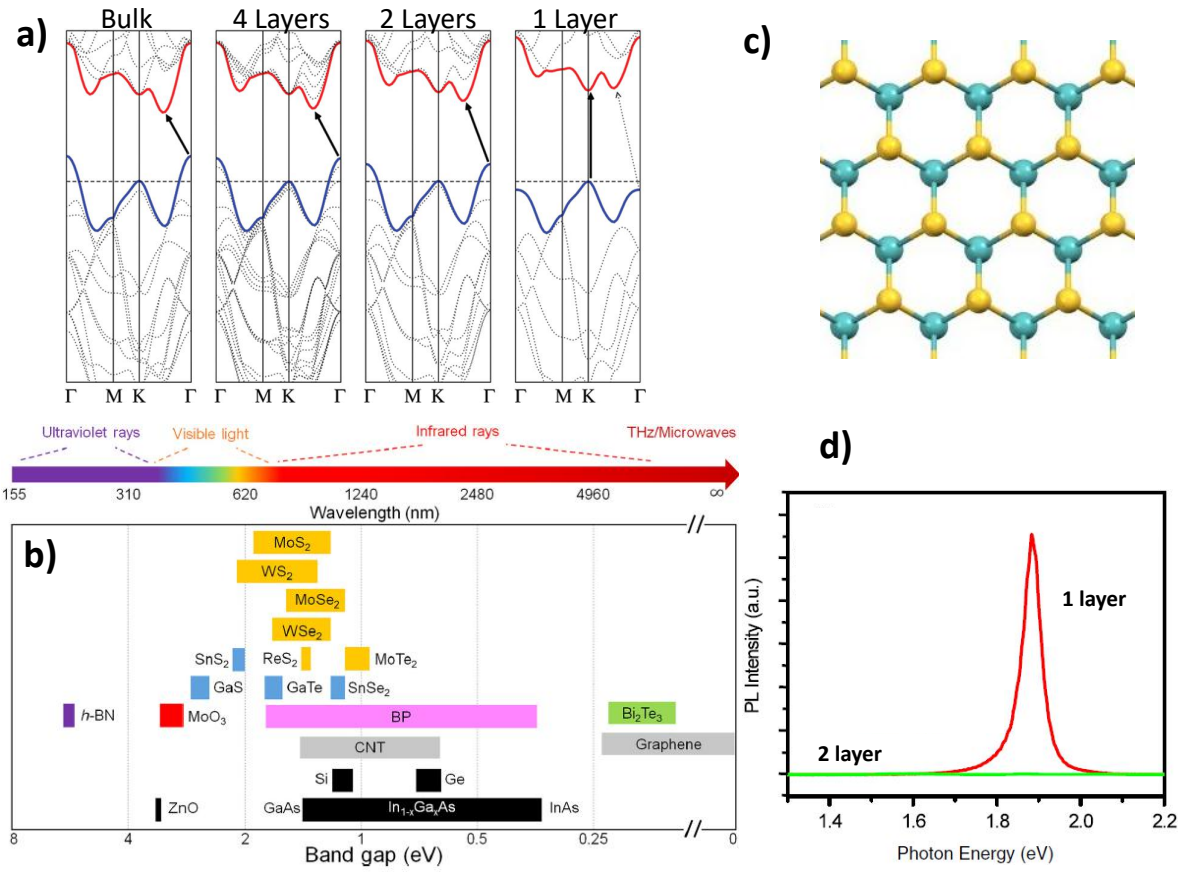

Figure 1.7 *– Band structure of semiconductor TMDCs. (a) The band structure of bulk, four layers (4L), bilayer (2L) and monolayer (1L) MoS_2 presenting an indirect to direct band gap transition. Adapted from[Splendiani10]. (b) Electromagnetic spectrum of 2D materials. (c) Top view of hexagonal structure of 2H MoS_2. (d) Photoluminescent of suspended monolayer and bilayer MoS_2. Adapted from [Mak10].*

and additional momentum. The position of the peak in PL spectra gives the energy to absorb or emit a photon called the **optical bandgap**. The group symmetry of TMDCs also changes with their thicknesses [Ribeiro-Soares14]. The inversion symmetry present in bulk or in odd number of layer thick samples is broken in monolayer or even number of few layers thick $Mo(S,Se)_2$ and $W(S,Se)_2$ [Chhowalla13, Yang17, Zeng13, Zhang14, Zeng12]. In monolayer MoS_2 for example, such inversion symmetry breaking combines with strong spin-orbit coupling (SOC) produces an out-of-plane valley dependent electron spin polarization at K and K' points. First principle calculations and photoluminescent experiments with left/right circular polarized light revealed such a spin valley polarization to be up to +30% and −30% at 10 K for spin up (K) and spin down (K') respectively [Zeng12, Mak12a]. All these properties, make SC-TMDCs interesting for flexible electronics, optoelectronics, spintronics and valleytronics.

Transport mechanism in SC-TMDCs: hopping process

In disordered systems consisting of randomly distributed localized charge impurities such as SC-TMDCs, the conduction is essentially driven by hopping [Shklovskii84]. In such systems, each localized charged impurity induces a set of discrete states within the gap of the semicon-

ductor. More than one electrons can occupied the discrete localized states of a single impurity and the Coulomb interaction between these on-site electrons is non negligible given their proximity. A simple description of such systems is based on the Mott model [Shklovskii84]. It assumes an ideal system consisting of an ensemble of impurities with the same Coulomb interaction potential $U(\vec{r_i})$ regularly distributed on impurities sublattice embedded in the main lattice of the matrix material. The impurities sublattice parameter is assumed to be b_0. When considering the entire impurity lattice, the individual discrete energy levels merge into impurities bands (Fig.1.8 (a)). Assuming 2 electrons per site and U_0 the average on-site e-e interaction energy, the properties of the system evolve with the distance b_0 between neighboring impurities. When b_0 is very large, the individual discrete states are very localized. It results two distinct narrow bands separated by a forbidden gap of width U_0 (Fig.1.8 (a)). The material is in an insolating state. However, when b_0 decreases, the impurities bands start spreading, reducing thus the gap. It exists a critical value of b_c below which the band overlap and the material undergoes a transition toward metallic state (Fig.1.8 (a)). It is the Mott transition [Shklovskii84].
The model can be complexified to make it closer to the reality by assuming a random distribution of impurities potential (i.e. disorder). For simplicity, the random distribution of impurities potential energy ε_i are assumed to remain within an interval $\pm\frac{E}{2}$ around an average value. In this condition, the properties of the system depend on the parameter $\pm\frac{E}{I}$ with I representing the overlap integral of impurities states. For large values of $\pm\frac{E}{I}$ (i.e. for small overlap integral), the impurities states are very localized, the system is in an insolating state. When $\pm\frac{E}{I}$ decreases, the states are delocalized within the insolating gap. It exists a critical value at which the delocalization recovers the entire forbidden gap (Fig.1.8 (a)) resulting to the Anderson type of transition of the system toward metallic state.

It is important to remark that Mott and Anderson transitions show both localization of charge carrier but their origins are fundamentally different: for Mott transition it comes from electron-electron interactions while for Anderson transition it results from disorder.

In semiconductors, the conduction mechanism strongly depends on the carrier density i.e. the position of the Fermi energy. From the insulating state with E_F located within the gap, modulating the carriers density enables realizing partial inversion layer with the Fermi level surrounded by randomly distributed localized states due to the "oscillatory" structure of the conduction band edges (Fig.1.8 (d), right panel)[2]. This makes SC-TMDCs FET and more historically CMOS devices such as MOSFET suitable systems to study Mott-Anderson metal-to-insulator transition. From its position close to the conduction band edges where E_F is surrounded by random localized states, a continuous doping progressively moves higher the E_F and the surrounding states become more and more delocalized [Schmidt15] (Fig.1.8 (d), right panel). Further doping takes E_F deep in the conduction band leading to insulator to metal transition [Shklovskii84, Schmidt15].

[2]This means that the localized states are not exclusively from extrinsic origin and may result from the intrinsic band configuration of the material Fig.1.8 (d).

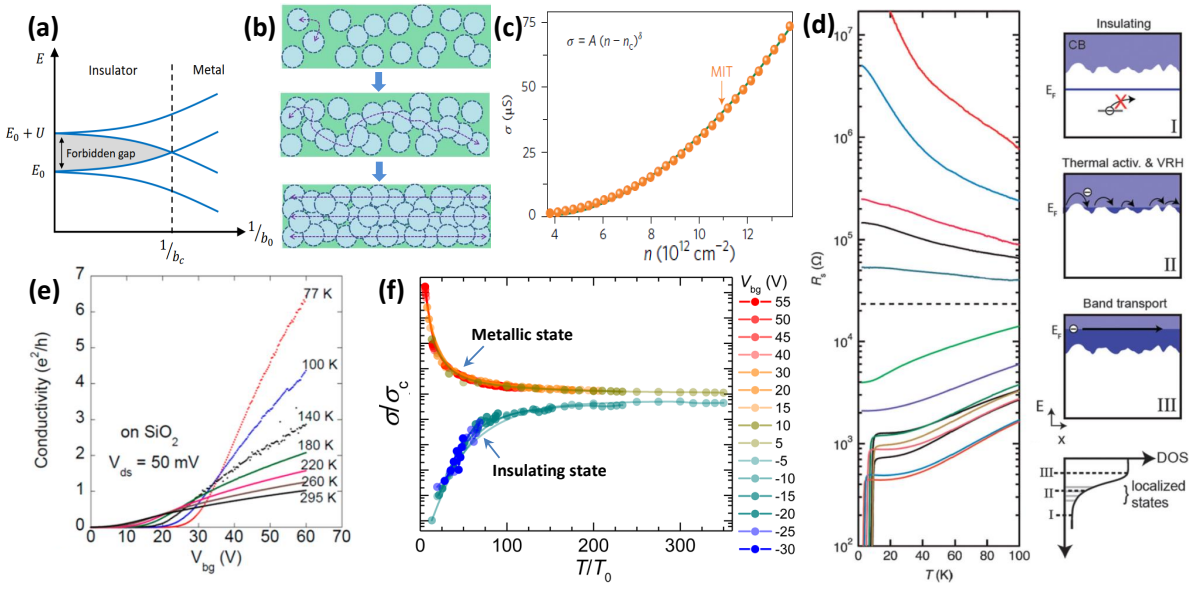

Figure 1.8 *– Transport mechanism in semiconductors: the case of SC-TMDCs . (a) Energy band of impurities. (b) Schematic of doping induced percolating conductive channels resulting to MIT as the electron density increase (from top to bottom). The circles denote isolated carrier puddles. (c) Conductivity dependency with the carrier density. The arrow highlights the critical point for MIT. (b-c) Adapted from [Chen15]. (d) The right schematic represents the energy band modulation in MoS_2 by doping and the corresponding transport mechanism. At the left, the corresponding T dependency of the resistivity for progressive doping (from top to bottom). One observes a transition from the insulating state (decrease of the resistivity) at low doping regime to a metallic state (increase of the resistivity) at intermediate doping regime to a superconductive state (the resistivity vanishes at low T) at high doping regime. Adapted from [Schmidt15]. (e) Conductivity dependence of $MoSe_2$ with both doping and T. The transition takes at the vicinity of quantum conductance. Adapted from [Chamlagain14]. (f) Scaling analysis of the renormalized conductivity of ReS_2 demonstrating metallic and insulating branches. Adapted from [Pradhan15a].*

Numerous of contributions have investigated both temperature and carrier density dependency of conductivity (or resistivity) of SC-TMDCs [Schmidt15, Pradhan15a, Chen15, Chamlagain14] (Fig.1.8 (b-f)). At low density, the Fermi energy lies within the gap and SC-TMDCs are in insulating state with no carriers contributing to the transport (Fig.1.8 (b)) [Chen15]. For n-type SC-TMDCs, positive Vg brings their Fermi energy to the conduction band edges (Fig.1.8 (d)) where it is effectively surrounded by random distributed states. Depending on the delocalization extention of such states, low temperature transport can be understood in the framework of percolation theory. In this theory, the sublattice of the random states is modeled as a network of random resistances. When the states are strongly localized (i.e. E_F in the gap) the conductance is given by $\sigma \propto \exp(-\xi)$, $\xi = \frac{E_C - E_F}{kT}$ [Shklovskii84]. In this strongly localized regime, with $E_C - E_F \gg kT$, ξ below a critical value ξ_c, the resistance of the system goes to infinity ($\sigma \to 0$) (Fig.1.8 (c)). In contrast, above ξ_c a percolating hoping channel is established in the resistance network (Fig.1.8 (b)). As ξ progressively increases more percolating parallel channels emerge in the material and the conductance obeys to the power law [Shklovskii84, Chen15] (Fig.1.8 (b)).

$$\sigma(\xi) \propto (\xi - \xi_c)^\alpha \quad , \quad \alpha > 0 \tag{1.11}$$

This behavior usually observed in MOSFET devices with $\xi = n$ (n being the charge density) has been observed in monolayer MoS_2, with $n_c \approx 3.2$ x 10^{12} cm^{-2} and the percolation component $\alpha \approx 1.7$ in the Eq. 1.11 (Fig.1.8.(c)) [Chen15].

For $\xi > \xi_c + 1$ the total resistance of the material becomes limited by the most resistive channels and the conductance takes the expression $\sigma \propto \sigma_0 \exp(\xi_c)$ and does not increase anymore with new percolating channels. In low temperature regime, the tunneling (hopping) probability between the neighboring states of the randomly distributed impurity states around the Fermi level is much smaller than the tunneling probability between the only few more distant states with energies close to E_F. The transport is thus mediated by hopping with a length determined by the balance between the distance to the more favorable states and the energy levels of the closer states. This is known as variable range hopping (VRH). The conductivity increases with temperature following the general formula expressed in Eq.1.12 [Schmidt15] (Fig.1.8 (c)).

$$\sigma(T) \propto \sigma_0 \exp[-(\frac{T_0}{T})^{1/(d+1)}] \tag{1.12}$$

Where σ_0 is the conductivity limit for an infinite temperature and d is the dimension of the system (= 2 for monolayer layers SC-TMDCs). T_0 is the limiting temperature which helps to quantify the disorder.
At high temperature regime, the hopping probability between the state becomes similar and the conduction is driven by thermally activated nearest neighbor hoping (NNH) [Schmidt15]. The T dependency of the conductivity becomes:

$$\sigma(T) \propto \sigma_0 \exp[-(\frac{E_a}{k_B T})] \tag{1.13}$$

With E_a the activation energy. From this hopping regime, further doping moved the Fermi energy deep in the conduction band and SC-TMDs undergo a transition to a metallic regime characterized by the decrease of conductivity with increasing T [Schmidt15, Yang17] (Fig.1.8 (c)).

Examples of nanoelectronic and optoelectronic applications

In the wake of graphene, research in 2D materials has evolved into a major branch of condensed matter physics, motivated by a search for novel physical phenomena in reduced dimensionnality and device engineering. Indeed, the presence of bandgap in TMDCs make them promising candidate for future transistor applications. SC-TMDCs have been intensively studied since their discovery including in nanoelectronic and optoelctronic. Their implementation in nanoelectronic devices has been made possible using either conventional dielectrics [Radisavljevic11, Pradhan14, Yu16, Mouafo17] or electrolytes [Zhang16, Yuan11] to tune charge transport both in their 2D plane and their interface with metallic electrodes. Dielectrics unveil electron transport in MoS_2, $MoSe_2$ and WS_2 while hole transport has been

demonstrated in WSe_2. For instance, Kis *et al.* used hafnium oxide and silicon oxyde on monolayer MoS_2 to demonstrate FET with On/Off ratio exceeding 10^8 and electron mobility of $217 cm^2 V^{-1} s^{-1}$ comparable with those achieved in silicon thin films [Gomez07]. Ambipolar transport, induced superconductivity and lateral *pn* junction have also been demonstrated in MoS_2 using electrolytes [Ye12, Zhang13a]. Thanks to the high charge carrier densities accessible with electrolytes.

SC-TMDCs based photodetectors have also been studied [Pospischil14, Mak16]. More generally, it consists of a channel of TMDC gate modulate or not, contacted by metallic contacts through which the conductivity changes upon illumination due to the variation in mobility or charge density or both. The mechanisms that give rise to photoconductivity in SC-TMDCs-based transistors are carefully studied in Ref. [Furchi14]. The devices involve are suitable for slow time response applications: Yin *et al.* [Yin11] provided the first demonstration of single layer MoS_2 phototransistor with 50 ms response time and a photoresponsivity of 7.5 mA/W. The second type of photodetector, based on WSe_2 is shown on Fig.1.9. It consists of the split-gate electrodes coupled to two different regions of a WSe_2 monolayer. By biasing one gate electrode with a negative voltage and the other with a positive voltage a lateral *pn* junction is made. Depending of the sign of the two gate voltages, *pn*, *np*, *pp* or *nn* junctions

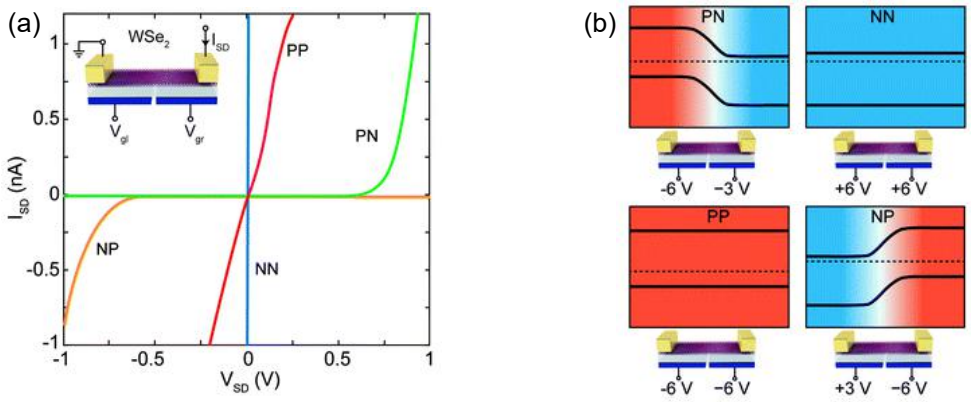

Figure 1.9 *– Lateral WSe2-photodiode. (a) Photocurrent as a function of the bias voltage under different biasing conditions, the inset presents the three-dimensional schematic view of a WSe_2 devices with split-gate electrodes. (b) Band diagrams of the junction at the same biases as in the photocurrent plot: the green line corresponds to pn junction (top left) ,the blue line nn (top right), the red line pp (bottom left), and the orange line np (bottom right). Figures extracted from Ref. [Pospischil14].*

(Fig. 1.9(b)) can be obtained on the same device. Such devices exhibit the typical photodiode characteristic as shown in Fig. 1.9(a) with a rectification behavior where the diode is achieved. They can thus operate as photodetector or photovoltaic devices. It is noteworthy that these devices suffer from the low light absorption because of their atomically thin thickness and spectral selectivity in the visible regime due to the rather large band gap which limits their performances. *One way to overcome those limitations is to sensitize thin channel materials with strongly light absorbing materials in MD-VdW-h, for instance thicker QDs or NCs film with strong light absorption as we will study in this work. Before talking about heterostructures, in the next*

session we will focus of colloidal nanocrystals.

1.2 Colloidal nanocrystals

1.2.1 Important concepts

Colloidal nanocrystals (CNCs) are semiconducting NCs synthesized in solution with a diameter of a few nanometer. The term NC refers to a crystalline nanoparticle. The nanometer-scale

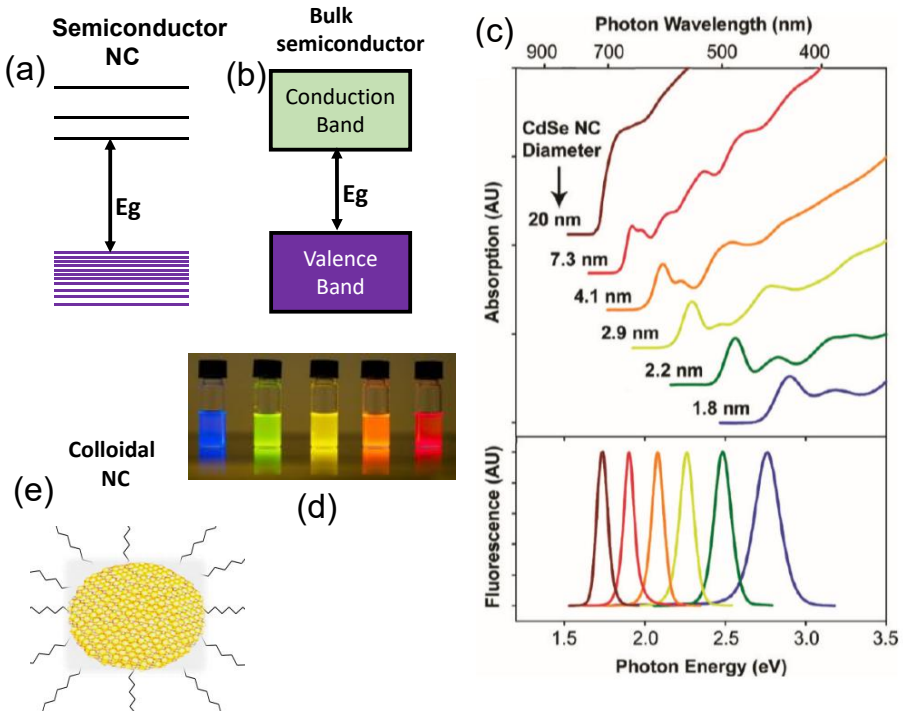

Figure 1.10 *– Electronic energy states of a semiconductor with: (a) discretization in nanocrystal and (b) continuum in bulk. (c) Absorption (top) and fluorescence (bottom) spectra of CdSe SC-CNC showing quantum confinement and size tunability below his exciton Bohr diameter of ≈ 9.6 nm. Adapted from [Smith10]. (d) Spherical colloidal nanocrystal surrounding by ligands. (e) CdSe CNCs of different size in solution, illuminated by UV light (©Nexdot).*

of the crystal allows to confine spatially both electrons and holes in three dimensions, then leads to interesting **quantum effects** [Talapin10, Kim15]: *Optical and electrical properties of the NCs can be tune by changing their size and shape during the synthesis* as shown in Fig.1.10. *So the most important feature of the quantum confinement is the size-tunable optical band gap allowing to tune the NC's absorption throughout a large spectra wavelength range from visible to mid infrared.* The first observations of these effects were collected from optical measurements on the semiconductor dots dispersed in glass matrices [Ekimov81] or aqueous semiconductor sols [Brus86]. Untill the mid-1990s the major challenge was to synthesize dots of uniform, size-tunable and isolable with tunable properties. Thanks to the hot injection technique in colloidal synthesis, introduced in 1993 by Murray, Norris and Bawendi to demonstrate the first colloidal synthesis of Cd chalcogenide NCs [Murray93] which unveiled bright luminescence

in the visible. The technique has the particularity to form highly monodisperse NCs which is very important for NCs to have the same confinement at the same energy. It is low cost with respect to expensive expitaxial growth achieved in ultra-high vacuum chamber and it allows ligand exchanges in solution. From that, many synthesis have been done on NCs with a wide spectra range of applications including photovoltaic [Carey15] and photodetection [Livache19, Saran16, Konstantatos10, Qian11, Li11a, Steckel03]. While CdS, ZnS, ZnSe, InP, Si and Ge NCs have been used for visible applications, lead chalcogenides, cadnium mercury chalcogenides and mecury chalcogenides NCs have shown prospects for IR applications.

Among these applications, low cost short-wave infrared (SWIR, 0.9 to 1.7 μm) and mid-wave infrared (MWIR, 3 to 5 μm) photodetectors are raising more and more interests [Lhuillier17, Lu19]. Mercury telluride (HgTe) appears as the most tunable material to address these ranges of wavelength, thanks to **the semimetal nature of the bulk material** [Lhuillier12, Allan12]. The latter allows to have narrow-band gap NCs due to quantum confinement. Fig.1.11 (a) shows the calculated band structure of HgTe bulk with zero gap at the center of the Brillouin zone Γ with a reversed band ordering compared to classical semiconductors: the Γ_6 band (usually a conduction band) is found deep below the first degenerated valence bands whereas the first conduction band is a Γ_8 band (which is usually a valence band) [Livache19]. As we said before, due to quantum confinement, decreasing the NC size below its Bohr exciton diameter leads to the increasing of the band-bap. Bohr exciton diameter of HgTe is about 80 nm, HgTe nanocrystals then feature low interband transition as shown in Fig.1.11 (b) ($1S_h$ to $1Se$) with size-tunable interband absorption from SWIR to MWIR(see Fig1.11 (c)). In this thesis, we will focus on HgTe NCs with band-edge around 4000 cm^{-1}

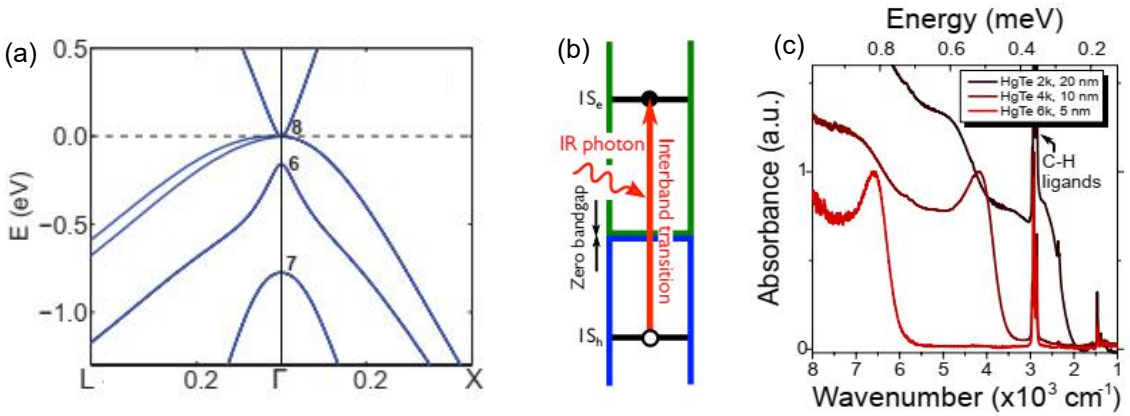

Figure 1.11 *– HgTe Characteristics. (a) Calculated band structure of the gapless bulk HgTe (semi-metal) from [Svane11]. (b) Low energy interband transition in HgTe NC between discrete electronic $1S_h$ state and $1S_e$ state (semiconductor) (b) Absorption spectra of HgTe NCs of 20 nn, 10nm and 5nm sizes displaying a size-tunable bandgap from SWIR to MWIR. "6k", "4k" and "2k" refer to the absorption band-edges of the nanocrystals, respectively around 6000 cm^{-1}, 4000 cm^{-1} and 2000 cm^{-1}. Figures Adapted from Ref. [Livache19].*

(≈ 2.5 μm) called "HgTe 4k", because they are currently generating strong interest for the design of high-performance and low-cost infrared sensors with low power consumption in MWIR. Thanks to their low cost, ease of fabrication, stability and integrability with existing

technology.

1.2.2 Transport in nanocrystal arrays

In the previous section we introduced some important concepts about CNCs and their applications. In this section, we will be interested in the transport mechanisms of an assembly of NCs densely packed films. To do so, let's consider a film of nanocrystals randomly distributed on a plane surface connected by two electrodes (source and drain), see Fig. 1.12 (a). NCs are

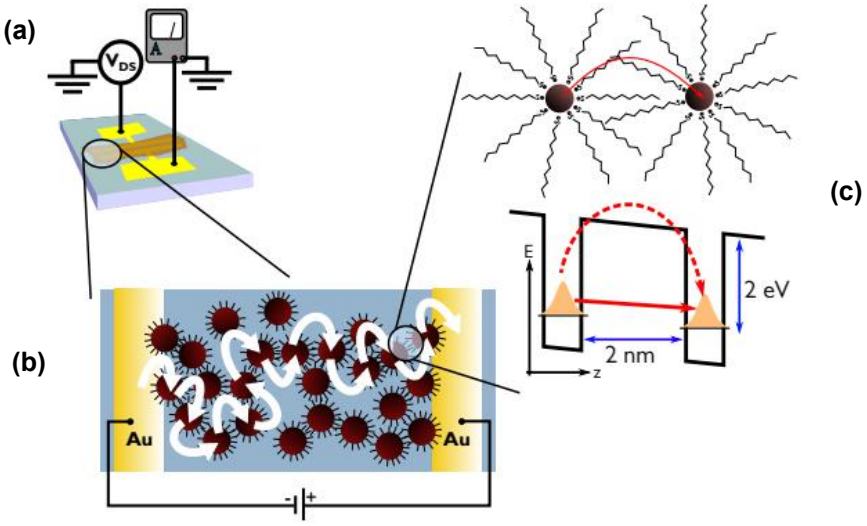

Figure 1.12 *– Hopping transport in a nanocrystal film. (a) Scheme of a nanocrystal film deposited on gold electrodes, connected to a bias source and to a current-meter. (b) Transport of an electron via multiple hopping steps in a nanocrystal film. (c) Sketch of two neighbour nanocrystals, separated by long organic ligands. The ligands constitute a barrier for a charge to hop from one nanocrystal to the other. The electron can either tunnel through the barrier (plain arrow) or be thermally activated other the barrier (dashed arrow). Adapted from Ref. [Livache19].*

separated from each other by a few nanometers because they are capped with long organic ligands. As a result, they are poorly electrically coupled. In order to transport carriers from one electrode to the other, a charge have to follow a percolation path through the film, i.e. *hopping* from NC to NC as shown in Fig. 1.12 (b). Another way to understand this *hopping transport* is to consider the wave-function extension of the ground states of a NC: the overlap between the wave-functions of two neighbour crystals is weak (Fig. 1.12 (c)), so each hopping step can be either a thermally activated transfer above the barrier, or a tunnel event through the barrier formed by the medium separating two NCs (mostly composed of ligands).
In hopping transport in NC arrays, the key parameter driving the carriers mobility is the tunnel barrier between two sites (i.e. two nanocrystals). The transparency of the barrier using the Wentzel, Kramers and Brillouin (WKB) approximation can be written as [Guyot-Sionnest12]:

$$T_{trans} = exp(-2z\sqrt{\frac{2m^* V_B}{\hbar^2}}) = exp(-\zeta z) \tag{1.14}$$

Where z is the barrier length, V_B the barrier height and m^* the effective mass of the carrier. ζ describes the extension of the wave-function in the barrier. Using a diffusive model in three

dimensions and using Einstein's equations:

$$D = \frac{\mu k_B T}{e} = \frac{R^2}{6\tau_{hop}} \tag{1.15}$$

The mobility of a carrier can be expressed as:

$$\mu = \frac{eR^2}{6\tau_{hop} k_B T} \tag{1.16}$$

Where D is the diffusion coefficient associated to charge transport, R is the nanocrystal size, k_BT the thermal energy and τ_{hop} is the hopping time. Each hopping step being a tunnel event, the hopping time can be written as a function of the interdot barrier transparency:

$$1/\tau_{hop} \simeq \frac{2E_a}{\hbar} T_{trans} exp(-E_a/k_B T) \tag{1.17}$$

With E_a the activation energy of the hopping process which depends on the NC charging energy and the degree of disorder of the channel. It is of the order of 50 meV for semiconductor nanocrystals film [Guyot-Sionnest12].
From Eq. 1.16 and 1.17, one can deduce the electronic mobility as:

$$\mu = \frac{eR^2}{3\hbar k_B T} exp(-\zeta z - E_a/k_B T) \tag{1.18}$$

To summarize, the transport in NCs films is controlled by the *hopping events from one electrode to the other*. Depending on the electrodes spacing, there is between 10 (for $\simeq$ 100 nm spaced electrodes) and a few thousands hopping steps (for $\simeq 10\mu$m electrodes). Thus, charge transport is a diffusive process, with charges flowing through multiple percolation paths that are susceptible to change with applied voltage, temperature and film chemistry such as ligands exchange [Livache19]. It is important to note that two main parameters compete for a carrier to choose its next site: the distance and the energy of the final state. Therefore it comes out two channel for hopping, the NNH and the VRH. Both channels are always active, but their relative contribution is tuned by temperature and density of states as introduced in the section 1.12.

1.3 Mixed-dimensional van der Waals heterostructures

2D materials are dangling-bond free sheets with fully satured chemical bonds at the surface which allow the integration of highly disparate materials, by van der Waals interactions without any constraints of crystal lattice matching with new functionalities. So 2D materials can be coupled to nanoparticles (0D), nanowires (1D), materials (2D) as well and crystalline bulks or polymers (3D) to built 2D-nD (n = 0, 1, 2, 3) mixed dimensional van der Waals heterostructures (MD-vdW-h) [Jariwala16, Liu16b]. *It is important to note that, in such MD-vdW-h, at least one 2D material is involved, which offers the flexibility, semi-transparency for vertical field, better scalability and low cost integrabilty compared with existing heterostructure in photovoltaic and*

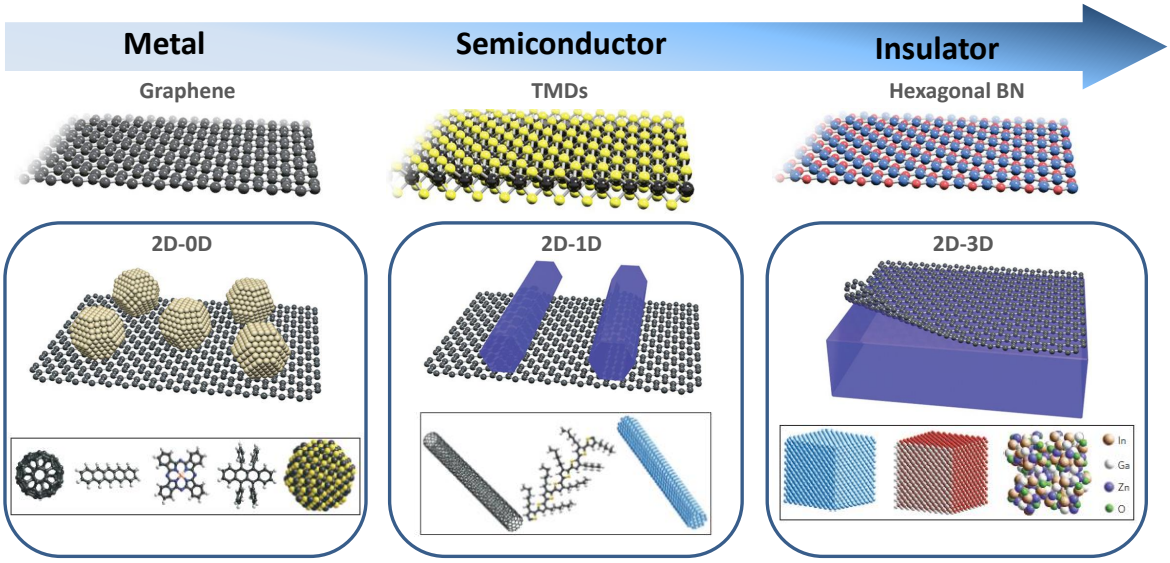

Figure 1.13 *– 2D-nD (n = 0, 1, 3) heterostructures consisting of the interaction of 2D material with material of other dimensionality : 0D (Nanoparticles, dispersed molecules, fluorine C_{60}), 1D (Nanowire and nanotube), 3D (2D material interact with bulk substrate and other bulk materials). Adapted from Ref [Liu16b, Jariwala16].*

LED industries [Casey12].

In general 2D-nD (n = 0, 1, 3) heterostructures are fabricated using conventional microfabrication techniques where the 2D material is either mechanically exfoliated or grown using chemical vapor deposition (CVD) or epitaxial methods. Then the nanoobjects are deposited by drop-casting or spin-coating [Houdy06] (Fig. 1.13). On the other hand, 2D-2D heterostructures are fabricated using much complex techniques such as direct assembly by micromechanical stacking. This technique takes advantages of the weak van der Waals nature of the interlayer interactions. Unfortunately, such a fabrication technique is not suitable for large scale production, then only suitable for fundamental research. In what follows, I will present some examples of MD-vdW-h.

The coupling of NCs (0D) with 2D materials to form 0D-2D MD-vdW-h geometry has been intensively investigated and revealed properties and functionalities that already lead to prospects even in our group for quantum electronics [Godel17], spintronics [Mouafo18, Song19] and optoelectronics [Konstantatos12, Zhang19].

For photodetection applications, 2D-0D heterostructures take advantages of high carrier mobilties of 2D materials and strong tunable light absorption of quantum dots. Indeed, the approach was first adopted using semiconductor quantum dots as sensitizers on graphene FETs. Fig.1.14(a) shows graphene-PbS heterostructure where PbS QD sensitizers play a key role and are used to convert photons into electric signals in the photodetector (by absorbing photons and generating electron-hole pairs). Generally, the carrier with the lowest band offset with respect to 2D materials is transferred in 2D materials while the other stays in QDs. This charge separation is induced by an internal electric field that comes from the band bending at graphene-QDs interface due to the work function mismatch between graphene

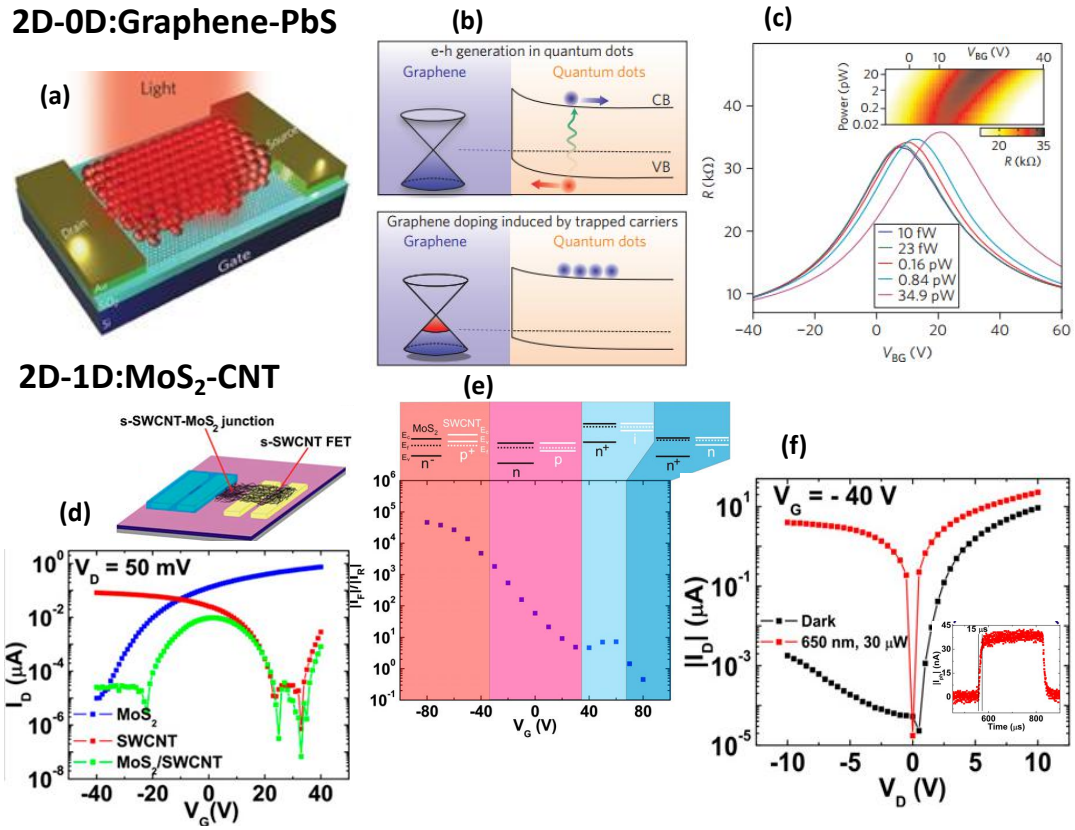

Figure 1.14 – 2D-0D and 2D-1D vdW-hs. *(a) Schematic of 2D-0D heterostructure based on graphene and PbS quantum dots, (b) Energy level diagram of the graphene-QD interface: A built-in electric field formed at the interface resulting from the transfer of electrons from QD to graphene as shown in the top panel, illustrating the bands for V_{BG}=V_D. On photoexcitation of PbS QDs, electrons are trapped in the PbS quantum dots while holes are transferred to the graphene under the built-in field, then shift down the Fermi energy in the graphene (bottom panel). (c) Resistance as a function of back-gate voltage for the graphene-QD structure for increasing illumination intensities provided by a collimated laser wavelength of 500 nm. Increasing the illumination leads to a photogating effect that shifts the Dirac point to higher back-gate voltage. This indicates hole photodoping of the graphene flake. Inset: two-dimensional plot of graphene resistance as a function of optical power. Figures extracted from Ref. [Konstantatos12]. (d) Top: Schematic of 2D-1D device. Bottom: Transfer curves displaying n-MoS_2 (blue), p-SWCNTs (red) and ambipolar transport in the junction (green). (e) Top: Gate dependent band diagrams for the SWCNT/SL-MoS_2 (2D-1D) heterostructure bias magnitude of 10 V, demonstrating n^-p^+, np, n^+i or n^+n junctions. Bottom: Gate dependent forward-to-reverse current ratio showing an important rectification at high negative voltage where the junction n^-p^+ is formed. (f) Current in the n^-p^+ in dark (black) with a clear signal rectification and under illumination (red) showing an important current modulation with On/Off ratio exceed 10^3, the inset shows the time dependent photoresponse of the p-n heterojunction showing fast rise and decay times of $\approx 15\mu s$. Adapted from [Jariwala13].*

and QDs. Indeed, when QDs are deposited on graphene, holes from graphene are transferred to the QD layer, forming a built-in electric field to equilibrate the Fermi levels. Upon illumination, photogenerated-electrons are trapped in QDs and holes taking advantages of the built-in field, are transferred in graphene (Fig.1.14(b)). Because of high carrier mobilities of graphene, hole will circulate many times and will contribute several times for the photocurrent during the lifetime of electron that remains trapped in QDs, this photogating effect leads to very large photo gain with high responsivity exceeding $10^7 AW^{-1}$, five decades

higher than the one obtained in graphene phototransistors and the highest value reported for graphene-based photodetector [Konstantatos12]. The photogating effect can also be seen on the graphene sheet resistance (Fig.1.14(c)), where one can observe shifts of the Dirac point to higher back-gate voltage when increasing the illumination, then indicates hole doping of the graphene flake. Plasmonic nanoantenas have also been coupled with graphene to enhance the photoresponse using the field enhancement resulting from plasmon surface.
Although these graphene based heterostructures have a large responsivity, they suffer from some key limitations such as the large dark current, and dramatically slow time response [Tang19c]. To reduce the dark current, it was later proposed to replace the gap-less graphene by SC-TMDCs [Lopez-Sanchez13, Kufer15, Yu17, Hu17, Huo17]. The responsivity of phototransistors has been improved to 880 and 10^6 AW^{-1} in the device consisting of p-PbS QDs decorating the surfaces of the monolayer and fewer-layers MoS_2 respectively [Kufer15]. By spin-coating a layer of n-type PbS QDs on top of the channel of n-type monolayer WS_2 transistor, Yu et al. demonstrated a stable 2D-0D photodetector with a responsivity of 14 $A.W^{-1}$ at 808 nm, a specific detectivity of 4x10^8 Jones and rise and decay time response of 153 and 226 μs respectively [Yu17]. *In these 2D-0D heterostructures the coupling between the 2D material and NCs occurs through a tunnel process and only the NCs in the very vicinity of the 2D material are actually contributing to the photoconduction.*

***P*-type semiconducting single-walled carbon nanotubes SWCNTs have been successfully deposited on the n-type MoS_2 monolayer to form vertical p-n heterojunction (2D-1D vdW-h)**, see Fig.1.14(d), to work both as logic gate FET and photodiode [Jariwala16]. The atomically thin nature of MoS_2 monolayer makes it transparent to the vertical electric field, then both the MoS_2 layer and the CNT films can be modulated by the gate voltage, allowing to figure out n^-p^+, np, n^+i or n^+n junctions (Fig.1.14(e)). In the n^-p^+ junction at high negative voltage, SWCNT completely becomes p-doped (the Fermi energy is in the valence band) while MoS_2 remains extrinsic n-doped (Fermi energy below but near the conduction band), the rectification become important, the photogenerated excited carriers are quickly separed by the built-in electric field, leading a photocurrent with On/Off ratio exceed 10^3 (Fig.1.14(f)) and a fast responsivity less than 15 μs. Graphene-GaAs nanowires and graphene-ZnS nanowires photodetectors have also been demonstrated with 71 μs and 120 ms time response respectively [Gong18, Wu17].

2D-2D vdW-h have been intensively studied, it implies not only graphene-hBN heterostructures but also hBN-TMDC heterostructures, graphene-TMDC heterostructures and TMDC-TMDC heterostructures. h-BN is an insulator, and is used to encapsulate graphene and TMDCs in order to prevent them from extrinsic sources of scattering such as substrate roughness or impurities and water molecules adsorbed during the sample processing. This enables to achieve high mobilities reaching 200000 $cm^2V^{-1}s^{-1}$ in Gr FET [Mayorov11]. Gr/h-BN heterostructures based vertical tunneling transistor have also been reported [Wang16, Pisoni18]. By reducing the scattering effect using a h-BN substrate, a mobility as high as 163 $cm^2V^{-1}s^{-1}$ was achieved for monolayer WS_2 FET [Iqbal15]. PL emission

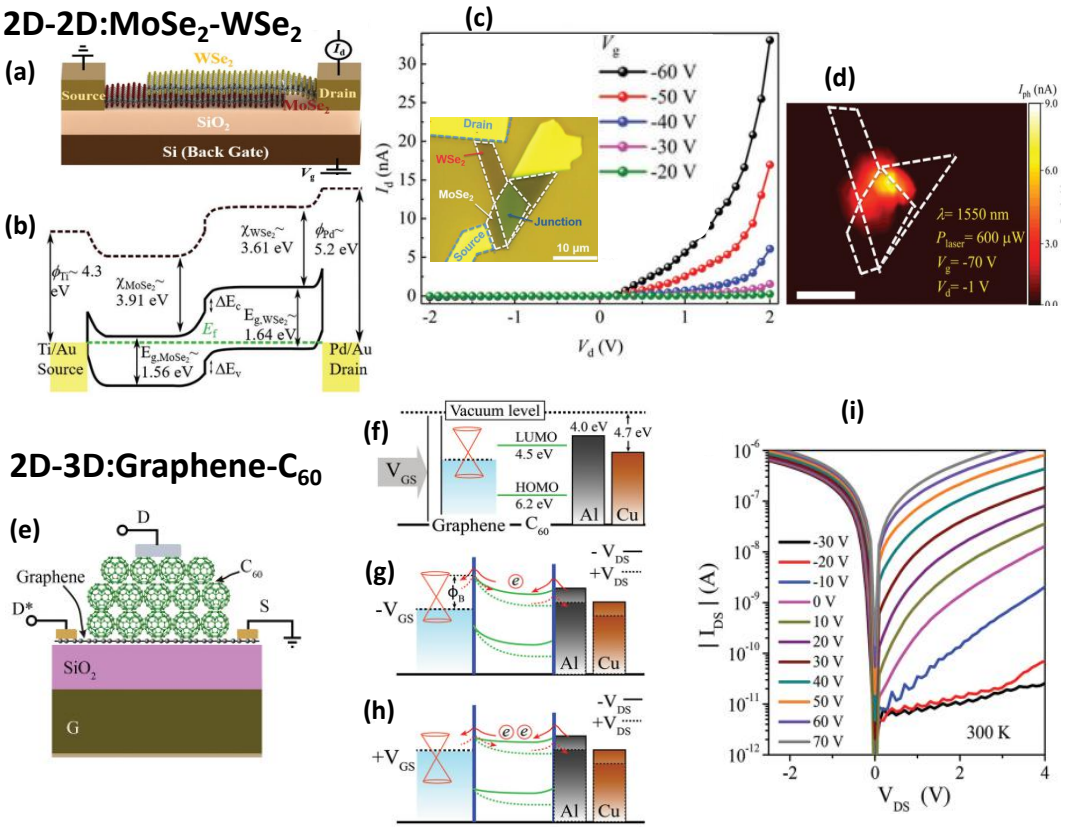

Figure 1.15 – 2D-2D and 2D-3D vdW-hs. *(a) Schematic of $MoSe_2$-WSe_2 (2D-2D) heterostructure. (b) Schematic band diagrams of the device, ϕ is the work function of the metal, χ the electron affinity of the flake, E_f the Fermi energy and E_g the band gap (c) I-V curves measured with variable back-gate voltages in dark showing a rectification at negative gate votages, the inset shows an optical image of the device. (d) Photocurrent mapping of the heterostructure (scale bar: 10μm). Adapted from [Xue18]. (e) Schematic of graphene-C_{60} (2D-3D) heterostructure based on CVD-growth graphene transferred on Si/SiO_2 and evaporated 280 nm film of C_{60}. (f) Band energy diagram of a FET, representing the hole-doped graphene strip, the molecular levels of C_{60} and the work function of the drain electrode (Al, Cu). The same energy diagram under (g) negative V_{GS} and (h) positive V_{GS} with grounded graphene film under negative V_{DS} (solid) and positive V_{DS} (dashed), respectively. (i) I-V curve of graphene-C_{60} heterostructure at different gate voltages, the gate allows to tune the interface and achieve a rectification behavior at negative voltages. Adapted from [Parui15].*

of TMDCs is dominated by defects at low temperature, when encapsulating them with h-BN, optical signatures become more cleaner with narrower peaks [Lorchat19]. In addition, a repeating stack of 2D TMDC semiconductors/h-BN constitutes stable quantum well with negligible leakage demonstrating efficient electron to photon conversion within the active semiconductor TMDC layers when an electric field is applied perpendicular to the stack. LEDs consisting of such heterostructures have shown quantum efficiency reaching 20% at room temperature [Novoselov16] comparable to organic LED and state of the art GaAs based quantum well LED.

In most of graphene-TMDC devices, graphene is used as tunable work function electrodes and SC-TMDCs as photoactive material with strong light-matter interaction. Britnell *et al.* [Britnell13] and Yu *et al.* [Yu13] have reported the first vdW-h photodetectors displaying a graphene-SC-TMDC-graphene structure. A bias between the two graphene electrodes

is applied in order to separate and collect the photogenerated carriers in the TMDC. Note that electrostatic doping of graphene layers can also create a buid-in electric field even without applying a bias voltage. Furthermore, Massicotte *et al.* [Massicotte16] have demonstrated an intrinsic response time shorter than 10 ps in such devices.
TMDC-TMDC heterostructure has been demonstrated by Hailing *et al.*, they have synthetized a vertical $MoSe_2$-WSe_2 heterojunction using sputtering-CVD method. They demonstrated that not only WSe_2 and $MoSe_2$ can be gate modulated with hole and electron mobilities of ≈ 2.2 and $\approx 15.1 cm^2 V^{-1} s^{-1}$ respectively, but also the rectifying $I-V$ behavior of the pn junction [Hailing18]. To go further, Xue *et al.* studied optoelectronic properties of such junctions (Fig.1.15(a-d)). They mechanically exfoliated from the bulk few layers p-WSe_2 and n-$MoSe_2$ and stacked them in $MoSe_2$-WSe_2 heterojunction on SiO_2/Si substrate as shown in Fig.1.15(a). They demonstrated a high-sensitivity $MoSe_2$-WSe_2 $p-n$ photodetector with a strong gate-dependent photoresponse. Usually in such junctions, the responsivity is limited by the high Schottky barrier at the contact regions and the insufficient band bending in the overlapping region (see Fig.1.15(b)). So by applying a high negative gate volatage, they reduced the Schottky barrier height at the metal-flake regions and achieved gate-modulated rectifying I_d-V_d curves (Fig.1.15(c)) indicating the formation of the $p-n$ junction at the $MoSe_2$-WSe_2 interface. Under a reverse bias, means applying a negative voltage on WSe_2 side, leads to increase band bending at the heterojunction region, then leads to an increase of the built-in electric field in the $p-n$ junction, thus allows a fast separation of photo-generated carriers. In those conditions, they found high sensivity photodetection suitable for telecommunication band (wavelength of 1550 nm) with a responsivity of $127 mA W^{-1}$ at room temperature [Xue18].

2D-3D heterostructures typically require growth or transfer of 2D material on the bulk 3D material. While CVD graphene has been growth on bulk germanium to form graphene-gemanium heterostructure [Kazemi17], MoS_2-GaN heterostructure has been made by epitaxial MoS_2 and bulk gallium nitride (GaN) [Ruzmetov16]. The latter demonstrated out of plane electrical conduction, confirming the potential of direct synthetized of 2D-3D heterostructure for vertical flow current. On the other hand, 2D-3D heterostructure was performed using bulk Parylene-C spincoated on CVD graphene. This graphene-Parylene-C heterostructure shown good mechanical properties suitable for many active components in MEMS technologies [Berger16]. A report on graphene-C_{60} thin film FET and phototransistor demonstrated a gate tunable interface energy barrier and a gate-modulated photocurrent (Fig.1.15(e-i)) [Parui15]. Indeed, a 280 nm thick of molecular semiconductor C_{60} has been evaporated on CVD-growth graphene (initially transferred on Si/SiO_2 substrate which acts as back gate) contacted by two metallic electrodes (D* and S used as source electrodes) to build 2D-3D hetorostructure as shown in Fig.1.15(e). Then, the C_{60} layer is contacted on the top (D used as the drain electrode) to form a vertical FET with a graphene source electrode. *This geometry is important not only for the possible modulation of the Fermy level, the corresponding work function and the low DOS of graphene which provides a tunable energy barrier at graphene-C_{60} interface but also the extend of the vertical electric field from the gate into C_{60} film, because of the low electric screening of monolayer graphene.* Fig.1.15(f) shows the band

energy diagram of a FET without contact, with the hole-doped graphene strip, the molecular levels of C_{60} and the work function of the drain electrode (Al, Cu). Once the materials get contacting, Fermi level alignments result in a band bending at both graphene-C_{60} and C_{60}-Al interfaces. Applying a negative V_{GS} (Fig.1.15(g)) shifts the Fermi level of the graphene downwards, effectively increasing the graphene-C_{60} junction energy barrier for electrons. In this case, when the graphene-C_{60} junction is under negative voltage V_{DS} (solid line) electron can easily move from top the contact to graphene troughthout the junction (forward diode condition) while the junction under positive V_{DS} (dotted line) leads to large energy barrier for electron (reversed condition). In case of a positive V_{GS} (Fig.1.15(h)), the graphene Fermi level shifts upwards while more electrons will be induced in the first few monolayers of C_{60}. This modifies the C_{60} energy levels alignment with respect to graphene and reduce the height of the graphene-C_{60} junction, such that the electron transport will be much easier for both negative and positive V_{DS}, thus a reduction of the rectification. It is important to note that, here the energy barrier modulation will only be at the graphene-C_{60} junction whereas the C_{60}-metal junction at the top will act as the a fixed barrier without any change at different V_{GS}, because of the large DOS of metals which requires an exceedingly large amount of induced charge to move their Fermi energy. Fig.1.15(i) shows I-V curves at different gate voltage at room temperature with high rectification curves at high negative gate voltages. Illuminating the junction under the reversed condition leads to the photocurrent which is also gate-modulated. *These demonstrated the prospects of graphene as carrier selective transparent electrodes for the vertical field*. Similarly, Liu *et al.* have epitaxially grown small-molecule C8-BTBT on top of graphene using a CVD approach and fabricated graphene-C8-BTBT hybrid phototransistors with high photoresponsivity and photogain up to 10^4 AW^{-1} and 10^8 respectively, and a time response of 25 ms [Liu16a], whereas under the same device concept, Chang *et al.* demonstrated graphene-polymer semiconductor (PTB7) hybrid phototransistors with responsivity exceeding 10^4 AW^{-1} and the temporal response of 7.8 ms [Chang17].

1.4 Post process doping of nanomaterials

The doping of nanomaterials at the device level is currently driven by two gating approaches in FET geometry: either the use of conventional dielectric such as SiO_2 or electrolytes. This allows to tune the carrier density in the nanomaterials by applying a perpendicular electric field, in order to get more insight about the transport feature (electrons transport or/and holes transport) and to evaluate the carrier mobility. In FET geometry, a semiconductor nanomaterial (either NCs or 2D materials) channel is contacted by two electrodes (source and drain) to drive the current in the channel when applying bias V_{sd}, a third electrode (gate) used either in the bottom or on the top allows to control the doping when sweeping with a voltage V_g, see Fig.1.16 (c) and Fig.1.17 (c). The linear part of the transconductance also called the transfer curve (which describes the evolution of the channel conductance at fixed bias V_{sd} as a function of gate voltage V_g) allows to deduce the carrier mobility as:

$$\mu = \frac{L}{CWV_{sd}} \frac{dI_{sd}}{dV_g} \tag{1.19}$$

wher L and W are the length and the width of the channel respectively, C the specific capacitance of the dielectrics or electrolytes used. This capacitance is very important for the performance of the device as we will describe in details for these two gating techniques in the following sections.

1.4.1 Conventional dielectrics

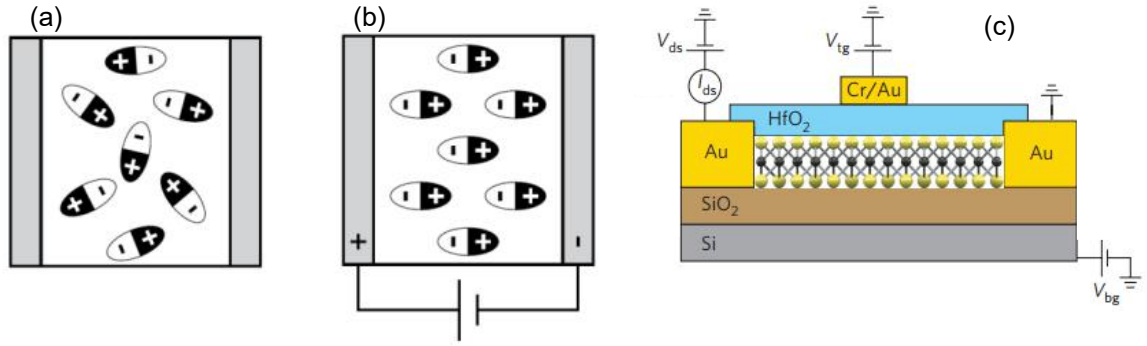

Figure 1.16 *– Dielectric gating. (a) Random orientation of permanent dipoles when no bias is apllied. (b) Dipole moment aligment with applying voltage (c) Schematic diagram of the dielectric gating device with both back (SiO_2) and top HfO_2 gates on 2D material. Adapted from [Zanettini15a].*

Dielectrics are insulating materials (no free charges) with a dielectric permittivity ϵ_r. The latter and the thickness of dielectric are impotant parameters for FET gating. Indeed, when gating FETs with dielectrics (SiO_2, HfO_2, Al_2O_3, etc), the application of gate voltage produces the polarization of the dielectric material by simply orienting the existing permanent dipoles or inducing temporary dipole moments which disappear when the electric field is removed [Zanettini15a]. Figures 1.16(a) and (b) show the polarization of a parallel plate capacitor with an insulating dielectric layer having permanent dipoles. The capacitance of such parallel-plate capacitor and the accumulate charges at the surface are given by:

$$C = \frac{\epsilon_0 \epsilon_r A}{d} \quad and \quad n = \frac{CV}{e} \tag{1.20}$$

with ϵ_0 the dielectric constant of the vacuum, A the capacitor plate area, d the dielectric thickness, V the apllied voltage and e the elementary charge. The specific capacitance of SiO_2 dielectric with a thickness (from 200 to 300nm) is in the range of few nanofarad per centimeter square (1-11.5 nF/cm^2) and can accumulate 10^{11} to 10^{12} charges/cm^2 while high k-dielectrics (HfO_2, ZrO_2, Ta_2O_5, Al_2O_3) can reached 0.1μF/cm^2 and charge densities of 10^{13}. *Dielectrics can be used for back and top gate devices (Fig.1.16 (c)), and allow fast sweep rate over a broad range of temperatures (from room temperature to 1 K) but require a large operating bias, then possible dielectric breakdown.*

1.4.2 Electrolyte gating

Contrary to dielectrics, electrolytes (ion gels, electrolyte solutions, ionic liquids, polyelectrolytes, polymer elctrolytes) are ionic materials with free ionic charges which can move

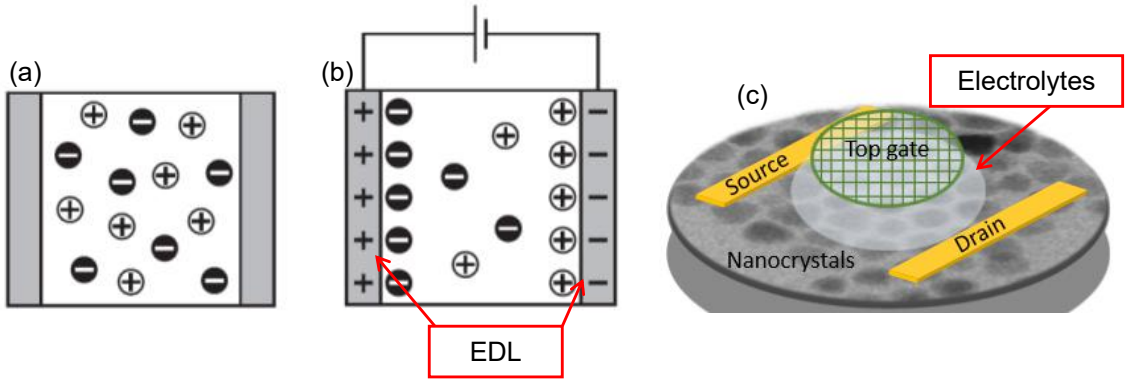

Figure 1.17 *– Electrolyte gating. (a) Free ions in the electrolyte parallel plate capacitor when no bias is apllied. (b) EDL formation at each interface at the equilibrium when applying a voltage. From [Zanettini15a]. (c) Schematic diagram of electrolyte gating device on nanocrystal (top gate). Adapted from [Lhuillier14].*

when an electric field is applied, so they are ion conducting but electronically insulating [Zanettini15a]. Fig.1.17 (c) shows an illustration of electrolyte parallel plate capacitor. When an external bias is applied, ions accumulate into the electrodes. While negative ions move towards the positive electrode, positive ions migrate to the negative electrode and form at the equilibrium electric double layers (EDL) with nanoscale thickness at the interfaces (Fig.1.17 (c)). This small thickness (in the range of nanometer) allows to have high specific capacitance (in the order of μF/cm^2), then to accumulate high charge carriers (10^{13} to 10^{14} charges/cm^2) at low bias, interesting to study fundamental propreties in materials. Iwasa's group used electrolyte gating to demonstrate superconductivity, lateral p-n and ambipolar transport in MoS_2 [Ye12, Zhang13b]. *Due to the froozen of ions at low temperature not far from room temperature, electrolytes are used at quasi-room temperature. Electrolytes are only used in top gate geometry which prevent the top access either for optical studies or to detect molecules or gases. This geometry also has a limitation to study or to control the interfaces between materials involved in vdW-h for instance.*

1.5 Figures of merit for photodetection

Photodetectors, also called photosensors are optoelectronic devices used to sense light or other electromagnetic radiation through electronic processes. In other words, they are devices which transform the light they absorb into a measurable quantity (generally an electric current or an electric voltage) by converting photons into electric charges. One distinguishes: photoconductors, photodiodes and phototransistors. So far, the developed photodetector technologies have covered the whole application spectrum that profoundly affects our daily lives [Huo18]: X-rays for biomedical imaging [Lussani15] ultraviolet for lithography and living cell inspection [Bartels02, Zeskind07] visible light detection for digital camera and video imaging [Fowler10] broad-range infrared detection for night vision, optical communications, atmospheric and quality inspection spectroscopy [Kallhammer06, Kim04, Kahn97, Formisano04] among others. To evaluate and compare their performances for different ap-

plications, figures of merit and standard terminologies are used. In this section, I recall the mechanism of photodetection and I define important parameters used in this work.

1.5.1 Photoconductors

A photoconductor typically consists of a semiconducting material, single-crystalline, polycrystalline or amorphous, contacted by two electrodes to form a two probes electrical device. Upon illumination with a light with photon energies (E_{ph}=hν) higher than the optical band gap energy of the semiconductor, the conductivity of the material changes $\Delta\sigma$ due to the generation of electron-hole pairs resulting in carrier density variation Δn as:

$$\Delta\sigma = q\mu\Delta n \tag{1.21}$$

where σ is the conductivity, n the carrier density, q the elementary charge and μ the mobility. The increase of conduction leads to a photon current:

$$I_{ph} = \Delta\sigma EWd = q\eta(\frac{P_{in}}{E_{ph}})(\mu\tau E), \quad and \quad \Phi_{in} = \frac{P_{in}}{E_{ph}} \tag{1.22}$$

where E, W, d, η, P_{in}, τ, Φ_{in} are electric field, channel width, depth of the absorption region, quantum efficiency, incident power, life time and incident photon flux respectively. The responsivity of the detector, describes how the detector responds to the light by measuring the output current per incoming optical power on the area WxL. It is expressed as [Kufer16b]:

$$R = \frac{I_{ph}}{P_{in}} = (\frac{\mu\tau E}{L})(\frac{q\eta}{E_{ph}}) = \frac{Gq\eta}{E_{ph}} \tag{1.23}$$

where G is the photoconduction gain given by:

$$G = \frac{\mu\tau E}{L} = \frac{\tau}{\tau_{transit}} \tag{1.24}$$

with $\tau_{transit}$ the transit time of the photocarrier and L is the channel length.
In fact, the response of a detector to light depends primarily on the conversion efficiency of photon flux into electron flux, known as the quantum efficiency. The latter typically takes into account all kind of external losses such as reflection and scattering and is often called external quantum efficiency (EQE). It is equal to the number of electron-hole pairs per second generated and effectively participating to the photocurrent, divided by the number of incident photons per second: EQE = $I_{ph}/q\Phi_{in}$, a value between 0 and 100% unless an internal gain mechanism is present.
The transit time $\tau_{transit} = \mu E/L$ can be understood as a time taken by a photogenerated carrier to cross the channel from one electrode to another. If its lifetime τ is longer than the transit time, the photoconduction gain takes values above unity: one electron (respectively hole) can loop around the polarization circuit several times before being recombined, hence contributing several times to the photocurrent, thus leading to high gain and by the way high responsivity. The common picture is that one of the carriers get trapped, allowing the other

one to circulate as long as its counterpart is not available for recombination [Huo18]. High gain values thus come at the price of a slow time response, since the recombination time τ is large: this is called the gain/bandwidth trade-off [Wang17, Lhuillier15]. So the gain has different origins: a large life time of photogenerated carriers (also referred to the trapping time), a difference of mobility between electrons and holes when trappings are neglected and finally a small transit time commonly observed in nanoscale devices with nanometer channel length.

1.5.2 Photodiodes

A photodiode, or photovoltaic detector, relies on an heterojunction to absorb photons and separate the photogenerated charges. The working principle is exactly the same as a solar cell, but photodiodes are optimized for detection rather than power generation. In a photodiode, an asymmetry is introduced in the device, either by forming a p-n junction due to oppositely doped semiconductors or a Schottky junction between a semiconductor and one of the metal electrodes, or using split-gates on a semiconductor. The junction leads to charge carrier separation after the excitation process and, electrons and holes drift in different directions towards the electrodes driven by the built-in electric field at the interface allowing to strongly suppress the dark current in the structure. The response time of diodes is determined by the transit time of carriers to their corresponding electrode, leading to high-bandwidth operation in high carrier mobility semiconductors [Kufer16a, Huo18]. Photodiodes are used either in photovoltaic mode at zero bias or in the photoconductive mode under reverse bias. In photovoltaic mode, the dark current is ultra-low with low power dissipation, improving the detectivity of the detector at the prize of absolute small responsivity. Reverse-bias operation however enhances the built-in electric field by reducing the junction capacitance, leading to increase the speed of the diode. The responsivity of the diode is given by:

$$R = \frac{I_{ph}}{P_{in}} = \frac{q\eta}{E_{ph}} \tag{1.25}$$

Another typical figure of merit used to characterize the performance of a photodetector is the specific detectivity D^* which mostly depends on the noise of the device. Indeed, it is known as the signal to noise ratio and, it shows the ability of the photodetector to discriminate the current generated by the incoming photons from the dark current (noise). The latter become important for small bandgap material where the thermal activation of carriers can be easily achieved. There are three major noise sources in photodetectors: the Johnson noise, the generation-recombination (G-R) noise, and low-frequency (1/f) noise [Kufer16a, Huo18, Livache19].

The Johnson noise also called the thermal noise is related to the mobility fluctuation of carriers due to thermal fluctuation and is dominant at high frequency range. For a semiconductor of resistance R operating in the electrical bandwidth Δf at the temperature T, the

Johson noise is given by:

$$i_{Johnson} = \sqrt{\frac{4k_B T \Delta f}{R}} \tag{1.26}$$

Generation-recombination (G-R) noise is due to the carrier density fluctuations due to spontaneous creation and annihilation of electron-hole pairs in the semiconductor. It is used for mid-frequency range. For a photoconductor operated in the electrical bandwidth Δf, this noise depends on the average dark current I_{dark} and on the gain of the detector G as:

$$i_{GR} = \sqrt{4qI_{dark}\Delta f} \tag{1.27}$$

At low frequency the predominant noise component is 1/f noise. As many photoconductors or phototransistors possess gain and relatively long time constants, the device bandwidth is often limited to low frequency operation of kHz or less and therefore falls into the range of low-frequency noise. The origin of 1/f noise is till not well understood and often assigned to surface traps or to contact effects such as non-ohmic contacts. This noise is generally dominant in NC-based devices [Livache19]. Taking into account the noise current density S_I, the 1/f noise can be express as:

$$i_N = S_I \sqrt{\Delta f} \tag{1.28}$$

The noise equivalent power (NEP) is the signal power where the signal-to-noise ratio is unity, usually expressed like:

$$NEP = \frac{i_N}{R} = \frac{S_I \sqrt{\Delta f}}{R} \tag{1.29}$$

Given that, and considering the area A of the photosensitive region, one can expressed the detectivity D^* as:

$$D^* = \frac{\sqrt{A\Delta f}}{NEP} = \frac{R\sqrt{A}}{S_I} \tag{1.30}$$

It is important to note that the detectivity D^* still depends on certain measurement conditions such as bias voltage, temperature and modulation frequency, which have to be specified for comparison with other systems.

1.5.3 Phototransistors

Phototransistors are light-sensitive transistors. Just like regular transistors, phototransistors can be both bipolar or unipolar. With ordinary bipolar transistors (NPN or PNP), an emitter-collector geometry is used, the basic semiconductor material is designed to be sensitive to the light and acts as current amplifier [Kufer16a]. In this work the focus lies on unipolar transistors, which operated as standard FETs. Indeed, the device configuration is similar to lateral photoconductors with a metal-semiconductor architecture forming the source and drain electrodes. While photodiodes and photoconductors are two terminal devices, an additional third electrode, the gate contact, is present in phototransistors. The gate electrode allows to tune carrier density in the semiconductor channel by a thin dielectric film or electrolytes. So, under dark conditions the applied gate voltage changes the carrier density inside the channel,

hence controlling the electrical conductivity between source and drain. Under illumination the channel conductance can additionally be altered by changing the carrier density after absorption of light, as it is the case in photoconductors. The two features combined make this type of phototransistor, also referred to as photo-FET, a promising system for high signal to-noise ratio photodetection. The gate voltage can be used to electronically switch off the dark conductivity and then minimizing noise or can be used to study the carrier dynamics of the device.

1.6 Conclusion

We have investigated the structural, electronic and optical properties of 2D materials (graphene and TMDCs) and nanocrystals. While properties of 2D material sheets depend on their thickness, nanocrystal properties depend on their size which can be controlled during the colloidal synthesis. High carrier mobilities of graphene and low light absorption make graphene a good candidate for transparent electrode design. Contrary to gapless graphene, TMDCs are semiconducting materials exhibiting a direct to indirect band gap transition when exfoliated down to a single layer. They have intrinsic doping for electrons or/and holes transport suitables for nanoelectronics, optoelectronics and spintronics. On the other hand, NCs have strong tunable light absorption from infrared to visible making them useful for photodetection applications in this spectral range. Free dangling bonds at the 2D materials surface make possible coupling with any kind of materials as demonstrated in MD-vdW-h. It is important to remark that all the studies made in MD-vdW-h have been perfomed in the low doping regime using conventional dielectric and, there is to date no reports highlighting the study of NCs in high doping regime using solid gating.

Chapter 2

Nanocrystal FET and phototransistor in high doping regime with ionic glass LaF_3

I report in this chapter the use of ionic glass LaF_3 as a high-capacitance gating to induce high charge densities in NCs thin film. The gating technique allows operation in the 180 to 300 K range of temperatures with capacitance exceeding 1 $\mu F.cm^{-2}$ and sheet density as large as $3x10^{13}$ carriers/cm^2. We show that HgTe and PbS based FET demonstrate ambipolar transport. The hole and electron mobilities reached $1.5x10^{-2}cm^2.V^{-1}s^{-1}$ and $4x10^{-2}cm^2.V^{-1}s^{-1}$ respectively in HgTe-FET at 260 K. We figure out the unique property of ionic glass gate to enable the unprecedented tunability of both the magnitude and the dynamics of the photocurrent in HgTe-based phototransistor, thanks to high charge-doping capability within an operating temperature window relevant for infrared photodetection. We demonstrate that by carefully choosing the operating gate bias, the signal-to-noise ratio can be improved by a factor of 100, the time response accelerated by a factor of 6. I also demonstrate n-type hybrid perovskite based FET consisting of FAPI perovskite matrix doped with PbS NCs, with an electron mobility of $2x10^{-3}cm^2.V^{-1}s^{-1}$ at room temperature.

Related articles

- P. Rastochi, A. Chu, C. Gréboval, J. Qu, U. N. Noumbé, S.-S. Chee, M. Goyal, A. Khalili, X. Z. Xu, H. Cruguel, S. Ithurria, B. Gallas, J.-F. Dayen, L. Dudy, M. G. Silly, G. Patriarche, A. Degiron, G. Vincent, E. Lhuillier. *Pushing Absorption of Perovskite Nanocrystals Into the Infrared.*, Nano Lett. 2020, 20 (5) 3999-4006

- C. Gréboval, U. N. Noumbé, N. Goubet, C. Livache, J. Ramade, J. Qu, A. Chu, B. Mar-

tinez, Y. Prado, S. Ithurria, A. Ouerghi, H. Aubin, J.-F. Dayen, and E. Lhuillier. *Field-Effect Transistor and Photo-Transistor of Narrow-Band-Gap Nanocrystal Arrays Using Ionic Glasses*, Nano Lett. 2019, (6), 3981-3986

In these projects, I characterized LaF_3 using electrochemical impedance spectroscopy measurements, designed and processed samples (electrodes on LaF_3 substrates) at IPCMS. Charlie Gréboval and Prachi Rastochi synthesized HgTe and PbS NCs and perovskite NCs respectively at INSP. Then, Charlie and I performed optoelectronic measurements of HgTe NCs phototransistor at INSP.

Beyond their bright luminescence in the visible, CNCs have raised interest for the design of optoelectronic devices and especially for infrared (IR) sensors because of their facile solution processing and their excellent performances [Hafiz19, Lhuillier17]. While lead chalco-

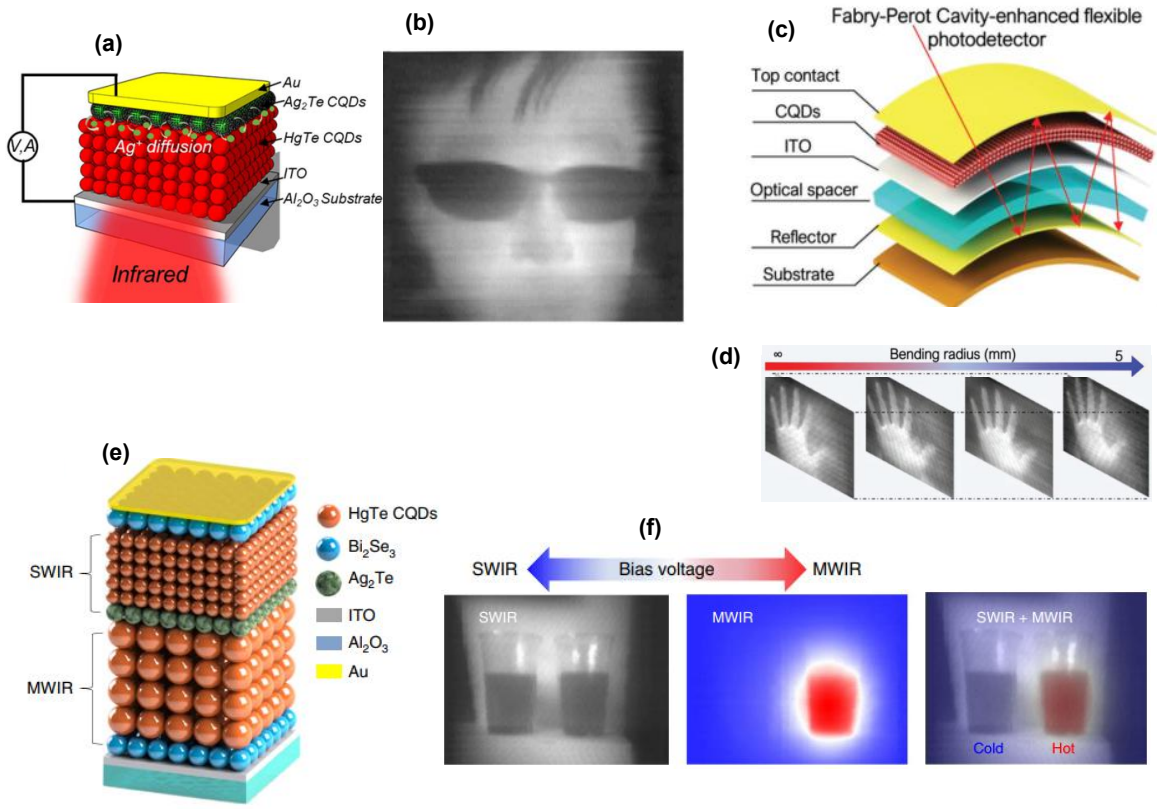

Figure 2.1 *– Recent achievements for photodetection with HgTe NCs in the MWIR and SWIR (a) Scheme of a MWIR photodiode based on a HgTe/Ag_2Te junction with high detectivity at 90 K. (b) Thermal image obtained with the diode shown in (a) by scanning a lens in front of the detector. Adapted from Ref. [Ackerman18]. (c) Scheme of Fabry-Perot cavity enhanced HgTe CQDs detectors. (d) A serie of thermal images obtained with the diode shown in (c), and captured at different bending radius of the flexible detectors, the image quality remains unchange with the bending radius. Adapted from Ref. [Tang19b]. (e) Scheme of a dual-band SWIR-MWIR HgTe photodiode. The device consists in two diodes built back-to-back, and the polarization bias allows to switch between MWIR and SWIR sensitivity. (f) SWIR, MWIR and merged dual-band images of hot and cold water. The SWIR and MWIR images are taken at room temperature and 85 K respectively. Adapted from Ref. [Tang19a].*

genides have attracted much attention for the design of solar cells collecting the near-infrared (NIR) (800 nm to 1μm) part of the solar spectrum, mercury chalcogenides particularly narrow-band-gap HgTe nanocrystals [Livache19, Killilea19, Kershaw13, Keuleyan11] are currently generating strong interest for the design of high-performance and low-cost infrared sensors in the SWIR (1 to 1.7μm) and MWIR (3 to 5 μm) [Lu19, Livache18b, Lhuillier17]. Recent developments include high-detectivity photodiodes: Ackerman *et al.* built a vertical photodetector using ITO/HgTe/Ag_2Te/Au on sapphire substrate (see Fig. 2.1 (a)), operating in zero-bias photovoltaic mode as the dark current approaches zero to minimize 1/f electrical noise. The heterojunction is formed between the n-type HgTe NCs and the p-type Ag_2Te

NCs. This device showed detectivity reaching 10^9 Jones with a cutoff wavelength between 4 and 5 μm at 230 K as well as prospects for thermal imaging [Ackerman18]. The introduction of plasmonic structures to boost the optical coupling in HgTe devices have been studied since 2014 [Chen14b], and has recently inspired the integration of a Fabry-Perot resonant cavity on polyimide flexible substrate to enhance the light absorption in flexible (HgTe) CQD detectors, see Fig. 2.1 (c). The detectivity of the device reached 7.5 x 10^{10} Jones with a cutoff wavelength of 2.2 μm at room temperature and a short response time ($\approx$ 260 ns) [Tang19b]. The Fabry-Perot (FP) resonant cavity made of a back reflector and an optical spacer has the particularity to be flexible and to control the absorption of HgTe NCs only by tuning the thickness of the optical spacer. When integrating in the imaging device, there is no degradation of the image quatilty with the bending radius as shown in Fig. 2.1 (d), thus can be used to develop infrared electronic eyes imaging with wide range of curvatures.
Multi-color devices have also been demonstrated and are very useful for applications were spectral contrast is needed to build versatile detectors able to produce images in different IR ranges [Tang19a, Tang16, Lhuillier14]. Recently a dual-band SWIR-MWIR photodiode device has been reported, where two HgTe diodes with two different NC sizes (see Fig. 2.1 (e)) allowed to built back-to-back (n-p-n) structure [Tang19a]. In such configuration, by controlling the polarization (bias polarity) and magnitude, the detector can be rapidly switched between SWIR and MWIR with detectivity above 10^{10} Jones at cryogenic temperature.
The integration of the HgTe active material in FETs allowed to build efficient phototransistors in MWIR using As_2S_3-capped HgTe NCs [Lhuillier13]. Very high responsivities above 100 mA/W and high detectivity above 10^{10} Jones in SWIR were reported on HgTe QDs phototransistors at room temperature [Chen17]. In phototransistors generally, the gate is not used to probe the majority carriers of the film but rather to reduce the dark current and bring the thin film in an operating point that maximizes the signal-to-noise ratio.

We explore here the possibility to use ionic glasses as a path to induce the gate effect in nanocrystal arrays. This approach has first been developed by Shukla's group on 2D materials using conventional glasses such as borosilicate and soda-lime glass. The glass is first melted at high temperature to give ions some mobility, and a large electric field is applied over the substrate to make them move. Conventional glasses, however require operating temperature around 500 K, which is incompatible with most nanomaterials such as NCs, molecules or polymers, for which melting temperatures are far below. This is especially the case for lead and mercury chalcogenides commonly used in the infrared, for whose synthesis temperatures are around 80 to 150 °C. Recently, the Cui's group explored the use of ionic glass LaF_3 to induce a gate effect in a MoS_2 flake [Wu18]. LaF_3 is originally used for infrared optics and presents a strong transparency in the mid infrared, which is promising to design phototransistors with back side illumination. In addition, ionic mobilities remain high enough to induce gating for temperatures down to 180 K.
In this part of my work, I investigate ionic glass LaF_3 as a substrate to induce back gate effect in thin films HgTe, PbS, and hybrid perovskite NCs. Below are detailed results of the study.

2.1 Ionic glass LaF_3 substrate for high doping regime

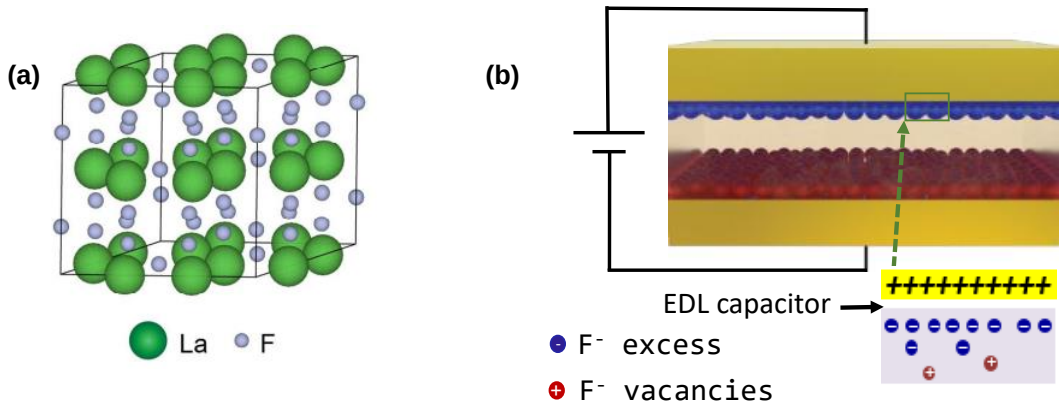

Figure 2.2 *– (a) Crystal structure LaF_3. Fluoride ions with small mass and size can transport via hopping into the existing F^- vacancies, adapted from [Wu18]. (b) Schematic diagram of LaF_3 sandwiched by metal electrodes.*

Lanthanum trifluoride LaF_3 crystallizes in a hexagonal structure with space group $P6_3/mcm$. It is a transparent solid state superionic conductor with fluoride ion conductors [Schoonman80, Solomon]. Because of the fluorine vacancies already existing in the crystal, small mass fluoride ions (F^-) can move by hopping throughout the crystal lattice while lanthanum ions stay immobile due to their large size and mass (see Fig.2.2.(a)) [Hoff97]. LaF_3 has a good mechanical stability and an electric band gap of 4.9 eV (insulator), thus can be used both as a substrate and a solid gate dielectric compatible with silicon-based device fabrication processes.

To understand the charging mechanism in the substrate, we sandwiched 1mm thick of 25 mm^2 substrate with Ti/Au (50nm) contacts (Metal/LaF_3/Metal) and we performed electrochemical impedance spectroscopies (EIS). When an external bias is applied, negative fluorine ions move towards the positive electrode while positive fluoride vacancies accumulate at the negative electrode and form an electric double layer (EDL) capacitor at the interfaces at the equilibrium as shown in Fig.2.2.(b).

2.1.1 Principle of electrochemical impedance spectroscopy

EIS is a valuable technique which has been utilized by many institutions for over a century [Warburg99, Nernst94] for purposes such as corrosion analysis [Nishikata95, Mansfield90], adsorption properties of molecules (interfacial behavior) [Mohsen12], and also used to monitor the functioning of batteries and fuel cells [Gomadam05, He09] amongst many other applications. The method involves the application of a small perturbation (either a single sine wave voltage or a superposition of a number of sine waves voltage) at the working electrodes and analyzes the resulting current in the frequency domain. So, when applying a small AC voltage $V(j\omega)$ by a potentiostat or whatever interfaced with NOVA control analysis software as we did in this work, from its measure response $I(j\omega)$, the operational impedance is defined

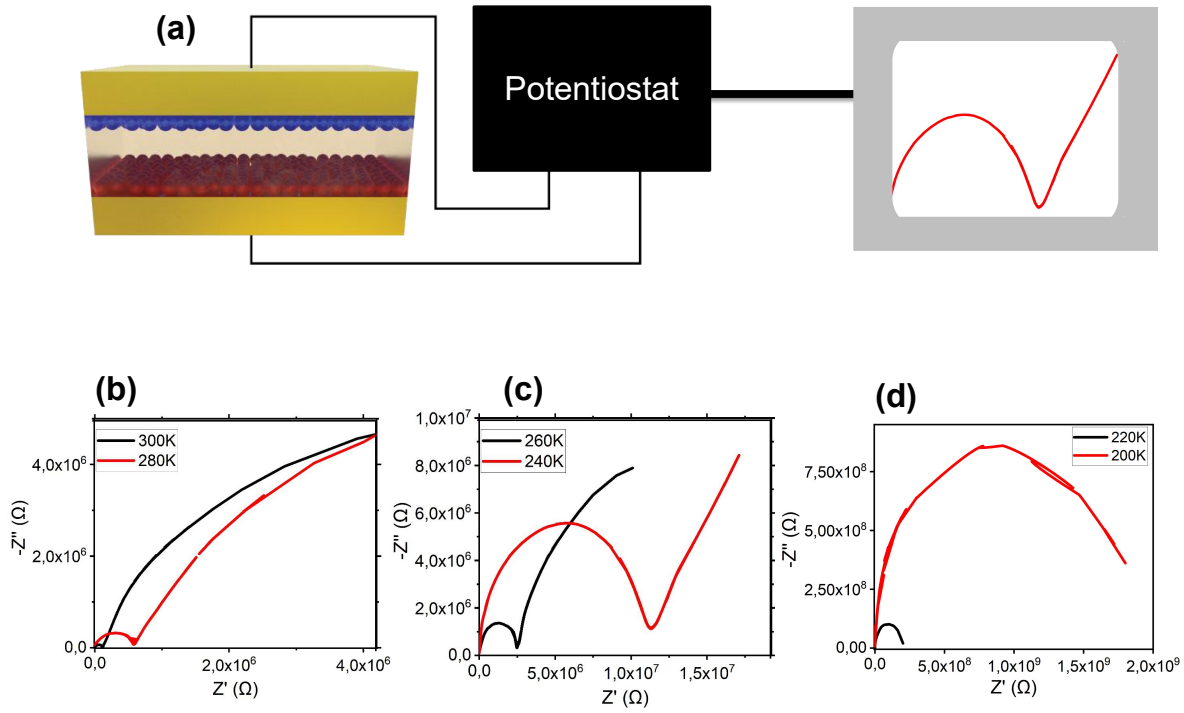

Figure 2.3 *– Nyquist plots under 10 mV AC from 0.1 Hz to 100 kHz: (a) Experimental setup for electrochemical impedance spectroscopy using a potentiostat interfaced by NOVA control analysis software. (b) 300 K and 280 K: a semi-circle characteristic at high frequency near the origin followed by a linear behavior at low frequency in the right. (c) 260K and 240K: a semi-circle characteristic at high frequency near the origin followed by a linear behavior at low frequency in the right. (d) 220 K and 200 K: Only a semi-circle characteristic.*

as the ratio between the complex voltage and the current [Randviir13]:

$$Z = \frac{V(j\omega)}{I(j\omega)} = \frac{|V| * \exp(j\omega t)}{|I| * \exp(j\omega t + \theta)} = |Z| * \exp(j\theta) = Z' + jZ'' \tag{2.1}$$

where Z is the impedance, j is the imaginary component, θ the phase angle between the response current and the input voltage and ω is the frequency.
The datas we recorded from NOVA can be presented in a variety of ways. For instance the real and imaginary impedance components Z' and Z'' are plotted against one another in what is known as Nyquist plots which have to be interpreted properly to deduce the kinetic (charge transfer process) and the diffusion process in the system. Furthermore, in the Bode plots, the impedance Z and phase angle θ are plotted against frequency to find capacitative or inductive effects of the electrochemical systems [Randviir13, Yuan10, Arzola05].

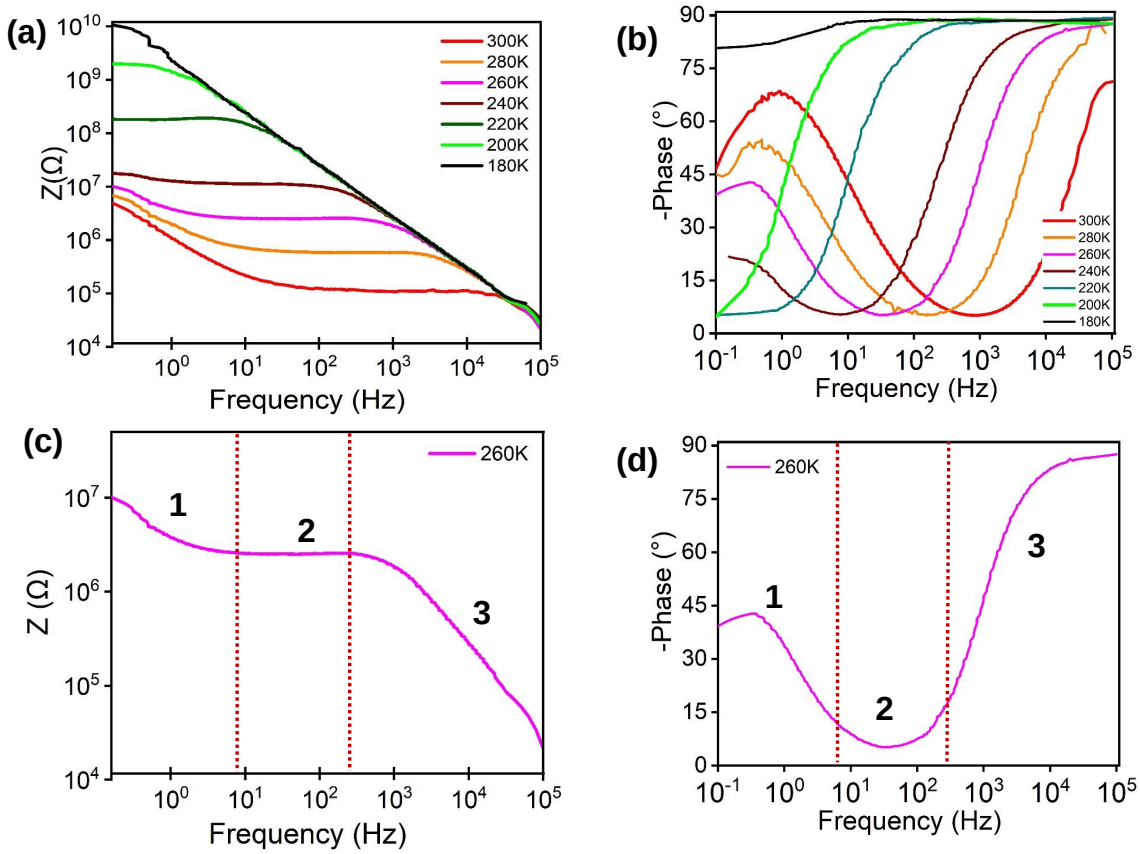

Figure 2.4 *– Bode plots under 10 mV AC from 0.1 Hz to 100 kHz: (a) \|Z\|-frequency dependence at different temperatures. (b) Phase-frequency dependence at different temperatures. (c) \|Z\| as a function of the frequency at 260 K. (d) Phase angle θ as a function of the frequency at 260 K where regions 1, 2 and 3 are well defined.*

2.1.2 Nyquist and Bode plots

Fig.2.3 shows Nyquist plots under 10 mV at different temperatures in the frequency range from 0.1 to 100 kHz. At higher temperatures (Fig.2.3 (b)), the response is practically the same. Indeed, we see a semi-circle characteristic near the origin followed by a linear behavior at the right. Because the impedance is always lower at the higher frequency, the semi-circle describes high frequency behaviors, it is the region used to control the kinetic of the system. The linear region however describes low frequency behaviors characteristic of diffusion process. We can see that the diameter of the semi-circle dramatically increases with decreasing the temperature because the fluorine ion mobilities get reduced, then reducing the charge transfer process (see Fig.2.3 (c)). At lower temperatures (Fig.2.3.(d)), the linear behavior disappears and the system is limited by the reduction of fluoride ion mobilities. Unlike the Nyquist plot, Bode plots show direct reading frequency information, thus they can be used to find capacitive effects of the system as I said before. We have plotted Bode plots of our system in Fig.2.4 for different temperatures in the range of 0.1 to 100 kHz under 10 mV AC. The curves follow almost the same trend. In Fig.2.4 (c), I show the Bode plot at 260 K, one can see: a slope at high frequency signature of bulk dielectric or bulk charging (region 3), a

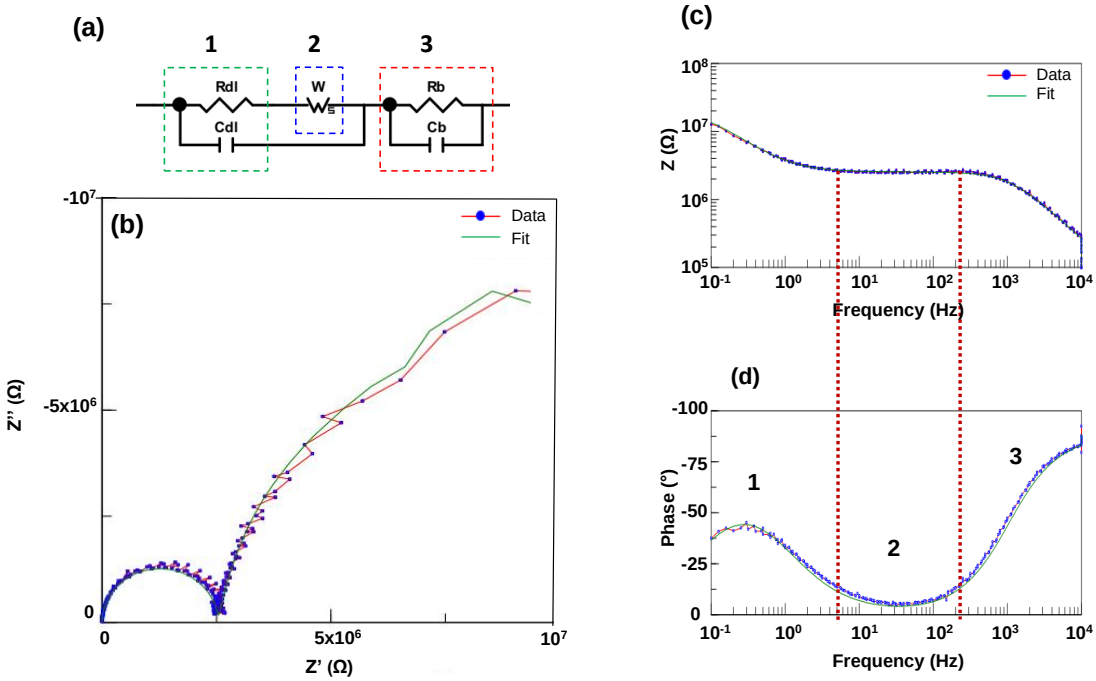

Figure 2.5 *– Fitting at 260K (a) Equivalent electric circuit, two RC circuits in series with additional Warburg impedance. (b) Nyquist plots: the red line is the data whereas the green line is the fit. (c) \|Z\|-frequency dependence: the red line is the data whereas the green line is the fit. (d) Phase-frequency dependence: the red line is the data whereas the green line is the fit. The slope at the region 3 represents the bulk charging, the plateau in the region 2 the formation on the ELD and the slope in the region 1 the EDL charging.*

plateau which begins just after the downward curvature corresponding to the formation of the EDL (fluoride ions migration, region 2) and finally the slope at lower frequency signatures of the EDL capacitor (region 1). So the slope at the region 3 at high frequency is the signature of bulk dielectric or bulk charging with small capacitances, the plateau at region 2 describes the fluorine ions migration and the slope at region 1 at lower frequency is the signature of the electric double layer capacitor with high capacitances.

At low temperature (180 K for instance), fluoride ion mobilities get strongly reduced, we have only a straight line with a phase angle which remains close to -90° in the wide spectral range (see Fig.2.4 (b)), signature of capacitive effects of bulk dielectric. Fig.2.6 (a) shows the temperature-frequency mapping for the phase angle of EIS, demonstrating a phase diagram to distinguish the charging mechanisms and the electrostatic nature of EDL interfaces. Three independent regions with two different charging mechanisms can be recognized by clear boundaries, which are defined by using the beginning and the end of the plateau in the impedance-frequency plots at each temperature (I mean the boundary between region 3 and 2 and the boundary between region 2 and 1 for each temperature in Fig.2.4 (a), (c)) and are

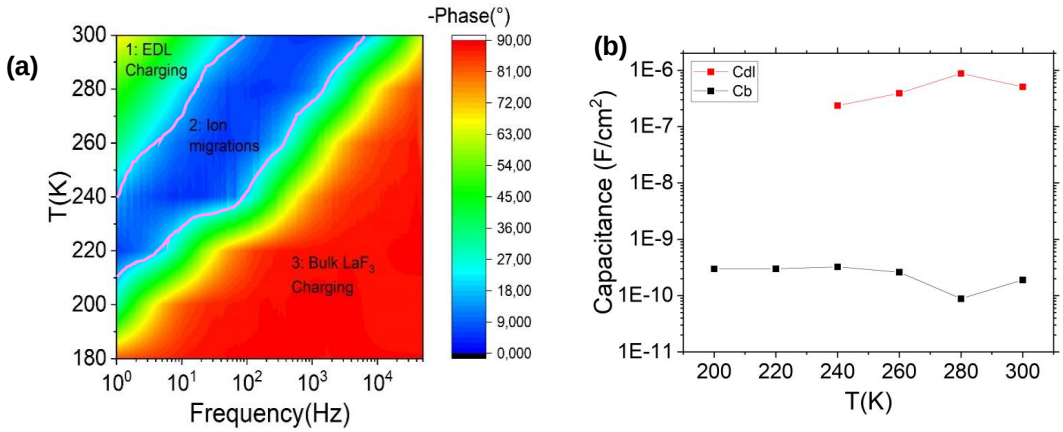

Figure 2.6 – *(a) Temperature-frequency mapping for the phase angle of the Bode plot. The pink curves, drawn by using the beginning and the end of the plateau in the impedance-frequency plots at each temperature is the critical boundary to distinguish three regions with two charging mechanisms:* ***3*** *Bulk dielectric behavior of LaF_3 with bulk capacitance Cb;* ***2*** *Fluorine ions migration and* ***1*** *EDL charging: Fluorine ions have enough time to reach the surface substrate and form EDL capacitor Cdl with nanoscale thickness. (b) Capacitance-temperature dependence (Cdl and Cb) from the fitting using the equivalent circuit.*

marked with pink lines. *It comes out from this mapping two paths to make EDL capacitor in our ionic glass with an electrostatic mechanism: low frequency (low enough to give enough time to fluoride ions to reach the surface) and low temperature (sufficient to the motion of fluoride ions) or intermediate frequency and high temperature (not high enough to thermally activate much fluorine ions and induce leakage in the system as in the region 1).*

To confirm the electrostatic doping nature in our (Metal/LaF_3/Metal) system, we have fitted datas with Zview software using the equivalent circuit shown in Fig.2.5 (a) in order to extract both bulk capacitance Cb and EDL capacitor Cdl. Indeed, the semi-circle characteristic means components in the system exhibit imaginary resistance behavior contrary to purely electronic resistors (which have a fixe phase with $|Z''|=0$). So to fit only the semi-circle (200 K and 220 K) only one resistor-capacitor (RC) circuit is used, where the bulk capacitance (Cb) is in parallel with the bulk resistance (Rb). To take into account the linear part at low frequency for interfacial charging, another RC circuit is added with additional Warburg impedance in series with the double layer resistance Rdl. The Warburg impedance is commonly used to model the diffusion of ionic species at the interface [Randviir13, Yuan10, Arzola05]. Fig.2.5 (b-d) show accuracy fits of both Nyquist and Bode plots using the equivalent circuit in Fig.2.5 (a). From the fitting for all the temperatures, we have extracted the bulk capacitance Cb and the EDL capacitor Cdl, then plotted in Fig.2.6 (b).

As expected the EDL (nanoscale) capacitor is much higher than the bulk capacitor. One can also see that capacitances Cb and Cdl are almost invariant with temperature (Fig.2.6 (b)). Such temperature independency of capacitance is similar to that of solid dielectrics [Arzola05], directly suggesting the electrostatic nature of EDL charging in our ionic glass LaF_3 substrate.

As our set-up is limited to lower frequencies down to 0.1 Hz (mechanical noise induced by our reliquefactor), we performed complementary measurements down to 0.01Hz at INSP (with

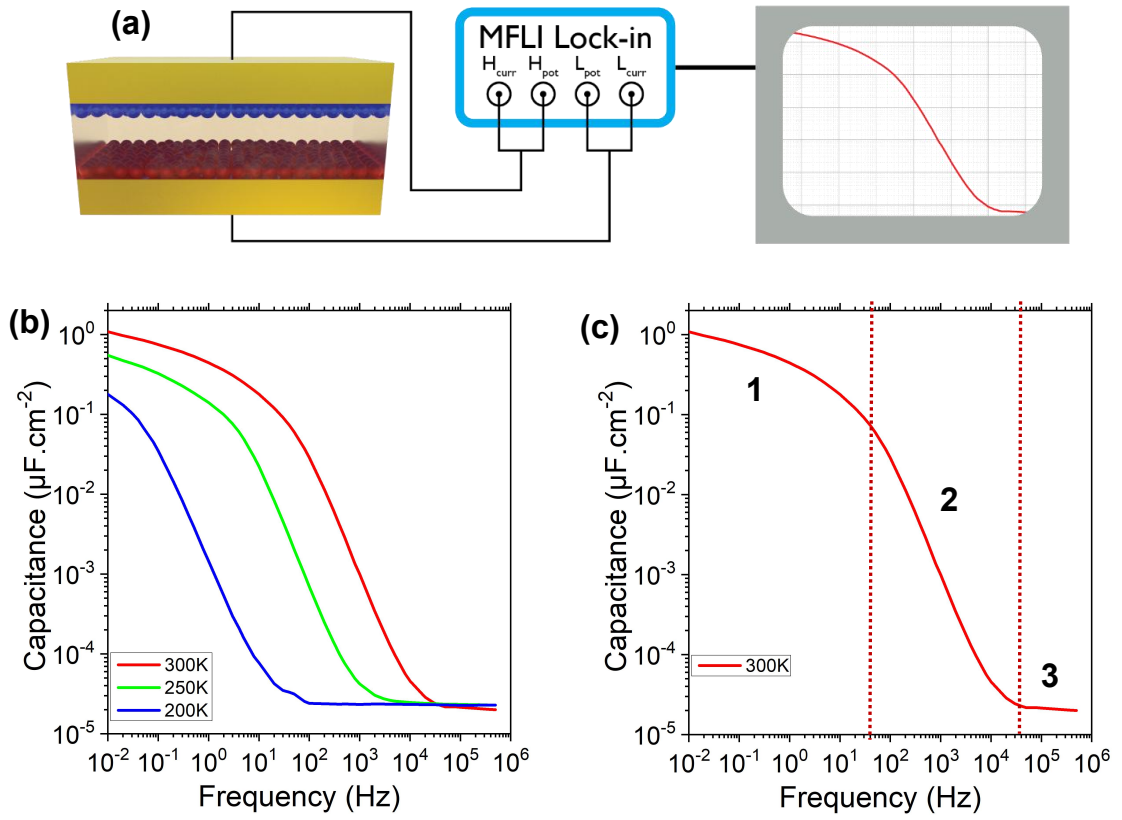

Figure 2.7 *– Lock-in measurements at INSP (a) Experimental setup for capacitance measurements using Lock-in amplifier. (b) Capacitance-frequency dependency for different temperature on LaF_3 substrate under 300 mV AC signal. (c) Capacitance-frequency at 300K: As described with Nyquist plots, the region 3 represents the bulk charging, the slope in the region 2 the migration of fluorine ions for the formation on the EDL and the region 1 the EDL charging where fluoride ions have enough time to reach the surface to form a nanoscale capacitor at the interface between the gold contact and the substrate.*

Charlie Gréboval) using a lock-in set-up.

Fig.2.7 (a) shows the experimental setup we used for capacitance-frequency measurements. We evaporated 80 nm of Au on both sides of the LaF_3 substrate and connected it to a MFLI lock-in amplifier. Thus, we used lock-in amplifier to apply 300 mV AC voltage at a given frequency in the range 0.01 Hz to 700 kHz. The lock-in then measures the current through the sample in order to calculate the capacitance. The evolution of the capacitance in frequency for different temperatures is given in Fig.2.7 (a), we can note a similar behavior as what we obtained with EIS. At high frequency, fluoride ions don't have enough time to reach the surface, the substrate behaves as a bulk dielectric with low capacitance (region 3 in Fig.2.7 (c)) untill they start to migrate toward the surface (described by the slope in region 2 in Fig.2.7 (c)), and form at the equilibrium a nanoscale capacitor with high capacitance (region 1).

Once we have understood the charging mechanisms in ionic glass LaF_3 and the operating temperature range, we can now used it to gate NC films and tune its photoconduction properties. We study in the following the properties of three different NC thin films over LaF_3 substrate measured during two measurement campaigns at INSP where I worked with Char-

lie Gréboval, and compare them to results obtained on the same NCs by INSP using more traditional SiO_2/Si back gate and electrolyte gating.

2.2 HgTe NCs ionic glass gating

2.2.1 HgTe 4k synthesis and optical characterization

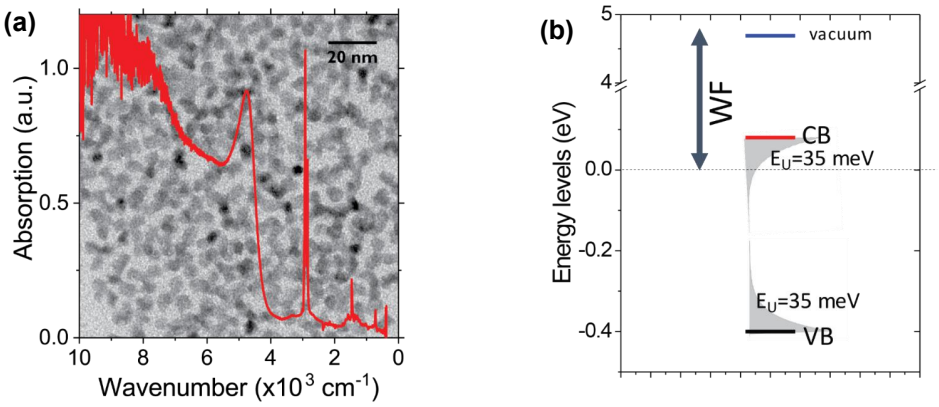

Figure 2.8 *– Absorption spectrum of HgTe nanocrystals with a band edge at 4000 cm^{-1} (2.5 µm). Background: transmission electron microscopy (TEM) image of the material showing tetrapod nanoparticles. (b) Electronic structure of the HgTe nanocrystals. Adapted from [Jagtap18].*

HgTe 4k nanocrystals are synthesized by Charlie Gréboval using the procedure described in appendix A.1: Fig.2.8 (a) shows the absorption spectrum of those NCs with a band edge energy around 4000 cm^{-1} (≈500 meV or 2.5μm). One can also see in this absorption spectra a fine, intense structure around 2900 cm^{-1} which is the signature of C-H bonds in the 12-C long DDT ligands, its height tells how efficient the ligand exchange [Livache19]. As we can see in the TEM image on the background, they are small NC sizes around 8 nm with a tetrapodic shape. The electronic structure (energy location of conduction and valence band, relative position of Fermi level, and in-gap trap states) of this material has been previously determined by the INSP team [Jagtap18, Martinez18]. As shown in Fig.2.8 (b), the material presents a 4.6 eV work function with the Fermi level in the band gap but clearly lies closer to the conduction band. The Urbach energy which describes the amount of trap states within the band gap has been estimated to be 35 meV for ethanedithiol-capped nanoparticles.

2.2.2 Device fabrication

Electrodes fabrication on Si/SiO_2 substrate: The electrode pattern for FET measurements is made of 25 pairs of interdigitated electrodes at INSP. They are 2.5 mm long and spaced by 20 μm. They are fabricated using optical lithography with a reversible resist AZ 5214E. The detailed steps and parameters we used are depicted in the following:

1. The Si/SiO_2 substrate (300 nm dry oxide) is cleaned first by sonication in acetone for 5 min. Then rinsed with isopropanol before being cleaned for 5 min in an O_2 plasma to remove remaining organics.

2. To improve the adhesion of the resist with the substrate, adhesion promoter (TI-PRIME)

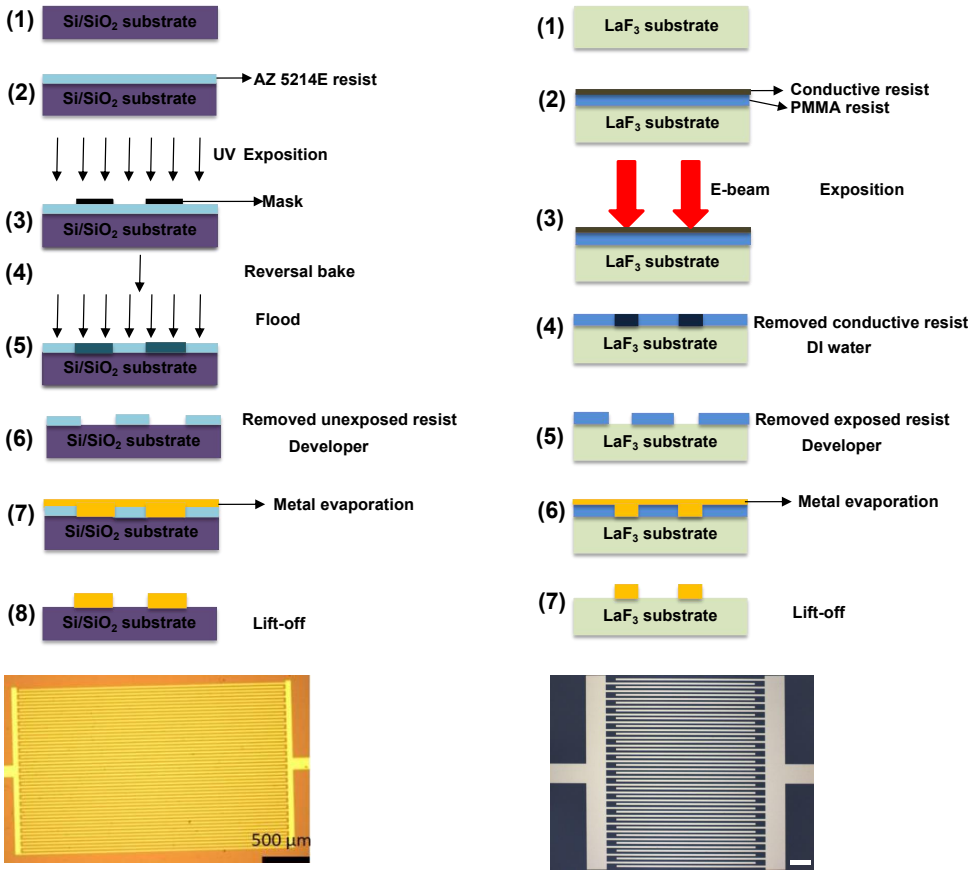

Figure 2.9 *– Schematic diagram of fabrication process of interdigitized electrodes on Si/SiO_2 (left) and on LaF_3 (right).*

is spin-coated on the substrate and baked for 2 min at 120 °C before AZ 5214E resist is spin-coated for 30 s at 4000 revolutions per minute (rpm), then baked at 110 °C for 1 min 30 s.

3. The substrate is exposed to UV light with MJB4 mask aligner in hard contact mode through a physical mask for 1.5 s. The exposed areas are polymerized, then become soluble in developer.

4. A reversal bake of the substrate at 125 °C for 2 min inverts the resist by cross-linking the exposed areas while remaining photoactive the unexposed areas.

5. Then a 40 s flood exposure is performed with MJB4 mask aligner (without mask), making soluble the unexposed areas in (3) in developer.

6. The resist is developed using a bath of AZ 726 for 20 s, before being rinsed in deionized (DI) water.

7. In a thermal evaporator, 5 nm of chromium are deposited as an adhesion layer before 80 nm of gold is evaporated.

8. The lift-off is performed by dipping the film in acetone for at least 1 h. The electrodes are finally rinsed using isopropanol and dried by a nitrogen flow.

The sketch illustrated in Fig.4.1 left (1-8) summarizes the photolithography steps, an optical image of interdigitated electrodes on Si/SiO_2 substrate in shown in Fig.4.1 lower-left.

Electrode fabrication on insulating LaF_3 substrate: Commercially available LaF_3 substrates (5mmx5mmx1mm) have been purchased at Crystran (UK). In such small size substrates, it becomes more difficult to perform optical lithography. I have then developed process in our group at IPCMS using electron beam (E-beam) lithography to pattern interdigitated electrodes on LaF_3 substrate. So 49 interdigits with 10 μm thickness and 750 μm length, spaced by 10 μm are patterned on insulating LaF_3 substrate by E-beam lithography using a Zeiss Supra 40 scanning electron microscope coupled to a Raith lithography system. We used a conductive resist AR-PC 5090.02 to write on the insulating substrate in addition to a standard bilayer PMMA (Polymethyl methacrylate) positive resists (AR-PMMA 669.04 and AR-PMMA 679.02). The detailed steps of this E-beam are the following:

1. The LaF_3 substrate (5mmx5mmx1mm) is cleaned first in acetone for 10 min. Then rinsed with ethanol and isopropanol for 5 min.

2. AR-PMMA 669.04 and AR-PMMA 679.02 are spin-coated at 4000 rpm during 1 min and annealed at 180 °C during 1 min 30 s. The e-spacer AR-PC 5090.02 is then spin-coated at the same speed (4000 rpm) but annealed at 90 °C during 1 min 30 s. 2 min waiting time have to be made after each baked.

3. Using an electron beam accelarated at 20 kV, the interest areas predesign by a software are exposed in order to polymerize the resist and make them soluble in developer.

4. The conductive resist is cleaned for 2 min in DI water the developing step.

5. Then PMMA resists are developed in the 1:3 MIBK-IPA to remove the exposed resists.

6. A metal deposition Ti (3 nm)/Au (57 nm) are performed by electron beam evaporator in high vacuum chamber, followed by lift-off for one day in acetone.

Fig.4.1 right (1-7) summarizes the E-beam lithography steps on insulating substrate, an optical image of interdigitated electrodes on LaF_3 substrate in shown in Fig.4.1 lower-right.

2.2.3 Transport properties of HgTe 4k NCs: Comparison of gating technologies

Here, we first study the transport properties of HgTe NCs with conventional gating method and, we then detail the performance of devices using LaF_3 ionic glass technology for sake of comparisons.
In Fig.2.10, we present the performances of HgTe-based FET using 300 nm SiO_2 layer as back-gate dielectric done at INSP. Fig.2.10(a) shows the transfer curves under 1V bias at different temperatures demonstrating ambipolar transport in HgTe NCs, thanks to their narrow-band-gap nature. Moreover, the charge neutrality point is clearly shifted toward negative biases,

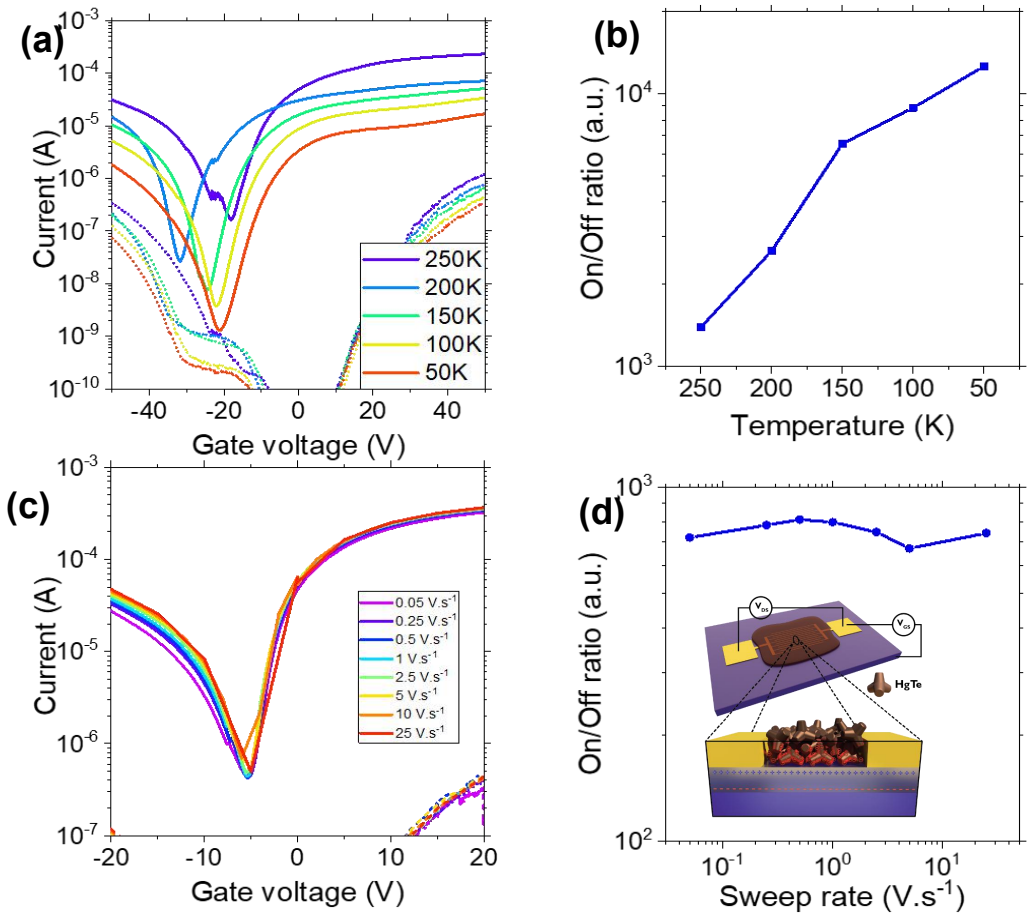

Figure 2.10 *– SiO_2 dielectric back-gate FET. (a) Transfer curves at different temperatures under 1 V drain-source bias. Drain-source (resp. gate) current in solid (resp. dash). (b) On/Off ratios measured from transfer curves for different temperatures under 1 V bias. (c) Transfer curves at 200 K under 1 V bias for different sweep-rates. (d) On/Off ratios measured from transfer curves for different sweep-rates. The inset shows the scheme of a HgTe back-gate FET on SiO_2 when $V_{GS} > 0$.*

which suggests n doping as observed in the electronic structure (Fig.2.8 (b)). Because of the reduction of the minimum of conductance at low temperature, we see an increase of the On/Off ratio with decrease temperature higher than 4 decades at 50 K (see Fig.2.10(b)). On the contrary, the mobility of the charge carrier increases with the temperature. Indeed, using the expression $\mu = \frac{L}{C_S W V_{ds}} \frac{dI_{ds}}{dV_{gs}}$, where L is the electrode spacing (10 μm), W is the electrode length (49 x 2.5 mm), C_S is the specific capacitance equals to 11.5 nF.cm^{-2} for a 300 nm thick SiO_2 layer, hole and electron mobilities of 10^{-2}cm^2.V^{-1}s^{-1} and 3x10^{-2}cm^2.V^{-1}s^{-1} respectively are found at 250 K. We can also see mostly no variation of the transfer curves with the sweep rate using SiO_2 gating (see Fig.2.10(c,d)).

Taking the same electrode as the one used in the case of SiO_2 gating, $LiClO_4$ electrolyte is brushed on top of the electrode of HgTe NCs film and contacted using a metallic copper grid for top gate. The performances of this electrolyte top-gate HgTe-based FET is shown in Fig.2.11. The transfer curves in Fig.2.11 (a) exhibit ambipolar transport as observed for

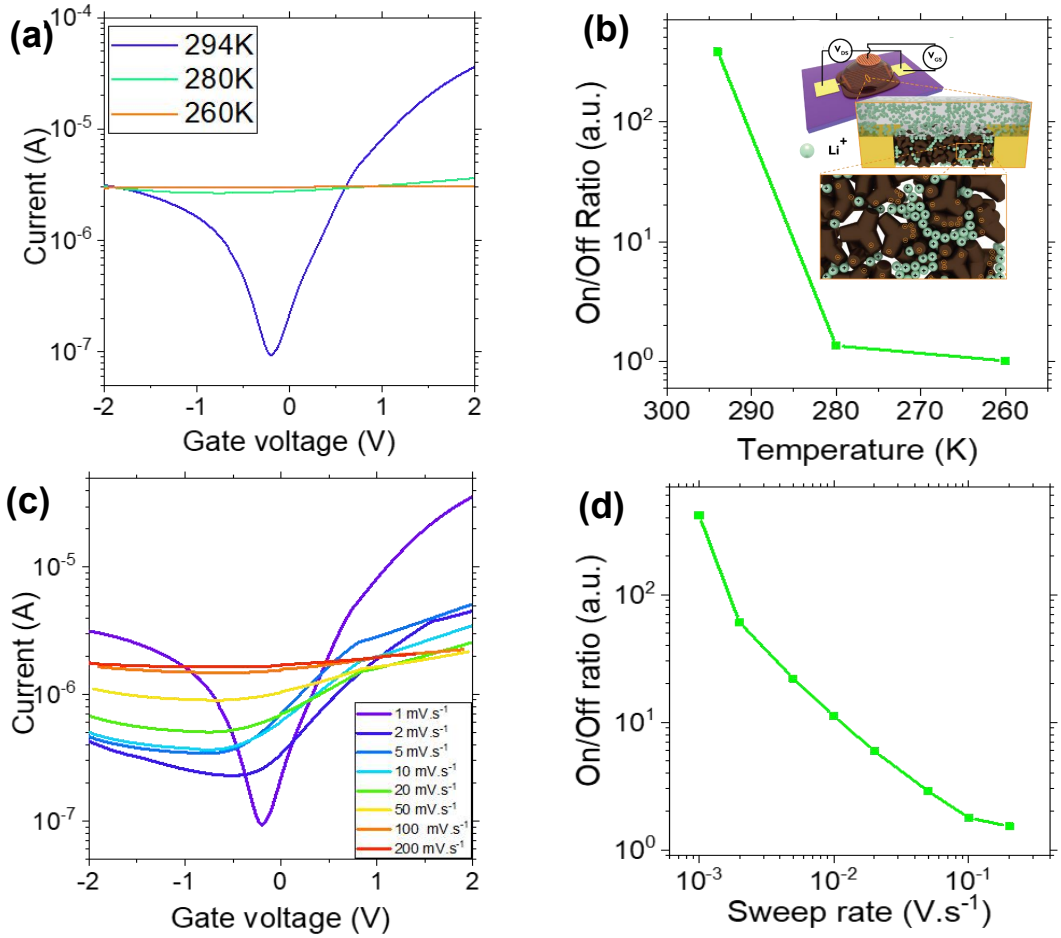

Figure 2.11 *– $LiClO_4$ electrolyte top-gate FET. (a) Transfer curves at different temperatures under 0.1 V drain-source bias. Gate current is at least two orders of magnitude lower than drain-source current. (b) On/Off ratios measured from transfer curves for different temperatures under 0.1 V bias. The inset shows the scheme of a HgTe top-gate FET with $LiClO_4$ electrolyte when $V_{GS} > 0$. (c) Transfer curves at 300K under 0.1 V bias for different sweep-rates. (d) On/Off ratios measured from transfer curves for different sweep-rates.*

SiO_2 gating, but with a small operating bias range. This is the result of the ions from the electrolyte that move inside the NC film and surround NCs (see the inset in Fig.2.11 (b)), then form a double layer capacitor with a high capacitance by injecting electrons in NCs in order to screen the positive charges, thus resulting efficient doping. Because the frozen of ions at low temperature (below 280 K here) we observe a drop of current when decreasing the temperature and the decreasing of the current modulation (Fig.2.11 (b)), thus limiting the use of electrolyte gating to room temperature measurements. We can also see a high variation of the transfer curve with the sweep-rate in electrolyte gating, with a fast-dropped of current modulation which also limits its used to room temperature processing (Fig.2.11 (c,d)).

For ionic glass gating, I have fabricated electrodes on the insulating LaF_3 substrate using the technique that I have developed in our group at IPCMS as described in section 4.1. The same HgTe ink as for SiO_2 gating is then deposited on the top of the electrodes, and the sample is inserted in a cryostat for measurements. Under 0.5 V drain-source bias,

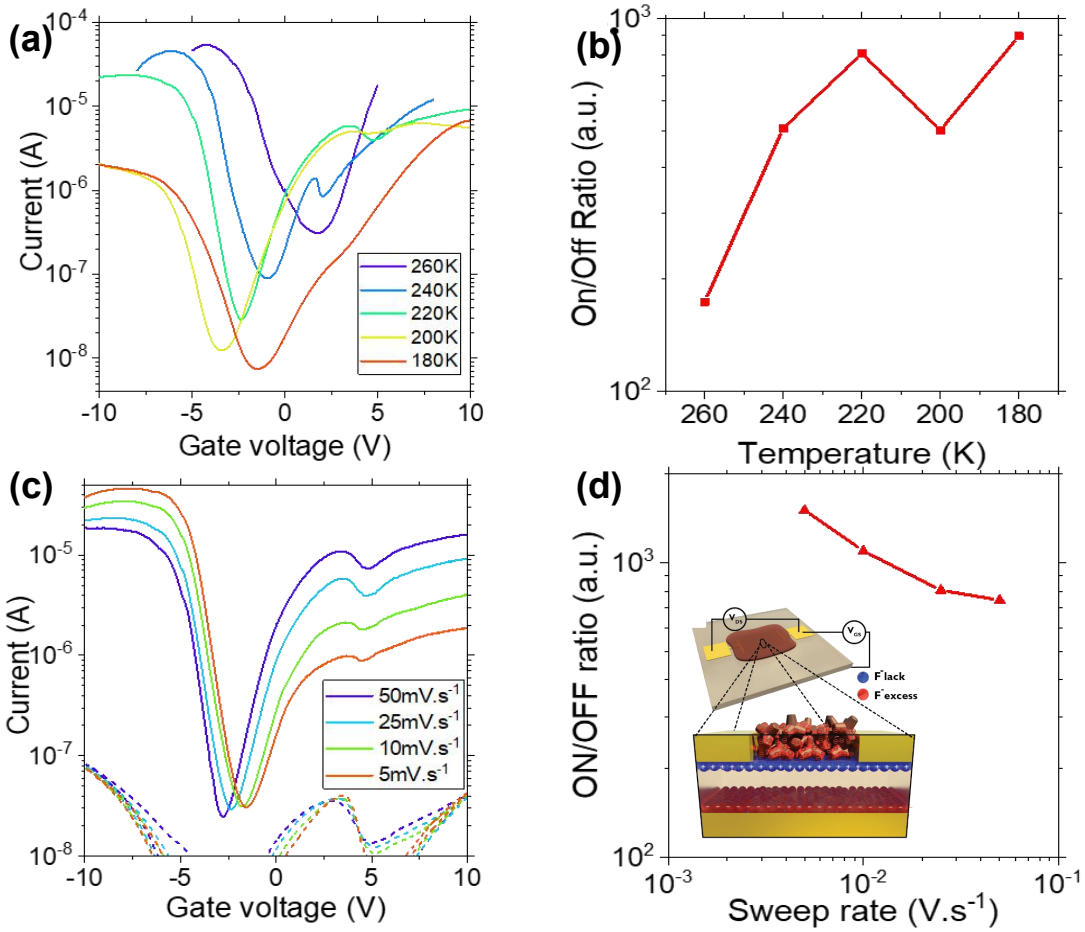

Figure 2.12 *– Ionic glass LaF_3 back-gate FET. (a) Transfer curves at different temperatures under 0.5 V drain-source bias. Gate current is at least one order of magnitude lower than drain-source current. (b) On/Off ratios measured from transfer curves for different temperatures under 0.5 V bias. (c) Transfer curves at 200K under 0.5 V bias for different sweep-rates. (d) On/Off ratios measured from transfer curves for different sweep-rates. The inset shows the scheme of a HgTe back-gate FET with LaF_3 ionic glass when $V_{GS} > 0$.*

the transfer curves obtained at different temperatures show ambipolar transport as observed for SiO_2 and electrolyte gating (see Fig.2.12(a)), in a gate voltage range 10 times lower than for SiO_2 and 2-3 times larger than for electrolyte. The On/Off ratio increases as the temperature is reduced because of the leakage reduction at low temperature through the substrate, see Fig.2.12(b). *We can also observe a large operating and low temperature range (260 K to 180 K) for LaF_3 gating not accessible for electrolyte gating.* As shown in section 2.1.1 from capacitance-frequency measurements, at 300 K and low frequency, a sheet capacitance as large as 1 μF.cm^{-2} can be achieved. As a reference, using the expression n=CV/e and applying 5 V of gate bias leads to a sheet density as large as 3x10^{13} carriers per square centimeter. The value of capacitance can also be used to determine the mobility of the film obtained with the LaF_3 gate. As the frequency dependence of the capacitance becomes a bit weak at low frequency, we can assume a gate capacitance of 500 nF.cm^{-2} with LaF_3 at 260 K, which leads to mobility of 1.5x10^{-2}cm^2.V^{-1}s^{-1} for the holes and 4x10^{-2}cm^2.V^{-1}s^{-1} for the electrons. These mobility values are very similar to those we have obtained with the SiO_2

gating. The LaF_3 gate presents a small dependence of the transfer curve with the sweep rate as shown in Fig.2.12(c,d) for a given temperature, the larger the sweep rate, the lower the current modulation.

Gate technology	Dielectric	Ionic glass	Electrolyte
Temperature range	4 K - 300 K	180 K- 260 K	300 K
Sweep-rate range	Fast (several $V.s^{-1}$)	Intermediate (0.1 $V.s^{-1}$)	Slow (1 $mV.s^{-1}$)
Gate voltage range	< 60 V (dielectric breakdown)	Up to 10 V at 200 K	< 3 V (electrochemical stability of the electrolyte)
Charge density n=CV/e	$3.6x10^{12}$ cm^{-2} for 50 V with C=11.5 $nF.cm^{-2}$	$2.6x10^{13}$ cm^{-2} for 8 V with C=0.5 $\mu F.cm^{-2}$ at 260 K	$1.9x10^{13}$ cm^{-2} for 3 V with C=1 $\mu F.cm^{-2}$
Carrier mobility	$\mu_h = 10^{-2}$ cm^2/Vs, $\mu_e = 3x10^{-2}$ cm^2/Vs at 300 K	$\mu_h = 1.5x10^{-2}$ cm^2/Vs, $\mu_e = 4.5x10^{-2}$ cm^2/Vs at 260 K	$\mu_h = 1.02x10^{-3}$ cm^2/Vs, $\mu_e = 7.2x10^{-4}$ cm^2/Vs at 300 K

Table 2.1 *– Typical ranges of use for the solid-state gating of HgTe NC-based FET.*

We summarize in the table 2.1 the advantages and limitations of each gating technology. *It comes out that ionic glass LaF_3 gating allows to achieve high doping in HgTe NCs not possible with SiO_2 gating, in an operating temperature window not possible with electrolytes (260 k to 180 K). Ionic glass is used in a small operating biases (up to 10 V at 200K) with no breakdown as sometime observed with SiO_2 gating. It has an intermediate time response (sweep rate range) compared with the slow sweep rate range of electrolytes and fast sweep rate of dielectric gating. Finally, our ionic glass allows for these systems to have higher carrier mobility than those obtained with the electrolyte gating but comparable to those of the dielectric gating*
Ionic glass gating is not limited to narrow-bang-gap NCs, we demonstrate ionic glass gating on PbS NCs and hybrid perovskite NCs in the next section.

2.3 PbS QDs and FAPI-PbS NCs ionic glass gating

To show the generality of the gating technique on NCs film, we build a transistor as described in section 4.1 on ionic glass LaF_3 substrate, with a channel of PbS NCs film. PbS NCs are the first historical example of nanocrystals with optical properties in the NIR range. Indeed, PbS has a bulk band-gap of 400 meV and relative large Borh exciton radius of 21 nm. Due to quantum confinement, PbS NCs feature strong optical absorption with size tunable in the NIR range. They have been extensively investigated for solar cell applications, and are promising materials for a new generation of NIR photodetectors. During the colloidal synthesis of PbS NCs, ligand-induced remote doping leads to different doping in the films. For instance PbS QD films exhibited n-type conductivity with a treatment by iodide ligands but

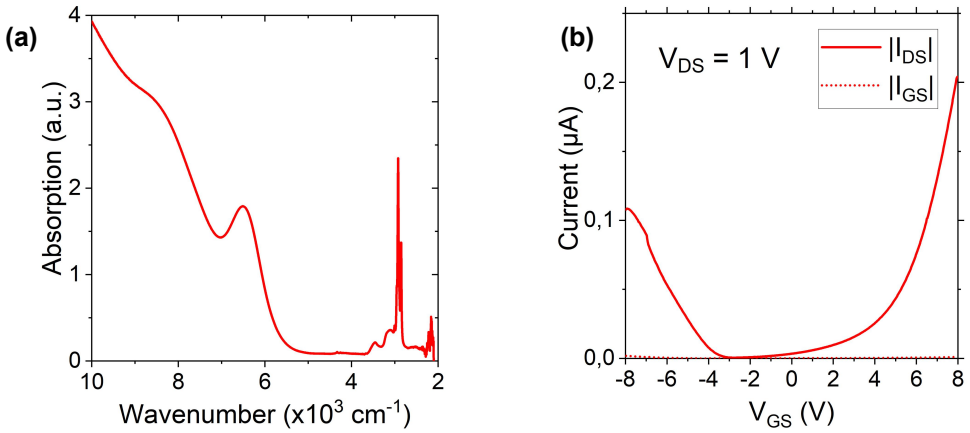

Figure 2.13 *– (a) Absorption spectrum of the PbS NCs used for the measurement. (b) Transfer curve of a PbS NCs film (with absorption peak at 1400 nm) on LaF_3 substrate. Measurements have been conducted at 200 K under 1 V bias.*

would switch to p-type with a treatment by hydroxide ligands. This extends the integration of PbS NCs film in many device architectures including vdW heterostructures as presented in the previous chapter [Yu17, Kufer15, Konstantatos12]. Here we demonstrate ionic glass gating of PbS NCs synthesized at INSP by Charlie Gréboval using the technique described in appendix A.2 where ligands exchange were performed in solution with 1,2-ethanedithiol (EDT). As shown in Fig 2.13 (a), the obtained PbS NCs have absorption band edge around 6000 cm^{-1} (1.54 μm or 0.82 eV). The transfer curve shows an ambipolar behavior with both electron and hole transport (see Fig 2.13 (b)).

Because of the promising interest of perovskite NCs and the lack of their implementation into FETs, we extend our gating method on perovskite NCs. Indeed, the transport in the networks of perovskite NCs remains a challenge. The know how that has been developed for chalcogenide NCs cannot be used because perovskite NCs are not stable enough [Jellicoe16]: They are easily dissolved by the solvents used for the ligand exchange steps. Recent progress has been made. However, devices as simple as the field effect transistor have not been demonstrated for networks of perovskite NCs. This is because they are almost intrinsic semiconductors with large band-gaps. They need very efficient gate to bring the Fermi level close to the bands, which is difficult with conventional dielectrics such as SiO_2. An alternative would be to use electrolytes as a gate, but the polar solvents used to dissolve the ions are incompatible with the ionic crystals of perovskites. We therefore use our high gating technique with ionic glass LaF_3 to perovskite NCs. The perovskite we used is hybrid organic-inorganic perovskite $(NH_2)_2CHPbI_3$ formamidinium lead iodide (FAPI). FAPI has a good structural stability with band edge energy around 1.65 eV, this high energy limits its absorption in visible range. To address absorption in IR at INSP, Prachi RASTOGI (Postdoctoral researcher at INSP) during the FAPI synthesis (as described in appendix A.3), doped the FAPI matrix with PbS NCs with a band edge energy of 0.82 eV. The resulting hybrid pervoskite FAPI-PbS (35% PbS content) shows absorption in SWIR at 1.5 μm (0.84 eV), whose absorption is governed by PbS in the

infrared and the transport is governed by FAPI. The relative wide gap of FAPI allows thus to reduce the number of thermally activated carriers and the dark current associated with it in the hybrid FAPI-PbS. We use ionic glass for back-gate in the FET geometry (see Fig. 2.14 (a)) to study transport properties in such hybrid perovskite NCs. Fig. 2.14 (b) shows the transfer curve at 300 K under 0.5 V drain-source bias. It exhibits n-type transport with On/Off ratio up to 10^4. This is two orders higher than the ambipolar behavior of the pristine PbS NCs obtained in the last section. This change is consistent because PbS dopants used were heavily

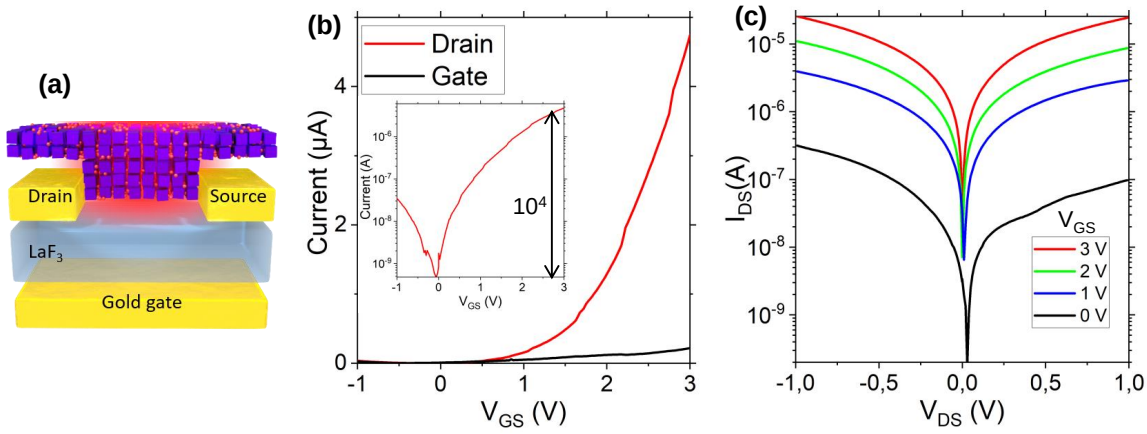

Figure 2.14 *– FAPI-PbS FET with LaF_3 gating: (a) Scheme of the device with a channel made of a FAPI-PbS (35% PbS content) NC thin film, FAPI have a characteristic square shape (purple), while PbS are small spheres (red). (b) Transfer curve at 300 K under 0.5 V drain-source bias. The inset is the plot in the log scale, with On/Off ratio of 10^4. (c) I-V curves at different gate voltages at 300 K.*

n-doped. Furthermore, we were able for the first time to extract the mobility of charge carriers in the FAPI NCs networks and demonstrate the first perovskite NCs based transistor. We have extracted the electron mobility of $2x10^{-3}cm^2.V^{-1}s^{-1}$ at room temperature. Such value is still lower for perovskite NC arrays compare to values obtained for CNCs where the surface chemistry and know how are well mastered, this result is nevertheless a breakthrough for NCs perovskite implementation into FET.

2.4 Phototransport properties of HgTe NCs in high doping regime

We start the study by measuring the photocurrent spectrum of HgTe NCs from the Fourier transform infrared (FTIR) spectrometer. HgTe-based FET is cooled down in a closed-cycle cryostat and biased by a DLPCA amplifier. IR light coming from FTIR spectrometer source is shone to the sample, then the photocurrent is amplified by the DLPCA before being sent to the detector entry of the FTIR to calculate the photocurrent spectrum, more details about the setup can be seen in appendix B.1. Fig. 2.15 (a) shows photocurrent spectrum of our device at different gate voltages. We can see a good correlation in shape between the photocurrent spectra and the absorption spectra shown in Fig. 2.8 (a). *This confirms that in our HgTe-based phototransistor, absorption is coming from the nanocrystals film.* One can also see a modulation of the absorption spectrum by the gate with more absorption under hole injections than electron injections because our HgTe NCs film being ambipolar and extrinsic n material, applying a positive voltage moves the Fermi in the conduction band for electron transport,

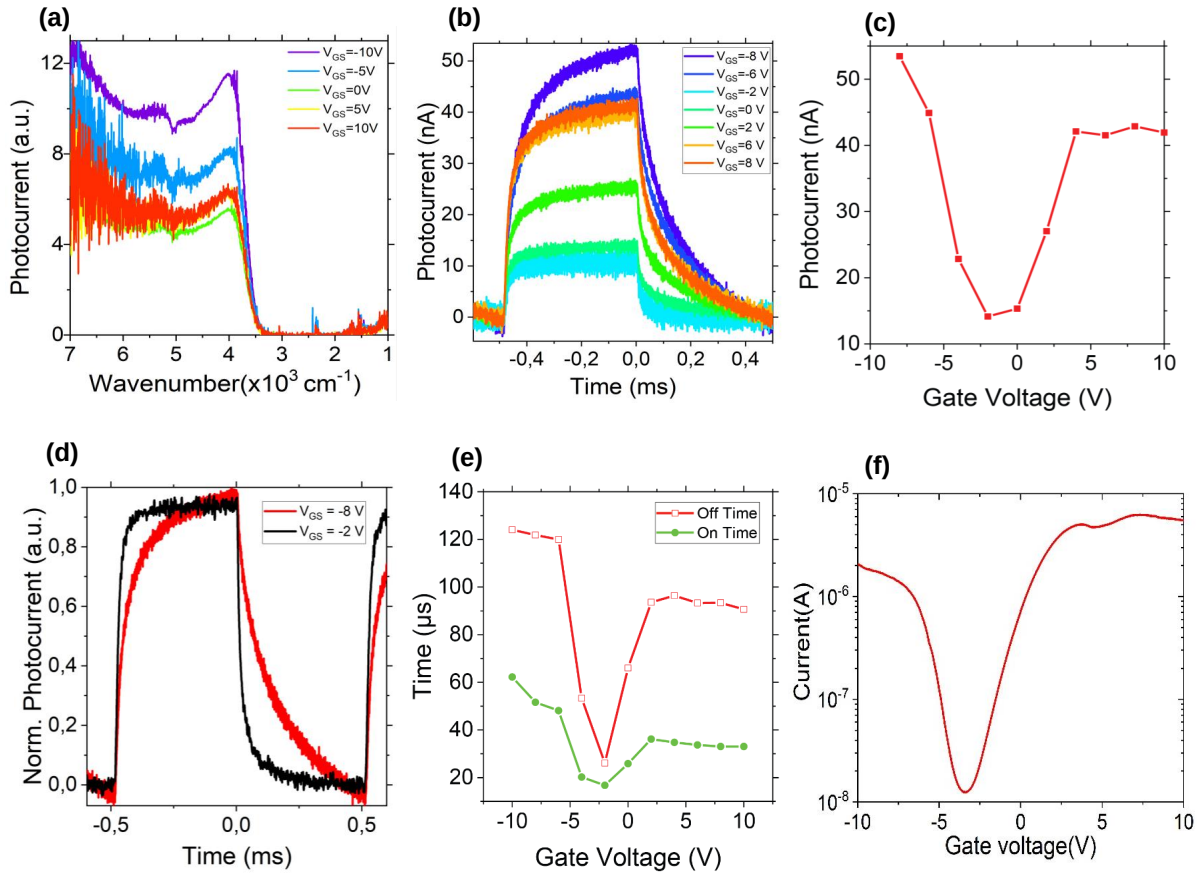

Figure 2.15 *– (a) Photocurrent spectrum of HgTe nanocrystals film on a LaF_3 substrate at 200 K at different gate voltages. (b) Photoresponse at 1 kHz of a HgTe film on a LaF_3 device under 4 mW at 1.55 µm excitation at different gate voltages at 200 K under 0.5 V drain-source bias. (c) Photocurrent amplitude gate-dependency extracted from the photoresponse curves. (d) Normalized photoresponse at 1 kHz under 4 mW at 1.55 µm excitation for -2 and -8 V gate voltages. (e) Response times at 1 kHz measured at 200 K for different gate voltages under 4 mW at 1.55 µm excitation (f) Transfer curve in the dark at 200 K under 0.5 V drain-source bias.*

and then resulting the bleach of absorption.

By exciting HgTe-FET with a pulsed laser diode operating at 1.55 μm under 4 mW power, this wavelength has been chosen to be close enough to the band edge (1.6 times the band edge energy) to avoid any hot-electron effect such as multi-exciton generation [Livache18a]. We have measured the photocurrent $I_{ph} = I_{light} - I_{dark}$ by applying 0.5 V between the source and drain at 200 K at different gate voltages, the detailed experimental setup is given in appendix B.2. As for what we observed with FTIR spectroscopy, the amplitude of the photocurrent can be modulated by the gate with a high modulation under hole injection, see Fig. 2.15 (b). We have extracted the amplitude of the photocurrent at each gate bias and we plotted in Fig. 2.15 (c) the photocurrent gate-voltage dependency, the photocurrent curve follows the dark current as expected for any phototransistor. Indeed, applying a gate bias allows to inject charges in the SC layer and reduce the Schottky barrier at metal-SC interfaces, thus resulting in more efficient photogenerated carriers extraction. A photocurrent modulation roughly a

factor of 4 when the system is at its minimum of conductance is observed. The modulation is much smaller than the one measured for the dark conductance (a factor of 400, see Fig.2.15 (f)). In this sense, using the gate to prepare the system at its minimum of conductance leads to an increase of the signal-to-noise ratio of our device by almost 2 orders of magnitude.

Finally, we have studied the carrier dynamics with ionic glass gating. By normalizing the photoresponse for each gate bias and extracting the time response, we plot in Fig.2.15 (e) the time response gate-dependency. The reduction of the photocurrent matches well with the acceleration of the photoresponse. Indeed, the time responses (on and off time) are faster when the gate bias corresponds to the minimum of conductance of the dark current and photocurrent curves. A modulation of a factor 6 of the carrier dynamics can then be induced by the gate. The dynamics under hole injections are slightly slower than the one for electron. The observed dynamics may result from transport phenomenon: in this case, the RC time constant will drive the dynamics of the photocurrent. This is unlikely to be the case here because the ambipolar character of the sample makes the resistance maximal close to charge neutrality point; thus, the longest RC time constant is expected to be in the minimum of conductance, while this corresponds to the one for which the fastest time response has been obtained, see Fig.2.15 (e). The observed dynamics is the prize of the gain-bandwith trade-off which may come to mid-band-gap recombination centers. Indeed, accordindly to what have been observed in NCs based phototransistors in INSP's team [Lhuillier14, Livache17], the change of responsivity ($R=I_{ph}/P_{in}$) is made at quasi-constant gain-bandwidth-product (which can be seen as the ratio of responsivity and the characteristic time response). In other words, a faster response comes at the prize of a smaller photoresponse as observed in our device.

2.5 Conclusion

I have presented in this chapter the detailed investigation of ionic glass LaF_3 substrate for high doping regime. From electrochemical impedance spectroscopy measurements, I figured out charging mechanisms in the LaF_3 substrate, which has a capability for the electrostatic tuning of electronic properties of nanomaterials. The capacitance of the ionic glass is the combination of a low-value dielectric capacitance and an ionic double layer high capacitance resulting from F^- vacancy existing in the crystals which allows the motion of fluorine ions. From the temperature-frequency mapping of EIS, it comes out that EDL capacitor in our ionic glass can be achieved at low frequency (low enough to give enough time to fluoride ions to reach the surface) and low temperature (sufficient to the motion of fluoride ions) or intermediate frequency and high temperature (not high enough to thermally activate much fluorine ions and induce leakage in the system.
The strategy allows to find sheet capacitance as high as 1 $\mu F.cm^{-2}$ and sheet carrier concentration exceeding 3-5 x 10^{13} carriers per square centimeter, very close to the reported value for electrolyte gating and one decade larger than traditional dielectric gating approaches such as SiO_2 while preserving the gate tunability down to 180 K. Moreover, using the ionic glass gat-

ing, we have demonstrated ambipolar transport in narrow-band-gap HgTe NCs and pristine PbS NCs, while a first demonstration of perovskite NCs based FET has n-type transport with FAFI-PbS perovskite NCs.
Finally, we unveil that this LaF_3 gating strategy can be used to control the magnitude and the dynamic of the photoresponse of HgTe nanocrystals. By carefully choosing the operating bias, the signal-to-noise ratio can be enhanced by a factor of 100 and the response time made faster by a factor of 6.

Chapter 3

Transport and phototransport properties of 2D materials in high doping regime

We have studied in the previous chapter the transport and phototransport properties of nanocrystals in high doping regime using ionic glass gating. We demonstrated that this gating technique can operate in a wide temperature range (180 K to 300 K) with the capacitance exceeding 1 $\mu F.cm^{-2}$ and the sheet carrier density as large as $3x10^{13}$ carriers/cm^2. In this chapter, we extend the use of ionic glass as high capacitance gate on 2D materials such as MoS_2, $MoSe_2$, WS_2 and WSe_2. We report on ionic glass gate tunable metal/WSe_2 interface in WSe_2 field effect transistors with Ti/Au contacts at 200 K. The solid gate electric field induces high doping in WSe_2 layer and allows band bending modulation for efficient carrier extraction. Finally, we combine high carrier density and direct optical addressability of ionic glass to explore $MoSe_2$ based phototransistor on LaF_3 substrate. The phototransistor demonstrates On/Off ratio exceeding five decades and photoresponse times down to 200 µs, up to two decades faster than $MoSe_2$ phototransistors reported so far. Ionic glass gating of 2D systems allows tuning the nature of the carrier recombination processes, while annihilating the traps' contribution in the electron injection regime. This interesting property results in a photoresponse that can be modulated electrostatically up to two orders of magnitude, while at the same time increasing the gain bandwidth product.

Related article

- U. N. Noumbé, C. Gréboval, C. Livache, T. Brule, B. Doudin, A. Ouerghi, E. Lhuillier, and J.-F. Dayen. *Ionic Glass-Gated 2D Material-Based Phototransistor: $MoSe_2$ over LaF_3 as Case Study*, Adv. Funct. Mater. 2019, 29 (33), 1902723.

In this project, I designed and processed samples (TMDCs-based FET on LaF_3 substrates) and study the gate tunable interface at IPCMS. Together with Charlie Gréboval we performed optoelectronic measurements of $MoSe_2$ phototransistor at INSP.

Optimizing the doping level in 2D materials is of utmost importance not only for the performances of the device, but also for exploring fundamental electronic properties. While the Iwasa's group used liquid electrolyte to achieve high doping in MoS_2 for nanoelectronic applications by inducing superconductivity [Ye12], developing ambipolar FET [Zhang12] and designing a lateral pn junction [Zhang13b], the Cui's group in order to avoid possible side electrochemical reactions or moisture sensitivity of liquid electrolytes recently introduced ionic glass as high capacitance solid gating to demonstrate metal-insulator transition in MoS_2 flake [Wu18]. In the latter, they accumulated high carrier density up to $4x10^{13}$ carriers/cm^2

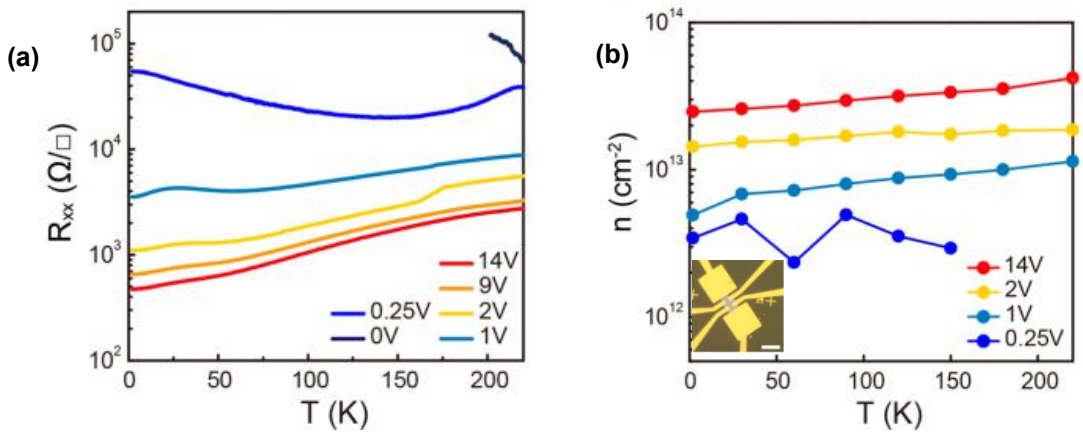

Figure 3.1 *– Low-temperature measurement on MoS_2/LaF_3 showing gate-induced insulator-metal transition. (a) Resistance-temperature (b) carrier density at different gate bias. Inset: optical image of the device. (Scale bar: 10 µm). Adapted from Ref. [Wu18].*

at 220 K with the back gate and they performed sheet resistance-temperature measurements. As shown in Fig.3.1 (a), at low gate bias (below 0.25 V), they observed an increase of the resistance with decreasing temperature. When increasing V_{gate} between 0.25 V and 1 V, the resistance starts to decrease with decreasing temperature, crosses the quantum of resistance[1], and always decreases for $V_{gate} > 1$ V, thus demonstrating a clear insulator-metal transition induced by high doping ionic glass gating . In this work, in addition to this high doping allowing to tune Schotty contacts at M/SC interfaces, we take advantages of the direct access of the surface area of the 2D materials on ionic glass which facilitates a direct optical excitation serving as additional possible probe for carrier density. Then, exploring for the first time photoconduction properties of 2D materials in high doping regime using glass gating.

3.1 Device fabrication and characterization

The device fabrication is a multi-step process including respectively: i) the production of single layer (SL) or multilayer (ML) SC-TMDCs (MoS_2, $MoSe_2$ WS_2 and WSe_2), ii) the patterning of electrodes using E-beam lithography, followed by iii) their macroscopic extension with a manual stencil mask alignment, and finally iv) the wire bonding of the sample on a chip holder or the direct silver paste connection of the sample on the measurement set-up.

[1] Quantum of resistance is the quantized unit of electrical resistance $R_Q = \frac{h}{e^2} \approx 25.6k\Omega$, e and h being respectively the elementary charge and Planck constant.

3.1.1 Mechanical exfoliation and dry transfer technique

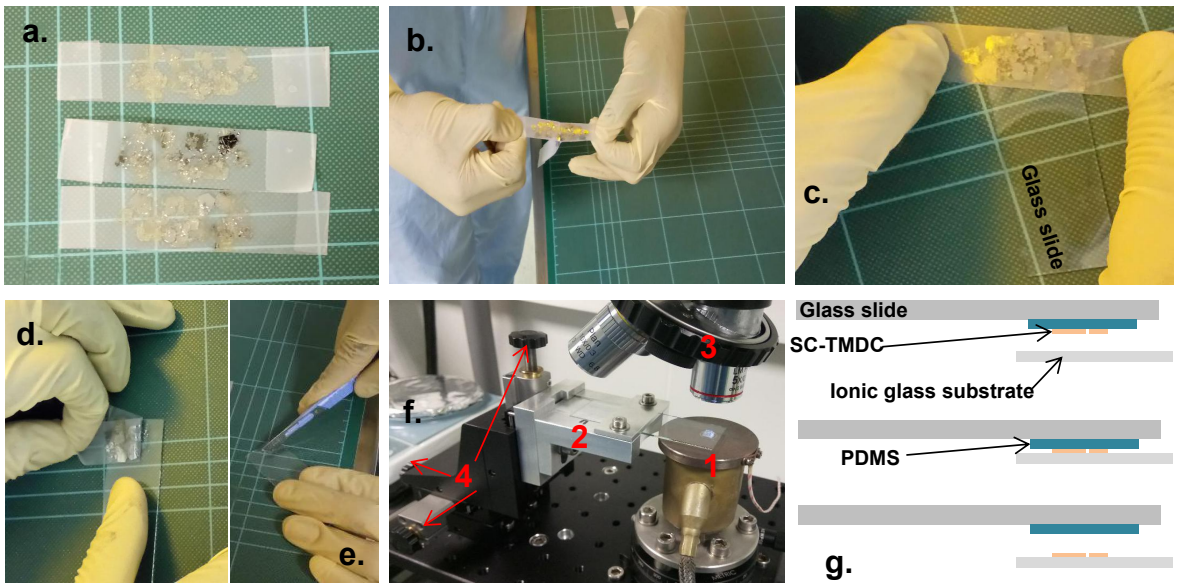

Figure 3.2 *– Exfoliation steps and transfer of TMDCs done during my thesis at IPCMS. (a-b) Mechanical exfoliation using adhesive tape, (c-d) Transfer on the PDMS initially placed on a glass slide. (e) Cutting the PDMS to keep a square of the interesting area. (f) Transfer station. 1: Sample holder connected to a heating system and a pump, 2: Glass slide holder, 3: Optical microscope connecting to a video camera, 4: Micromechanical platform with (x,y,z) degree of freedoms. (g) Sketch of the transfer process.*

The production of SL or ML SC-TMDCs used in this thesis relies mainly on a dry exfoliation method as first proposed by Novoselov et al. [Novoselov04]. Its consists of using a scotch tape to cleave from the corresponding pristine bulk material a SL or ML SC-TMDCs. Thanks to interlayer weak vdW forces. The exfoliated flake is subsequently transferred on LaF_3 substrate using a micromechanical transfer station of the STnano cleanroom at IPCMS as shown Fig.3.2 (f). The process is the following:

1. A piece of bulk crystal (2H phase purchased from graphene supermarket) is placed on an adhesive tape. A repeated process of folding and separating the adhesive tape enables to cleave the crystal on a large surface of the tape (Fig.3.2 (a)).

2. Stick another adhesive tape to the previous one. Gently press the two tapes on each other to improve their adhesion. Then, slowly peel off the two tapes in order to increase the chances of obtaining large flake on both tapes (Fig.3.2 (b)). Repeat this step as many times as needed with clean tapes until obtaining a transparent thin films of crystals susceptible to be a SL or ML TMDCs.

3. Clean a glass slide and stick a small square of polydimethylsiloxane (PDMS) film onto it, then put the area of interest of the material on the PDMS (Fig.3.2 (c)). Proceed to a gentle massage on the area of interest for a few minutes, then put a small weight on it to apply an uniform pressure and wait a few minutes.

4. Quickly remove the scotch tape from the PDMS in order to have a good adhesion of the

material on the PDMS (Fig.3.2 (d)). Use an optical microscope to identify the interesting flake, then cut and remove the PDMS around the interesting area to keep a square of PDMS (Fig.3.2 (e)), the sizes of this square of PDMS have to be smaller than the sizes of the substrate.

5. Put the substrate on the sample holder and the glass slide on the glass slide holder of the transfer station such that the PDMS is oriented to the ground (Fig.3.2 (f)). Then use the microscope and the x; y; z mechanical platform to align the flake and the center of the substrate. Approach the glass slide to the substrate with the z screw until being able to focus the flake and the substrate on the microscope at the same time. Slowly continue the approach until the contact line appears on the microscope, this line tells about the contact between the PDMS and the substrate. Place this contact line close to the interesting flake (a few μm distance) and stop any mechanical motion.

6. Use the heating system connected to the sample holder to slowly increase the temperature. This will slowly increase the polymer-substrate contact. Increasing the temperature by steps of one or two degree should insure a slow enough contact. Be very careful when going through the flake to avoid its break. Once the contact line passes through the interesting flake, stop the heating and let the temperature gets down. The contact line should go back very slowly, if it stops moving, a very careful mechanical motion can be useful. Be extremely careful when going through the flake.

7. Once the contact line completely came back from the flake, the contact can be removed mechanically with the z screw. If the transfer is successful the sample is ready for optical characterizations and E-beam lithography to pattern contacts.

The sketch shown on Fig.3.2 (g) summarizes the transfer steps (step 5 to 7).

After the transfer step, the flake is identified on LaF_3 substrate by optical contrast using an optical microscope, then electrodes are patterned on the flake using electron beam (E-beam) lithography.

3.1.2 Electron beam (E-beam) lithography of electrodes

To pattern the electrodes, we follow two E-beam lithography steps using a Zeiss Supra 40 scanning electron microscope (SEM) coupled with a Raith lithography system allowing a precise control of the electron beam. For each E-beam lithography step, we used a standard bilayer PMMA (Polymethyl methacrylate) positive resist and a conductive Protective Coating resist (e-spacer). The bilayer PMMA resist consisting of AR-PMMA 669.04 and AR-PMMA 679.02, are spin-coated at 4000 revolutions per minute (rpm) during 1 min and annealed at 180 °C during 1'30s with a delay of 2 min before the second spincoating. This results to a total (AR-PMMA 669.04)/(AR-PMMA 600.02) bilayer resist thickness of 290 nm corresponding to 220 nm for the first layer and 70 nm for the second layer. The e-spacer AR-PC 5090.02 is afterwards then spincoated at the same speed (4000 rpm) but annealed at 90 °C during 1'30s for a thickness of 90nm. While the use of a bilayer PMMA resist facilitates the lift-off, the

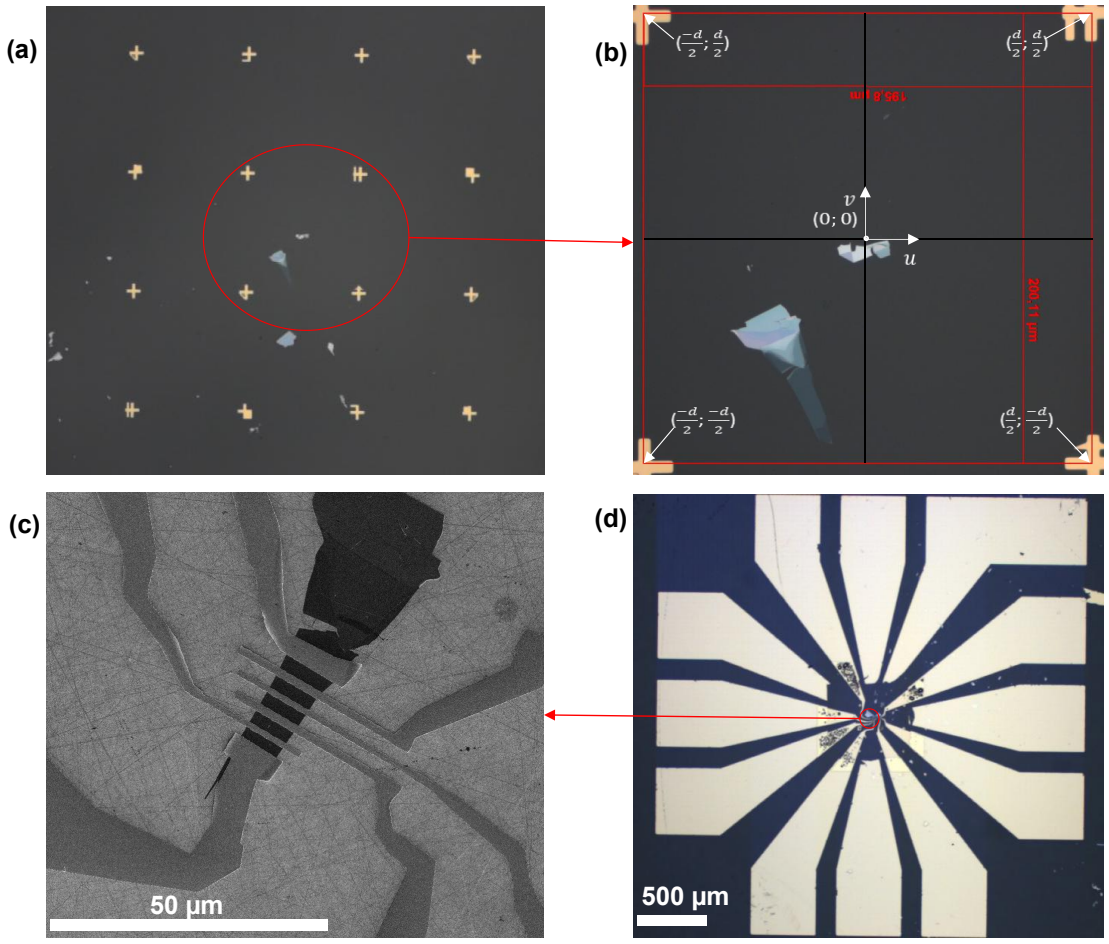

Figure 3.3 *– Sequence of the lithography steps: The case shown is few layers $MoSe_2$ contacted by E-beam lithography. (a) Optical image of the identification and alignment marks. (b) Coordinate used to align the beam before the exposure of the fines leads. (c) SEM image of the contacts on the flake. (d) The optical image of the device after macroscopic extension of the contacts using manual stencil mask alignment.*

conductive resist allows to write and extract charges on the insulating substrate. The latter has to be cleaned with DI water after the electron beam insolation before the development step.

The first lithography step consists of patterning a network of marks around the position of the selected flake using the coordinated provided by the optical microscope. The marks are used for the identification of the region of interest and to a precise alignment of the design electrodes on the flake during the second lithography steps. We resume the lithography steps as followed:

Step 1 : Identification and alignment marks.

After resists coating, we used the coordinate obtained from optical imaging to move the beam to the region of interest and exposed the predesign mark patterns. The sample is then taken out of the SEM, then cleaned during 2 min in DI water to remove the conductive resist and developed during 25 s in 1:3 MIBK-IPA (methyl isobutyl ketone-isopropyl) at 25°C.

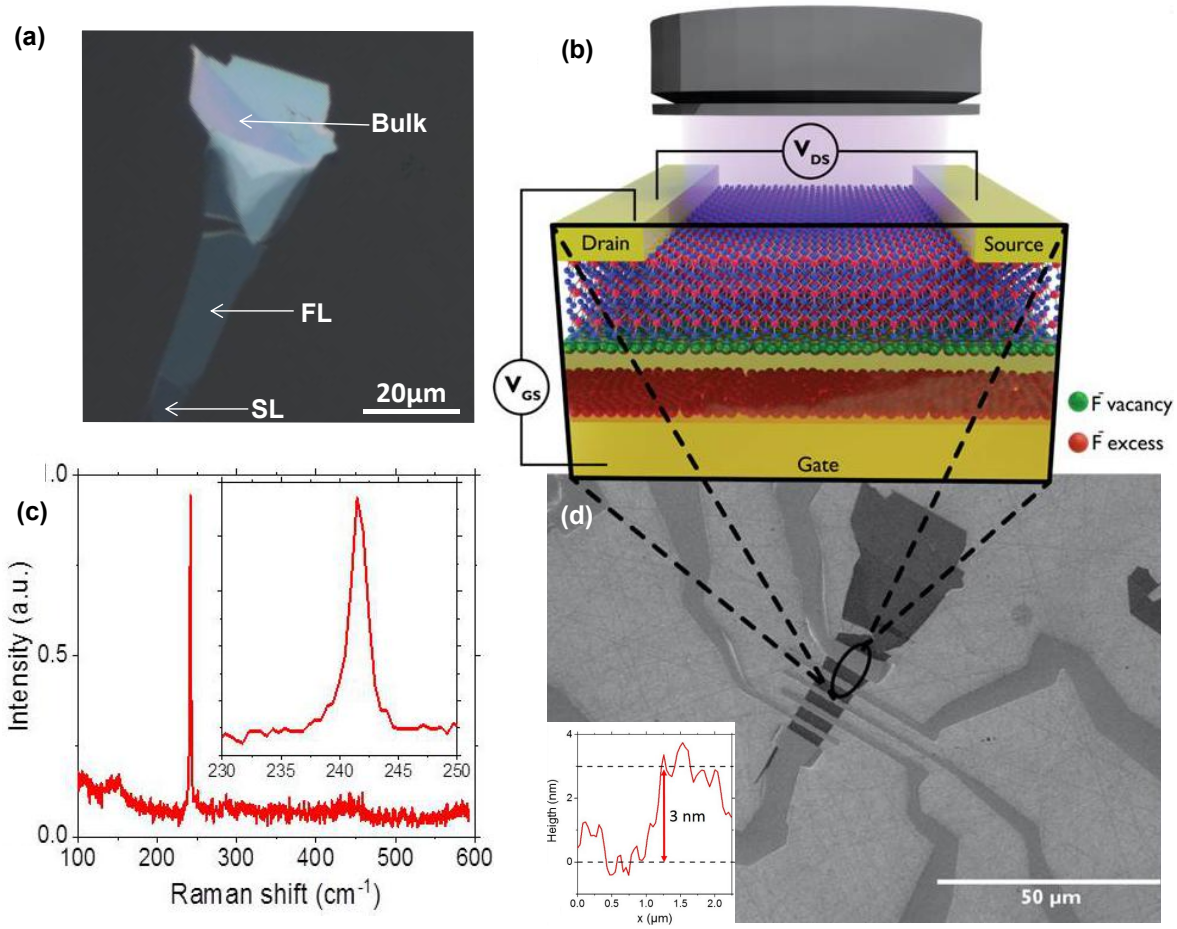

Figure 3.4 *– (a) Optical image of exfoliated $MoSe_2$ on LaF_3 substrate: By optical contrast, single layer and few layers can be distinguished from bulk material. (b) Scheme of the photodetector device and electrical connections. Tri-layer $MoSe_2$ on a LaF_3 substrate is contacted by two gold electrodes (drain and source), and gating is performed by applying a bias between drain and a bottom gold contact below LaF_3. Top access allows addressing optically the $MoSe_2$ channel while reaching higher carrier density thanks to the ionic glass gate. (c) Raman spectra of the $MoSe_2$ flake with A_{1g} mode at 242 cm^{-1}. The inset is a zoom on the peak relative to the A_{1g} mode of $MoSe_2$. Done at HORIBA Scientific by Abdelkarim Ouerghi and Thibault Brule. (d) SEM image of the flake and gold contacts. Length and width of the channel are 2.6 and 9.3 µm respectively. The inset height profile from AFM measurements with a thickness of 3 ± 0.5 nm corresponding to 3-4 layers $MoSe_2$.*

The evaporation of the Ti(3 nm)Au(47 nm) is performed in electron beam evaporator in high vacuum chamber. A lift-off in acetone complete this step. Fig.3.3.(a) shows an optical image of few layer $MoSe_2$ surrounded by a network of identification and alignment marks.

Step 2 : electrodes.

After the lift-off of marks, the sample is again imaged with the optical microscope. An image with the marks is imported in the E-beam lithography software for the design of the electrodes pattern. The design of electrodes is done directly on the flake with the desired shape, size and orientation. Subsequently, the same bilayer resist and conductive resist are coated on the sample which is then reintroduced in the SEM for electron beam insolation of

the predesign electrodes pattern. Prior to the insolation, to ensure the proper alignment of the electrodes pattern to the flake, the beam is accurately aligned by affecting to three marks surrounding the flakes (out of four) their exact coordinates. This is known as three marks alignment method (Fig.3.3.(b)). In the so defined coordinate system, the predesigned pattern automatically locates at the coordinates of the flake. This procedure enables patterning electrodes with the best possible alignment. After the beam insolation, the sample is taken out of the SEM, cleaned 2 min in DI water and developed 25 s in 1:3 MIBK-IPA as already mentioned. This step is particularly sensitive to the develop time and it is important to regularly check the proper developing time by making a dose test.
The sample is then inserted into the high vacuum evaporator for evaporation of Ti(3 nm)Au(47 nm) followed by a lift-off in acetone. The Fig.3.3.(c) shows a SEM image of the metal electrodes on $MoSe_2$ flake.

3.1.3 Shadow stencil mask extension of the leads

Shadow stencil mask deposition: Because E-beam lithography is used to design pattern with accuracy at the nanoscale, our E-beam software is limited to a working area of 1715x1715 μm^2. At this scale, electrodes are too small to be connected with the experimental setup. One way to solve this issue is to use many position lists during the beam insolation, this at the prize of high time consuming. Another practical way is to use stencil mask using an optical microscope for a manual alignment of the stencil mask on the Ti/Au electrodes patterned during the last lithography step. This enables a shadow deposition of Ti(3 nm)Au(47 nm) of macroscopic extension of the electrodes (Fig.3.3 (d)) in order to make possible a manual bonding of the sample either onto a chip holder with gold wires allowing its adaptation onto the measurement set-up or directly in the cryostat pads using a silver paste.

3.1.4 Flake characterizations

Raman spectroscopy is a very important tool for characterizing 2D materials and compare their SL to their ML or bulk. It is a fast, non-destructive and high resolution technique. It gives structural and electronic information of materials which can be applied at both laboratory and commercial production scales. In addition, from the Raman shift, layer thickness can be determined for 2D materials. In our work, we use Raman spectroscopy to characterize few-layer $MoSe_2$. Fig.3.4 (a) shows the optical image of $MoSe_2$ flake transferred on LaF_3 substrate, by optical contrast we can state that we have few layers $MoSe_2$. This is confirmed in Fig.3.4.(c) by the lack of photoluminescence (PL) signal and by the Raman spectra done at HORIBA Scientific by Abdelkarim Ouerghi (researcher, *Centre de Nanosciences et Nanotechnologies* (C2N) Paris-Saclay) and Thibault Brule (researcher, HORIBA Scientific Palaiseau). From the Raman shift of $MoSe_2$, the relative position of A_{1g} out of plan vibration mode can be used to precisely distinguish bulk materials from few-layer or single layer $MoSe_2$ [Lu14, Pawbake16, Mouafo17]. The A_{1g} vibration mode in our flake appears at 242 cm^{-1}, while it is expected to be at 240 cm^{-1} for SL $MoSe_2$, confirming the multilayer aspect of our flake. Finally, we have performed atomic force microscopy (AFM) measurements to determine more carefully the exact thickness of the flake. It is found to be 3 ± 0.5 nm which

corresponds to 3-4 layers of $MoSe_2$ (see the inset in Fig.3.4 (d)).

3.2 2D based field effect transistor in high doping regime with ionic glass LaF_3

3.2.1 TMDCs based field effect transistor on laF_3

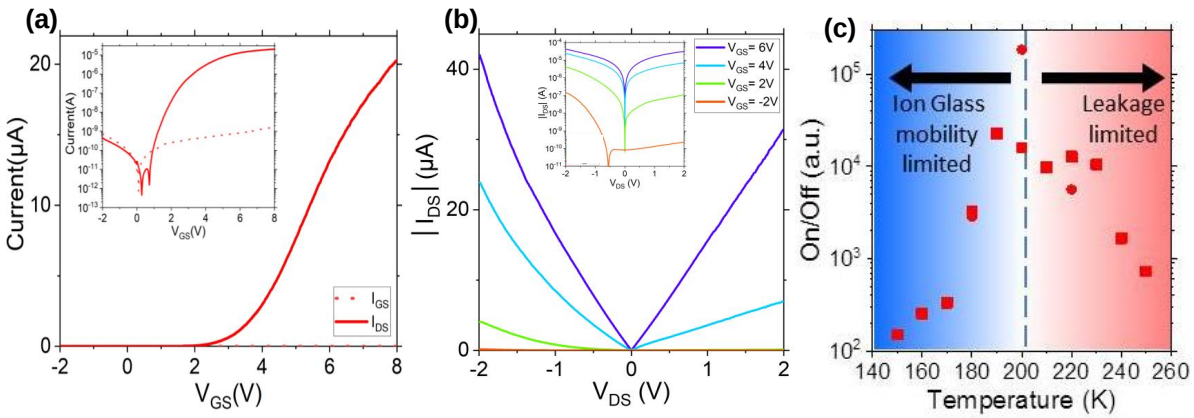

Figure 3.5 *– (a) Transfer curve of a $MoSe_2$ flake under 1 V drain-source bias at 200 K in linear scale. Inset: Transfer curve in logarithmic scale. (b) IV curves at different gate biases measured at 200 K. Inset: IV curves in logarithmic scale. (c) On/Off ratios for two devices at several temperatures showing the ion glass mobility and the leakage limited regimes with a maximum value at 200 K. Sphere: Device studied in this section. Square: Another sample with additional data sets to confirm the trend. On/Off ratios were calculated from transfer curves at $V_{DS} = 1V$.*

We validate in this section the feasibility of building FET with several TMDCs on LaF_3. A scheme of the device made of tri-layer $MoSe_2$ contacted by gold electrodes on LaF_3 as well as the scanning electron microscopy image are given in Fig.3.4 (b,d). Then the sample is inserted into a cryostat and cooled down for low temperature measurements. As shown in the previous chapter, when a gate bias is applied, F^- ions move toward or away from the surface and form EDL capacitor with a high capacitance (up to 1 μF.cm^2) which induces the electrostatic gating in $MoSe_2$ flake. Under 1 V drain-source voltage at 200 K, the transfer curve presents n-type characteristic consistent with previous $MoSe_2$-based FET using SiO_2 as dielectric in our group [Mouafo17] (Fig.3.5 (a)). As we can see in Fig.3.5.(c), the field effect is preserved even at 180 K. We observe a maximum of the current modulation for a device temperature around 200 K where the I_{On}/I_{Off} current modulation exceeds 4 to 5 orders of magnitude in a small bias operation range (below 10 V). Above 200 K, the On-Off ratio is limited by a large Off current due to the relatively large leakage through LaF_3. At a temperature below 180 K, the ionic mobility of the F^- vacancy gets strongly reduced and the On current gets lower. Using the expression n=CV/e, applying 8 V of gate bias leads to a carrier concentration as large as 5x10^{13} cm^{-2}, a value quite similar to what is observed with electrolytes gating [Ye12, Zhang13b]. Using the expression of the field effect electronic mobility $\mu = \frac{L}{C_S W V_{DS}} \frac{dI_{DS}}{dV_{GS}}$, where L is the channel length (2.6 μm), W is the electrode width (9.3 μm), C_S is the surface capacitance equals to 0.1 μF.cm^{-2} at 200 K. We found electron mobility to be $\approx$ 15 cm^2.V^{-1}s^{-1} at 200 K. This value is very similar to the one reported in our

group for bilayer $MoSe_2$ gated with silica [Mouafo17].
It is worth noting that the ionic glass gating is not limited to $MoSe_2$ flake. In Fig.3.6, we have demonstrated electron transport in both MoS_2 and WS_2 flakes and extended their concept to hole transport in WSe_2 flake. Before study the photoresponse of our $MoSe_2$ FET in high doping regime, we will investigate in the next section the gate dependency of the Schottky barrier height (SBH) in TMDC FET.

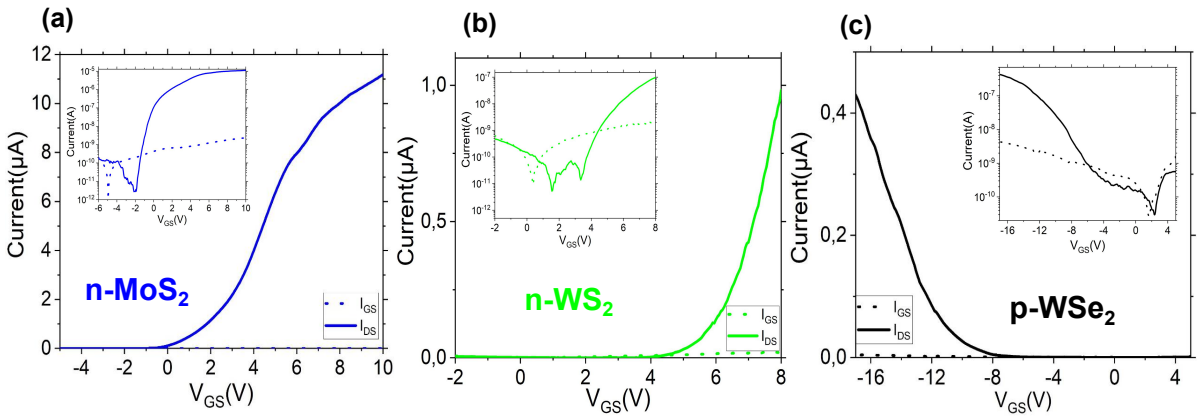

Figure 3.6 *– Transfer curve at 200 K with LaF_3 gating (a) n-transport in MoS_2 flake under 0.3 V drain-source bias. Inset: Transfer curve in logarithmic scale. (b) n-transport in WS_2 flake under 2 V drain-source bias. Inset: Transfer curve in logarithmic scale. (c) p-transport in WSe_2 flake under 2 V drain-source bias. Inset: Transfer curve in logarithmic scale.*

3.2.2 Schottky junctions in high doping regime with LaF_3

We explore here how the Schottky contact can be tuned by electrostatic gating with ionic glass. For this purpose, I have choose tungsten diselenide (WSe_2) because it is an attractive TMDC since its Fermi energy close to the mid gap [Yuan13] makes it an excellent candidate for realizing p-n junction devices [Pospischil14], n-FET [Liu13], p-FET [Pradhan15b] and ambipolar FET [Wang18]. It thus offers exciting opportunities for potential applications in both digital electronics and optoelectronic devices. The carrier type evolves with increasing WSe_2 channel thickness, namely, p-type (<3 nm), ambipolar (≈ 4 nm) and n-type (>5 nm). This thickness dependent carrier type can be attributed to the change in the bandgap of WSe_2 as a function of the thickness. Another particularity of WSe_2 flake is that one can induce carrier type (electron and/or hole) transport by electrodes engineering, which is challenging for other TMDC materials such as MoS_2 and $MoSe_2$ due to their extrinsic native doping property. Indeed, Liu et al have demonstrated the n-WSe_2 FET by using indium as a contact metal [Liu13]. Chuang et al have revealed that graphene can be a work-function-tunable electrode material for few-nanometer WSe_2 FETs [Chuang14]. Using Ni/Au contacts, Chen et al used ionic liquid as top gate to demonstrate ambipolar FET in monolayer WSe_2 [Chen14a]. This is made possible by ionic liquid gating where by inducing high doping in WSe_2 flake, allows to tune its Fermi energy close to the conduction and valence bands for both electron and hole transport respectively. It is also important to remark that SL-WSe_2 being initially p-type, when contacting them with metals with high work functions such as Ni or Pd (Φ_{Ni} = 5.15 eV,

Φ_{Pd} = 5.22 eV), form ohmic or semi-ohmic contacts at the metal/WSe_2 interfaces with small contact resistances.

In this section, we investigate single layer WSe_2 contacted with Ti/Au in high doping regime with the solid gating ionic glass LaF_3 substrate.

Electric Characterization

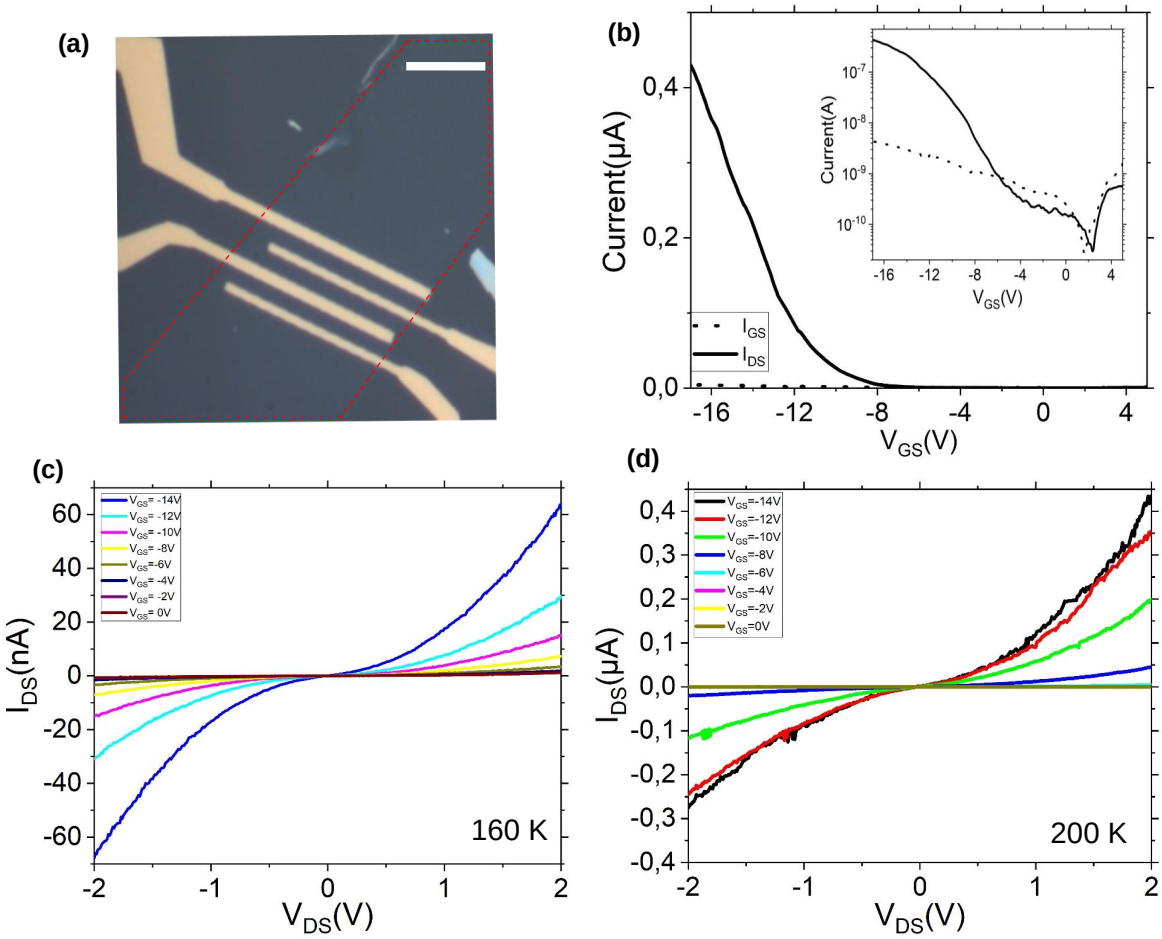

Figure 3.7 *– (a) Optical image of the multi-electrodes device fabricated using e-beam lithography, the region in dash line is the flake. Scale bar: 10 μm. (b) Transfer curve at 200 K under 2 V drain-source bias with LaF_3 gating showing hole conduction in WSe_2 flake. Inset: Transfer curve in logarithmic scale. (c) I_{DS}-V_{DS} curves for different gate voltages with increasing current with the gate voltages at 160 K. (d) I_{DS}-V_{DS} curves for different gate voltages with increasing current with the gate voltages at 200 K.*

Using the technique described in section 3.1, we have fabricated WSe_2 FET on LaF_3 substrate, an optical image of the multi-electrodes device made of monolayer WSe_2 is shown in Fig.3.7 (a). In Fig.3.7(b), we present the transfer curve of ionic glass gating WSe_2 FET demonstrating an p-type or unipolar hole transport at 200 K, similar for what has been found in WSe_2 FET with conventional dielectric [Pradhan15b, Xue18]. The On/Off ratio reaches $\sim 10^4$ at 200 K in a small operating voltage range compare to conventional dielectric such SiO_2 generally used as back-gate dielectric for TMDC based FETs. Using the expression $\mu = \frac{L}{C_S W V_{DS}} \frac{dI_{DS}}{dV_{GS}}$, where L is the channel length (0.9 μm), W is the electrode width (20 μm), C_S is the surface capacitance equals to 0.1 μF.cm^{-2} at 200 K. We have found the hole mobility

to be ≈ 1.5 x 10^{-2} $cm^2.V^{-1}s^{-1}$ at 200 K. This value is one to three decades smaller than what have been found in multilayer WSe_2 FET with Ni and Pd as S/D electrodes respectively at room temperature [Kang17]. In the latter, the high mobilities obtained came not only from the type of the ohmic contacts form by Ni and Pd but also from the high thickness of the flake and the oxygen plasma treatment of their devices at room temperature.

Fig. 3.7 (c) and (d) show the representative I_{DS}-V_{DS} curves for different gate voltages at

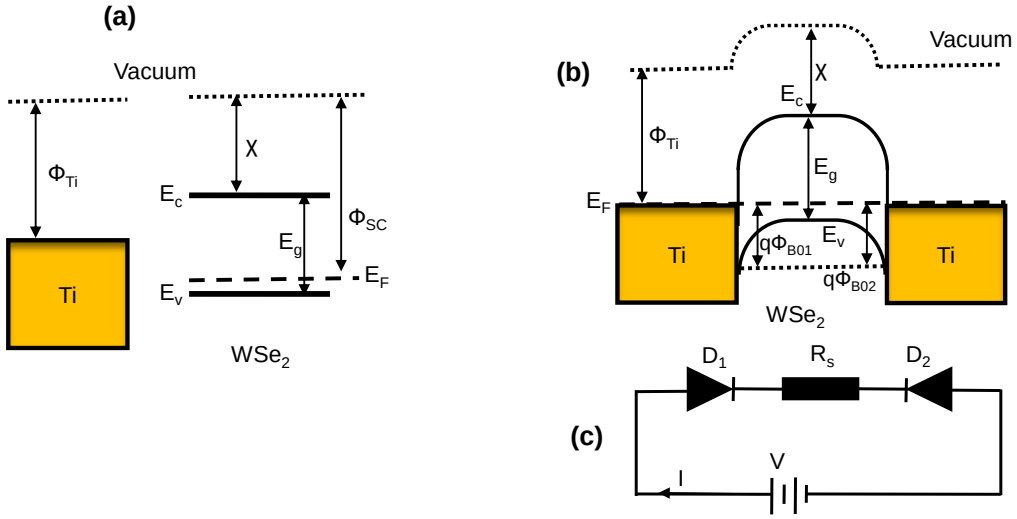

Figure 3.8 *– (a) Band alignment of metal and WSe_2. ϕ_{Ti} is the titanium's work function, χ is the electron affinity of WSe_2, E_g is the band gap, ϕ_{SC} is the work function of WSe_2, E_C is the conduction band minimum, and E_V is the valence band maximum. (b) Band diagram of WSe_2 based FET at the equilibrium with Schottky barrier at the interfaces resulting from Fermi levels alignment. Equivalent model of the device with two back-to-back diodes connected to the total series resistance.*

160 K and 200 K respectively. One can see an increase of the current for negative gate voltages confirming hole transport in our WSe_2 FET with LaF_3 gate tunability down to 160 K. It can be also seen the increasing of the current with the temperature. The quasi-symmetric non-linear behavior are typical for contacts with a Schottky barrier at the interfaces which have Ti as the S/D metal electrodes. Indeed, the work functions of WSe_2 ~ 4.65 eV [Xiao18] is slightly higher than that of Ti (ϕ_{Ti}=4.33 eV) [Pan16]. Metal/semiconductor interface is expected to be rectifying (non-ohmic) when the metal work function is smaller compare to the work function of an p-type semiconductor [Mathieu09]. When the two materials are in contacts, electrons move from the metal to the semiconductor. It appears a deficit of electrons at the metal side, at the very first nanometer of the interface. In the semiconductor, electrons which come from the metal recombine with holes creating a depletion zone due to the presence of ionized acceptor ions which are no longer compensated by the holes. It thus appears a space charge region which is spread out in the semiconductor, resulting a formation of an energy barrier at the metal-SC interfaces with a downward curvature of the bands as shown in Fig. 3.8 (b). The system evolves until the resulting diffusion field and voltage stop the electron diffusion. Generally, the height of the interface barrier for holes to pass from the semiconductor to the metal is equal to the sum of the semiconductor band gap (E_g) and

electron affinity (χ) minus the work function (ϕ_M) of the metal as: $E_b = E_g + \chi - \phi_M$, see the band alignment in Fig. 3.8 (a). From the gate-dependence of I_{DS}-V_{DS} curves at 200 K, we will analyze and extract the Schottky barrier height at Ti/WSe_2 interfaces.

Analyzed of Ti/WSe_2 interface from I_{DS}-V_{DS} curves

When two contacts are deposited on a semiconductor, the metal-semiconductor-metal junction forms a configuration which is known as a back-to-back Schottky diode (BBSD). This is the case in our device Ti-WSe_2-Ti. Since both contacts form Schottky junctions, the current will be always limited by one of the junctions operated in reverse bias. Assuming the current transport follows the thermionic emission theory at each metal-SC interface, we can extracted junction properties directly from the measured I_{DS}-V_{DS} characteristic of the BBSD using the thermionic emission theory following the method introduced in [Azmi18]. Fig. 3.8 (c) shows the equivalent model of the device with two Schottky diodes D_1 and D_2 connected back-to-back with the total series resistance R_S. The latter come from Ti/WSe_2 contact resistances and the WSe_2 channel resistance. R_S value can be estimated from the linear region at high positive bias of the I_{DS}-V_{DS} curve i.e. $R_S \approx \Delta V/\Delta I$. When a positive bias is applied, the diode 2 is reverse biased and the diode 1 is forward biased. Conversely, when a negative bias is applied, the first diode is reverse biased while the second diode is forward biased. When excluding the voltage drops at R_S i.e. IR_S from the applied voltage V in order to obtain the effective voltage drop across D_1 and D_2, and taking the formula of current from the thermionic emission theory at M/SC interface detailed in appendix C, in the Eq. C.11, the current of the equivalent circuit is expressed by:

$$I \approx I_{S2}\exp\left(\frac{-q(V-IR_S)}{n_2K_BT}\right)\left[\exp\left(\frac{q(V-IR_S)}{K_BT}\right)-1\right] \quad for \quad V>0 \tag{3.1}$$

$$I \approx I_{S1}\exp\left(\frac{q(V-IR_S)}{n_1K_BT}\right)\left[1-\exp\left(\frac{q(V-IR_S)}{K_BT}\right)\right] \quad for \quad V<0 \tag{3.2}$$

with $I_{S1} = S_1A^*T^2\exp\left(\frac{-q\phi_{0B1}}{K_BT}\right)$ and $I_{S2} = S_2A^*T^2\exp\left(\frac{-q\phi_{0B2}}{K_BT}\right)$.
I_S is the reverse saturation current, T is the temperature in Kelvin, q is the elementary charge, k_B is the Boltzmann constant, S the contact area and A^* is the Richardson's constant of WSe_2. Numbers 1 and 2 in subscript of I_S, ϕ_{0B} and n refer to corresponding junction number. Eq. 3.1 and 3.2 can be rewritten as:

$$\ln\left\{\frac{I}{\left[\exp\left(\frac{q(V-IR_S)}{K_BT}\right)-1\right]}\right\} = \ln(I_{S2}) - \frac{q(V-IR_S)}{n_2K_BT} \quad for \quad V>0 \tag{3.3}$$

$$\ln\left\{\frac{I}{\left[1-\exp\left(\frac{q(V-IR_S)}{K_BT}\right)\right]}\right\} = \ln(I_{S1}) + \frac{q(V-IR_S)}{n_1K_BT} \quad for \quad V<0 \tag{3.4}$$

Plotting $\ln\left\{\frac{I}{\left[\exp\left(\frac{q(V-IR_S)}{K_BT}\right)-1\right]}\right\}$ versus $(V-IR_S)$ for positive bias gives a linear graph. From the slope and y-axis intercept of the linear graph, we can deduce n_2 and I_{S2} respectively. I_{S2} can

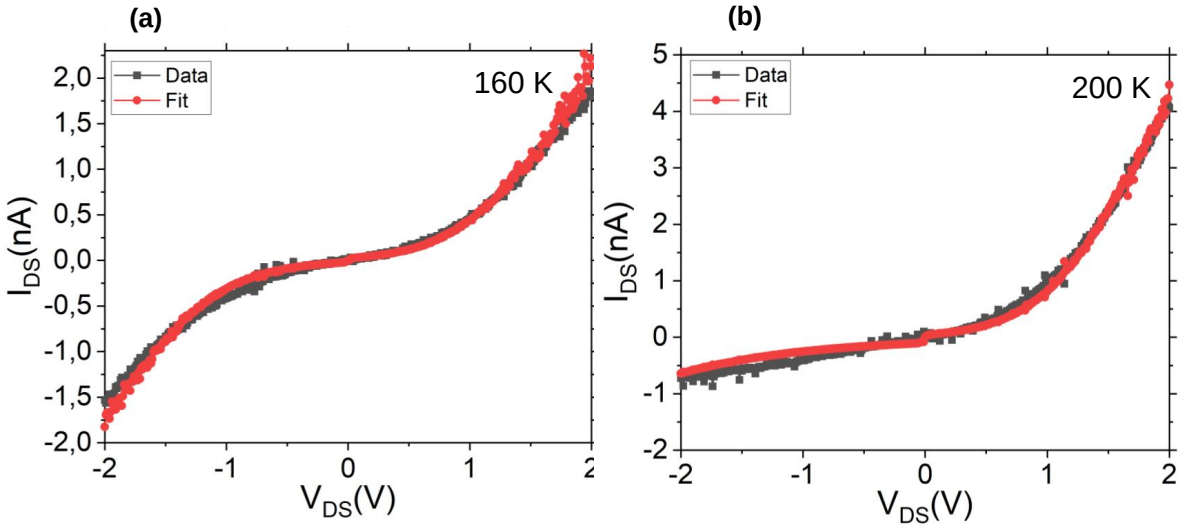

Figure 3.9 *– Example fit of I_{DS}-V_{DS} curves to back-to-back Schottky diode using the equivalent model for: (a) V_{GS} = -4 V at 160 K. (b) V_{GS}=-6V at 200K.*

thus be used to calculate the height of the second Schottky junction as:

$$\phi_{0B2} = \frac{K_B T}{q} \ln\left(\frac{S_2 A^* T^2}{I_{S2}}\right) \tag{3.5}$$

Similarly, using equation 3.4, n_1 and I_{S1} can be deduced and then used to calculate the height of the first Schottky junction as:

$$\phi_{0B1} = \frac{K_B T}{q} \ln\left(\frac{S_1 A^* T^2}{I_{S1}}\right) \tag{3.6}$$

The I_{DS}-V_{DS} curves were fitted using Eq. 3.1 and 3.2 for datas at 200 K. The Richardson's constant used was 27.6 $Acm^{-2}K^{-2}$ for p-WSe_2 [Klein98].

Examples of the fit curves at -4 V gate bias at 160 K and -6 V gate bias at 200 K are shown in Fig. 3.9 (a) and (b) respectively using the model in Fig. 3.8 (c). One can see a good accuracy with the measurement curves. In order to analyze the back gate dependency of the SBH, we have fitted all the datas at different gate biases at 200 K. The calculated SBH values from equations 3.6 and 3.5 for different gate voltages are presented in Fig.3.10 (a) and (b) respectively. For the two junctions, one observes a linear decrease of the SBH when decreasing the gate voltage until the flat band regime where the slope changes. At gate voltages above -10 V, the bands are bending at the interfaces of the two junctions (Fig. 3.8 (b)). At V_{GS} = -10 V, the slope in the curve of ϕ_{0B1} in function of gate voltage changes. This change indicates the flat band regime of the first junction while keeping the bending of the second junction as shown in the Fig.3.10 (d). Further decreasing the gate voltage down to -14 V allows to reach the flat band of the second junction, thus the flat band of the BBSD, see Fig. 3.10 (e), thanks to ionic glass LaF_3 gating which by decreasing the gate voltages induces high hole doping in WSe_2 channel. The increase of the ideality factor n [Sze81] of the two junctions with the gate

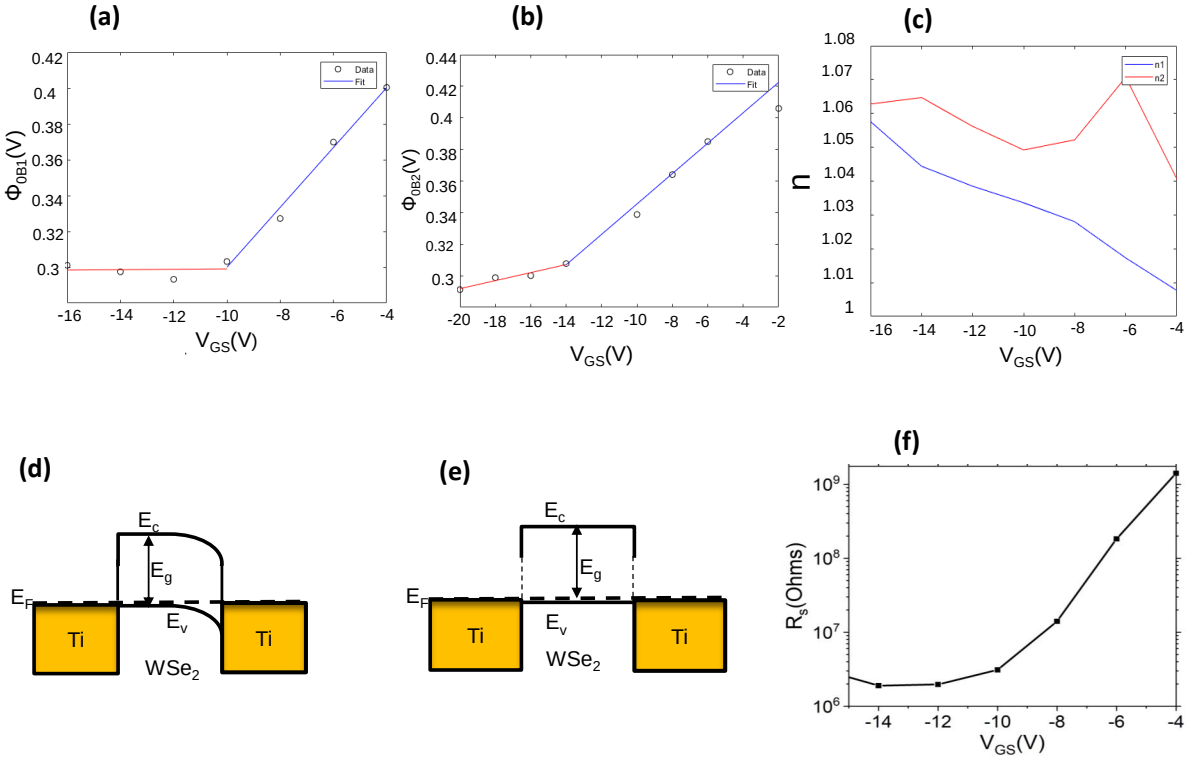

Figure 3.10 *– (a) Gate dependency of the Schottky barrier for junction 1. (b) Gate dependency of the Schottky barrier for junction 2. (c) Gate dependency of the ideality factor: the blue curve for the junction 1 and the red for the junction 2. (d) Band diagram of the system with the flat band of the first junction at V_{GS} = - 10 V. (e) Band diagram of the system with the flat band of the second junction when V_{GS}= - 14 V (g) Total series resistance in function of the gate voltage.*

voltage (Fig. 3.10 (c)) and moreover the exponential decrease of the total series resistance with the gate (Fig. 3.10 (f)) confirm our model to take into account the two junctions in the study. It also confirms the efficiency of our gating technology which is the signature of the reduction of contact resistances resulting in efficient carrier extractions.

Now that we know the efficiency of our gating technology for reducing Schottky barrier height at metal/semiconductor interfaces, we will use the direct optical addressability of LaF_3 to study the photoresponse of $MoSe_2$ in high doping regime in the next section.

3.3 Phototransport properties of $MoSe_2$ in high doping regime

In order to study the optoelectronics properties of the $MoSe_2/LaF_3$ phototransistor, I made another measurement campaign at INSP, and performed photoconduction measurements with Charlie Gréboval. Under illumination of the $MoSe_2$ flake with a 405 nm blue laser (the laser spot diameter was 1 mm) with 0.012 μW received power, we observe a photoconductive signal which amplitudes can be strongly tuned using the gate bias (Fig.3.11 (a)). As shown in Fig.3.11 (b), the responsivity of the flake follows the dark current. It reaches 50 mA/W at 0 V of gate bias and it is enhanced by a factor of 4 under strong positive gate bias now exceeding 0.2 A/W. This is made possible thanks to high doping regime with ionic glass LaF_3 which

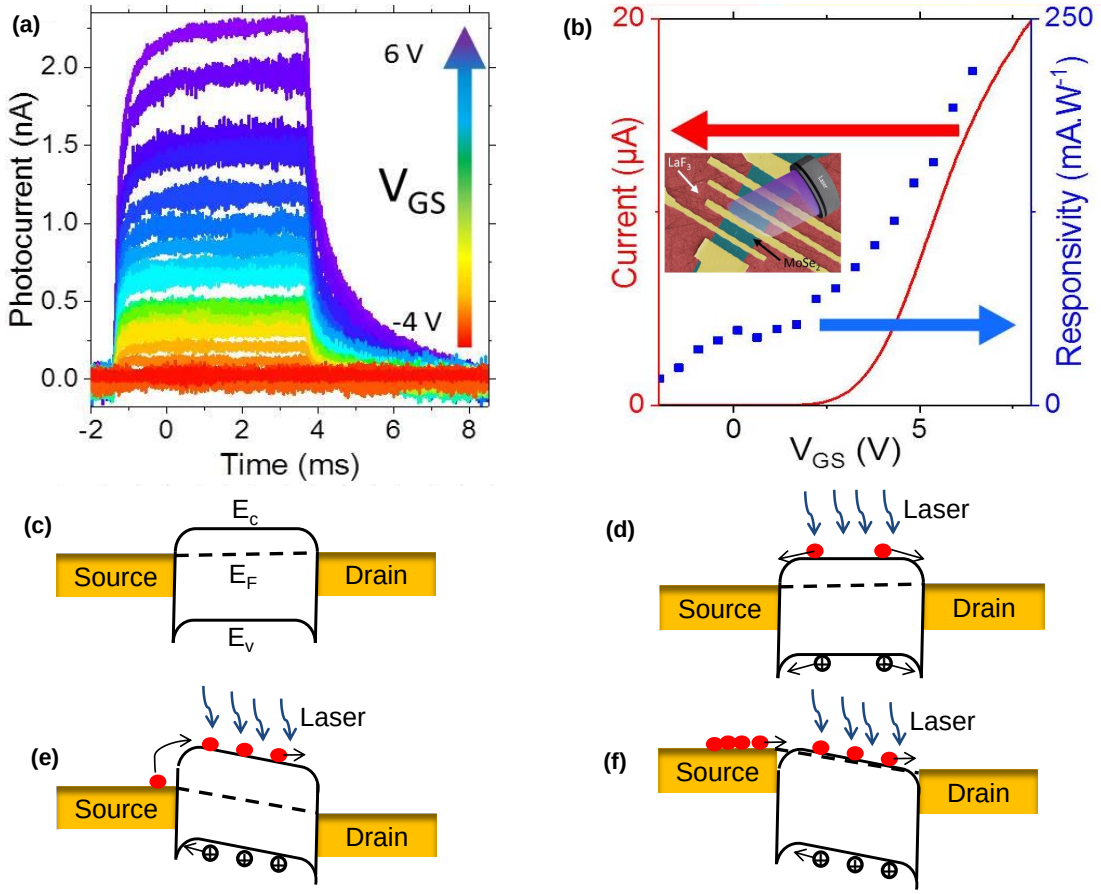

Figure 3.11 *– (a) Photocurrent of the device illuminated under 0.012 μW received power from a 405 nm laser chopped at 100 Hz and 180 K at different voltages. Drain-source bias is 1 V. (b) Red: Transfer curve under 1 V drain-source bias at 200 K. Blue: responsivity of the device under different gate voltages calculated with the power received by the device at 100 Hz and 180 K. The inset is an optical image of the device. (c) Band diagram of the device at the equilibrium with Schottky barrier at the interfaces resulting from Fermi levels alignment. (d) The corresponding band diagram with the laser illumination under $V_{DS} = 0$ V and $V_{GS} = 0$ V. (e) Band diagram of the device under illumination when applying a positive V_{DS} in the Off state of the transistor. (f) Band diagram of the device under illumination when applying a positive V_{DS} in the On state of the transistor.*

efficiently allows the reduction of Schottky barrier height at metal-SC interfaces with the applied gate as shown in the previous section. Indeed, the quasi-symmetric non-linear behavior IV curves in Fig.3.5 (b) are typical for contacts with a Schottky barrier at the interfaces. The work functions of $MoSe_2$ ~ 4.7 eV is slightly higher than that of Ti (Φ_{Ti} = 4.3 eV) [Pan16]. When the two materials are brought into contact, the work function of the SC being higher than that of metal, electrons move from metal to semiconductor. The system evolves until the Fermi levels are aligned. It appears in the SC an accumulation area, this results in a downward curvature of the valence and conduction bands, thus a formation of an energy barrier at the metal-SC interfaces, see Fig.3.11 (c). Under illumination, photogenerated carriers are created in $MoSe_2$ (electrons in the conduction band and holes in the valence band). Applying a positive drain-source bias leads to the extraction of those carriers at the electrodes, thus a photocurrent in the device. Using the gate to bring the system in the Off state as shown

in Fig.3.11 (e) leads to enhance the Schottky barrier at the interfaces and by the way the reduction of the photocurrent. However, increasing the gate bias in the On state leads to the reduction of the height of this barrier (see Fig.3.11 (f)), then efficient photogenerated carriers extraction with high photocurrent and responsivity.

In our system, the increase of the responsivity is not as fast as the one of the dark current. As

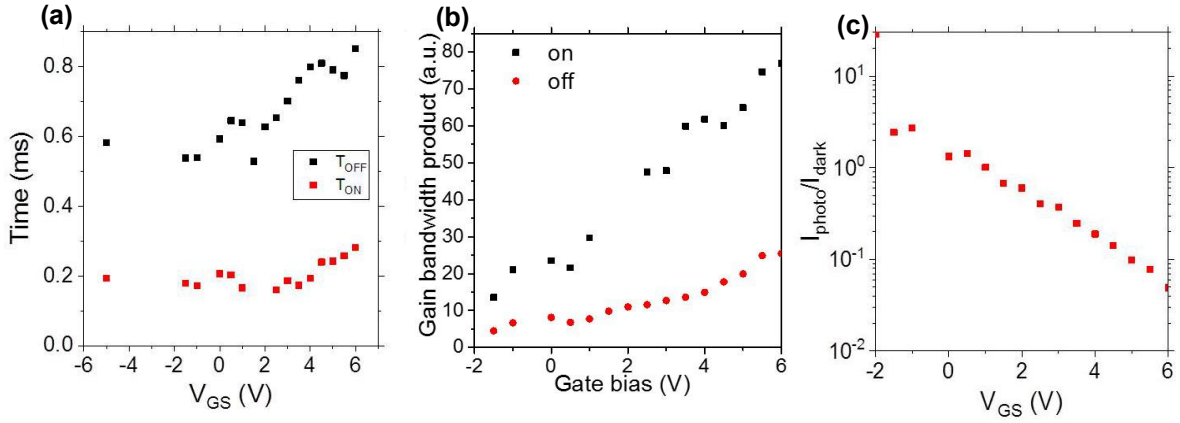

Figure 3.12 *– (a) Rise and fall times extracted from photocurrent curves using a single exponential fit at different gate voltages (b) Photoresponse gain bandwidth product as a function of the applied gate bias. (c) Photocurrent over dark current at 100 Hz and 180 K for different gate voltages under 1 V drain-source bias.*

a result, the gate bias which maximizes the signal-to-noise ratio is obtained under hole injection (Figure 3.12 (c)). This regime corresponds to the one which minimizes the dark current. Rise and fall times (t_{ON} and t_{OFF} in Fig. 3.12 (a) respectively) extracted from the photocurrent characteristics under negative gate bias are close to 200 and 600 μs, respectively. This is two orders of magnitude faster than time responses previously reported on usual exfoliated and chemical vapor deposited (CVD) $MoSe_2$ [Abderrahmane14, Jung15, Dai19, Xia14], 50 times faster than encapsulated MoS_2 devices [Kufer16a], and more than one decade shorter than the fastest $MoSe_2$ phototransistor reported so far [Lee18].

Another very striking feature comes from the very weak gate dependence of the time response with gate bias (Fig. 3.12 (a)). The on and off times change by less than 30 % from the hole injection to the electron injection regimes. This is remarkable since the gain bandwidth product (which can be seen as the ratio of responsivity divided by the characteristic time constant) is actually increasing with the applied gate as shown in Fig. 3.12 (b). This result contrasts with what was observed in the previous chapter section 2.4 for the phototransistor based on nanocrystal film, where the change of responsivity is made at quasiconstant gain bandwidth product [Lhuillier14]. In other words, a higher photoresponse comes at the prize of a slower response, on the contrary to our device. Indeed, the increase of the responsivity with the gate bias is the signature of gain. The ratio of the recombination time τ over the transit time t_{tr} increases with the applied gate bias. At first order, the transit time $t_{tr} = \frac{L^2}{\mu V_{DS}}$ with L being the channel length and μ the mobility being barely affected by the gate bias. The increase of the gain is mostly due to a longer living time for the photocarrier. Due to the n-type nature of the sample, a negative gate bias brings the Fermi Level close to the middle

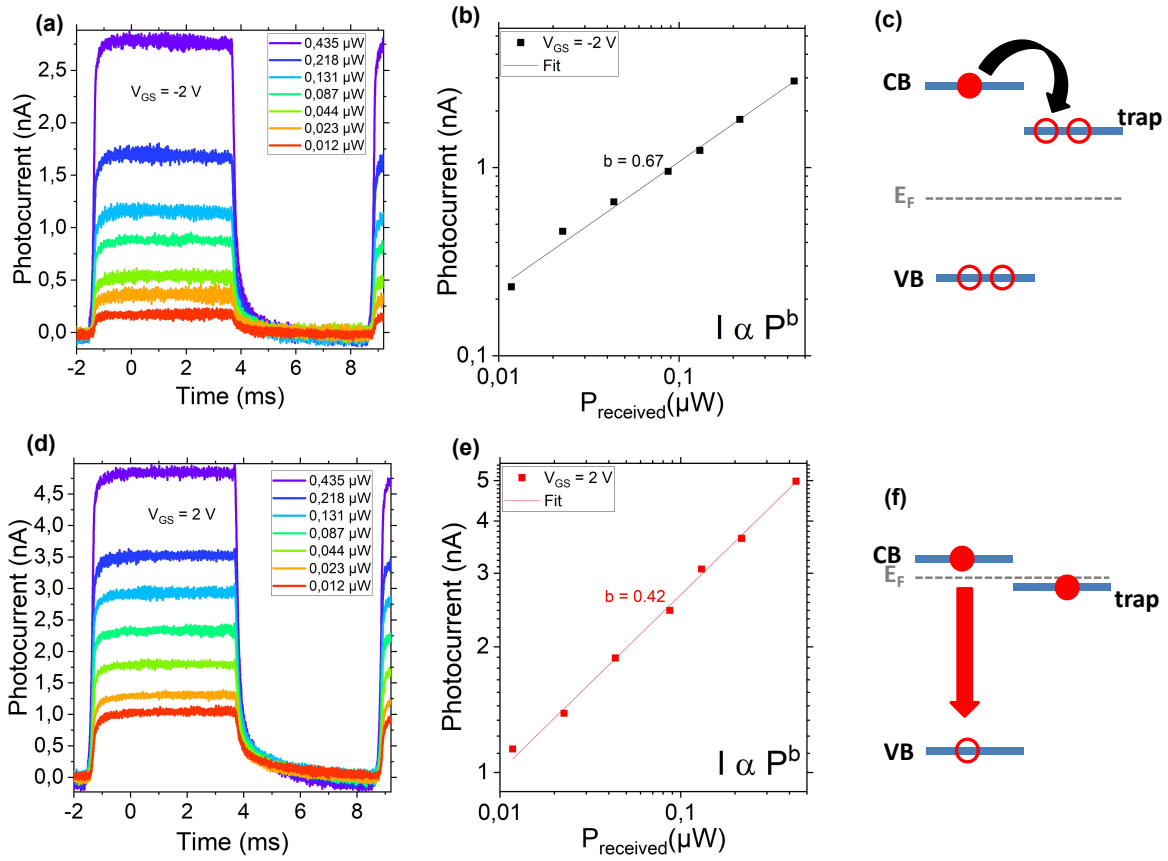

Figure 3.13 *– (a) Photocurrent at 100 Hz and 180 K for different incident power (from 0.012 µW to 0.435 µW) under -2 V of gate bias. (b) Power dependency of the photocurrent at 100 Hz and 180 K under -2 V of gate voltage with the power law fit of the data point. (c) Scheme of the associated relaxation mechanism for the monomolecular process. (d) Photocurrent at 100 Hz and 180 K for different incident power (from 0.012 µW to 0.435 µW) under 2 V of gate bias. (e) Power dependency of the photocurrent at 100 Hz and 180 K under 2 V of gate voltage with the power law fit of the data point. (f) Scheme of the associated relaxation mechanism for the bimolecular process.*

of the gap (Fig. 3.13 (c)), and the later behaves as a recombination center. When the gate bias is increased, the Fermi level is moved closer to the conduction band (Fig. 3.13 (f)) and the recombination centers get filled with electron [Kufer16a]. Thus, only band-to-band recombination becomes possible, and the photocarrier lifetime is extended. The fact that the time response of the detector is only poorly affected by the filling with the gate of these trap states suggests that only shallow traps with shorter lifetimes close to the conduction band are involved because the implication of deeper traps will have led to longer release time and thus slower time response. To confirm the hypothesis that the photoresponse is limited by recombination, we used the power dependence of the photocurrent. We have measured the photocurrent-power dependency in the interesting region for the photodetection where the signal to noise ratio (I_{ph}/I_{dark}) is maximal, see Fig.3.12 (c). For both hole and electron regime, the photoresponse rises with the increase of the light power (see Fig.3.13 (a,d)), this because the number of exciton increases with the incident power.

Under hole injection (V_{GS} = -2 V) the current as a function of incident power follows a

power law with an exponent of 0.67, see Fig.3.13 (b). This value is typically intermediate between the value of 1/2 expected for a bimolecular process and the value of 1 obtained for a monomolecular process or first order dynamic (i.e., for trapping), thus indicating that the recombination kinetic of photocarriers involves both trap states and band to band recombination [Willis09, Rose63]. So, by applying a negative gate bias, the Fermi level is brought more deeply in the bandgap where the recombination centers get unfilled and can act as trap states by changing their state under illumination, which explain the increase of the power law exponent. Fig.3.13 (c) sketches the associated mechanism behind the power dependence. On the other hand, under electron injection (V_{GS} = 2 V) we observe a decrease of the exponent value reaching 0.42 (Fig.3.13 (d)), which is quite close to the value of 1/2 expected for a bimolecular process or second order dynamics (i.e., recombination occurs through electron-hole recombination). As illustrated in Fig.3.13 (f), applying a positive gate moves the Fermi level closer to the conduction band and completely fills shallow trap states, thanks to high doping capability of ionic glass LaF_3. Thus, under illumination, direct band to band recombination occurs from electrons in the conduction band and holes in the valence band.

3.4 Conclusion

We have explored the potential of LaF_3 ionic glass to build a TMDC-based FET and phototransistor with low operating bias and preserving gate tunability down to 160 K. Optimal operating temperature is around 200 K and limits the leakage through the substrate while preserving a strong ionic mobility, with I_{ON}/I_{OFF} ratio exceeding four decades.

We have presented the detail investigation of the Schottky junction in monolayer WSe_2 FETs in high doping regime using ionic glass LaF_3 gating. Contrary to previous studies using only one Schottky barrier in their model, we presented a complete study of Ti/WSe_2 Schottky interfaces using a back-to-back Schottky diode model from the thermionic emission theory taking into account the Schottky barrier of each junction. This allowed to investigate the gate effect of each junction. Ionic glass by inducing high doping in the WSe_2 channel, reduces the band bending at each Ti/WSe_2 interface. we observed an exponential decrease of the total series resistances when increasing the gate voltage which is the signature the decrease of contact resistances for efficient carrier extractions. Furthermore, we probed the photoresponse of $MoSe_2$ phototransistor on LaF_3. Not only the dark conductance can be tuned by the gate, but also the photoresponse with time responses down to 200 μs, up to two decades faster than state of the art $MoSe_2$ phototransistors reported so far. Careful analysis of photocurrent properties reveals that the relative contribution of traps on the carrier recombination can be dramatically suppressed thanks to the very high accumulated carrier concentration achieved by ion glass gating. Remarkably, this novel functionality allows for modulating the device photoresponse by more than two orders of magnitude, while at the same time increasing its gain bandwidth product.

This study shows that ionic glass gate is a complementary method to the usual electrolyte gate technique to reach the high doping regime, as it enables optical experiments in high doping regime that are not possible when the 2D material is buried into the electrolyte gate and elec-

trostatic tunability at lower temperature. The performances of our ionic glass photodetector demonstrate the potential of this method to explore novel photoconduction processes and alternative architectures of devices.

Chapter 4

2D-0D Graphene/HgTe heterostructure in high doping regime for IR detection

The large capacitance and the direct optical adressability of LaF_3 solid-state gating allowed in the previous chapter to study transport and phototransport properties of HgTe nanocrystals and few layer $MoSe_2$ in high doping regime with metallic electrodes in FET geometries. With metallic electrodes, the gate dependence of the photocurrent follows the gate-induced change of the dark current. In this chapter, we used other properties of graphene such as its vertical electric field transparency and carrier selectivity under gate to build graphene/HgTe heterostructure. The introduction of graphene electrodes combined with ionic glass enables to reconfigure selectively the HgTe nanocrystals and the graphene electrodes between electron-doped (n) and hole-doped (p) states. We analyze the impact of unusual electrostatic profile on the performances of our 2D-0D phototransistor. Thus, we demonstrate a 2D/0D p-n junction that expands throughout the device, with a built-in electric field that assists charge dissociation allowing to improve the signal-to-noise ratio for infrared photodetection by 2 orders magnitude.

Related article

- U. N. Noumbé, C. Gréboval, C. Livache, A. Chu, H. Majjad, L. E. P. Lopez, L. D. N. Mouafo, B. Doudin, S. Berciaud, J. Chaste, A. Ouerghi, E. Lhuillier, J.-F. Dayen. *Reconfigurable 2D/0D p-n Graphene/HgTe Nanocrystal Heterostructure for Infrared Detection*, ACS Nano 2020, 14, 4, 4567-4576

In this project, I designed and processed samples (graphene Hall bar and graphene electrodes

on LaF_3 substrates) at IPCMS and Charlie Gréboval synthesized HgTe NCs at INSP. During an additional measurement campaign at INSP we performed the optoelectronic measurements detailed in this chapter.

As I mentioned in the chapter 1 section 1.3, the coupling of NCs with graphene has already been done taking advantages of high carrier mobilities of graphene and strong tunable light absorption of quantum dots [Konstantatos12]. In those geometries the high carrier mobility of graphene allowed the charge transport to occur only into the graphene, whereas nanocrystals are used as a light sensitizer that traps one type of carrier and injects the other type of carrier into graphene. During the long lifetime of the trapped carriers in QDs, the transferred carrier will circulate many times in graphene and will contribute several times for the photocurrent, signature of the presence of the gain mechanism. This leads to devices with very high responsivities but at the price of dramatically slow time response. Here, in the continuity of our fruitfull collaboration with Emmanuel Lhuillier's team, we propose with Charlie Gréboval a change of paradigm compared to previous 2D/0D photodetectors: we show that for 2D/0D devices, charge transport should involve the nanocrystal film to absorb more strongly the incident light. This requires firstly to make the conduction within the nanocrystal array more efficient using a ligand exchange step to get high carrier mobility and secondly the gate tunable electronic properties of graphene electrodes combined with high capacitance ionic glass gating technology that enables high carrier density to be reached and the doping profile to be spatially tuned through the whole 2D/0D heterostructure and then induces the p-n junction directly into the nanocrystal thin film.

4.1 Device fabrication and characterization

On the top of the LaF_3 substrate, chemical vapor deposition (CVD) monolayer graphene is grown (done by Grapheal and Graphenea following fabrication process detailed in ref [Han14]) and processed using laser lithography (μPG 101) and reactive ion etching (Oxford Instrument RIE) to process two samples: one with interdigitated graphene electrodes and the orther with a graphene Hall bar. The substrates were first cleaned with acetone and rinsed with ethanol and isopropanol. AZ 1505 positive resist was then spin-coated and baked at 105 °C. The well-defined area on the substrates was exposed under a UV laser. The exposed resist was developed using a bath of AZ 726 for 20 s, before being rinsed in DI water. We then used the mixture of argon and oxygen plasmas (RIE) to etch the exposed area during 15 s before cleaning samples during 1 min in acetone, rinsed using isopropanol and dried by a nitrogen jet gas. The sketch illustrated in Fig.4.1 left (1-6) summarizes those process steps. After the etching step, a shadow mask evaporation is finally used to contact graphene pads of the interdigits with Ti(10 nm)/Au(40 nm) whereas for graphene Hall bar another laser lithography is performed (Fig.4.1 left 1-4), followed with metal deposition and lift-off in acetone. Microscopy images of grahene Hall bar and graphene interdigitated electrodes on LaF_3 substrates are shown in Fig.4.1 (b) and (c) respectively.

Abdelkarim Ouerghi and Julien Chaste (researchers, C2N Paris-Saclay) did Raman map and spectra to check whether graphene is well echted. Indeed, the 2D mode which is a resonant Raman process involving phonons at the edges of the BZ (K and K' points), is used as an unambiguous fingerprint of the presence of graphene and allows mapping of the interdigitated pattern (Fig.4.1 (d,e)). The full width at half-maximum of 46 cm^{-1} (Fig.4.1 (d)), a value

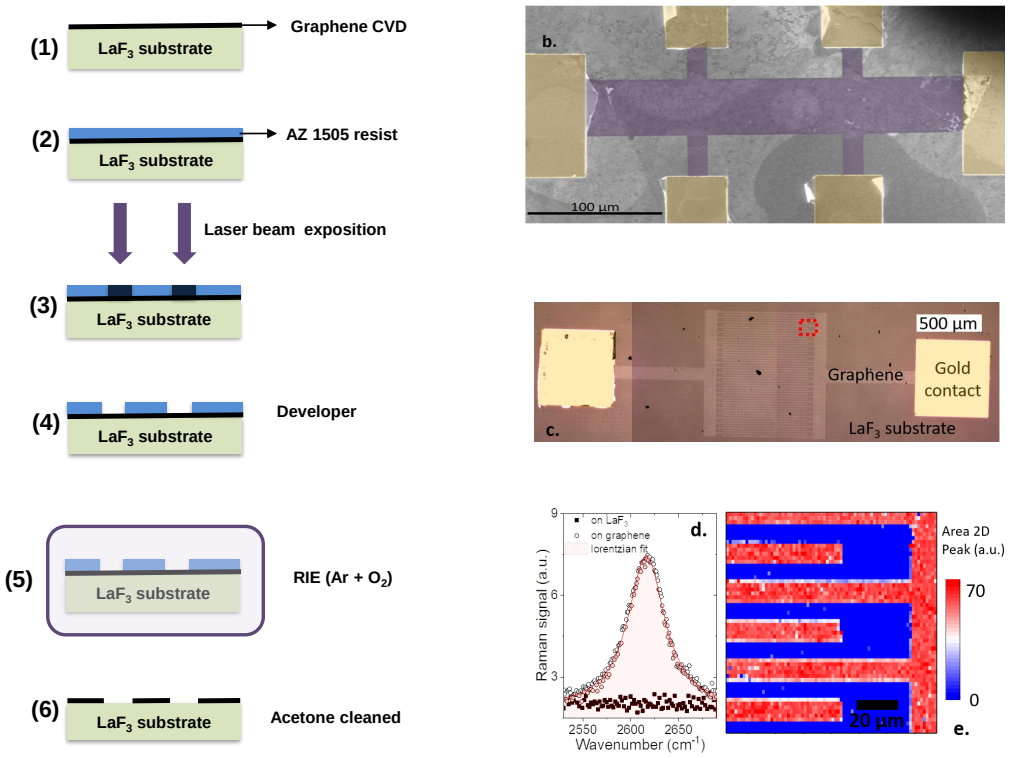

Figure 4.1 *– Left: Schematic diagram of fabrication process of interdigitized graphene on LaF_3: laser lithography and reative ion etching. Right: (b) Microscopy image of the graphene Hall bar on LaF_3. (c) Microscopy image of the graphene interdigitated electrode on a LaF_3 substrate. The area in the red square is mapped using Raman in part (e). (d) Raman spectra of the graphene electrode on LaF_3. (e) Map of the intensity of the 2D Raman peak (2560 cm^{-1}) in the area of the graphene interdigitated electrodes. Raman measurements have been done at C2N by Abdelkarim Ouerghi.*

somewhat larger than that in mechanically exfoliated monolayers on silicon oxide, suggesting [Berciaud09] a contribution from nanoscale strain variations [Neumann15] arising from the transfer process onto the LaF_3 substrate. Spatial mapping of the 2D peak is fully consistent with the targeted pattern (Fig.4.1 (e)), confirming that graphene is fully etched between the digits.

4.2 Electric characterization of the devices

Before building the graphene/HgTe heterostructure, we study the transport properties of graphene and HgTe NCs independently over LaF_3 gate to account for possible charge transfer between the material and the substrate.

Using four probe measurements at 240 K, the transfer curve of the graphene Hall bar reveals an ambipolar behavior with minimum of conductance at the Dirac point reached for a negative gate bias of V_D=V_{GS}=-4.2 V which is a signature of electron doped-graphene, see Fig.4.2 (e). This suggests a partial electron transfer from the LaF_3 to the graphene which displaces the Fermi level above the Dirac point of graphene. From the gate bias associated with the

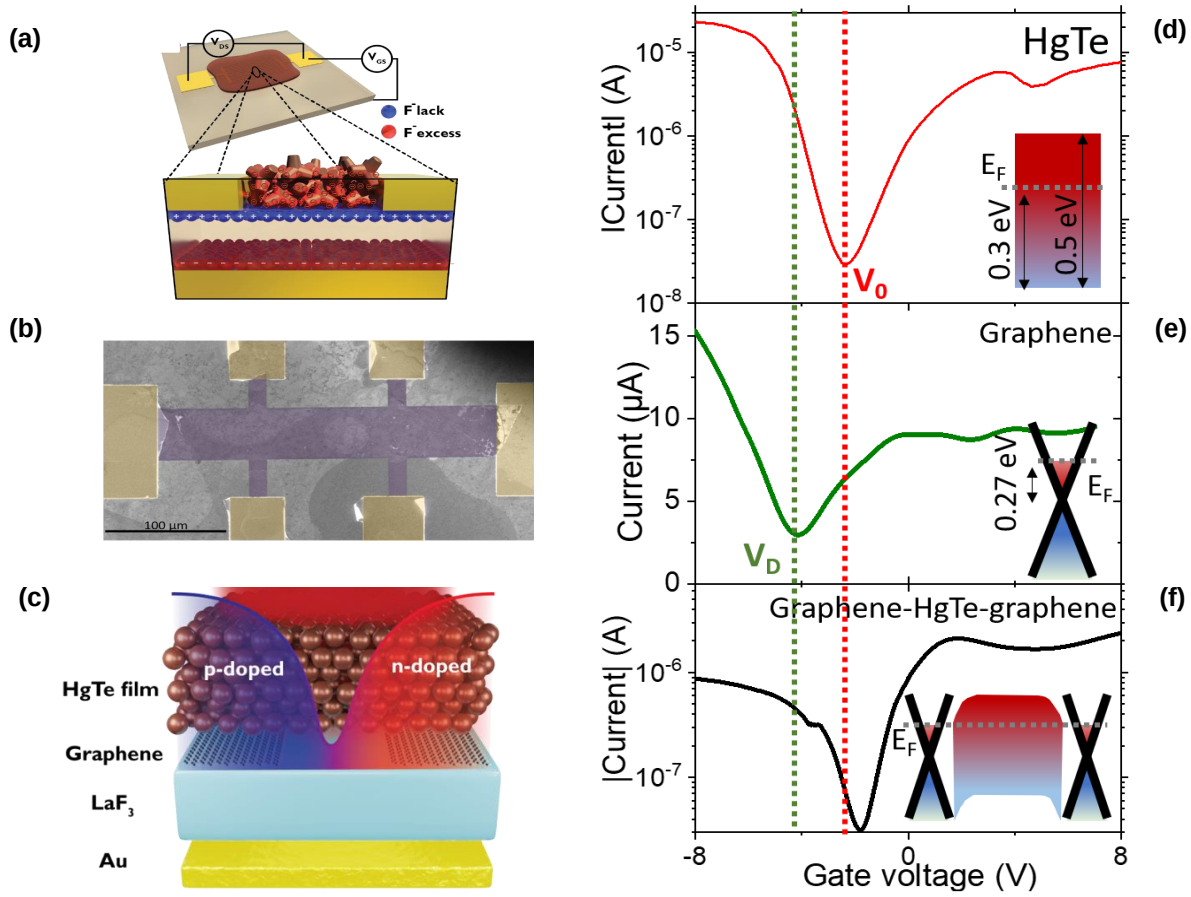

Figure 4.2 – *(a) Scheme of a HgTe back-gate field-effect transistor with gold electrode on LaF_3 ionic glass when $V_{GS} > 0$. (b) Microscopy image of the graphene Hall bar on LaF_3. (c) Scheme of the field effect transistor under consideration where the gate is made of a LaF_3 ionic substrate, the drain and source electrodes are made of interdigitated graphene electrodes, and the channel is made of HgTe NC arrays. (d) Transfer curve (drain current as a function of gate bias) for a HgTe NC array on LaF_3 substrate and connected to a gold electrode at 220 K. The inset is a scheme of the pristine HgTe electronic structure. (e) Transfer curve for a graphene Hall bar on a LaF_3 substrate at 240 K. The inset is a scheme of the pristine graphene electronic structure. (f) Transfer curve for a HgTe NC array on a LaF_3 substrate and connected to a graphene electrode at 220 K. Scheme of the electronic structure of a graphene/HgTe/graphene junction assuming that Fermi level is 0.27 eV above the Dirac point.*

Dirac point, we can determine the relative position of the Fermi level with respect to the Dirac point due to the relation [Yu09] $E_F = \frac{h v_F}{2\pi}\sqrt{\frac{\pi C_{LaF_3}}{e}(V_{GS} - V_D)} = 0.27$ eV at zero gate bias, where h is the Planck's constant, v_F the Fermi velocity [Trevisanutto08] $\approx 10^6$ m/s, $C_{LaF_3} = 0.4\ \mu$F.cm^{-2} and e the elementary charge.

As already studied in chapter 2, n-doped HgTe NCs device with metallic gold electrodes presents a clear ambipolar behavior, with a charge neutrality point (V_0) appearing under negative gate bias at -2.3 V (see Fig.4.2 (d)). However, after depositing 120 nm thick film of HgTe NCs on graphene electrodes (a scheme of the device is given in Fig.4.2 (c)), the transfer curve of the graphene-HgTe-graphene heterojunctions demonstrates a preserved ambipolar behavior, but with a charge neutrality point at V_{GS} = -1.8 V $\approx V_0$ (Fig.4.2(f)). A value very close to that of HgTe film contacted by gold electrodes. The switching of the graphene elec-

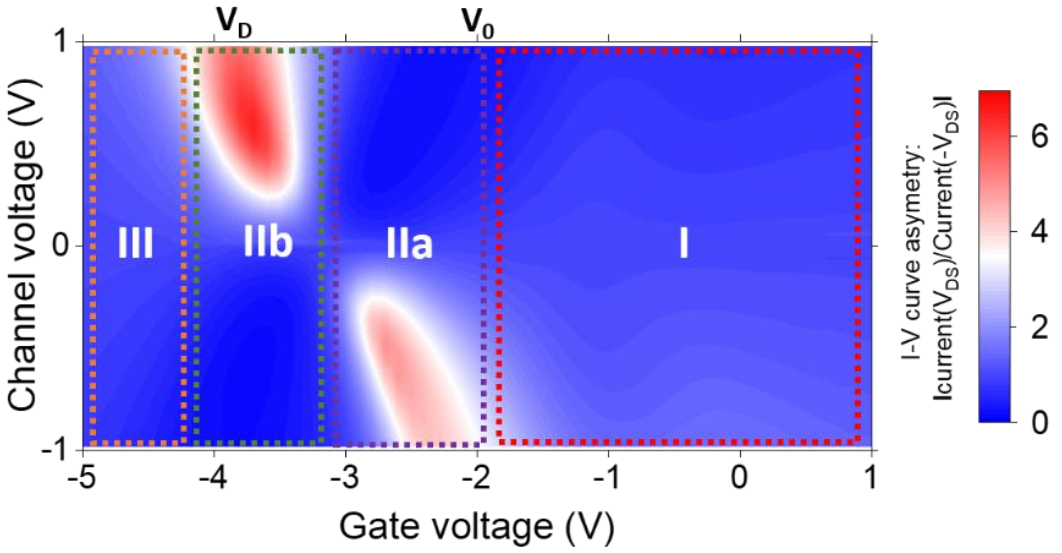

Figure 4.3 *– 2D color map of the asymmetry of the I-V curve at 240 K, quantized through the ratio of the current under a given bias and the current under the opposite bias, as a function of the channel voltage between the source and drain electrodes and gate voltage V_{GS}. The regions in red correspond to the domains of p-n junction within the graphene/HgTe/graphene junction.*

trode doping state is reflected in the transconductance curve by an inflection of the transfer curve at the Dirac point V_{GS} = -3.6 V ≈ V_D in the figure 4.2 (f).

From these transconductance measurements, we can describe the band alignment in the

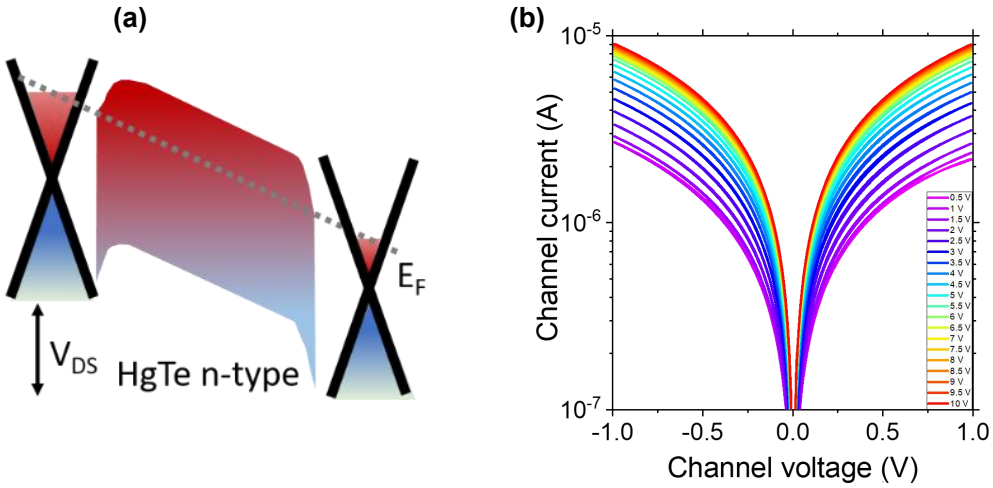

Figure 4.4 *– Zone I: $V_{GS} > V_0$, regime n-n'-n. (a) Band alignment of the graphene/HgTe/ graphene junction in the n-n'-n configuration. (b) The associated quasi-ohmic I-V curves at different gate voltages at 240 K.*

graphene-HgTe-graphene junction. Indeed, both materials appear to be n-doped in the absence of a gate: the Fermi level lies above the Dirac point in graphene and in the upper part of the semiconductor nanocrystals at V_{GS} = 0 V. Moreover the work function of HgTe NCs (≈ 4.6 eV) [Jagtap18] is higher than our n-doped graphene estimated to be ≈ 4.3 eV [Yu09]. Therefore, when the two materials are in contact, electrons move from graphene to NCs resulting in

a downward curvature at graphene-HgTe interfaces with the Fermi energy level alignment at the equilibrium (see the inset in Fig.4.2 (f)). In such a junction, the key difference with metallic contacts comes from the gate-tunable nature of the graphene doping level and its electric field transparency. The gate will tune the position of the Fermi level not only within the HgTe film but also within the graphene electrodes. This enables the formation of electron and hole extracting layers. We investigate in detail the graphene-HgTe-graphene current-voltage (I-V) characteristic dependence on ionic glass gate voltage V_{GS}. To do so, we report in Fig. 4.3 the charge transport phase diagram of the 2D/0D device. It emphasizes on the evolution of the asymmetry of the source-drain I-V curve (ratio of current at $+V_{DS}$ bias over current under $-V_{DS}$ bias) under the back-gate voltage V_{GS}. Three different zones corresponding to distinct doping states of the graphene/HgTe heterojunctions can be discriminated:

(i) For gate bias $V_{GS} > V_0$ (zone I), exceeding the HgTe film charge neutrality point V_0 and V_D , the Fermi level remains above the Dirac point for both electrodes, whereas the HgTe NC film remains in the electron doping state, forming n-n' junctions at the graphene/HgTe NC interfaces. Under such a condition, we observe a symmetric quasi-ohmic I-V behavior; see Fig. 4.4 (b).

(ii) When the gate bias is in the range of $V_0 > V_{GS} > V_D$ (zone II), the I-V curve acquires

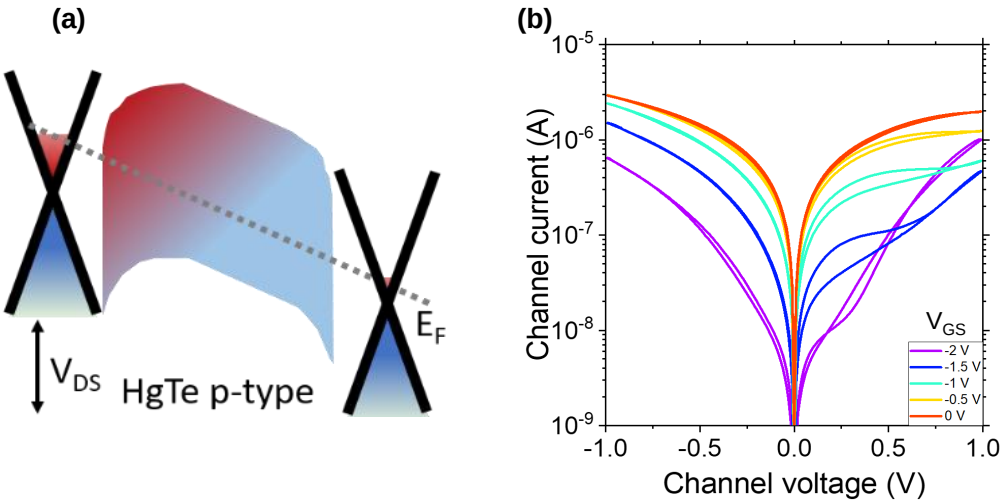

***Figure 4.5** – Zone IIa: $V_{GS} \approx V_0$, regime n-n'-p'-n (a) Band alignment of the graphene/HgTe/graphene junction in the n-n'-p'-n configuration. (b) The associated rectifying I-V curves at different gate voltages at 240 K.*

a rectifying behavior as shown in figures 4.5 (b) and 4.6 (b). The high value of the current asymmetry in Fig. 4.3 (clearly above 1) highlights the areas of occurrence (red part) of p-n junctions, with two distinct heterojunction configurations that can be discriminated. It is worth noticing that, because of the large capacitance of the LaF_3 substrate, applying moderate drain-source bias may lead to distinct vertical gate bias conditions near the source and the drain electrodes. For gate bias voltages close to charge neutrality points of HgTe or graphene, this induces electron and hole doping in the vicinity of each electrode.

A first p junction state appears when V_{GS} gets closer to V_0 (zone IIa; see Fig. 4.3); this cor-

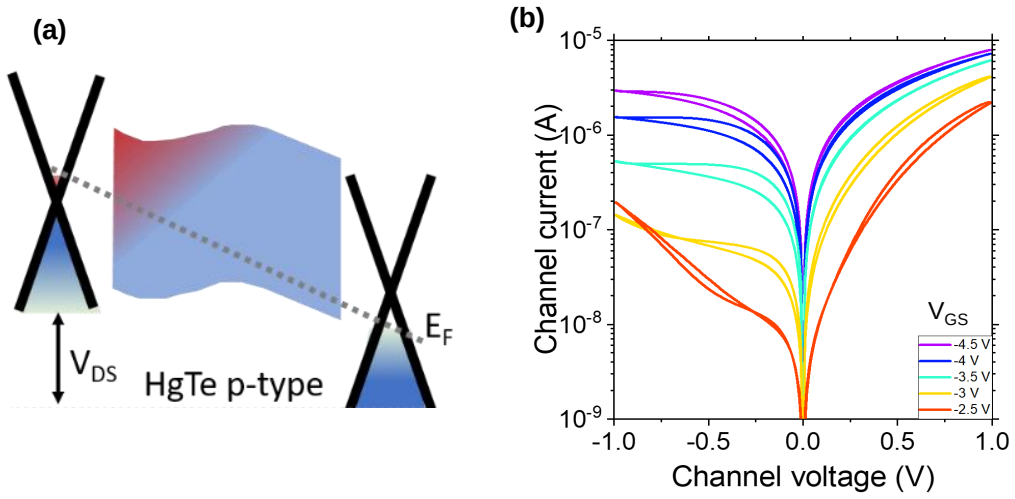

Figure 4.6 *– Zone IIb: $V_{GS} \approx V_D$, regime n-p'-p (a) Band alignment of the graphene/HgTe/ graphene junction in the n-p'-p configuration. (b) The associated rectifying I-V curves at different gate voltages at 240 K*

responds to p-n junction formation between electron-doped graphene electrodes and hole-doped HgTe NC arrays, forming two back-to-back p-n junctions. A strong current asymmetry appears while increasing V_{DS} amplitude (with value of the asymmetry clearly above 1 in the red area of the graph), highlighting the formation of a p-n junction expanding throughout the HgTe film. Indeed, in the case of an ambipolar semiconducting HgTe NC array, for gate bias below but close to the charge neutrality point $V_{GS} < V_0 \approx$ -2 V, applying a negative V_{DS} voltage on the drain electrode results in switching back the HgTe doping state from the p-doped to n-doped state. This creates a p-n junction within the HgTe thin film, with a p-doped state at the source side and n-doped state at the drain side. The second p-n junction state (zone IIb) is triggered once V_{GS} is decreased to V_D. There, applying source-drain bias voltage results in Fermi level positioning on different sides of the Dirac point for the drain and source graphene electrodes (see band diagram in Fig. 4.6 (a)). One electrode gets electron-rich, whereas the other is hole-rich, resulting in the n-p diode on the drain side.

The observation of the p-n junction is made possible by the combination of the high capacitance gate from the LaF_3, the tunable charge carrier polarities of graphene and HgTe NC arrays, both the low density of state and the low electric screening of graphene. Electric charge density Δq at the graphene/LaF_3 interface of the source (drain) electrode is defined as $\Delta q = C_{TOT} V_{GS}$ ($\Delta q = C_{TOT} V_{DS}$). The total capacitance is defined as $1/C_{TOT} = 1/C_{LaF_3} + 1/C_Q$, $C_{LaF_3} = 0.4\ \mu$F.cm^{-2} and C_Q being the quantum capacitance. The quantum capacitance C_Q captures the band filling of graphene that results from its low density of states and can be approximated by $C_Q \approx e^2 D(E_F)$, with e being the electron charge and $D(E_F)$ being the graphene density of states at the Fermi energy [Xia09a, Das08, Luryi88]. Experimental studies estimated C_Q within 3 to 10 μF.cm^{-2} , depending on the graphene doping level. Given these orders of magnitude for the capacitances, approximately 90% of the charge induced by the

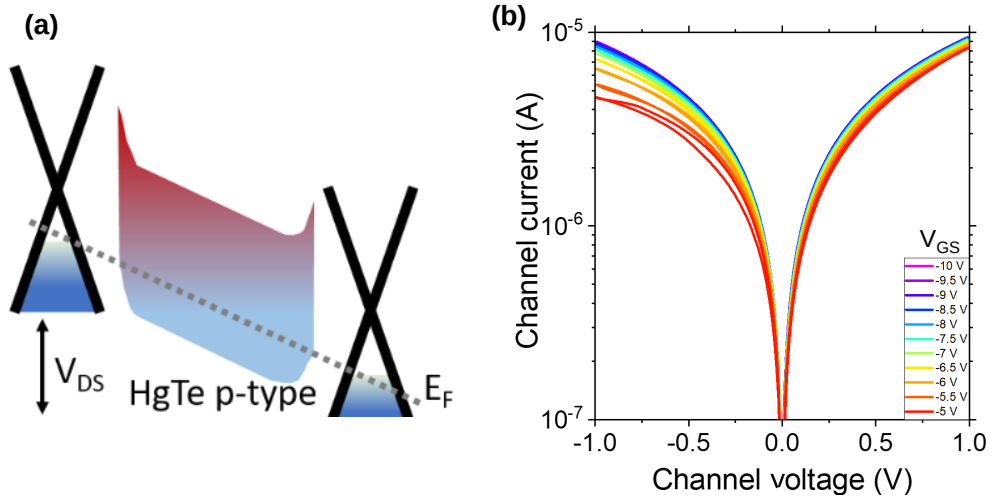

Figure 4.7 *– Zone III: $V_{GS} < V_D$, regime p-p'-p (a) Band alignment of the graphene/HgTe/ graphene junction in the p-p'-p configuration. (b) The associated quasi-ohmic I-V curves at different gate voltages at 240 K*

ionic substrate are present on the top of the graphene, whereas no charge will be present in the case of metal electrodes. This low screening propagates the spatial extension of the p-n junction above the electrodes. **Graphene thus plays a dual role: it allows carrier selectivity which first enables the formation of the p-n junction, and it also favors the spatial extension of the junction, leading to a higher volume of the HgTe film exposed to the gate-induced electric field.**

(iii) Finally, under large hole injection, when $V_D > V_{GS}$ (zone III), the two graphene electrodes and the HgTe film become hole-rich, then forming p-p' junctions and the I-V curve recovers their quasi-ohmic behavior as shown in Fig. 4.7. Now that we have revealed the interesting operating region in our device where a 2D/0D p-n junction can be formed, in the following section, we will study optoelectronic properties of the p-n junction.

4.3 Optoelectronic properties of graphene/HgTe p-n junction

4.3.1 Photoresponse of the graphene/HgTe/graphene junction.

We probe in Fig. 4.8 (b) the photocurrent in the graphene-HgTe-graphene junction when illuminating the device by a short-wave infrared laser at 1.55 μm (i.e. above the band edge of the HgTe NCs) chopped at 1 kHz. We used the same experimental setup as in section 2.4 at INSP.

The curve presents a well-defined maximum of photocurrent in the range of gate bias corresponding to the existence of p-n junction formation (can also be seen in the absorption spectrum Fig. 4.9 (c) with a high photocurrent amplitude in p-n region). This is a signature of a large electric field that appears at the interface between the hole- and electron-rich areas responsible for the enhancement of charge dissociation (same as region II, introduced previously in Fig. 4.3). This behavior dramatically differs from the one observed for the HgTe film, with LaF_3 gating but using gold metallic electrodes instead of graphene (Fig. 4.8 (a)). In this

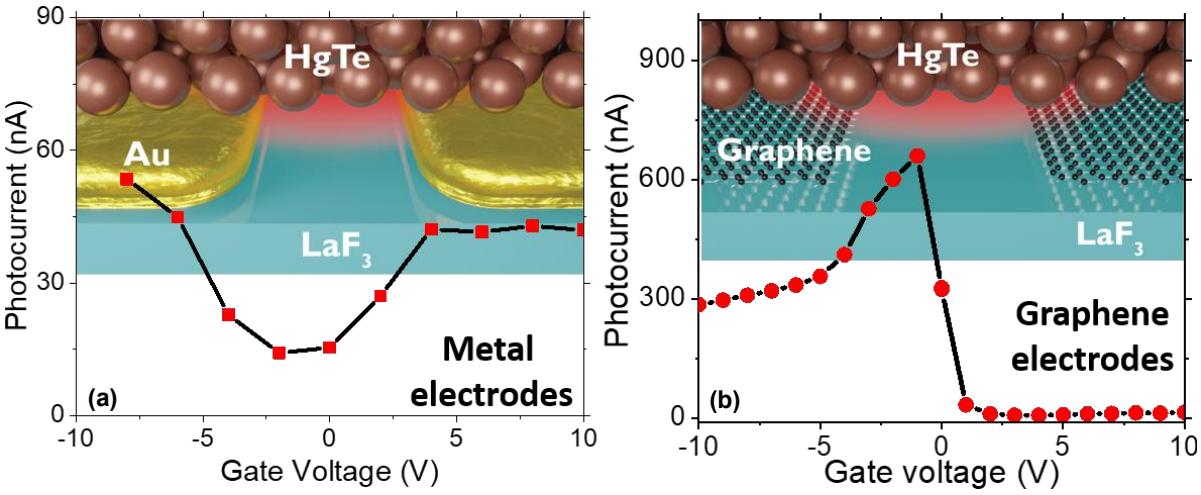

Figure 4.8 *– (a) Photocurrent as a function of gate bias for the gold/HgTe/gold junction under 0.5 V drain-source bias at 200 K. The top part is a scheme of the device. (b) Photocurrent as a function of gate bias for the graphene/HgTe/graphene junction under 0.5 V drain-source bias at 220 K. The top part is a scheme of the device.*

case, the photocurrent is minimal at the minimum of conductance of HgTe. Conventional phototransistors actually display this kind of behavior, where photocurrent follows the dark current. In other words, in conventional phototransistors with metallic electrodes, applying gate bias enhances the photocurrent but barely improves the signal-to-noise ratio. This has been observed for many nanocrystals including CdSe [Lhuillier14] and HgTe on various dielectrics [Chen19] and electrolytic gates [Livache17]. Combining graphene electrodes together with a high capacitance gate substrate allow us to overcome this limitation. There is a gate bias window extremely promising for photodetection where the photoresponse is maximized while the dark current is minimized, promoted by the formation of the p-n junction through the 2D/0D heterostructure.

We notice that the photoresponse is much higher under negative gate bias, that is, under hole injection, compared to the value obtained under electron injection conditions (Fig. 4.9 (c)). This actually results from the initial n-type nature of the HgTe. By injecting holes in the material, it gets more intrinsic, which reduces the recombination pathway for the minority carriers and thus extend their lifetime, leading to a larger photoconductive gain.

The photovoltaic operation mode of the p-n junction, a signature of the extension of the p-n junction into the NC arrays, is further confirmed by the investigation of the photocurrent under zero applied electric field. Under positive gate bias, where no p-n junction exists, there is no photocurrent under zero drain-source bias (Figure 4.9 (a)). Once the gate bias is applied within the window enabling the p-n junction formation, we observe a clear photosignal even in the absence of an applied bias, which is the signature of a built-in electric field. The magnitude of the photocurrent modulation at 1 kHz under zero drain-source bias is given in Fig. 4.9 (b) and follows pretty well the data obtained under DC conditions in Fig. 4.8 (b).

Although the magnitude of the photocurrent spectrum also follows the same trend with a

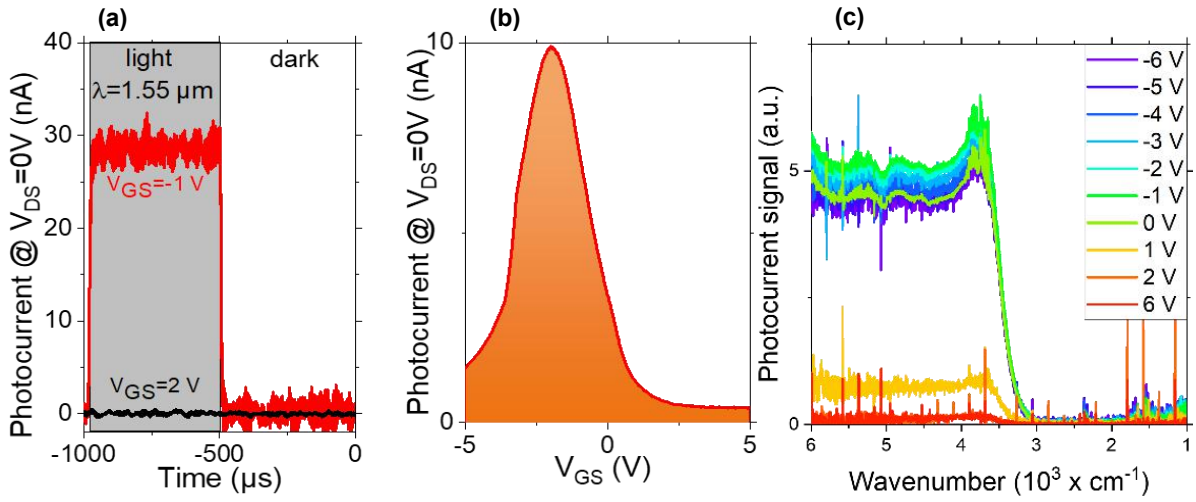

Figure 4.9 *– (a) Photocurrent under 0 V drain-source bias as the light ($\lambda = 1.55\mu m$) is turned on and off for two values of the gate bias. (b) Photocurrent under 0 V, where the light is chopped at 1 kHz, as a function of the gate bias. (c) Photocurrent spectra taken at different gate voltages from -6 to 6 V under 0.5 V drain-source bias at 220 K from FTIR spectroscopy.*

gate bias, the shape of the spectral response remains unchanged for all gate biases (Fig. 4.9 (c)). In particular, it is worth noticing that, in spite of the large gate electric field associated with LaF_3, no bleach of the band edge transition is observed [Liu12]. The p-n junction is formed while the electron and hole carrier densities are kept well below 1 carrier per dot, which is critical to avoid any excessive increase of the dark current. More qualitatively, we can estimate the carrier density in the n and p area under 1 V of drain-source bias, assuming a balanced p-n junction. The sheet charge density induced by the gate is given by $C_{LaF_3} V_{DS}/2e$, which corresponds to $1.25\text{x}10^{12}$ carriers.cm^{-2}. If we assume the density is spread over the whole film thickness, this corresponds to a volume density of $1\text{x}10^{17}$ carriers.cm^{-3}. We can estimate that the particle density is $2.4\text{x}10^{18}$ nanocrystals.cm^{-3}, assuming a spherical shape for HgTe with a radius of 4 nm and a random close packing (film density of 0.64). This means that the average gate-induced doping density is $4\text{x}10^{-2}$ carrier per nanocrystal. This is far below 1 as expected from the photocurrent spectrum.

4.3.2 Photodetection performances of the graphene/HgTe/graphene junction.

In this section, we investigate the potential of this gate-induced p-n junction for infrared photodetection. Under moderate excitation power (i.e irradiance of 133 μW.cm^{-2} corresponding to ≈ 1 μW of incident light on the sample), the responsivity reaches 6 mA.W^{-1} under negative gate bias (Fig. 4.10 (a)). The noise in the p-n junction appears to be 1/f limited, as commonly observed for the NC array [Liu14, Lai14] (Fig. 4.10 (c)). As shown in Fig. 4.10 (d), the detectivity clearly presents a maximum $1.2\text{x}10^9$ Jones for the gate bias where the p-n junction is formed. This is typically 2 orders of magnitude larger than the value obtained for the same film in the absence of a p-n junction, but remains 1 order of magnitude weaker than the best value reported for HgTe-based nanocrystals in vertical geometry [Tang19a, Tang18]. How-

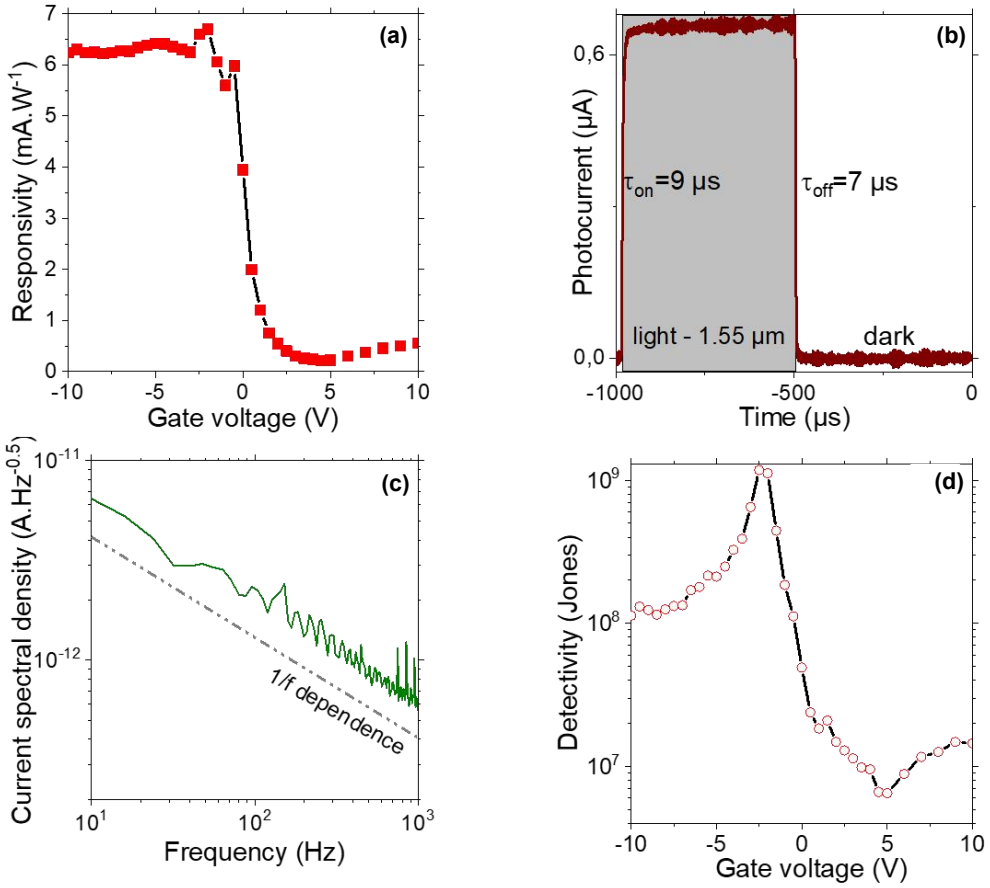

Figure 4.10 *– (a) Responsivity at 1.55 µm of the graphene/HgTe/graphene junction, as a function of the applied gate bias. (b) Temporal response of the graphene/HgTe/graphene junction, under -1 V of gate bias. Dynamics appears to be limited by experimental setup. (c) Current spectral density as a function of signal frequency, under -2.5 V of gate bias. The noise appears to be 1/f limited. (d) Detectivity (i.e signal-to-noise ratio) at 1 kHz and 220 K as a function of the applied gate bias for the graphene/ HgTe/graphene junction.*

ever, this limitation mostly results from the film thickness (≈ 120 nm), which only absorbs 8% of the incident light. For the sake of comparison, films with a thickness above 500 nm and absorbing 30% of the incident light and based on the same particles and surface chemistry achieved a detectivity of 3x10^9 Jones [Martinez19]. This indicates that charge dissociation is more efficient in the planar p-n junction developed here than for common stack of nanocrystals used in HgTe nanocrystal-based photodiodes. The time response of the device has been found to be below 10 μs (Fig. 4.10 (b)), with a weak incident power dependence (Fig. 4.11 (a) and (b)). It actually appears to be fully limited by the experimental setup.

Note that the fast time response of our device is not driven by the large gate capacitance but rather by the capacitance of the nanocrystal film, which relates to the HgTe thickness, its dielectric constant, and the device area. Overall, our graphene/HgTe nanocrystal heterostructures demonstrate a fast time response below a few microseconds, which is enough for all video applications. Such a fast response strongly contrasts with the slower response commonly observed in quantum dot arrays coupled to 2D materials, usually locked in the tens of milliseconds [Tang19c] or even slower [Robin16]. In such a usual 2D/0D device ge-

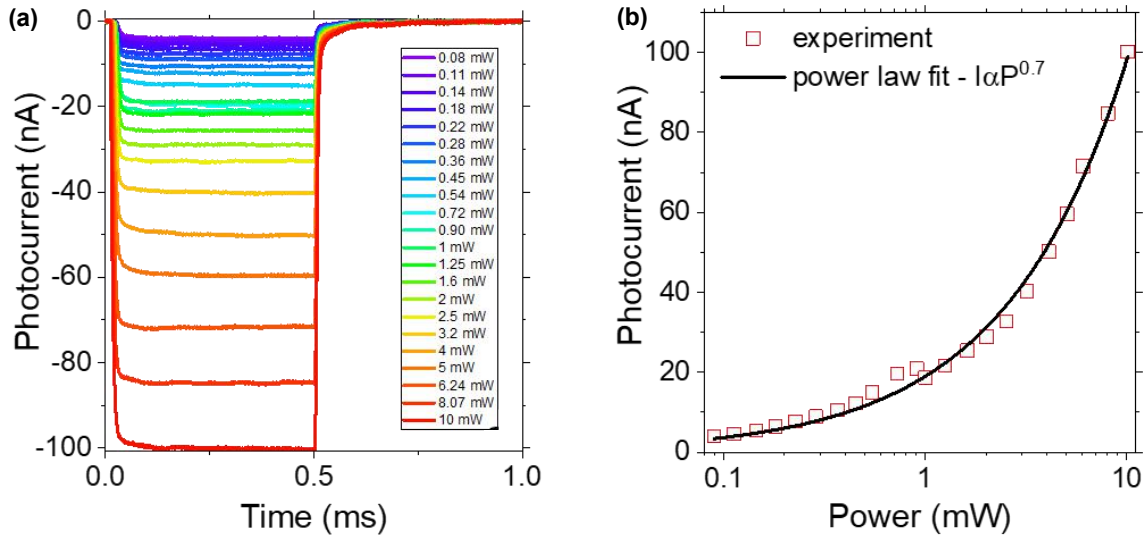

Figure 4.11 – *(a) Photocurrent at 1kHz and 220 K for different incident power (from 0.08 to 10 mW).(b) Power dependency of the photocurrent at 1kHz and 220 K. Power law fit of the data points.*

ometry, absorption usually occurs in the quantum dots, and the carrier with the lowest band offset with respect to the 2D material is transferred to the 2D layer, whereas the second carrier stays in the quantum dot. This photogating process leads to very large photoconduction gains and to large response but also hampers the current dynamics that gets driven by the recombination of the carriers trapped in the quantum dot arrays. In other words, the photogain increase is balanced by the drop of the device bandwidth. In our 2D/0D p-n junction geometry, the enhancement of the signal-to-noise ratio is obtained without degradation of the device bandwidth. So beyond the fast time response, our device offers an interesting trade-off in term of signal-to-noise ratio and bandwidth, quantized through the ratio of the detectivity over the time response.

Finally, we use the power dependence of the photocurrent to study the carrier recombination mechanism in our system. As shown in Fig. 4.11 (a) and (b), the photocurrent increases with the light power. A power law fit of the current plotted as function of the light power unveils a 0.7 exponent (Fig. 4.11 (b)). This value is intermediate between the value of 1 expected for monomolecular process (trapping) and the value of half resulting from a bimolecular process (electron hole recombination) [Willis09, Rose63], meaning that both processes may be involved in our system.

4.4 Conclusion

In this chapter, we have designed a phototransistor architecture based on a graphene-HgTe nanocrystal-graphene heterostructure to build a reconfigurable p-n junction. The formation of the p-n junction is made possible by the combination of the large gate capacitance of the LaF_3 ionic glass substrate, the carrier selectivity of graphene, and its partial transparency to a vertical electric field. Whereas previous phototransistors based on metallic electrodes led to marginal improvements of the signal-to-noise ratio under an applied gate bias, the graphene electrode/ionic glass combination enables a significant enhancement of the signal-to-noise

ratio.

The formation of a p-n junction, which widely expands over the nanocrystal film thickness due to the graphene low screening capability, allows the device detectivity to be improved by more than 2 orders of magnitude under applied gate bias and to demonstrate extremely fast photoresponse time below 10 μs.

The photovoltaic operation of the 2D/0D p-n junction is clearly exhibited by the presence of a photocurrent under zero drain-source bias. Hence, combining the high doping density provided by ionic glass, the electric field transparency and tunability of charge carriers of graphene, and the large scale processability of nanocrystals, our 2D/0D device offers the possibility of being switched electrostatically from an IR phototransistor to a photovoltaic device. Futhermore, as the p-n junction is the most ubiquitous component of modern electronics, the prospects opened by this 2D/0D p-n junction technology embrace a wider scope of application, including integrated circuits, detectors, and photovoltaics, and appears as an interesting approach to revisit the gate-induced light-emitting diode.

Conclusion and perspectives

General conclusion

To conclude this thesis having the aim to investigate the transport and phototransport properties in high doping regime of nanolectronic and optoelectronic devices consisting of colloidal nanocrystals, 2D materials and their heterostructure. I summarize below the third main achievements of this work.

First (Chapter 2), we have studied in detail ionic glass LaF_3 substrate for high doping regime using electrochemical impedance spectroscopy measurements. It came out that the capacitance of the ionic glass is the combination of a low-value dielectric capacitance and an ionic double layer high capacitance resulting from F^- vacancy existing in the crystals which allows the motion of fluorine ions. The strategy allowed to find sheet capacitance as high as 1 μF.cm^{-2} and sheet carrier concentration exceeding 10^{13} cm^{-2} at low gate voltage not accessible with a conventional dielectric, in an operating temperature from 180 K to 260 K not possible for electrolytic gating. LaF_3 has many features such as electrostatic high back gating, low temperature back gating, transparent infrared substrate and top access. Using the electrostatic gating of ionic glass, we have demonstrated ambipolar transport in narrow-band-gap HgTe NCs and pristine PbS NCs at low temperature, while a first demonstration of perovskite NCs based FET with electron transport at room temperature with FAFI-PbS perovskite NCs. The top optical acccess of our LaF_3 substrate, combined with its high charge-doping capability allowed to tune both the magnitude and the dynamics of the photocurrent in HgTe-based phototransistor at 200 K, the signal-to-noise ratio have been improved by a factor of 100 while the time response accelerated by a factor of 6.

Second (Chapters 3), we have extended the use of ionic glass LaF_3 as high capacitance gate on 2D materials such as MoS_2, $MoSe_2$, WS_2 and WSe_2. The detailed fabrication steps of our small scale process with a technique that I have developped in our group for e-beam lithography on an insulator substrate have been presented. Careful analysis of Schottky contacts at metal/WSe_2 interfaces using thermionic theory with a model which includes the two interfaces in WSe_2 FET have been done. Ionic glass induces high doping in WSe_2 channel and allows band bending modulation up to the flat band regime for efficient carrier extraction

at the contacts. Moreover, we have investigated properties of $MoSe_2$ phototransistors using LaF_3 gating. The later allowed to tune both the dark conductance and the photoresponse of the device. Our device demonstrated a fast reponse with time responses down to 200 μs, up to two decades faster than state of the art $MoSe_2$ phototransistors reported so far. The high accumulated carrier concentration achieved by our ionic glass gate suppressed the relative contribution of traps on the carrier recombination, enhanced the photoresponse of the device by more than two orders of magnitude, while at the same time increasing its gain bandwidth product.

Third (Chapter 4), we combined the two classes of nanomaterials and their advantages to fabricate a reconfigurable 2D-0D graphene-HgTe heterojunction for infrared photodetection. First, graphene presents infrared transparency (absorption of 2%), vertical electric field transparency, carrier selectivity under gate bias and large scale production with the possibility for manufacturing electrodes with tunable and low resistance interface. Second, the relatively high carrier mobility of HgTe NCs ($> 1 cm^2.V^{-1}s^{-1}$) enables NCs to be involved in the transport in our device. Thus, the introduction of graphene electrodes combined with ionic glass enabled to reconfigure selectively the HgTe nanocrystals and the graphene electrodes between electron-doped (n) and hole-doped (p) states, and by this way to tune graphene-HgTe heterojunctions from the p-p' or n-n' configuration to p-n junctions. The p-n junction expands throughout the device, with a built-in electric field that assists charge dissociation. We have demonstrated that, in this specific configuration, the signal-to-noise ratio for infrared photodetection has been enhanced by 2 orders of magnitude, a fast time response (< 10 μs) and a detectivity of 10^9 Jones, whereas the device only absorbs 8% of the incident light. We have also demonstrated the photovoltaic mode of our 2D/0D device which can be switched electrostatically by the gate from a photovoltaic mode to an IR phototransistor mode. All these performances make our detector compatible with optoelectronic applications especially for all video rate applications. It is noteworthy that our system, being less complex than the best devices observed in the literature generally made of complex stack of NCs in vertical geometries, can still be improved.

This work opens on the realization of original nanodevices exploiting the phenomena and properties demonstrated in this manuscrit, below are some of them.

Perspectives

First, vertical geometry infrared NCs based diode is, among possible geometries, the one that has led to the best performances so far because they can be operated at zero bias, thus reducing the dark current as well as the noise. However, this geometry suffers from a lack of gate tunability after its fabrication not only because of geometry issue but also because of the large thickness of absorbing materials involved (see Fig. 2.1 (a) and (d)), slowing down possible improvements [Ackerman18, Tang19a]. LaF_3 being an infrared transparent material and taking its high capacitance, can be used to design and study a gate tunable

vertical infrared photodiode on LaF_3, with a back side illumination. So it will have two roles: an infrared transparent bottom substrate and a high capacitance gate medium to control the carrier density of the NC film. In close collaboration with the Lhuillier's group at INSP (Paris) we are currently working in a device in which the active layer is made of a vertical stack of one electrode of graphene, thick films of HgTe NCs (for more light absorption) with different sizes to create a vertical diode. The gate bias can thus be used to tune the doping and the band profile of both graphene electrode and NCs. This strategy will introduce electrostatic doping in vertical diodes by controlling the intrinsic doping of absorbing layer and finally will enhance device performances directly come from the poor doping profile usually observed in the vertical diode.

Second, an additional important perspective of this work is to explore organic electronic and optoelectronic properties of organic film in high doping regime using ionic glass. Organic electronics offer the possibility of large area, solution processability, low-cost production (drop casting, spin-coating, printing...), low temperature processability (below 200 °C), physical and chemical tunability, making them relevant for industrial purposes. Many efforts have been done for the production of better-controlled organic materials with the improvements of numerous physico-chemical properties such as the carriers mobility [Parui17]. Because of the fundamental different structure of polymers compared to metals, the main issue that remains to overcome is the large contact resistance at the organic-inorganic interfaces which limit the injection of charge carriers, and the performances of organic based devices. While electrolytes have been used to induce high doping in organic FETs, then to reduce the contact resistances [Braga10, Zanettini15b], there is to date no investigation of optoelectronic properties of those films in high doping regime using ionic glass substrate. In collaboration with the SAMORI's group at ISIS (Strasbourg), we started

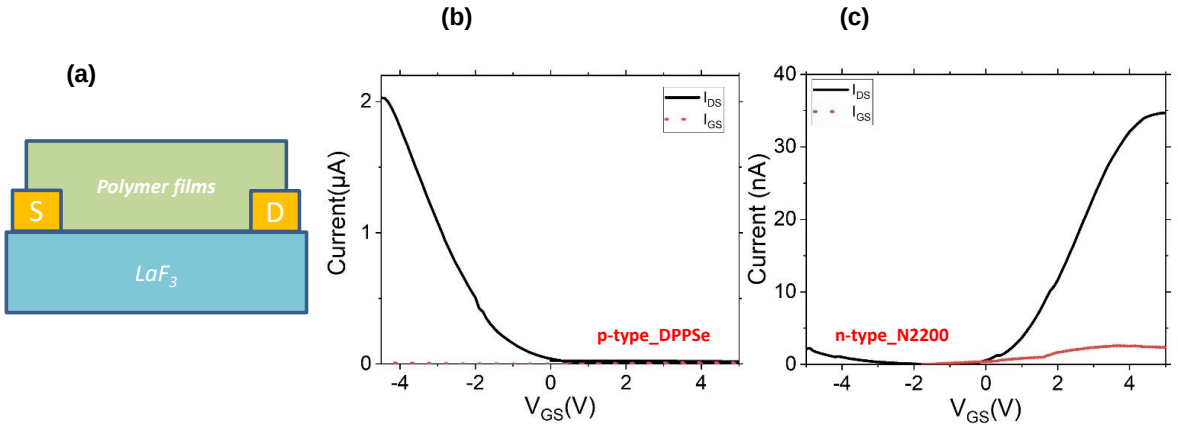

Figure 4.12 *– (a) Schematic of polymer films FET on LaF_3. (b) Transfer curve at 220 K with p-transport in PDSSe film flake under 6 V drain-source bias. (c) Transfer curve at 220 K with p-transport in N2200 film flake under 3 V drain-source bias.*

to work on organic film based FET on LaF_3 with promising results already obtained. We have contacted selenophene substituted Diketopyrrolopyrrole polymer film (PDPPSe) and Polynaphtalene-bithiophene organic film (N2200) on LaF_3 substrate. While at 220 K PDSSe demonstrates hole-transport, N2200 shows electron-transport. This confirms that our gating technique can be extented to organic films. One step further must be to use the direct optical accessability of LaF_3 to probe optoelectronic properties of those films in high doping regime which seem interesting for organic photovoltaic cells and organic light emitting diode. Another interesting direction will be the used of large scale electrode graphene introduced in section 4.1 to create tunable junctions.

Finally, all the processes I have developed in this work section 3.1 and section 4.1 can be extended to 2D magnetic materials, in order to modulate their electronic and magnetic states, and 2D/0D hybrid systems in high doping regime or to control the light emission characteristics.

List of publications

- L. D. N. Mouafo, F. Godel, L. Simon, Y. J. Dappe, W. Baaziz, U. N. Noumbé, E. Lorchat, M.-B. Martin, S. Berciaud, B. Doudin, O. Ersen, J.-F. Dayen. *0D/2D Heterostructures Vertical Single Electron Transistor*, Adv. Funct. Mater. Dec. 2020, DOI: 10.1002/adfm202008255
- U. N. Noumbé, C. Gréboval, C. Livache, T. Brule, B. Doudin, A. Ouerghi, E. Lhuillier, and J.-F. Dayen. *Ionic Glass-Gated 2D Material-Based Phototransistor: $MoSe_2$ over LaF_3 as Case Study*, Adv. Funct. Mater. 2019, 29 (33), 1902723.
- P. Rastochi, A. Chu, C. Gréboval, J. Qu, U. N. Noumbé, S.-S. Chee, M. Goyal, A. Khalili, X. Z. Xu, H. Cruguel, S. Ithurria, B. Gallas, J.-F. Dayen, L. Dudy, M. G. Silly, G. Patriarche, A. Degiron, G. Vincent, E. Lhuillier. *Pushing Absorption of Perovskite Nanocrystals Into the Infrared.*, Nano Lett. 2020, 20 (5) 3999-4006
- U. N. Noumbé, C. Gréboval, C. Livache, A. Chu, H. Majjad, L. E. P. Lopez, L. D. N. Mouafo, B. Doudin, S. Berciaud, J. Chaste, A. Ouerghi, E. Lhuillier, J.-F. Dayen. *Reconfigurable 2D/0D p-n Graphene/HgTe Nanocrystal Heterostructure for Infrared Detection*, ACS Nano 2020, 14, 4, 4567-4576
- U. N. Noumbé, C. Gréboval, C. Livache, T. Brule, B. Doudin, A. Ouerghi, E. Lhuillier, and J.-F. Dayen. *Ionic Glass-Gated 2D Material-Based Phototransistor: $MoSe_2$ over LaF_3 as Case Study*, Adv. Funct. Mater. 2019, 29 (33), 1902723.
- C. Gréboval, U. N. Noumbé, N. Goubet, C. Livache, J. Ramade, J. Qu, A. Chu, B. Martinez, Y. Prado, S. Ithurria, A. Ouerghi, H. Aubin, J.-F. Dayen, and E. Lhuillier. *Field-Effect Transistor and Photo-Transistor of Narrow-Band-Gap Nanocrystal Arrays Using Ionic Glasses*, Nano Lett. 2019, (6), 3981-3986

Chapter A

Materials and synthesis

Nanocrystal synthesis

The NC synthesis has been done by our collaborators in Lhuillier's team at INSP. For sake of information, I provide general information on the synthesis routes done by our partners. The HgTe and PbS NCs have been synthesized by Charlie Gréboval (PhD student, INSP), FAPI-PbS NCs have been synthesized by Prachi Rastogi (Postdoctoral researcher, INSP).

A.1 HgTe nanocrystals

1 M trioctylphosphine (TOP):Te precursor: 2.54 g of Te powder is mixed in 20 mL of TOP in a three neck flask. The flask is kept under vacuum at room temperature for 5 min and then the temperature is raised to 100 °C. Furthermore, the degassing of flask is conducted for the next 20 min. The atmosphere is switched to Ar and the temperature is raised to 275 °C. The solution is stirred until a clear orange coloration is obtained. The flask is cooled down to room temperature and the color switches to yellow. Finally, this solution is transferred to an Ar filled glove box for storage.

Mercury compounds are highly toxic. Handle them with special care.

HgTe 4k CQD synthesis: 513 mg of $HgCl_2$ was added to 60 mL of oleylamine in a 100 mL round flask. The solution was placed under vacuum and heated to 110 °C for 1 h. Then, the temperature is decreased to 80 °C and the solution placed under Ar atmosphere. 1.9 mL of TOP:Te (1 M) with 10 mL of oleylamine are added to the mercury solution. The solution color gradually turns to dark brown and the reaction is stopped 3 min. A solution made of 1 mL of dodecanethiol (DDT) and 9 mL of toluene is quickly added to quench the reaction. The nanocrystals are then precipitated with ethanol. After centrifugation, the nanocrystals are redispersed in chloroform. The washing step is repeated one more time. The solution is filtered with a 0.2 μm filter and redispersed in 6 mL of chloroform.

HgTe CQD ink preparation: 5 mg of $HgCl_2$, 100 μL of mercaptoalcool (MPOH) and 900 μL

of N,N dimethylformamide (DMF) are mixed. 0.5 mL of this solution is added to 0.5 mL of a HgTe solution at 50 mg.mL^{-1} in toluene. A few mL of hexane can be added to help phase dissociation: the QDs migrate to the bottom phase (DMF), showing efficient ligand exchange. After 3 washing steps with hexane, the QDs are mixed to 2-3 drops of ethanol and centrifuged at 6000 rpm for 2 min. The clear supernatant is discarded and the QDs are redispersed in 100 μL of fresh DMF to reach a concentration of 250 mg.mL^{-1}. To ensure that the colloidal stability is good, the sample is then re-centrifuged at 3000 rpm for 4 min.

A.2 PbS nanocrystals

Briefly speaking, 300 mg of $PbCl_2$ are mixed with 7.5 mL of oleylamine and degassed at 110 °C for 30 min. Meanwhile 32 mg of Sulfur powder are sonicated in 7.5 mL of oleylamine, leading to a clear orange solution. Under Ar at 160 °C, the Sulfur solution is quickly injected and the reaction is continued for 15 min. At the end the mixture is quenched with 1 mL of oleic acid and 10 mL of hexane. The solution is then washed using ethanol as non-solvent and toluene as non-polar solvent. The obtained PbS NCs have an exciton around 6000 cm^{-1}.

A.3 Formamidinium lead iodine FAPI nanocrystals

In a 100 mL three-neck flask, 240 mg of PbI_2 are added in 18 mL of octadecene (ODE) and degassed at 110 °C under vacuum. After 20 min of degassing 2 mL of oleylamine were added. Once vacuum has recovered, 4 mL of oleic acid was added. At this point, the lead salt was fully dissolved and the solution turns clear yellow. The atmosphere is switched to N_2 and the temperature set at 80 °C. Under N_2 20 mL of the formamidinium oleate is quickly injected. The solution turns dark red. After 15 s the heating mantle is removed and a water bath is used to cool the flask. The solution was centrifuged at 6000 rpm. The supernatant was discarded and the formed pellet redispersed in hexane. Ethyl acetate was added to precipitate the nanocrystals the second time. After centrifugation, the pellet was dispersed in toluene.

Chapter B

Experimental setups

Below are the experimental set-ups we used at INSP for optical meassurements.

B.1 FTIR setup

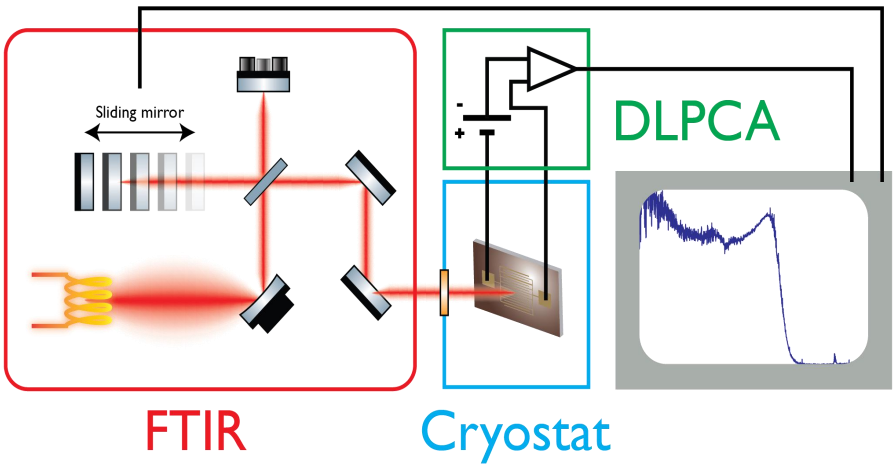

Figure B.1 *– An experimental setup to probe photocurrent spectrum on LaF_3 substrate:The sample is cooled down in a cryostat and biased by a DLPCA amplifier. IR light comes from FTIR spectrometer to the sample. The photocurrent is then amplified by the DLPCA before being sent to the FTIR to calculate the photocurrent spectrum.*

The sample is cooled down at the desired temperature and biased using a femto DLPCA

200 which is also used as current amplifier. The infrared signal from an IS50 FTIR from Thermo Fisher is shone on the sample and the output of the amplifier is connected to the custom detector entry of the FTIR to calculate the photocurrent spectrum.

B.2 Experimental setup to probe photocurrent dynamic in HgTe-NCs and $MoSe_2$

Transistor measurement: Once inserted in the cryostat, the sample is connected to a Keithley K2634 B. It controls the applied gate voltage (V_{GS}) and the applied drain-source bias (V_{DS}).
Photocurrent measurement: The HgTe NCs (respectively $MoSe_2$) sample is illuminated by a 1.55 μm (respectively a 405 nm) laser optically chopped at 1 kHz (respectively 100 Hz). Then, the sample is biased by a Keithley 2634 B and the photocurrent is measured by a DLPCA-200 transimpedance amplifier connected to a GHz oscilloscope.

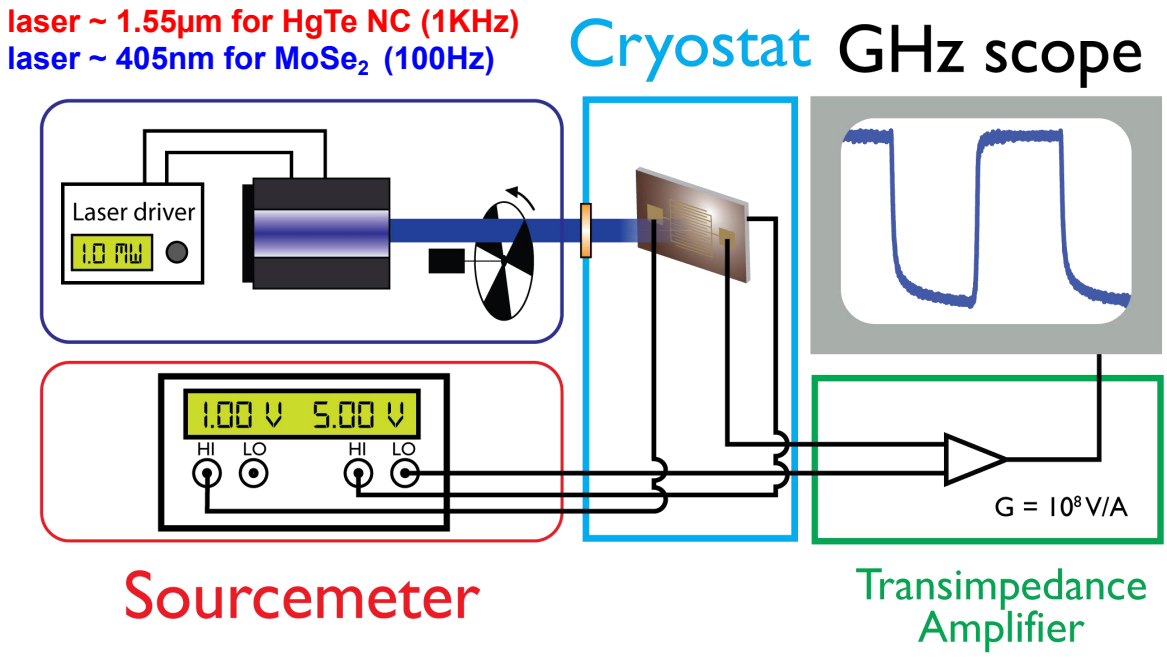

Figure B.2 *– An experimental setup to probe photocurrent dynamics under LaF_3 gate control of HgTe NCs (respectively $MoSe_2$, the excitation source is a 1.55 µm (respectively a 405 nm) laser is optically chopped at 1 kHz (respectively 100 Hz) and illuminates the sample in the cryostat. Sample is biased by a Keithley 2634 B and the photocurrent is measured by a DLPCA-200 transimpedance amplifier connected to a GHz oscilloscope. A gate bias is applied using a Keithley 2634 B.*

Raman and photoluminescence spectra: The micro-Raman and photoluminescence (PL) measurements were conducted using commercial confocal HORIBA LabRAM HR Evolution

micro-Raman microscope with an objective focused 532 nm and 633 nm lasers in an ambient environment at room temperature. The excitation laser was focused onto the samples with a spot diameter of ≈0.5 μm and incident power of ≈0.1 mW. Measurements were performed on the same microscope with a 100x objective and a CCD detector (detection range from 1.2 to 6.2 eV).

Scanning electron microscopy: SEM is made using a FEI Magellan microscope. Images are acquired with the e-beam accelerated with a 3 kV bias and the current from the electronic gun set at 6 pA.

Chapter C

Thermionic current at metal/semiconductor interface

At the metal/semiconductor interface, the inter-diffusion of charges necessary to establish the equilibrium is materialized by the alignment of the Fermi levels of both materials. It results an interface Schottky energy barrier $q\phi_B = e\phi_m - e\chi$, $e\phi_m$ and $e\chi$ are respectively the metal work function and the semiconductor electron affinity in electron volt. However, a combine effect of the built-in potential V_b due to interface charge depletion/accumulation as well as the image force and the applied electric fields induces a rounding of the conduction band of the semiconductor at the interface and modifies the interface energy barrier energy which becomes $E_b = q\phi_B - (E_c^0 - E_c^\infty)$, E_c^0 and E_c^∞ are respectively the conduction band minimum at the interface and far from the interface. At absolute temperature there are no electrons crossing the interface. At finite temperature however, thermal excitation statistically provides to some electrons sufficient energy to overcome the interface energy barrier. Some, from metal to semiconductor and others in the opposite direction. This process is known as thermionic emission. We provide here the derivation of the electric current expected from such a process. This derivation can be founded in most of the semiconductor text books [Sze81, Mathieu09, Mouafo19].

Thermionic regime assumes two main hypothesis : (i) The interface energy barrier is much larger than the thermal energy $E_b \gg K_B T$ such that the current arises essentially from electrons statistically promoted across the barrier by thermal excitation. (ii) The metal/semiconductor interface thermal equilibrium is not affected by the presence of a net current flow. Under these assumptions, the shape of the barrier is not relevant and the current flow depends solely on its height E_b. Therefore, only electrons with sufficient energy crossing perpendicularly the interface in the $x\vec{i}$ direction contribute to the current. The semiconductor

to metal current is given by :

$$I_{sc\to m} = S\int_{E_F+E_b}^{\infty} qv_x dn \tag{C.1}$$

$E_F + E_b$ is the minimum energy required for thermal emission into the metal, S the area of the junction. $dn = N(E)F(E)dE$, where $N(E) = \frac{4\pi(2m^*)^{3/2}}{\hbar^3}\sqrt{E-E_c}$ is the 3D DOS and $F(E) = exp[-(E-E_F)/K_BT]$ is the Fermi-Dirac distribution function in Boltzmann approximation since $E - E_F > E_b \gg K_BT$. The energy of electrons is assumed to be essentially kinetic.

$$E = E_c + \frac{1}{2}m^*v^2 = E_F + E_b + \frac{1}{2}m^*v^2 \Rightarrow dE = m^*vdv \quad and \quad \sqrt{E-E_c} = v\sqrt{m^*/2} \tag{C.2}$$

therefore,

$$dn = 2(\frac{m^*}{h})^3 \exp(-\frac{E_b}{K_BT})\exp(-\frac{m^*v^2}{2K_BT})(4\pi v^2 dv) \tag{C.3}$$

Taking $\vec{v} = \vec{v_x} + \vec{v_y} + \vec{v_z}$, $4\pi v^2 dv$ is spherical coordinate equivalent of elementary volume and one can write $dv_x dv_y dv_z = 4\pi v^2 dv$. Hence, the Eq.C.1 becomes.

$$I_{sc\to m} = 2{*}q{*}S(\frac{m^*}{h})^3 \exp(-\frac{E_b}{K_BT})\int_{v_{0x}}^{\infty} v_x \exp(-\frac{m^*v_x^2}{2K_BT})dv_x \int_{-\infty}^{\infty}\exp(-\frac{m^*v_y^2}{2K_BT})dv_y \int_{-\infty}^{\infty}\exp(-\frac{m^*v_z^2}{2K_BT})dv_z \tag{C.4}$$

$$\Rightarrow I_{sc\to m} = 2*q*S(\frac{m^*}{h})^3 \exp(-\frac{E_b}{K_BT})(\frac{K_BT}{m^*})[\exp(-\frac{m^*v_x^2}{2K_BT})]_{v_{0x}}^{\infty}\frac{2\pi K_BT}{m^*} \tag{C.5}$$

$$= 2*q*S(\frac{m^*2\pi k_B^2T^2}{h^3})\exp(-\frac{E_b}{K_BT})\exp(-\frac{m^*v_{0x}^2}{2k_BT}) \tag{C.6}$$

Here, v_{0x} is the minimum velocity of the carrier in the conduction band and depends on the built in potential V_b and the applied bias as $\frac{1}{2}v_{0x}^2 = q(V_b - V)$. However, the component related to V_b which the effect is the modification of E_F to E_C distance is already included in the term E_b. Finally,

$$I_{sc\to m} = SA^*T^2\exp(-\frac{E_b}{K_BT})\exp(\frac{qV}{k_BT}) \quad ; \quad A^* = \frac{4\pi qm^*k_B^2}{h^3} \tag{C.7}$$

Where $A^* = \frac{4\pi m^*2k_B^2}{h^3}$ represents the Richardson constant for a bulk materials.
Since $I_{sc\to m} = I_{m\to sc}$ at equilibrium i.e. when V = 0, the metal to semiconductor current is given by :

$$I_{m\to sc} = SA^*T^2\exp(-\frac{E_b}{K_BT}) \tag{C.8}$$

Hence, the total current across the Metal/Semiconductor interface is $I = I_{sc\to m} - I_{m\to sc}$ and takes the general form of Eq.C.9.

$$I = SA^*T^2\exp(-\frac{E_b}{K_BT})[\exp(\frac{qV}{K_BT}) - 1] \tag{C.9}$$

The ideality factor n can be introduced to account for a voltage dependence of the Schot-

tky barrier height. This factor can also increase due to tunneling through the barrier or carrier recombination in the depletion region. Taking into account the ideality factor, the modified barrier height is written as [Hajzus18, Azmi18]:

$$\phi_B = \phi_{0B} + V(1 - \frac{1}{n}) \tag{C.10}$$

ϕ_{0B} being the true Schottky barrier height of the junction.

The total current across the junction can thus be expressed as:

$$I \approx SA^*T^2 \exp(\frac{-q\phi_{0B}}{K_BT}) \exp(\frac{qV}{nK_BT})[1 - \exp(\frac{-qV}{K_BT})] \tag{C.11}$$

This expression is more appropriate to quantify the current across the interface i.e. to analyze I-V characteristics of the Schottky contact because it takes into account the barrier height lowering due to electric field, tunneling effects, and carrier recombination in the space charge region of the metal-semiconductor contact.

Bibliography

[Abderrahmane14] A. Abderrahmane, J. Ko, T. V. Thu, S. Ishizawa, T. Takamura, and A. Sandhu. *High photosensitivity few-layered $MoSe_2$ back-gated field-effect phototransistors*. Nanotechnology **25** (36), 365202 (2014). 17, 95

[Ackerman18] M. M. Ackerman, X. Tang, and P. Guyot-Sionnest. *Fast and Sensitive Colloidal Quantum Dot Mid-Wave Infrared Photodetectors*. ACS Nano **12**, 7264-7271 (2018). 11, 59, 60, 114

[Ajayan16] P. M. Ajayan, P. Kim, and K. Banerjee. *Two-dimensional van der Waals materials*. Phys. Today **69** (9), 38-44 (2016). 32

[Allan12] G. Allan and C. Delerue. *Tight-Binding Calculations of the Optical Properties of HgTe Nanocrystals*. Phys. Rev. B **86**, 165437 (2012). 41

[Arzola05] S. Arzola and J. Genesca. *The effect of H_2S concentration on the corrosion behavior of API 5L X-70 steel*. Journal of Solid State Electrochemistry **9** (4), 197-200 (2005). 62, 65

[Ashcroft76] N. W. Ashcroft and N. D. Mermin. *Solid state physics*. Holt, Rinehart and Winston, 1976. 29

[Avouris10] P. Avouris. *Graphene: Electronic and Photonic Properties and Devices*. Nano Lett. **10** (11), 4285-4294 (2010). 28

[Azmi18] S. N. C. Azmi, S. F. A. Rahman, A. Nawabjan, and A. M. Hashim. *Junction properties analysis of silicon back-to-back Schottky diode with reduced graphene oxide Schottky electrodes*. Microelectronic Engineering **196**, 32-37 (2018). 91, 127

[Bae10] S. Bae, H. Kim, Y. Lee, X. Xu, J. Park, .Y Zheng, J. Balakrishnan, T. Lei, H. R. Kim, Y. I. Song, Y. Kim, K. S. Kim, B. Özyilmaz, J.-H. Ahn, B. H. Hong, and S. Iijima. *Roll-to-roll production of 30-inch graphene films for transparent electrodes*. Nat. Nanotechnol. **5**, 574-578 (2010). 28

[Bartels02] R. A. Bartels, A. Paul, H. Green, H. C. Kapteyn, M. M. S. Murnane, Backus, I. P. Christov, Y. Liu, D. Attwood, and C. Jacobsen. *Generation of spatially coherent light at extreme ultraviolet wavelengths.* Science **297**, 376-378 (2002). 51

[Berciaud09] S. Berciaud, S. Ryu, L. E. Brus, and T. F. Heinz. *Probing the Intrinsic Properties of Exfoliated Graphene: Raman Spectroscopy of Free-Standing Monolayers.* Nano Lett. **9** (1), 346-352 (2009). 102

[Berger16] C. N. Berger, M. Dirschkab, and A. Vijayaraghavan. *Ultra-thin graphene-polymer heterostructure membranes.* Nanoscale **8**, 17928-17939 (2016). 48

[Braga10] D. Braga, W. Xie M. Ha, and C. D. Frisbie. *Ultralow Contact Resistance in Electrolyte-Gated Organic Thin Film Transistors.* Appl. Phys. Lett. **97**, 193311 (2010). 115

[Britnell13] L. Britnell, R. M. Ribeiro, A. Eckmann, R. Jalil, B. D. Belle, A. Mishchenko, Y.-J. Kim, R. V. Gorbachev, T Georgiou, S. V. Morozov, A. N. Grigorenko, A. K. Geim, C. Casiraghi, A. H. Castro Neto, and K. S. Novoselov. *Strong light-matter interactions in heterostructures of atomically thin films.* Science **340** (6138), 1311–1314 (2013). 47

[Brus86] L. Brus. *Electronic wave functions in semiconductor clusters: experiment and theory.* Journal of Physical Chemistry **90**, 2555-2560 (1986). 40

[Carey15] G. H. Carey, A. L. Abdelhady, Z. Ning, S. M. Thon, O. M. Bakr, and E. H. Sargent. *Colloidal Quantum Dot Solar Cells.* Chemical Reviews **115**, 12732-12763 (2015). 41

[Casey12] H. C. J. Casey. *Heterostructure lasers.* Elsevier, 2012. 44

[Castro Neto07] A. H. Castro Neto and F. Guinea. *Electron-phonon coupling and Raman spectroscopy in graphene.* Phys. Rev. B **75**, 045404 (2007). 28

[Castro Neto09] A. H. Castro Neto, F. Guinea, N. M. R. Peres, K. S. Novoselov, and A. K. Geim. *The electronic properties of graphene.* Rev. Mod. Phys. **81**, 109–162 (2009). 30

[Chamlagain14] B. Chamlagain, Q. Li, N. J. Ghimire, H.-j. Chuang, M. M. Perera, Honggen Tu, Y. Xu, M. Pan, D. Xaio, J. Yan, D. Mandrus, and Z. Zhou. *Mobility Improvement and Temperature Dependence in $MoSe_2$ Field-Effect Transistors on Parylene-C Substrate.* ACS nano **8** (5), 5079–5088 (2014). 37

[Chang17] P.-H. Chang, Y.-C. Tsai, S.-W. Shen, S.-Y. Liu, K.-Y. Huang, C.-S. Li, H.-P. Chang, and C.-I. Wu. *Highly Sensitive Graphene-Semiconducting Polymer*

Hybrid Photodetectors with Millisecond Response Time. ACS Photonics **4** (9) (2017). 49

[Charlier07] J.-C. Charlier, X. Blase, and S. Roche. *Electronic and transport properties of nanotubes*. Rev. Mod. Phys. **79** (2), 677–732 (2007). 27

[Chen08] J. H. Chen, C. Jang, S. Xiao, M. Ishigami, and M. S. Fuhrer. *Intrinsic and extrinsic performance limits of graphene devices on SiO_2*. Nature Nanotechnology **3** (4), 206–209 (2008). 31

[Chen14a] C.-H. Chen, C.-L. Wu, J. Pu, M.-H. Chiu, P. Kumar, Taishi. Takenobu, and L.-J. Li. *Hole mobility enhancement and p-doping inmonolayer WSe_2 by gold decoration*. 2D Materials **1**, 034001 (2014). 88

[Chen14b] M. Chen, L. Shao, S. V. Kershaw, H. Yu, J. Wang, A. L. Rogach, and N. Zhao. *Photocurrent Enhancement of HgTe Quantum Dot Photodiodes by Plasmonic Gold Nanorod Structures*. ACS Nano **8**, 8208-8216 (2014). 60

[Chen15] X. Chen, Z. Wu, S. Xu, L. Wang, R. Huang, Y. Han, W. Ye, W. Xiong, T. Han, G. Long, Y. Wang, Y. He, Y. Cai, P. Sheng, and N. Wang. *Probing the electron states and metal-insulator transition mechanisms in molybdenum disulphide vertical heterostructures*. Nature Communications **6**, 6088 (2015). 28, 37, 38

[Chen17] M. Chen, H. Lu, N. M. Abdelazim, Y. Zhu, Z. Wang, W. Ren, S. V. Kershaw, A. L. Rogach, and N. Zhao. *Mercury Telluride Quantum Dot Based Phototransistor Enabling High-Sensitivity Room-Temperature Photodetection at 2000 nm.* ACS Nano **11**, 5614-5622 (2017). 11, 60

[Chen19] M. Chen, X. Lan, X. Tang, Y. Wang, M. H. Hudson, D. V. Talapin, and P. Guyot-Sionnest. *High Carrier Mobility in HgTe Quantum Dot Solids Improves Mid-IR Photodetectors*. ACS Photonics **6**, 2358-2365 (2019). 108

[Chhowalla13] M. Chhowalla, H. S. Shin, G. Eda, L.-J. Li, K. P.ing Loh, and H. Zhang. *The chemistry of two-dimensional layered transition metal dichalcogenide nanosheets*. Nat. Chem. **5** (4), 263–275 (2013). 32, 34, 35

[Chuang14] H. J. Chuang, X. Tan, N. J. Ghimire, M. M. Perera, B. Chamlagain, M. M. C. Cheng, J. Yan, D. Mandrus, D. Tomànek, and Z. Zhou. *High Mobility WSe_2 p- and n-Type Field-Effect Transistors Contacted by Highly Doped Graphene for Low-Resistance Contacts*. Nano Lett. **14**, 3594-3601 (2014). 88

[Cresti08] A. Cresti, N. Nemec, B. Biel, G. Niebler, F. Triozon, G. Cuniberti, and S. Roche. *Charge transport in disordered graphene-based low dimensional materials*. Nano Research **1** (5), 361–394 (2008). 27

[Dai19] T. Dai, D. Xie Y. Liu, X. Liu, and Y. Li. *High performance photodetectors constructed on atomically thin few-layer $MoSe_2$ synthesized using atomic layer deposition and a chemical vapor deposition chamber*. J. Alloys Compd. **785**, 785 (2019). 17, 95

[Das Sarma11] S. Das Sarma, S. Adam, E. H. Hwang, and E. Rossi. *Electronic transport in two-dimensional graphene*. Rev. Mod. Phys. **83**, 407–470 (2011). 28, 30, 31

[Das08] A. Das, S. Pisana, B. Chakraborty, S. Piscanec, S. K. Saha, U. V. Waghmare, K. S. Novoselov, H. R. Krishnamurthy, A. K. Geim, A. C. Ferrari, and A. K. Sood. *Monitoring dopants by Raman scattering in an electrochemically top-gated graphene transistor*. Nat. Nanotechnol. **3** (4), 210–215 (2008). 106

[Deacon07] R. S. Deacon, K.-C. Chuang, R. J. Nicholas, K. S. Novoselov, and A. K. Geim. *Cyclotron resonance study of the electron and hole velocity in graphene monolayers*. Phys. Rev. B (2007). 27

[Dean10] C. R. Dean, A. F. Young, I. Meric, C. Lee, L. Wang, S. Sorgenfrei, K. Watanabe, T. Taniguchi, P. Kim, K. L. Shepard, and J. Hone. *Boron nitride substrates for high-quality graphene electronics*. Nat. Nanotechnol. **5** (10), 722–726 (2010). 28

[Ekimov81] A. I. Ekimov and A. A. Onushchenko. *Quantum size effects in 3-dimensional microscopic semiconductor crystals*. JETP Lett. **34**, 345-349 (1981). 40

[Formisano04] V. Formisano and N. Ignatiev M. Giuranna S. Atreya, T. Encrenaz. *Detection of Methane in the Atmosphere of Mars*. Science **306**, 1758 (2004). 51

[Fowler10] B. Fowler, C. Liu, S. Mims, J. Balicki, W. Li, H. Do, J. Appelbaum, and P. Vu. *A 5.5 Mpixel 100 frames/sec wide dynamic range low noise CMOS image sensor for scientific applications*. Proc. SPIE **7536**, 753607 (2010). 51

[Froehlicher16] G. Froehlicher. *Optical spectroscopy of two-dimensional materials: graphene, transition metal dichalcogenides and van der Waals heterostructures*. PhD thesis, Université de Strasbourg, (2016). 28, 33

[Fuchs08] J.-N. Fuchs and M. O. Goerbig. *Introduction to the physical properties of graphene*. 2008. 27

[Furchi14] M. M. Furchi, D. K. Polyushkin, A. Pospischil, and Thomas. Mueller. *Mechanisms of photoconductivity in atomically thin MoS_2*. Nano Lett. **14** (11), 6165–6170 (2014). 39

[Gabor11] N. M. Gabor, Justin. C. W. Song, Q. Ma, N. L. Nair, T. Taychatanapat, K. Watanabe, T. Taniguchi, L. S. Levitov, and P. Jarillo-Herrero. *Hot carrier–assisted intrinsic photoresponse in graphene*. Science **334** (6056), 648–652 (2011). 31

[Gan13] X. Gan, R.-J. Shiue, Y. Gao, I. Meric, T. F. Heinz, K. Shepard, J. Hone, S. Assefa, and D. Englund. *Chip-integrated ultrafast graphene photodetector with high responsivity*. Nat. Photonics **7** (11), 883–887 (2013). 31

[Garcia11] G. Garcia, R. Buonsanti, E. L. Runnerstrom, R. J. Mendelsberg, A. Llordes, A. Anders, T. J. Richardson, and D. J. Milliron. *Dynamically Modulating the Surface Plasmon Resonance of Doped Semiconductor Nanocrystals*. Nano Lett. **11**, 4415-4420 (2011). 28

[Geim07] A. K. Geim and K. S. Novoselov. *The Rise of Graphene*. Nat. Mater. **6**, 183-191 (2007). 29

[Geim09] A. K. Geim. *Graphene: status and prospects*. Science **324** (5934), 1530–1534 (2009). 26

[Godel17] F. Godel, L. D. N. Mouafo, G. Froehlicher, B. Doudin, S. Berciaud, Y. Henry, J.-F. Dayen, and D. Halley. *Conductance Oscillations in a Graphene/Nanocluster Hybrid Material: Toward Large-Area Single-Electron Devices*. Adv. Mater **29**, 1604837 (2017). 44

[Gomadam05] P. M. Gomadam and J. W. Weidner. *Analysis of electrochemical impedance spectroscopy in proton exchange membrane fuel cells*. Int. J. Energy Res. **29**, 1133 (2005). 12, 61

[Gomez07] L. Gomez, I. Aberg, and J. L. Hoyt. *Electron transport in strained-silicon directlyon insulator ultrathin-body n-MOSFETs with body thickness ranging from 2 to 25 nm*. IEEE Electron Dev. Let. **28**, 285-287 (2007). 39

[Gong18] C. Gong, K. Hu, X. Wang, P. Wangyang, C. Yan, J. Chu, M. Liao, L. Dai, T. Zhai, C. Wang, L. Li, and J. Xiong. *2D Nanomaterial Arrays for Electronics and Optoelectronics*. Advanced Functional Materials **28** (16), 1706559 (2018). 46

[Guyot-Sionnest12] P. Guyot-Sionnest. *"Electrical Transport in Colloidal Quantum Dot Films"*. The Journal of Physical Chemistry Letters **3** (9), 1169-1175 (2012). 42, 43

[Hafiz19] S. B. Hafiz, M. Scimeca, A. Sahu, and D.-K. Ko. *Colloidal Quantum Dots for Thermal Infrared Sensing and Imaging.* Nano Converg. **6** (7) (2019). 11, 59

[Hailing18] L. Hailing, , S. Hussain, A. Ali, B. A. Naqvi, D. Vikraman, W. Jeong, W. Song, K.-S. An, and J. Jung. *A vertical WSe_2-$MoSe_2$ p-n heterostructure with tunable gate rectification*. RSC Adv. **8**, 25514 (2018). 48

[Hajzus18] Jenifer R. Hajzus, A. J. Biacchi, S. T. Le, C. A. Richter, A. R. Hight Walkerb, and L. M. Porter. *Contacts to solution-synthesized SnS nanoribbons: Dependence of barrier height on metal work function*. Nanoscales **10**, 319-327 (2018). 127

[Han14] Z. Han, A. Kimouche, D. Kalita, A. Allain, H. Arjmandi-Tash, A. Reserbat-Plantey, L. Marty, S. Pairis, V. Reita, N. Bendiab, J. Coraux, and V. Bouchiat. *Homogeneous Optical and Electronic Properties of Graphene Due to the Suppression of Multilayer Patches During CVD on Copper Foils.* Adv. Funct. Mater. **24**, 964-970 (2014). 101

[He09] Z. He and F. Mansfield. *Exploring the use of electrochemical impedance spectroscopy (EIS) in microbial fuel cell studies*. Energy Environ. Sci. **2**, 215-219 (2009). 12, 61

[Hoff97] C. Hoff, H.-D. Wiemhofer, O. Glumov, and I. V. Murin. *Orientation dependence of the ionic condctivity in single crystals of lanthanum and cerium trifluoride*. Solid State Ionics **101**, 445-449 (1997). 11, 61

[Houdy06] P. Houdy, C. Dupas, and M. Lahmani. *Les nanosciences. Tome 1, Nanotechnologies et nanophysique*. La Collection Echelle, Edition Bellin, 2006. 44

[Hu17] C. Hu, D.D. Dong, X.K. Yang, K.K. Qiao, D. Yang, H. Deng, S.J. Yuan, J. Khan, Y. Lan, H.S. Song, and J. Tang. *Synergistic effect of hybrid PbS quantum dots/2d-WSe2 toward high performance and broadband phototransistors*. Adv. Funct. Mater. **27**, 1603605 (2017). 46

[Huo17] N. Huo, S. Gupta, and G. Konstantatos. *MoS_2-HgTe Quantum Dot Hybrid Photodetectors beyond 2 μm.* Adv. Mater. **30**, 1606576 (2017). 46

[Huo18] N. Huo and G. Konstantatos. *Recent Progress and Future Prospects of 2D-Based Photodetectors*. Adv. Mater. **29**, 1801164 (2018). 8, 21, 51, 53

[Iqbal15] M.W. Iqbal, M.Z. Iqbal, M.Z. Khan, M.A. Shehzad, Y. Seo, J.H. Park, C. Hwang, and J. Eom. *High-mobility and air-stable single-layer WS2*

field-effect transistors sandwiched between chemical vapor deposition-grown hexagonal BN films. Sci. Rep. **5**, 10699 (2015). 46

[Jagtap18] A. Jagtap, N. Goubet, C. Livache, A. Chu, B. Martinez, C. Greboval, J. Qu, E. Dandeu, L. Becerra, N. Witkowski, S. Ithurria, F. Mathevet, M. G. Silly, B. Dubertret, and E. Lhuillier. *Short Wave Infrared Devices Based on HgTe Nanocrystals with Air Stable Performances*. J. Phys. Chem. C **122**, 14979-14985 (2018). 67, 104

[Jariwala13] D. Jariwala, V. K. Sangwan, C.-C. Wu, P. L. Prabhumirashi, M. L. Geier, T. J. Marks, L. J. Lauhon, and M. C. Hersam. *Gate-tunable carbon nanotube-MoS_2 heterojunction p-n diode*. Proceedings of the National Academy of Sciences **110** (45), 18076–18080 (2013). 45

[Jariwala16] D. Jariwala, T. J. Marks, and M. C. Hersam. *Mixed-dimensional van der Waals heterostructures*. Nature Mat. **16** (2), 170-181 (2016). 25, 43, 44, 46

[Jellicoe16] T. C. Jellicoe, J. M. Richter, H. F. J. Glass, M. Tabachnyk, R. Brady, S. E. Dutton, A. Rao, R. H. Friend, D. Credgington, N. C. Greenham, and M. L. Bohm. *Synthesis and Optical Properties of Lead-Free Cesium Tin Halide Perovskite Nanocrystals*. J. Am. Chem. Soc. **138**, 2941-2944 (2016). 74

[Jung15] C. Jung, S. M. Kim, H. Moon, G. Han, J Kwon, Y. K. Hong, I. Omkaram, Y. Yoon, S. Kim, and J. Park. *Highly Crystalline CVD-grown Multilayer $MoSe_2$ Thin Film Transistor for Fast Photodetector*. Sci. Rep. **5**, 15313 (2015). 17, 95

[Kahn97] J. M. Kahn and J. R. Barry. *Wireless infrared communications*. Proc. IEEE **85**, 265-298 (1997). 51

[Kallhammer06] J.-E. Kallhammer. *Imaging: The road ahead for car night-vision*. Nat. Photonics **1**, 12 (2006). 51

[Kang17] W.-M. Kang, S. Lee, I.-T. Cho, T. H. Park, H. Shin, C. S. Hwang, C. Lee, B.-G. Park, and J.-H. Lee. *Multi-layer WSe_2 Field Effect Transistor with Improved Carrier-injection Contact by Using Oxygen Plasma Treatment*. Solid-State Electronics **140**, 2-7 (2017). 90

[Kappera14a] R. Kappera, D. Voiry, S. E. Yalcin, B. Branch, G. Gupta, A. D. Mohite, and M. Chhowalla. *Phase-engineered low-resistance contacts for ultrathin MoS_2 transistors*. Nature Materials **13**, 1128-1134 (2014). 32

[Kappera14b] R. Kappera, D. Voiry, S. E. Yalcin, W. Jen, M. Acerce, S. Torrel, B. Branch, S. Lei, W. Chen, S. Najmaei, J. Lou, P. M. Ajayan, G. Gupta, A. D. Mohite, and M. Chhowalla. *Metallic 1T phase source/drain electrodes for field effect*

transistors from chemical vapor deposited MoS_2. APL Materials **2**, 092516 (2014). 32

[Kazemi17] A. Kazemi, S. Vaziri, S. J. D. Morales, S. Fregonese, F. Cavallo, M. Zamiri, N. Dawson, K. Artyushkova, Y. B. Jiang, S. J. R. Brueck, and S. Krishna. *Vertical Charge Transfer and Lateral Transport in Graphene/Germanium Heterostructures*. ACS Appl. Mater. Interfaces **9** (18), 15830-15840 (2017). 48

[Kershaw13] S. V. Kershaw, A. S. Susha, and A. L. Rogach. *Narrow bandgap colloidal metal chalcogenide quantum dots: synthetic methods, heterostructures, assemblies, electronic and infrared optical properties*. Chem. Soc. Rev. **42**, 3033-3087 (2013). 11, 59

[Keuleyan11] S. Keuleyan, E. Lhuillier, V. Brajuskovic, and P. Guyot-Sionnest. *Mid-infrared HgTe colloidal quantum dot photodetectors*. Nat. Photonics **5**, 489-493 (2011). 11, 59

[Killilea19] N. Killilea, M. Wu, M. Sytnyk, A. A. Yousefi Amin, O. Mashkov, E. Spiecker, and W. Heiss. *Pushing PbS/Metal-Halide-Perovskite Core/Epitaxial-Ligand-Shell Nanocrystal Photodetectors beyond 3 µm Wavelength*. Adv. Funct. Mater. **29** (2019). 11, 59

[Kim04] S. Kim, Y. T. Lim, , E. G. Soltesz, A. M. D. Grand, J. Lee, A. Nakayama, J. A. Parker, T. Mihaljevic, R. G. Laurence, D. M. Dor, L. H. Cohn, M. G. Bawendi, and J. V. Frangioni. *Near-infrared fluorescent type II quantum dots for sentinel lymph node mapping*. Nat. Biotechnol. **22**, 93-97 (2004). 51

[Kim15] J.Y. Kim, V. Adinolfi, B. R. Sutherland, O. Voznyy, S. J. Kwon, T. W. Kim, J. Kim, H. Ihee, K. Kemp, M. Adachi, M. Yuan, I. Kramer, D. Zhitomirsky, S. Hoogland, and E. H. Sargent. *Single-step fabrication of quantum funnels via centrifugal colloidal casting of nanoparticle films*. Nat. Com. **6**, 7772 (2015). 40

[Klein98] A. Klein, Y. Tomm, R. Schlaf, C. Pettenkofer, W. Jaegerman, M. Lux-Steiner, and E. Bucher. *Photovoltaic Properties of WSe_2 Single Crystals Studied by Photoelectron Spectroscopy*. Solar Energy Material and Solar Cell **51**, 181-191 (1998). 92

[Konstantatos10] G. Konstantatos and E. H. Sargent. *Nanostructured materials for photon detection*. Nature nanotechnology **5**, 391-400 (2010). 41

[Konstantatos12] G. Konstantatos, M. Badioli, L. Gaudreau, J Osmond, M. Bernechea, F. P. G. de Arquer, F. Gatti, and F. H. L. Koppens. *Hybrid graphene-*

quantum dot phototransistors with ultrahigh gain. Nat. Nanotechnol. **7** (6), 363–368 (2012). 17, 19, 44, 45, 46, 74, 101

[Kufer15] D. Kufer, I. Nikitskiy, T. Lasanta, G. Navickaite, Frank H. L. Koppens, and G. Konstantatos. *Hybrid 2D-0D MoS_2-PbS quantum dot photodetectors*. Advanced Materials **27** (1), 176–180 (2015). 17, 46, 74

[Kufer16a] D. Kufer. *Photodetectors based on low-dimensional materials and hybrid systems*. PhD thesis, Universitat Politécnica de Catalunya ' Barcelona, (2016). 17, 53, 54, 95, 96

[Kufer16b] D. Kufer and G. Konstantatos. *Photo-FETs: phototransistors enabled by 2D and 0D nanomaterials*. ACS Photonics **3** (12), 2197-2210 (2016). 52

[Lai14] Y. Lai, H. Li, D. K. Kim, B. T. Diroll, C. B. Murray, and C. R. Kagan. *Low-Frequency (1/f) Noise in Nanocrystal Field-Effect Transistors*. ACS Nano **8**, 9664-9672 (2014). 109

[Lee18] H. Lee, , J. Ahn, S. Im, J. Kim, and W. Choi. *High-Responsivity Multilayer $MoSe_2$ Phototransistors with Fast Response Time*. Sci. Rep. **8** (2018). 17, 95

[Lhuillier12] E. Lhuillier, S. Keuleyan, and P. Guyot-Sionnest. *Optical Properties of HgTe Colloidal Quantum Dots*. Nanotechnology **23**, 175705 (2012). 41

[Lhuillier13] E. Lhuillier, S. Keuleyan, P. Zolotavin, and P. Guyot-Sionnest. *Mid-Infrared HgTe/As_2S_3 Field Effect Transistors and Photo- detectors*. Adv. Mater. **25**, 137-141 (2013). 11, 60

[Lhuillier14] E. Lhuillier, A. Robin, S. Ithurria, H. Aubin, and B. Dubertret. *Electrolyte-Gated Colloidal Nanoplatelets-Based Phototransistor and Its Use for Bicolor Detection.* Nano Lett. **14**, 2715-2719 (2014). 9, 51, 60, 77, 95, 108

[Lhuillier15] E. Lhuillier, J.-F. Dayen, D. O. Thomas, A. Robin, B. Doudin, and B. Dubertret. *Nanoplatelets Bridging a Nanotrench: A New Architecture for Photodetectors with Increased Sensitivity*. Nano Lett. **15**, 1736-1742 (2015). 53

[Lhuillier17] E. Lhuillier and P. Guyot-Sionnest. *Recent Progresses in Mid Infrared Nanocrystal Optoelectronics*. EEE J. Sel. Top. Quantum Electron **23**, 6000208 (2017). 8, 11, 21, 41, 59

[Li08] Xiaolin Li, Xinran Wang, Li Zhang, Sangwon Lee, and Hongjie Dai. *Chemically Derived, Ultrasmooth Graphene Nanoribbon Semiconductors*. Science **319** (5867), 1229–1232 (2008). 29

[Li11a] L. Li, A. Pandey, D. J. Werder, B. P. Khanal, B. P. Pietryga, and V. I. Klimov. *Efficient synthesis of highly luminescent copper indium sulfide-*

based core/shell nanocrystals with surprisingly long-lived emission. Journal of the American Chemical Society **133**, 1176-9 (2011). 41

[Li11b] Q. Li, E. H. Hwang, and S. Das Sarma. *Disorder-induced temperature-dependent transport in graphene: Puddles, impurities, activation, and diffusion*. Phys. Rev. B **84** (11), 115442 (2011). 29

[Li17] X. Li, L. Tao, Z. Chen, H. Fang, X. Li, X. Wang, J. B. Xu, and H. Zhu. *Graphene and related two-dimensional materials: Structure-property relationships for electronics and optoelectronics*. (2017). 32

[Liu12] H. Liu, S. Keuleyan, and P. Guyot-Sionnest. *n- and p-Type HgTe Quantum Dot Films*. J. Phys. Chem. C **116**, 1344-1349 (2012). 109

[Liu13] W. Liu, J. Kang, D. Sarkar, Y. Khatami, D. Jena, and Banerjee K. *Role of Metal Contacts in Designing High-Performance Monolayer n-Type WSe_2 Field Effect Transistors*. Nano Lett. **13** (90), 1983 (2013). 88

[Liu14] H. Liu, E. Lhuillier, and P. Guyot-Sionnest. *1/f Noise in Semiconductor and Metal Nanocrystal Solids*. J. Appl. Phys. **115**, 154309 (2014). 109

[Liu16a] X. Liu, X. Luo, H. Nan, H. Guo, P. Wang, L. Zhang, M. Zhou, Z. Yang, Y. Shi, W. Hu, Z. Ni, T. Qiu, Z. Yu, J.-B. Xu, and X. Wang. *Epitaxial Ultrathin Organic Crystals on Graphene for High-Efficiency Phototransistors*. Adv. Mater. **28**, 5200 (2016). 49

[Liu16b] Y. Liu, N. O. Weiss, X. Duan, H.-C. Cheng, Y. Huang, and X. Duan. *Van der Waals heterostructures and devices*. Nature Reviews Materials **1**, 16042 (2016). 25, 43, 44

[Livache17] C. Livache, E. Izquierdo, B. Martinez, M. Dufour, D. Pierucci, S. Keuleyan, H. Cruguel, L. Becerra, J. L. Fave, H. Aubin, A. Ouerghi, E. Lacaze, M. G. Silly, B. Dubertret, S. Ithurria, and E. Lhuillier. *Charge Dynamics and Optolectronic Properties in HgTe Colloidal Quantum Wells*. Nano Lett. **17**, 4067 (2017). 77, 108

[Livache18a] C. Livache, N. Goubet, B. Martinez, A. Jagtap, J. Qu, S. Ithurria, M. G. Silly, B. Dubertret, and E. Lhuillier. *Band Edge Dynamics and Multiexciton Generation in Narrow BandGap HgTe Nanocrystals*. ACS Appl. Mater. Interfaces **10**, 11880-11887 (2018). 76

[Livache18b] C. Livache, B. Martinez, N. Goubet, J. Ramade, and E. Lhuillier. *Road Map for Nanocrystal Based Infrared Photodetectors*. Front. Chem. **6**, 575 (2018). 11, 59

[Livache19] C. Livache. *Quantum-confined nanocrystals for infrared optoelectronics: Carrier dynamics and intraband transitions*. PhD thesis, Université de Sorborne, (2019). 11, 41, 42, 43, 53, 54, 59, 67

[Lopez-Sanchez13] Oriol Lopez-Sanchez, Dominik Lembke, Metin Kayci, Aleksandra Radenovic, and Andras Kis. *Ultrasensitive photodetectors based on monolayer MoS2*. Nat. Nanotechnol. **8** (7), 497–501 (2013). 46

[Lorchat19] E. Lorchat. *Optical spectroscopy of heterostructures based on atomically-thin semiconductors*. PhD thesis, Université de Strasbourg, (2019). 47

[Lu14] X. Lu, M. I. B. Utama, J. Lin, X. Gong, J. Zhang, Y. Zhao, S. T. Pantelides, J. Wang, Z. Dong, Z. Liu, W. Zhou, and Q. Xiong. *Large-area synthesis of monolayer and few-layer $MoSe_2$ films on SiO_2 substrates*. Nano Letters **14**, 2419-2425 (2014). 86

[Lu19] H. Lu, G. M. Carroll, N. R. Neale, and M. C Beard. *Infrared Quantum Dots: Progress, Challenges, and Opportunities*. ACS Nano **23**, 939-953 (2019). 11, 41, 59

[Luryi88] S. Luryi. *Quantum capacitance devices*. Appl. Phys. Lett. **52** (6), 501–503 (1988). 29, 106

[Lussani15] F. C. Lussani, R. F. C. Vescovi, R. F. C. Souza, C. A. P. Leite, and C. Giles. *Graphene/HgTe Quantum-Dot Photodetectors with Gate-Tunable Infrared Response*. Rev. Sci. Instrum. **86**, 063705 (2015). 51

[Mak10] K. F. Mak, C. Lee, J. Hone, J. Shan, and T. F. Heinz. *Atomically Thin MoS_2: A New Direct-Gap Semiconductor*. Phys. Rev. Lett. **105**, 136805 (2010). 34, 35

[Mak12a] K. F. Mak, K. He, J. Shan, and T. F. Heinz. *Control of valley polarization in monolayer MoS_2 by optical helicity*. Nat. Nanotechnol. **7** (8), 494–498 (2012). 35

[Mak12b] K. F. Mak, L. Ju, F. Wang, and T. F. Heinz. *Optical spectroscopy of graphene: from the far infrared to the ultraviolet*. Solid State Commun. **152** (15), 1341–1349 (2012). 28

[Mak16] K. F. Mak and J. Shan. *Photonics and optoelectronics of 2D semiconductor transition metal dichalcogenides*, (2016). 39

[Mansfield90] F. Mansfield. *Electrochemical impedance spectroscopy as a new tool for investigating methods of corrosion protection*. Electrochimica Acta **35**, 1533 (1990). 61

[Martinez18] B. Martinez, C. Livache, N. Goubet, A. Jagtap, H. Cruguel, A. Ouerghi, E. Lacaze, M. G. Silly, and E. Lhuillier. *Probing Charge Carrier Dynamics to Unveil the Role of Surface Ligands in HgTe Narrow Band Gap Nanocrystals.* J. Phys. Chem. C **122**, 859-865 (2018). 67

[Martinez19] B. Martinez, J. Ramade, C. Livache, N. Goubet, A. Chu, C. Greboval, J. Qu, W. L. Watkins, L. Becerra, E. Dandeu, J. L. Fave, C. Methivier, E. Lacaze, and E. Lhuillier. *HgTe Nanocrystal Inks for Extended Short-Wave Infrared Detection*. Adv. Opt. Mater. **7**, 1900348 (2019). 110

[Massicotte16] M. Massicotte, P. Schmidt, F. Vialla, K. G. Schädler, A. Reserbat-Plantey, K. Watanabe, T. Taniguchi, K. J. Tielrooij, and F. H. L. Koppens. *Picosecond photoresponse in van der Waals heterostructures*. Nat. Nanotechnol. **11** (1), 42–46 (2016). 48

[Mathieu09] H. Mathieu and H. Fanet. *Physique des semiconducteurs et des composants électroniques: cours et exercices corrigés*. Sciences sup. Dunod, 2009. 90, 125

[Mayorov11] A. S. Mayorov, R. V. Gorbachev, S. V. Morozov, L. Britnell, R. Jalil, L. A. Ponomarenko, P. Blake, K. S. Novoselov, K. Watanabe, T. Taniguchi, and A. K. Geim. *Micrometer-Scale Ballistic Transport in Encapsulated Graphene at Room Temperature*. Nano Lett. **11**, 2396 (2011). 30, 46

[Mohsen12] Q. Mohsen, S. Fadl-allah, and N. S. El-Shenawy. *Electrochemical Impedance Spectroscopy Study of the Adsorption Behavior of Bovine Serum Albumin at Biomimetic Calcium -Phosphate Coating*. Int. J. Electrochem. Sci. **7**, 4510 (2012). 12, 61

[Morozov08] S. V. Morozov, K. S. Novoselov, M. I. Katsnelson, F. Schedin, D. C. Elias, J. A. Jaszczak, and A. K. Geim. *Giant Intrinsic Carrier Mobilities in Graphene and Its Bilayer*. Phys. Rev. Lett. **100**, 016602 (2008). 28, 31

[Mouafo17] L. D. N. Mouafo, F. Godel, G. Froehlicher, S. Berciaud, B. Doudin, M. Venkata Kamalakar, and J-F. Dayen. *Tuning contact transport mechanisms in high on/off ratio bilayer $MoSe_2$ transistors up to Fowler-Nordheim regime*. 2D Mater. **4**, 015037 (2017). 16, 38, 86, 87, 88

[Mouafo18] L. D. N. Mouafo, F. Godel, G. Melinte, S. Hajjar-Garreau, H. Majjad, B. Dlubak, O. Ersen, B. Doudin, L. Simon, and J.-F Seneor, P.and Dayen. *Anisotropic Magneto-Coulomb Properties of 2D-0D Heterostructure Single Electron Device*. Adv. Mater **30**, 1802478 (2018). 44

[Mouafo19] L. D. N. Mouafo. *Two-dimensional materials, nanoparticles and thier heterostructures for nanoelectronics and spintronics*. PhD thesis, Université de Strasbourg, (2019). 27, 31, 33, 34, 125

[Mueller10] T. Mueller, F. Xia, and P. Avouris. *Graphene photodetectors for high-speed optical communications*. Nat. Photonics **4** (5), 297–301 (2010). 31

[Murray93] C. B. Murray, D. J. Norris, and M. G. Bawendi. *Synthesis and characterization of nearly monodisperse CdE (E = sulfur, selenium, tellurium) semiconductor nanocrystallites*. Journal of the American Chemical Society **115**, 8706-8715 (1993). 40

[Nair08] R. R. Nair, P. Blake, A. N. Grigorenko, K. S. Novoselov, T. J. Booth, T. Stauber, N. M. R. Peres, and A. K. Geim. *Fine structure constant defines visual transparency of graphene*. Science **320** (5881), 1308–1308 (2008). 28

[Nernst94] W. Nernst. *Method for determining dielectric constants.* Z. phys. Chem. **14**, 622 (1894). 12, 61

[Neumann15] C. Neumann, S. Reichardt, P. Venezuela, M. Drögeler, L. Banszerus, M. Schmitz, K. Watanabe, T. Taniguchi, F. Mauri, B. Beschoten, S. V. Rotkin, and C. Stampfer. *Raman spectroscopy as probe of nanometre-scale strain variations in graphene*. Nat. Commun. **6**, 8429 (2015). 102

[Nishikata95] A. Nishikata, Ichihara Y., T. Tsuru, K. Tanabe, and H. Mabuchi. *An electrochemical impedance study on atmospheric corrosion of steels in a cyclic wet-dry condition.* Corros. Sci. **37**, 2059-2069 (1995). 61

[Novoselov04] K. S. Novoselov, A. K. Geim, S. V. Morozov, D. Jiang, Y. Zhang, S. V. Dubonos, I. V. Grigorieva, and A. A. Firsov. *Electric field effect in atomically thin carbon films*. Science **306** (5696), 666–669 (2004). 26, 30, 82

[Novoselov16] K. S. Novoselov, A. Mishchenko, A. Carvalho, and A. H. Castro-Neto. *2D materials and van der Waals heterostructures*. Science **353** (6298), aac9439 (2016). 47

[Pan16] Y. Pan, S. Li, Meng Ye, R. Quhe, Z. Song, Y. Wang, J. Zheng, F. Pan, W. Guo, J. Yang, and J. Lu. *Interfacial Properties of Monolayer $MoSe_2$/Metal Contacts*. The Journal of Physical Chemistry C **120**, 26278-26283 (2016). 90, 94

[Parui15] S. Parui, L. Pietrobon, D. Ciudad, S. Vélez, X. Sun, F. Casanova, P. Stoliar, and L. E. Hueso. *Gate-controlled energy barrier at a graphene/molecular semiconductor junction*. Advanced Functional Materials **25**, 2972-2979 (2015). 47, 48

[Parui17] S. Parui, R. Llopis F. Casanova M. Ribeiro, A. Atxabal, and L. E. Hueso. *Graphene as an electrode for solution-processed electron-transporting organic transistors*. Nanoscale **9**, 10178-10185 (2017). 115

[Pawbake16] A. S. Pawbake, M. S. Pawar, S. R. Jadkar, and D. J. Late. *Large area chemical vapor deposition of monolayer transition metal dichalcogenides and their temperature dependent Raman spectroscopy studies*. Nanoscale **8**, 3008-3018 (2016). 86

[Peres07] N. M. R. Peres and E. V. Castro. *Algebraic solution of a graphene layer in transverse electric and perpendicular magnetic fields*. Journal of Physics: Condensed Matter **19** (40), 406231 (2007). 27, 28

[Pisoni18] R. Pisoni, Z. Lei, P. Back, M. Eich, H. Overweg, Y. Lee, K. Watanabe, T. Taniguchi, T. Ihn, and K. Ensslin. *Gate-tunable quantum dot in a high quality single layer MoS2 van der Waals heterostructure*. Applied Physics Letters **112** (12), 123101 (2018). 46

[Pospischil13] A. Pospischil, M. Humer, M. M. Furchi, D. Bachmann, R. Guider, T. Fromherz, and T. Mueller. *CMOS-compatible graphene photodetector covering all optical communication bands*. Nat. Photonics **7** (11), 892–896 (2013). 31

[Pospischil14] Andreas Pospischil, Marco M. Furchi, and Thomas Mueller. *Solar-energy conversion and light emission in an atomic monolayer p-n diode*. Nat. Nanotechnol. **advance online publication** (2014). 39, 88

[Pradhan14] N. R. Pradhan, D. Rhodes, S. Feng, Y. Xin, S. Memaran, B.-H. Moon, H. Terrones, M. Terrones, and L. Balicas. *Field-Effect Transistors Based on Few-Layered α-$MoTe_2$*. ACS Nano **8**, 5911 (2014). 38

[Pradhan15a] N. R. Pradhan, A. McCreary, D.l Rhodes, Z. Lu, S. Feng, E. Manousakis, D. Smirnov, R. Namburu, M. Dubey, A. R. Hight Walker, H. Terrones, M. Terrones, V. Dobrosavljevic, and L. Balicas. *Metal to insulator quantum-phase transition in few-layered ReS_2*. Nano letters **15** (12), 8377–8384 (2015). 37

[Pradhan15b] N. R. Pradhan, D. Rhodes, S. Memaran, J. M. Poumirol, D. Smirnov, S. Talapatra, S. Feng, N. Perea-Lopez, A. L. Elias, M. Terrones, P. M. Ajayan, and L. Balicas. *Hall and field-effect mobilities in few layered p-WSe_2 field-effect transistors*. Scientific Reports **5** (8979) (2015). 88, 89

[Qian11] L. Qian, J. Xue Y. Zheng, and P. H. Holloway. *Stable and efficient quantum dot light-emitting diodes based on solution-processed multilayer structures*. Nature Phothonics **5**, 543-548 (2011). 41

[Qu19] J. Qu, C. Livache, B. Martinez, C. Greboval, A. Chu, E. Meriggio, J. Ramade, H. Cruguel, X. Z. Xu, A. Proust, F. Volatron, G. Cabailh, N. Goubet, and E. Lhuillier. *Transport in ITO Nanocrystals with Short- to Long-Wave*

Infrared Absorption for Heavy-Metal-Free Infrared Photodetection. ACS Appl. Nano Mater. **2**, 1621-1630 (2019). 28

[Radisavljevic11] B. Radisavljevic, A. Radenovic, J. Brivio, V. Giacometti, and A. Kis. *Single-layer MoS_2 transistors.* Nature Nanotechnology **6** (3), 147–150 (2011). 38

[Radisavljevic13] B. Radisavljevic and A. Kis. *Mobility engineering and a metal-insulator transition in monolayer MoS_2.* Nature Materials **12** (9), 815–820 (2013). 8, 21

[Randviir13] E. P. Randviir and Craig E. B. *Electrochemical impedance spectroscopy: an overview of bioanalytical applications.* Anal. Methods **5**, 1098 (2013). 12, 62, 65

[Reich02] S. Reich, J. Maultzsch, C. Thomsen, and P. Ordejón. *Tight-binding description of graphene.* Phys. Rev. B **66**, 035412 (2002). 27

[Ribeiro-Soares14] J. Ribeiro-Soares, R. M. Almeida, E. B. Barros, P. T. Araujo, M. S. Dresselhaus, L. G. Cancado, and A. Jorio. *Group theory analysis of phonons in two-dimensional transition metal dichalcogenides.* Phys. Rev. B **90** (11), 115438 (2014). 33, 34, 35

[Robin16] A. Robin, E. Lhuillier, X. Z. Xu, S. Ithurria, H. Aubin, A. Ouerghi, and B. Dubertret. *Engineering the Charge Transfer in all 2D Graphene-Nanoplatelets Heterostructure Photodetectors.* Scientific Reports **6** (1), 24909 (2016). 110

[Rose63] A. Rose. *Concepts in Photoconductivity and Allied Problems.* Interscience Publishers, New York, NY, 1963. 97, 111

[Ruzmetov16] D. Ruzmetov, K. Zhang, G. Stan, B. Kalanyan, G. R. Bhimanapati, M. S. Eichfeld, R. A. Burke, P. J. Shah, F. O'Regan, T. P. anf JCrowne, A. G. Birdwell, A. Robinson, A. V. Davydov, and T. G. Ivanov. *Vertical 2D/3D semiconductor heterostructures based on epitaxial molybdenum disulfide and gallium nitride.* ACS Nano **10**, 3580-3588 (2016). 48

[Saran16] R. Saran and R. J. Curry. *Lead sulphide nanocrystal photodetector technologies.* Nature Phothonics **10**, 81-92 (2016). 41

[Schmidt15] H. Schmidt, F. Giustiniano, and G. Eda. *Electronic transport properties of transition metal dichalcogenide field-effect devices: surface and interface effects*, (2015). 32, 34, 36, 37, 38

[Schoonman80] J. Schoonman, G. Oversluizen, and K. E. D. Wapenaar. *Solid electrolyte properties of LaF_3.* Solid State Ionics **1** (3), 211-221 (1980). 11, 61

[Seneor07] P. Seneor, A. Bernand-Mantel, and F. Petroff. *Nanospintronics: When spintronics meets single electron physics*. Journal of Physics Condensed Matter **19** (16), 165222 (2007). 8, 21

[Shklovskii84] B. I. Shklovskii and A. L. Efros. *Electronic properties of doped semiconductors*, volume 45. Springer Science, 1984. 35, 36, 37

[Smith10] A. M. Smith and S. Nie. *Semiconductor Nanocrystals: Structure, Properties, and Band Gap Engineering*. Acc. Chem. Res. **43**, 190-200 (2010). 40

[Solomon] R. Solomon, A. Sher, and M. W. Muller. 11, 61

[Song19] G. Song, M. Ranjbar, D. R. Daughton, and R. A. Kiehl. *Nanoparticle-Induced Anomalous Hall Effect in Graphene*. Nano Letter **19**, 7112-7118 (2019). 44

[Splendiani10] A. Splendiani, L. Sun, Y. Zhang, T. Li, J. Kim, C.-Y. Chim, G. Galli, and F. Wang. *Emerging Photoluminescence in Monolayer* MoS_2. Nano Lett. **10** (4), 1271–1275 (2010). 35

[Steckel03] J. Steckel, V. Bulovic S. Coe-Sullivan, and M. Bawendi. *1.3μm to 1.55μm Tunable Electroluminescence from PbSe Quantum Dots Embedded within an Organic Device*. Advanced Materials **15**, 1862-1866 (2003). 41

[Svane11] A. Svane, N. E. Christensen, M. Cardona, A. N. Chantis, M. van Schilfgaarde, and T.l. Kotani. *Quasiparticle band structures of beta-HgS, HgSe, and HgTe.* Physical Review B **84** (20) (2011). 41

[Sze81] S.M. Sze. *Physics of Semiconductor Devices*. John Wiley & Sons, 1981. 92, 125

[Talapin10] D. V. Talapin, M. V. Kovalenko J.-S. Lee, and E. V. Shevchenko. *Prospects of colloidal nanocrystals for electronic and optoelectronic applications*. Chemical Reviews **110**, 389-458 (2010). 40

[Tang16] X. Tang, X. Tang, and K. W. C. Lai. *Scalable Fabrication of Infrared Detectors with Multispectral Photoresponse Based on Patterned Colloidal Quantum Dot Films*. ACS Photonics **3**, 2396-2404 (2016). 60

[Tang18] X. Tang, M. M. Ackerman, and P. Guyot-Sionnest. *Thermal Imaging with Plasmon Resonance Enhanced HgTe Colloidal Quantum Dot Photovoltaic Devices*. ACS Nano **12**, 7362-7370 (2018). 109

[Tang19a] X. Tang, M. M. Ackerman, M. Chen, and P. Guyot-Sionnest. *Dual-band infrared imaging using stacked colloidal quantum dot photodiodes*. Nat. Photonics **13**, 277-282 (2019). 59, 60, 109, 114

[Tang19b] X. Tang, M. M. Ackerman, G. Shen, and P. Guyot-Sionnest. *Towards Infrared Electronic Eyes: Flexible Colloidal Quantum Dot Photovoltaic Detectors Enhanced by Resonant Cavity*. Small **15**, 1804920 (2019). 59, 60

[Tang19c] X. Tang and K. W. C Lai. *Graphene/HgTe Quantum-Dot Photodetectors with Gate-Tunable Infrared Response*. ACS Appl. Nano Mater **2**, 6701-6706 (2019). 46, 110

[Trevisanutto08] P. E. Trevisanutto, C. Giorgetti, L. Reining, M. Ladisa, and V. Olevano. *Ab Initio GW Many-Body Effects in Graphene*. Phys. Rev. Lett. **101**, 226405 (2008). 103

[Vicarelli12] L. Vicarelli, M. S. Vitiello, D. Coquillat, A. Lombardo, A. C. Ferrari, W Knap, M. Polini, V. Pellegrini, and A. Tredicucci. *Graphene field-effect transistors as room-temperature terahertz detectors*. Nat. Mater. **11** (10), 865–871 (2012). 31

[Voiry13] D. Voiry, H. Yamaguchi, J. Li, R. Silva, D. C. B. Alves, T. Fujita, M. Chen, T. Asefa, V. B. Shenoy, G. Eda, and M. Chhowalla. *Enhanced catalytic activity in strained chemically exfoliated WS_2 nanosheets for hydrogen evolution*. Nature Materials **12**, 850 (2013). 32

[Wallace47] P. R. Wallace. *The band theory of graphite*. Phys. Rev. **71** (9), 622 (1947). 27

[Wang12] Qing Hua Wang, Kourosh Kalantar-Zadeh, Andras Kis, Jonathan N. Coleman, and Michael S. Strano. *Electronics and optoelectronics of two-dimensional transition metal dichalcogenides*. Nature Nanotechnology **7**, 699 (2012). 32

[Wang16] K. Wang, T. Taniguchi, K. Watanabe, and P. Kim. *Engineering Quantum Confinement in Semiconducting van der Waals Heterostructure*. arXiv: Mesoscale and Nanoscale Physics (2016). 46

[Wang17] H. Wang, E. Lhuillier, Q. Yu, A. Zimmers, B. Dubertret, C. Ulysse, and H. Aubin. *Transport in a single self-doped nanocrystal*. ACS nano **11** (2), 1222–1229 (2017). 53

[Wang18] Z. Wang, Q. Li, Y Chen, B. Cui, Y. Li, F. Besenbacher, and M. Dong. *The ambipolar transport behavior of WSe_2 transistors and its analogue circuits*. NPG Asia Mater **10**, 703-712 (2018). 88

[Warburg99] E. Warburg. *About the behavior of so-called non-polarizable electrodes against alternating current*. Ann. Phys. Chem. **303**, 493 (1899). 12, 61

[Willis09] L. J. Willis, M. D. Fischbein J. A. Fairfield, T. Dadosh, and M. Drndic. *Highly Sensitive, Encapsulated MoS_2 Photodetector with Gate Controllable Gain and Speed*. Nano Lett. **9**, 4191 (2009). 97, 111

[Wu17] C. Wu, F. Wang, C. Cai, Z. Xu, Y. Ma, F. Huang, F. Jia, and M. Wang. *Integration of graphene/ZnS nanowire film hybrids based photodetector arrays for high-performance image sensors*. 2D Materials **4** (2), 025113 (2017). 46

[Wu18] C. L. Wu, H. Yuan, Y. Li, Y. Gong, H. Y. Hwang, and Y. Cui. *Gate-Induced Metal-Insulator Transition in MoS_2 by Solid Superionic Conductor LaF_3*. Nano Lett. **18**, 2387-2392 (2018). 9, 12, 60, 61, 81

[Xia09a] F. Xia, T. Mueller, R. Golizadeh-Mojarad, M. Freitage, Y. M. Lin, J. Tsang, V. Perebeinos, and P. Avouris. *Photocurrent imaging and efficient photon detection in a graphene transistor*. Nano Letters **9** (3), 1039–1044 (2009). 29, 106

[Xia09b] Fengnian Xia, Thomas Mueller, Yu-ming Lin, Alberto Valdes-Garcia, and Phaedon Avouris. *Ultrafast graphene photodetector*. Nat. Nanotechnol. **4** (12), 839–843 (2009). 31

[Xia14] J. Xia, M. Wang L. Wang B. Huang D.-. Zhu J.-J. Li C.-Z. Gu X. Huang, L.-Z. Liu, and X.-M. Meng. *CVD Synthesis of Large-Area, Highly Crystalline MoSe2 Atomic Layers on Diverse Substrates and Application to Photodetectors*. Nanoscale **6**, 8949 (2014). 17, 95

[Xiao18] J. Xiao, Y. Zhang, H. Chen, N. Xu, and S. Deng. *Enhanced Performance of a Monolayer MoS_2/WSe_2 Heterojunction as a Photoelectrochemical Cathode*. Nano-Micro Lett. **10**, 60 (2018). 90

[Xu11] H. Xu, Z. Zhang, Z. Wang, S. Wang, X. Liang, and L.-M. Peng. *Quantum Capacitance Limited Vertical Scaling of Graphene Field-Effect Transistor*. ACS Nano **5** (3), 2340–2347 (2011). 30

[Xue18] H. Xue, Y. Wang, Y. Dai, W. Kim, H. Jussila, M. Qi, J. Susoma, Z. Ren, Q. Dai, J. Zhao, K. Halonen, H. Lipsanen, X. Wang, X. Gan, and Z. Sun. *A $MoSe_2$-WSe_2 Heterojunction-Based Photodetector at Telecommunication Wavelengths*. Adv. Funct. Mater **20**, 1804388 (2018). 47, 48, 89

[Yang17] H. Yang, S. W. Kim, M. Chhowalla, and Y. H. Lee. *Structural and quantum-state phase transition in van der Waals layered materials*. Nature Physics **13**, 931-937 (2017). 32, 35, 38

[Ye11] J. Ye, M. F. Craciun, M. Koshino, S. Russo, S. Inoue, H. Yuan, H. Shimotani, A. F. Morpurgo, and Y. Iwasa. *Accessing the transport properties*

of graphene and its multilayers at high carrier density. Proceedings of the National Academy of Sciences **108** (32), 13002–13006 (2011). 30

[Ye12] J. T. Ye, Y. J. Zhang, R. Akashi, R. Bahramy, M. S. Arita, and Y. Iwasa. *Superconducting Dome in a Gate-Tuned Band Insulator*. Science **338**, 1193-1196 (2012). 39, 51, 81, 87

[Yin11] Zongyou Yin, Hai Li, Hong Li, Lin Jiang, Yumeng Shi, Yinghui Sun, Gang Lu, Qing Zhang, Xiaodong Chen, and Hua Zhang. *Single-Layer MoS_2 Phototransistors*. ACS nano **6** (1), 74–80 (2011). 39

[Yu09] Y.-J. Yu, Y. Zhao, S. Ryu, L. E. Brus, K. S. Kim, and P. Kim. *Tuning the Graphene Work Function by Electric Field Effect*. Nano Lett. **9**, 3430-3434 (2009). 103, 104

[Yu13] W. J. Yu, Y. Liu, H. Zhou, A. Yin, Z. Li, Y. Huang, and X. Duan. *Highly efficient gate-tunable photocurrent generation in vertical heterostructures of layered materials*. Nat. Nanotechnol. **8** (12), 952–958 (2013). 47

[Yu16] Z. Yu, Z. Y. Ong, Y. Pan, Y. Cui, R. Xin, Y. Shi, B. Wang, Y. Wu, T. Chen, Y. W. Zhang, G. Zhang, and X. Wang. *Realization of Room-Temperature Phonon-Limited Carrier Transport in Monolayer MoS_2 by Dielectric and Carrier Screening*. Advanced Materials **28** (3), 547–552 (2016). 38

[Yu17] Y. Yu, Y. T. Zhang, X. X. Song, H. T. Zhang, M. X. Cao, Y. L. Che, H. T. Dai, J. B. Yang, H. Zhang, and J. Q. Yao. *PbS-decorated WS_2 phototransistors with fast response*. ACS Photonics **4**, 950 (2017). 46, 74

[Yuan10] H. Yuan, H. Shimotani, J. Ye, S. Yoon, H. Aliah, A. Tsukazaki, M. Kawasaki, and Y. Iwasa. *Electrostatic and Electrochemical Nature of Liquid-Gated Electric-Double-Layer Transistors Based on Oxide Semiconductors*. J. AM. CHEM. SOC. **132**, 18402-18407 (2010). 62, 65

[Yuan11] H. T. Yuan, M. Toh, K. Morimoto, W. Tan, F. Wei, H. Shimotani, Ch. Kloc, and Y. Iwasa. *Liquid-gated electric-double-layer transistor on layered metal dichalcogenide SnS_2*. Appl. Phys. Lett. **98**, 012102 (2011). 38

[Yuan13] H. Yuan, M. S. Bahramy, K. Morimoto, S. Wu, K. Nomura, B.-J. Yang, H Shimotani, R. Suzuki, M. Toh, C. Kloc, X. Xu, R. Arita, N. Nagaosa, and Y. Iwasa. *Zeeman-type spin splitting controlled by anelectric field*. Nat. Phys. **9** (9), 563 (2013). 88

[Zanettini15a] S. Zanettini. *High mobility materials for Organic Spintronic applications*. PhD thesis, Université de Strasbourg, (2015). 9, 50, 51

[Zanettini15b] S. Zanettini, N. Leclerc M. V. Kamalakar J. F. Dayen, C. Etrillard, and B. Doudin. *Magnetoconductance Anisotropy of a Polymer Thin Film at the Onset of Metallicity*. Appl. Phys. Lett. **106**, 2-6 (2015). 115

[Zeng12] H. Zeng, J. Dai, W. Yao, D. Xiao, and X. Cui. *Valley polarization in MoS_2 monolayers by optical pumping*. Nature Nanotechnology **7** (8), 490–493 (2012). 35

[Zeng13] H. Zeng, G.-B. Liu, J. Dai, Y. Yan, B. Zhu, R. He, L. Xie, S. Xu, X. Chen, W. Yao, and X. Cui. *Optical signature of symmetry variations and spin-valley coupling in atomically thin tungsten dichalcogenides*. Sci. Rep. **3**, 1608 (2013). 35

[Zeskind07] B. J. Zeskind, C. D. Jordan, W. Timp, L. Trapani, G. Waller, V. Horodincu, D. J. Ehrlich, and P. Matsudaira. *Nucleic acid and protein mass mapping by live-cell deep-ultraviolet microscopy.* Nat. Methods **4**, 567 (2007). 51

[Zhang12] Y. J. Zhang, J. T. Ye, Y. Matsuhashi, and Y. Iwasa. *Ambipolar MoS_2 Thin Flake Transistors*. Nano Lett. **12** (3), 1136-1140 (2012). 81

[Zhang13a] X. Zhang, W. P. Han, J. B. Wu, S. Milana, Y. Lu, Q. Li, A. C. Ferrari, and P. H. Tan. *Raman spectroscopy of shear and layer breathing modes in multilayer* MoS_2. Phys. Rev. B **87**, 115413 (2013). 39

[Zhang13b] Y. J. Zhang, J. T. Ye, Y. Matsuhashi, and Y. Iwasa. *Formation of a Stable p-n Junction in a Liquid-Gated MoS_2 Ambipolar Transistor*. Nano Lett. (2013). 51, 81, 87

[Zhang14] Y. Zhang, T. R. Chang, B. Zhou, Y. T. Cui, H. Yan, Z. Liu, F. Schmitt, J. Lee, R. Moore, Y. Chen, H. Lin, H. Tay Jeng, S. K. Mo, Z. Hussain, Ar. Bansil, and Z. X. Shen. *Direct observation of the transition from indirect to direct bandgap in atomically thin epitaxial $MoSe_2$*. Nature Nanotechnology **9**, 111-115 (2014). 35

[Zhang16] K. Zhang, T. Zhang, G. Cheng, T. Li, S. Wang, W. Wei, X. Zhou, W. Yu, Y. Sun, P. Wang, D. Zhang, C. Zeng, X. Wang, W. Hu, H. J. Fan, , J. Shen, Chen X., K. Duan, X. Chang, and N. Dai. *Interlayer Transition and Infrared Photodetection in Atomically Thin Type-II $MoTe_2$-MoS_2 van der Waals Heterostructures*. ACS Nano **10** (3), 3852–3858 (2016). 38

[Zhang19] Z. Zhang, P. Lin, Q. Liao, Z. Kang, H. Si, and Y Zhang. *Graphene-Based Mixed-Dimensional van Der Waals Heterostructures for Advanced Optoelectronics*. Adv. Mater **31**, 1806411 (2019). 44